

Copyright

By

Qinwu Xu

2014

**The Dissertation Committee for Qinwu Xu certifies that this is the approved  
version of the following dissertation:**

**Development of a Computational Method for Inverting Dynamic  
Moduli of Multilayer Systems with Applications to Flexible  
Pavements under FWD Tests**

**Committee:**

---

Jorge A. Prozzi, Supervisor

---

Amit Bhasin

---

Raissa P. Ferron

---

Omar Ghattas

---

Krishnaswamy Ravi-Chandar

---

Kenneth H. Stokoe II

**Development of a Computational Method for Inverting Dynamic  
Moduli of Multilayer Systems with Applications to Flexible  
Pavements under FWD Tests**

**by**

**Qinwu Xu, B.E.; M.S.**

**Dissertation**

Presented to the Faculty of the Graduate School of  
The University of Texas at Austin  
in Partial Fulfillment  
of the Requirements  
for the Degree of

**Doctor of Philosophy**

**The University of Texas at Austin  
August 2014**

## **Acknowledgements**

I deeply appreciate Dr. Jorge A. Prozzi, my Ph.D. supervisor, for his patient and insightful guidance during my Ph.D. studies and dissertation research as well as his kind encouragement and support. I am thankful for the knowledge gained from my studies with him in pavement engineering. I also greatly appreciate my dissertation committee members: Dr. Kenneth H. Stokoe II for his critical advice on soil and structural dynamics, which helped me make significant improvements in the numerical models; Dr. Omar Ghattas and his group for their many instances of selfless and very helpful guidance, reviews, and discussions on computational science, and his always kind support; Dr. Amit Bhasin for his important reviews and comments on material viscoelasticity and his kind support during all my study; Dr. K. Ravi-Chandar for his key insights and comments on solid mechanics; and Dr. Raissa P. Ferron for her constructive feedback.

I also offer my sincere thanks to those at the University of Texas at Austin (UT Austin): Dr. Georg Stadler at the Institute of Computational Science and Engineering (will be an Associate Professor at New York University, Applied Mathematics since fall 2014) for his patience and many valuable appointments, discussions, advice, and comments on inverse computations; Hongyu Zhu and Tobin G. Isaac, Ph.D. candidates at the Department of Computational and Applied Mathematics—to Dr. Zhu for her multiple detailed discussions, reviews, and comments on the mathematical models—and to Dr. Isaac for his valuable comments; and to Arash Fathi, Ph.D. candidate, and Dr. Loukas Kallivokas in Structural Mechanics for their constructive comments on finite element (FE) modeling.

Other thanks go to Dr. Pengcheng Fu at the Lawrence Livermore National Laboratory for his very helpful discussions; Dr. Andre Smit at the Center for Transportation Research, UT Austin; Dr. George Chang at the Transtec Group, Inc.; Dr. Dr. Yigong Ji, and Dr. Tommy Nantung at the Indiana Department of Transportation; Dr. Ervin Dukatz at the Mathy Construction Co., and Dr. Soheil Nazarian at the University of

Texas at EL Paso—all of whom helped me with experimental tests and data collection. I am also very grateful for the Long-term Pavement Performance Program of the Federal Highway Administration and that program's valuable contribution to my work.

I also thank Dan Rozycki and those at the Transtec Group, Inc, who offered me a job and a flexible work schedule from June 2007 to January 2014. I am also very thankful for their memorable friendships.

Finally, my deepest thanks go to my parents and sister in China for their unconditional understanding, support, and encouragement during my university studies.

**Development of a Computational Method for Inverting Dynamic  
Moduli of Multilayer Systems with Applications to Flexible Pavements  
under FWD Tests**

Qinwu Xu, Ph.D.

The University of Texas at Austin, 2014

Supervisor: Jorge A. Prozzi

Most existing computational methods for inverting material properties of multilayer systems have focused primarily on elastic properties of materials or a static approach. Typically, they are based on a two-stage approach: (I) modeling structural responses with a computer program, and (II) estimating layer properties mathematically using the response outputs determined in stage I without interactions with the governing state partial-differential-equation (PDE) of stage I. This two-stage approach may not be accurate and efficient enough for inverting larger scale model parameters. The objective of this research was to develop a computational method to invert dynamic moduli of multilayer systems with applications to flexible pavements under falling weight deflectometer (FWD) tests, thereby advancing existing methods and fostering understanding of material behaviors. This research first developed a finite-element and Newton-Raphson method to invert layer elastic moduli using FWD data. The model improved the moduli seeds estimation and achieved a satisfactory accuracy based on Monte Carlo simulations, addressing the common back-calculation issue of no unique solutions. Consequently, a time-domain finite-element method was developed to simulate dynamic-viscoelastic responses of the multilayer systems under loading pulses.

Simulation results demonstrated that the dynamic-viscoelastic-damping-coupled model could emulate structural responses more accurately, thereby advancing existing simulation approaches. By using the dynamic-viscoelastic-response model as one computation module, this research led to the development of a PDE-constrained Lagrangian optimization method to invert dynamic moduli and viscoelastic properties of multilayer systems. The Lagrangian function was used as an objective function, with a regularization term and governing-state PDE constraint. Both the first-order (gradient) and second-order variation (Hessian matrix) of the Lagrangian were computed to satisfy necessary and sufficient optimality conditions, and Armijo rule was modified to determine a stable step length. The developed method improved computation speed significantly, and it is superior for large-scale inverse problems. The model was implemented for evaluating flexible pavements under FWD tests and for inverting the master curve of dynamic moduli of the asphalt layer. Independent computer coding was developed for all numerical methods. The computational methods developed may also be applied to other multilayer systems, such as tissues and sandwich structures at different time and length scales.

## Table of Contents

|   |      |
|---|------|
| Acknowledgements .....  | iv   |
| Table of Contents .....   | viii |
| List of Tables .....  | xii  |
| List of Figures .....   | xiii |
| Notations .....   | xvi  |
| Chapter 1: Introduction .....   | 1    |
| 1.1 Background and Literature Review .....  | 1    |
| 1.1.1 Material Viscoelasticity and Models of Solids .....   | 1    |
| 1.1.2 Damping Models .....  | 8    |
| 1.1.3 Multilayer Systems with Viscoelastic Properties .....   | 9    |
| 1.1.4 FWD Nondestructive Test .....   | 11   |
| 1.1.5 Pavement Design Methods with Moduli Inputs .....  | 13   |
| 1.1.5.1 Material parameters input .....   | 14   |
| 1.1.5.2 Building master curve based on time-temperature superposition .....                                 | 17   |
| 1.1.5.3 Response model .....  | 20   |
| 1.1.6 Multilayer Property Backcalculation .....   | 20   |
| 1.1.6.1 General principles of backcalculation- a two-stage approach .....                                   | 20   |
| 1.1.6.2 Inverse approach for multilayer systems in science & engineering .....                              | 22   |
| 1.1.6.3 Commonly used response models of flexible pavements .....   | 23   |
| 1.1.6.4 Commonly used optimization algorithms for multilayer systems .....                                  | 24   |
| 1.1.6.5 Static FWD backcalculation programs .....   | 25   |
| 1.1.6.6 Dynamic or static viscoelastic FWD backcalculation research .....                                   | 26   |
| 1.2 Research Problems .....   | 30   |
| 1.3 Research Objective .....  | 32   |
| 1.4 Research Scope .....  | 32   |
| Chapter 2: A Finite-element Model and Newton-Raphson Method for Inverting Elastic Moduli <sup>1</sup> ..... | 34   |
| 2.1 Background .....  | 35   |
| 2.2 Finite Element Model Development for Pavement Analysis .....  | 37   |
| 2.2.1 Axisymmetric Model .....  | 37   |
| 2.2.1.1 Stress Equilibrium .....  | 38   |
| 2.2.1.2 State Equation .....  | 40   |
| 2.2.1.3 Boundary Conditions .....   | 41   |
| 2.2.2 Temperature Profile and Modulus Variation .....   | 42   |
| 2.2.3 Numerical Solution .....  | 42   |
| 2.2.3.1 Finite elements .....   | 43   |
| 2.2.3.2 Infinite elements .....   | 44   |
| 2.2.3.3 FE solution of displacements .....  | 45   |
| 2.3 Newton-Raphson Inverse Algorithm .....  | 48   |
| 2.3.1 Guess initial moduli seed values .....  | 48   |
| 2.3.2 Inverse computing layer elastic moduli .....  | 50   |

|   |   |     |
|---|---|-----|
| 2.3.3   | Computer coding for numerical solution .....      | 53  |
| 2.4   | Validation Method .....                           | 54  |
| 2.5   | Results and Analyses .....                        | 56  |
| 2.5.1   | FE Model Validation .....                         | 56  |
| 2.5.2   | Inversion Results and analyses .....              | 58  |
| 2.5.2.1   | Simulated responses compared to true values ..... | 58  |
| 2.5.2.2   | Comparison with popular commercial software ..... | 58  |
| 2.5.2.2   | Effect of iteration steps .....                   | 59  |
| 2.5.2.3   | Effects of initial moduli seed values .....       | 60  |
| 2.5.2.4   | Moduli profile as temperature dependent .....     | 64  |
| 2.5.2.5   | Effect of Root Mean Square .....                  | 67  |
| 2.6   | Summary .....                                     | 69  |
| Chapter 3: A Time-domain Finite Element Method for Dynamic Viscoelastic Solution of Layered-half-space Responses under Loading Pulse..... |   | 71  |
| 3.1.  | Background .....                                  | 72  |
| 3.2.  | Research Motivation and Significance .....        | 77  |
| 3.3.  | Model Development.....                            | 80  |
| 3.3.1   | Model domain and governing state equation .....   | 80  |
| 3.3.2   | Material model.....                               | 83  |
| 3.3.3   | Stress-strain constitutive relations.....         | 86  |
| 3.3.4   | Weak form of state equation .....                 | 87  |
| 3.4.  | Numerical Solution Method.....                    | 88  |
| 3.4.1   | Finite element and shape function.....            | 88  |
| 3.4.2   | FE formulation.....                               | 89  |
| 3.4.3   | Time discretization .....                         | 91  |
| 3.4.4   | Viscoelastic stiffness matrix .....               | 93  |
| 3.4.5   | Formulation of global linear system .....         | 94  |
| 3.4.6   | Space discretization .....                        | 95  |
| 3.4.7   | Solution of global linear system .....            | 97  |
| 3.4.8   | Computer code development .....                   | 100 |
| 3.5.  | Experimental Design.....                          | 101 |
| 3.6.  | Results and Analysis .....                        | 103 |
| 3.6.1   | Model validations .....                           | 103 |
| 3.6.1.1   | Pavement structure and material properties.....   | 103 |
| 3.6.1.2   | FE model.....                                     | 105 |
| 3.6.1.3   | Validation results .....                          | 106 |
| 3.6.2   | Simulations of FWD testing .....                  | 109 |
| 3.6.2.1   | Deflections .....                                 | 109 |
| 3.6.2.1   | Velocity and acceleration.....                    | 114 |
| 3.6.2.2   | First principal stress .....                      | 116 |
| 3.6.3   | Simulations of vehicle loading.....               | 117 |
| 3.6.3.1   | Deflections .....                                 | 117 |
| 3.6.3.2   | Stress and strain .....                           | 118 |

|  |   |     |
|--|---|-----|
| 3.6.4  | Temperature and moduli profiles.....  | 121 |
| 3.7.   | Summary.....  | 124 |
| Chapter 4: A Lagrangian Optimization Method for Inverting Dynamic Moduli of Multilayer Systems ..... |   | 127 |
| 4.1.   | Background.....   | 128 |
| 4.2.   | Inverse Problem and Lagrangian Function.....  | 133 |
| 4.2.1  | Model Domain.....   | 133 |
| 4.2.2  | Inverse Problem .....   | 135 |
| 4.2.3  | Cost Function .....   | 136 |
| 4.2.4  | Lagrangian Function .....   | 137 |
| 4.3.   | Inverse Computation Method .....  | 137 |
| 4.3.1  | Optimality Conditions .....   | 137 |
| 4.3.2  | Inverse procedures .....  | 138 |
| 4.3.2.1  | Framework .....   | 138 |
| 4.3.2.2  | Calculation of Gradient and Hessian .....   | 140 |
| 4.3.2.3  | Determining Search Direction and Step Length .....                                    | 142 |
| 4.3.3  | Computation Time.....   | 143 |
| 4.4.   | Numerical Solution Method.....  | 144 |
| 4.4.1  | Lagrangian Weak Form.....   | 144 |
| 4.4.2  | Computation of Gradient Vector .....  | 145 |
| 4.4.2.1  | State equation to determine deflection $u$ .....                                      | 145 |
| 4.4.2.2  | Adjoint equation to determine test function $p$ .....                                 | 146 |
| 4.4.2.3  | Decision equation to determine gradient $g$ .....                                     | 152 |
| 4.4.3  | Second Order Variational Method Computing Hessian Matrix .....                        | 158 |
| 4.4.3.1  | Incremental state equation to determine incremental deflection $\mathbf{u}$ .....     | 158 |
| 4.4.3.2  | Incremental adjoint equation to determine incremental test function $\mathbf{p}$ .... | 161 |
| 4.4.3.3  | Incremental decision equation to determine Hessian.....                               | 164 |
| 4.4.4  | BFGS Algorithm for Hessian Matrix Computation.....                                    | 166 |
| 4.4.5  | Inverse Computation of Material Properties .....                                      | 166 |
| 4.5.   | Computer Program Development and Validation.....                                      | 167 |
| 4.5.1  | Computer Program Development.....   | 167 |
| 4.5.2  | Validation Method.....  | 168 |
| 4.5.2.1  | Validation of gradient .....  | 168 |
| 4.5.2.2  | Validation of material property inversion.....  | 168 |
| 4.6.   | Implementation .....  | 169 |
| 4.6.1  | Experimental Design.....  | 169 |
| 4.6.2  | Pavement Model Domain and Numerical Solution.....                                     | 170 |
| 4.6.3  | Examples and Results Analysis .....   | 173 |
| 4.6.3.1  | Example 1-A theoretical validation .....  | 173 |
| 4.6.3.2  | Example 2- LTPP test data in Florida .....  | 177 |
| 4.6.3.3  | Example 3-seasonal monitoring test.....   | 180 |
| 4.7.   | Summary .....   | 184 |
| Chapter 5: Conclusion.....   |   | 185 |

|     |                     |     |
|-----|---------------------|-----|
| 5.1 | Main Findings ..... | 185 |
| 5.2 | Future Study.....   | 187 |
|     | Bibliography .....  | 189 |
|     | Vita.....           | 204 |

## **List of Tables**

|  |     |
|--|-----|
| Table 1. Materials modulus inputs in MEPDG at different levels.....                | 17  |
| Table 2. Examples of static forward analysis software for flexible pavements.....  | 23  |
| Table 3. Examples of dynamic forward analysis for flexible pavements .....         | 23  |
| Table 4. Examples of static backcalculation programs for flexible pavements.....   | 26  |
| Table 5. Examples of dynamic backcalculation programs for flexible pavements. .... | 26  |
| Table 6 Layer moduli range (in MPa) from LTPP program.....                         | 49  |
| Table 7 Pavement structure layer thickness/moduli values .....                     | 54  |
| Table 8 Average engineering error of inversed moduli .....                         | 64  |
| Table 9. Material model parameters .....   | 110 |
| Table 10. Computation time comparison.....   | 144 |
| Table 11. FWD test site information.....   | 177 |
| Table 12. Back-calculated unbound material modulus vs. measurements in MPa.....    | 180 |
| Table 13. Backcalculated elastic moduli using ModTag (MPa).....                    | 180 |

## List of Figures

|   |    |
|---|----|
| Figure 1. Relaxation modulus and creep compliance. ....   | 1  |
| Figure 2. Mechanical viscoelastic models of solids.....   | 3  |
| Figure 3. Master curves of dynamic modulus by mechanical models.....  | 6  |
| Figure 4. Multilayer systems: a foam memory mattress (www.sleep-matters.co.uk),<br>human skin, and heart arterial wall (Hossain et al. 2012). ....        | 10 |
| Figure 5. FWD Load Platen and Sensor Offsets. ....  | 11 |
| Figure 6. Examples of FWDs from KUAB, JILS, and Dynatest. ....  | 12 |
| Figure 7. Time Histories of FWD Load and Deflection.....  | 13 |
| Figure 8. Master curve input (Level 1) of AC materials in MEPDG with import/export<br>facilities.....   | 15 |
| Figure 9. Layer Modulus input (level 2) of unbound materials in MEPDG.....  | 16 |
| Figure 10. Time-temperature superposition of AC master curves: a) laboratory tests; b)<br>master curve fit (Xu 2007). ....                                | 19 |
| Figure 11. Master curve of dynamic modulus. ....  | 20 |
| Figure 12. Measured and Predicted FWD Deflection Bowl for Backcalculation.....  | 21 |
| Figure 13. Two-step approach of FWD backcalculation.....  | 22 |
| Figure 14. Artificial neural network method.....  | 25 |
| Figure 15. Creep compliance by power law.....   | 28 |
| Figure 16. Backcalculation of dynamic moduli master curve $E^*$ .....   | 29 |
| Figure 17. FWD test and displacement basin. ....  | 35 |
| Figure 18. Axisymmetric model stress state of solid.....  | 39 |
| Figure 19. Axisymmetric FE model under FWD loading.....   | 42 |
| Figure 20. Isoparametric finite and infinite elements at the local coordinates.....   | 43 |
| Figure 21. Sketch example of finite elements and nodes. ....  | 48 |
| Figure 22. Gradient calculation. ....   | 51 |
| Figure 23. Flow chart for the numerical computation procedure.....  | 53 |
| Figure 24. Probability density of randomly generated moduli in normal-distribution.....   | 55 |
| Figure 25. Pavement displacements simulated by the developed FE model and computer<br>coding for a) Case I, b) Case II, c) Case III, and d) Case IV. .... | 57 |
| Figure 26. Pavement displacement basin predictions vs. true values. ....  | 58 |
| Figure 27. Comparison with other commercial software. ....  | 59 |
| Figure 28. Inversed moduli with iteration steps. ....   | 60 |
| Figure 29. Inversed moduli vs. true values of AC.....   | 61 |
| Figure 30. Inversed moduli vs. true values using random seed values.....  | 63 |
| Figure 31. Temperature profile of AC layer at 2:00 PM and 8:00 PM: a) cold weather; b)<br>normal weather; c) hot weather.....                             | 66 |

|  |     |
|--|-----|
| Figure 32. Inversed AC moduli profile vs true values: a) cold weather; b) normal weather; c) hot weather. ....   | 66  |
| Figure 33. Simulated deflections: a) cold weather; .....   | 67  |
| Figure 34. Inversed moduli vs. true values with different RMS targets.....   | 68  |
| Figure 35. Final iteration steps vs. RMS. ....   | 69  |
| Figure 36. A layered half-space of flexible pavement structure on soil under circular loading.....   | 73  |
| Figure 37. Analytical solutions of (layered) half space.....   | 75  |
| Figure 38. Dynamic stress state of the axisymmetric model .....  | 81  |
| Figure 39. Finite element model and boundary conditions on the $r - z$ plane.....  | 82  |
| Figure 40. Material models of the multilayer structure in a 1-D mode.....  | 84  |
| Figure 41. Eight-node isoparametric ring element.....  | 88  |
| Figure 42. Time discretization.....  | 93  |
| Figure 43. Finite element diagram: a) Method in this research (arrows show the element and node number assignment direction as from left to right and from top to bottom); b) FE mesh produced by ANSYS-14.5 software..... | 98  |
| Figure 44. Linear system in the matrix-vector format.....  | 99  |
| Figure 45. Flowchart of the developed computer coding for.....   | 101 |
| Figure 46. (a) Time-domain FWD loading and deflection histories; (b) FFT transformed frequency-domain spectrum of loading pulse.....   | 103 |
| Figure 47. Pavement structure and material properties – trial values.....  | 104 |
| Figure 48. FE simulated peak deflections vs. ELSYM 5 .....   | 107 |
| Figure 49. Coding modeled results vs. ANSYS simulations.....   | 108 |
| Figure 50. Static modeled deflections.....   | 111 |
| Figure 51. Dynamic elastic modeled deflections with and without damping.....   | 112 |
| Figure 52. Dynamic viscoelastic model simulation results vs. measurements: (a) without considering damping; (b) with consideration of damping.....   | 113 |
| Figure 53. Vertical displacement ( $t = 0.023$ second).....  | 114 |
| Figure 54. Velocity (m/s) of depth direction.....  | 115 |
| Figure 55. Acceleration (m/s <sup>2</sup> ) of depth direction .....   | 115 |
| Figure 56. Simulations of velocity and acceleration on the top of AC of depth direction for distances of 0 m and 1.5 m from loading.....   | 116 |
| Figure 57. First principal stress of AC layer at time length (MPa).....  | 117 |
| Figure 58. Vehicle loading pulse and simulated dynamic viscoelastic deflections.....   | 118 |
| Figure 59. Radial stress profile of pavement structure (dynamic viscoelastic model)....  | 119 |
| Figure 60. Simulated radial stress and strain of AC layer .....  | 120 |

|   |     |
|---|-----|
| Figure 61. Simulated radial stress and strain of AC layer using dynamic viscoelastic model.....   | 121 |
| Figure 62. (a) Temperature profile of AC layer and $\alpha T$ ; and (b) simulated deflections vs. control ones at the reference temperature of 40 oC. ....        | 122 |
| Figure 63. (a) Moduli profile of soil foundation and (b) simulated deflections.....   | 124 |
| Figure 64. Viscoelastic multiplayer systems at variable length scale. ....  | 129 |
| Figure 65. Multilayer system forward and inverse computation.....   | 134 |
| Figure 66. Flow chart for the numerical inverse computation.....  | 139 |
| Figure 67. Inverse computation illustration (plotted using Surfer® software). ....  | 140 |
| Figure 68. Integration of 2-D time field of $0 < \tau < t < t_d$ .....  | 147 |
| Figure 69. Time discretization for solution of test function. ....  | 149 |
| Figure 70. Integration of the combined function of displacement and test function. ....   | 154 |
| Figure 71. Flow chart of the developed computer program for inverse computation. ....   | 168 |
| Figure 72. a) Highway pavement under FWD tests; b) axisymmetric structure model ..  | 170 |
| Figure 73. Isoparametric finite elements and Gauss points for the domain body and loading area. ....  | 172 |
| Figure 74. Loading pulse and deflection observations. ....  | 174 |
| Figure 75. Inverted deflections vs. observations ( $u_i$ is deflection at $i$ th distance). ....  | 174 |
| Figure 76. Inverted deflections - loading loop.....   | 175 |
| Figure 77. Simulated test function pulses ( $p_i$ is test function at $i$ th distance). ....  | 175 |
| Figure 78. Inverse computation results of master curve in Prony series vs. true values fitted in sigmoidal function: a) storage modulus and b) loss modulus. .... | 176 |
| Figure 79. Inverted deflections with time. ....   | 177 |
| Figure 80. LTPP data: a) FWD measured loading and deflection pulses and b) laboratory measured dynamic moduli. ....   | 178 |
| Figure 81. Inverse results vs. measurements. ....   | 179 |
| Figure 82. Seasonal FWD tests on the West Lafayette Test Track 2007. ....   | 181 |
| Figure 83. Frequency domain of FWD test after fast Fourier transform: a) April, b) August, and c) December.....   | 183 |
| Figure 84. Inverted master curves of dynamic moduli of asphalt concrete. ....   | 184 |

## Notations

### Operators

$\nabla$  Gradient  $\nabla = \frac{\partial f}{\partial x_1} i + \frac{\partial f}{\partial x_2} j + \frac{\partial f}{\partial x_3} k$  with  $i, j, k$  as the unit vectors

$\nabla \cdot$  Divergence

$$\nabla \cdot \text{Vector } \mathbf{f} = \frac{\partial f_1}{\partial x_1} + \frac{\partial f_2}{\partial x_2} + \frac{\partial f_3}{\partial x_3};$$

$$(\nabla \cdot \text{tensor } \mathbf{F})_i = \frac{\partial F_{i1}}{\partial x_1} + \frac{\partial F_{i2}}{\partial x_2} + \frac{\partial F_{i3}}{\partial x_3} \text{ for } i = 1, 2, 3$$

$$\nabla \cdot \nabla \text{ Laplacian operator } \nabla \cdot \nabla f = \frac{\partial^2 f_1}{\partial x_1^2} + \frac{\partial^2 f_2}{\partial x_2^2} + \frac{\partial^2 f_3}{\partial x_3^2}$$

$\cdot$  Inner product of vectors  $\mathbf{a} \cdot \mathbf{b} = \sum_i a_i b_i$

$:$  Inner product of tensors  $\mathbf{A} : \mathbf{B} = \sum_i \sum_j A_{ij} B_{ij}$

$\text{tr}(\cdot)$  Trace of a matrix  $\text{tr}(\mathbf{A}) = \sum_i A_{ii}$

$\partial$  1<sup>st</sup> order partial differential

$\partial^2$  2<sup>nd</sup> order partial differential

$\int$  Integration

$\ell$  Laplace transform

$:=$  To be defined as

$\forall$  For all and arbitrary

$\in$  In

$\approx$  Almost equals to

$[\cdot]^T$  Transpose of a matrix

$> 0$  Positive definite

## Symbols

|                            |   |
|----------------------------|---|
| $\Omega$                   | Three-dimensional space domain $\mathbb{R}^3$ |
| $H^1(\cdot)$               | Sobolev space of vector fields on $(\cdot)$   |
| $\partial \Omega$          | Two-dimensional area                          |
| $\partial^2 \Omega$        | One-dimensional line                          |
| $[0, t_d]$                 | Close range time domain                       |
| $\mathbf{u}$               | Displacement                                  |
| $\hat{\mathbf{u}}$         | Variation of $\mathbf{u}$                     |
| $\tilde{\mathbf{u}}$       | Incremental variation of $\mathbf{u}$         |
| $\mathbf{p}$               | Test function                                 |
| $\hat{\mathbf{p}}$         | Variation of $\mathbf{p}$                     |
| $\tilde{\mathbf{p}}$       | Incremental variation of $\mathbf{p}$         |
| $f$                        | Loading pressure                              |
| $b$                        | Body force                                    |
| $\boldsymbol{\sigma}$      | Stress tensor                                 |
| $\mathbf{S}$               | Deviatoric stress tensor                      |
| $\sigma_h$                 | Hydrostatic stress                            |
| $\boldsymbol{\varepsilon}$ | Strain tensor                                 |
| $\mathbf{e}$               | Deviatoric strain tensor                      |
| $\varepsilon_h$            | Hydrostatic strain                            |
| $\rho$                     | Density                                       |
| $m$                        | Material model parameters vector              |

|              |  |
|--------------|--|
| $\tilde{m}$  | Incremental differential of $m$ or search direction      |
| $E$          | Young's modulus  |
| $G$          | Shear modulus  |
| $K$          | Bulk modulus   |
| $E(t)$       | Relaxation modulus at time $t$                           |
| $G(t)$       | Shear relaxation modulus at time $t$                     |
| $K(t)$       | Bulk relaxation modulus at time $t$                      |
| $E^*$        | Dynamic modulus  |
| $E'$         | Storage modulus  |
| $E''$        | Loss modulus   |
| $E_b$        | Elastic modulus of base                                  |
| $E_{sb}$     | Elastic modulus of subbase                               |
| $E_s$        | Elastic modulus of soil                                  |
| $\eta$       | Viscosity  |
| $\delta$     | Phase angle  |
| $\nu$        | Poisson's ratio  |
| $\mathbf{C}$ | Elasticity tensor  |
| $\mathbf{M}$ | Mass matrix  |
| $\mathbf{C}$ | Damping matrix   |
| $\mathbf{I}$ | Identity matrix  |
| $\Phi$       | Shape function matrix in finite element formulation      |
| $\mathbf{B}$ | Strain-displacement matrix in finite element formulation |

**g** Gradient vector  $\mathbf{g} = \frac{\partial \mathcal{L}}{\partial \mathbf{m}}$

**H** Hessian matrix  $\mathbf{H} = \frac{\partial^2 \mathcal{L}}{\partial \mathbf{m}^2}$

## Briefs

**AC** Asphalt concrete

**FWD** Falling weight deflectometer

**PDE** Partial differential equation

**VE** Viscoelastic

## Chapter 1: Introduction

This chapter presents the following contents: 1) background and literature review; 2) research problems; 3) research objectives; and 4) scope of the dissertation.

### 1.1 Background and Literature Review

#### 1.1.1 Material Viscoelasticity and Models of Solids

Two types of models are primarily used to capture the linear viscoelastic behavior of materials: 1) mechanical models; and 2) mathematical models. To understand the mechanical models, a few modulus concepts and related terms are reviewed: 1) the relaxation modulus,  $E(t)$ ; 2) the creep compliance,  $D(t)$ , and 3) the dynamic or complex modulus,  $E^*$ .

The relaxation modulus describes stress relaxation over time under constant strain as shown in Figure 1a. At loading time zero or infinite loading frequency, this corresponds to the instantaneous modulus. The creep compliance describes the displacement and strain increase over time under a constant stress, as illustrated in Figure 1b.

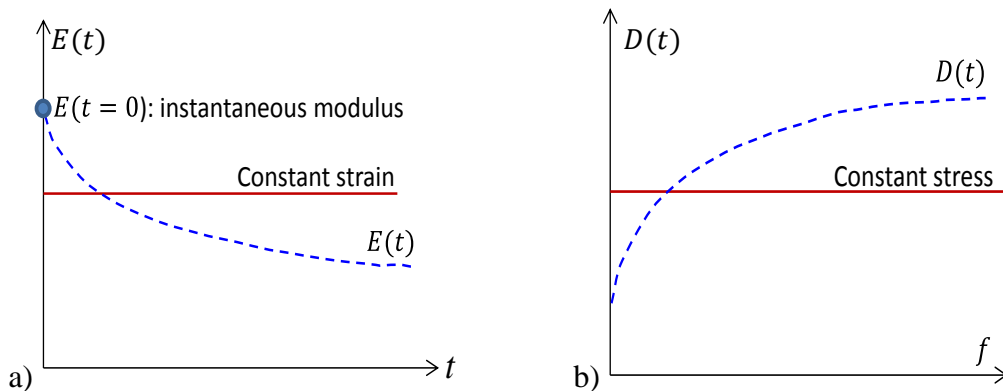


**Figure 1. Relaxation modulus and creep compliance.**

The relaxation modulus and creep compliance has a constitutive relationship as follows (Park and Schapery 1999):

$$\int E(t)D(t) = 1 \quad (1-1)$$

The dynamic or complex modulus is equal to stress over strain under the vibratory conditions as follows (Huang 2003):

$$E^* = \frac{\sigma_0 e^{i\omega t}}{\epsilon_0 e^{i(\omega t - \phi)}} \quad (1-2)$$

where  $\sigma_0$  is the peak stress;  $\epsilon_0$  is peak strain;  $\phi$  is phase angle (radians);  $\omega$  is angular velocity (radians/sec); and  $t$  is time (seconds).

As defined by equation (1-2), the complex modulus is time-dependent for a given temperature. The absolute value of dynamic modulus  $|E^*|$  is defined as follows. Note that  $|E^*|$  is often called “dynamic modulus” in the pavement engineering community, while  $E^*$  is called complex modulus:

$$|E^*| = \frac{\sigma_0}{\epsilon_0} \quad (1-3)$$

The dynamic modulus is a characterization of material viscoelasticity.  $E^*$  can be decomposed to  $E' + iE''$ , where  $E'$  is the storage modulus (elastic portion) and  $E''$  is the loss modulus (viscous portion). Several mechanical models have been proposed to describe the material viscoelastic behavior and dynamic modulus, including:

#### I. Maxwell model

This model consists of one spring and one dashpot in series (see Figure 2a). The spring is used to represent the elastic modulus of a material. The dashpot is used to represent the viscosity of a material as strain-rate dependent as presented by Christen (2009):

$$\sigma = \eta \frac{d\epsilon}{dt} \quad (1-4)$$

where  $\sigma$  is stress, Pa;  $\eta$  is viscosity, Pa.s, and  $\epsilon$  is strain.

The Maxwell model expresses the relaxation modulus of material as follows:

$$E(t) = E_1 e^{-\frac{E_1}{\eta_1} t} \quad (1-5)$$

#### II. Kelvin model

This model consists of one spring and one dashpot in a parallel arrangement, plus one spring to express the creep compliance of material (see Figure 2b).

### III. Burgers model

This is a combination of the Maxwell and Kelvin models in series (see Figure 2c).

### IV. Generalized Maxwell model

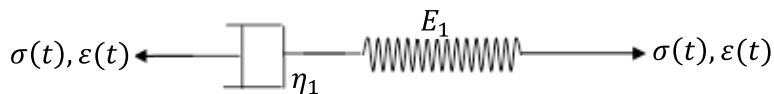
This is a combination of multiple terms of the Maxwell model in parallel (see Figure 2d). The expression of relaxation modulus will be detailed in Chapter 3.

### V. Generalized Kelvin model

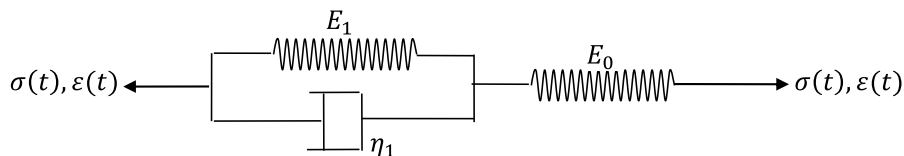
This model is a combination of multiple terms of the Kelvin model in series (see Figure 2e).

### VI. Huet-Sayegh model

When compared to the generalized Maxwell, Kelvin, and Burgers models, a variable dashpot rather than a linear dashpot is used (Pronk 2001), as shown in the following Figure 2f, which also shows all the models mentioned up to this point.

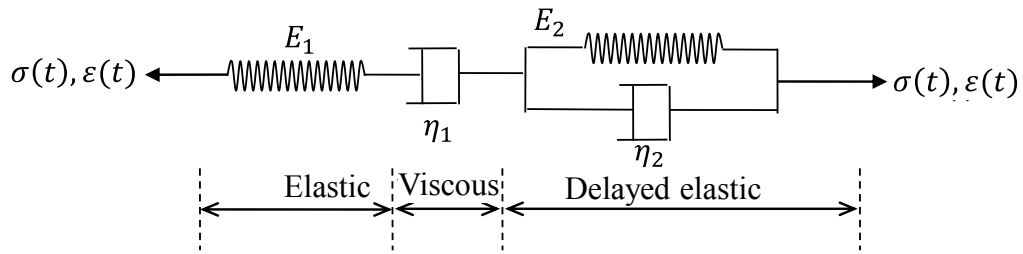


**(a) Maxwell Model**

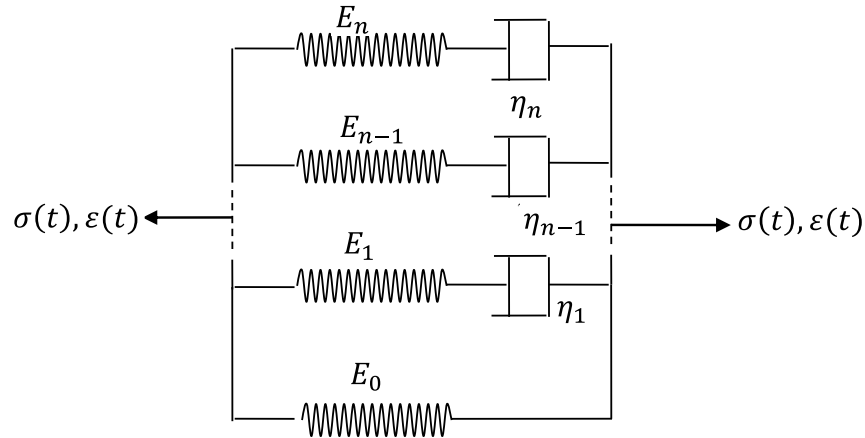


**(b) Kelvin model**

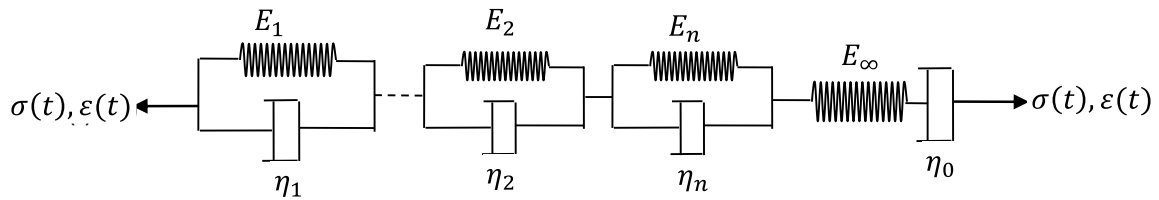
**Figure 2. Mechanical viscoelastic models of solids.**



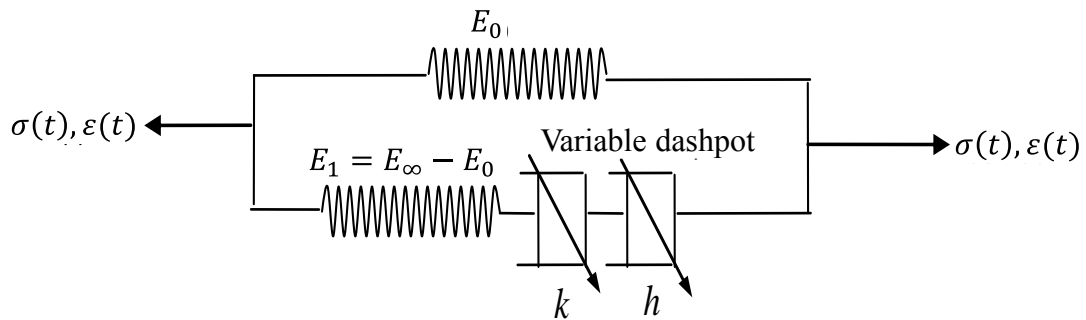
(c) Burgers model



(d) Generalized Maxwell model



(e) Generalized Kelvin model



(f) Huet-Sayegh model

Figure 2. Mechanical viscoelastic models of solids (continued).

The mathematical models include:

I. The 3-parameter power-law model for creep compliance

$$D(t) = D_0 + D_1 t^n \quad (1-6)$$

where  $D_0, D_1, n$  are material model parameters, and  $t$  is time.

II. The sigmoidal function model

As a result of the National Cooperative Highway Research Program (NCHRP) Project 1-37A development (Glover and Mallela 2009), the mathematical model in a sigmoidal function has been proposed to describe the absolute dynamic modulus as follows:

$$\log|E^*| = \delta + \frac{\alpha}{1 + e^{\beta + \gamma \log(t_r)}} \quad (1-7)$$

where  $\delta$  is the minimum dynamic modulus (often termed the “lower shelf”);  $\delta + \alpha$  is maximum dynamic modulus (often termed the “upper shelf”), and  $\beta, \gamma$  are parameters describing the location and slope of the transition region of the sigmoidal function.

This model has been widely adopted to represent the laboratory test data of asphalt concrete (AC) material in this country and used in the Mechanistic-Empirical Pavement Design Guide (MEPDG) for stress-strain response modeling as discussed previously. The MEPDG has evolved and it is currently known as the AASHTOWare Pavement ME Design.

The Maxwell model, Kelvin model, and Burgers model would not be able to well capture the master curve of complex moduli of AC material at a full-range of reduced frequency (Xu and Solaimanian 2008) due to the limited term numbers as shown in Figure 3a (e.g., only one parallel spring and dashpot used for the Maxwell model). The generalized Maxwell model (Figure 3b), generalized Kelvin model (Figure 3b), Huet-Sayegh model (Figure 3c), and sigmoidal function (Figure 3c) could capture the master curve of dynamic modulus at a wide range of reduced frequency (Xu and Solaimanian 2008).

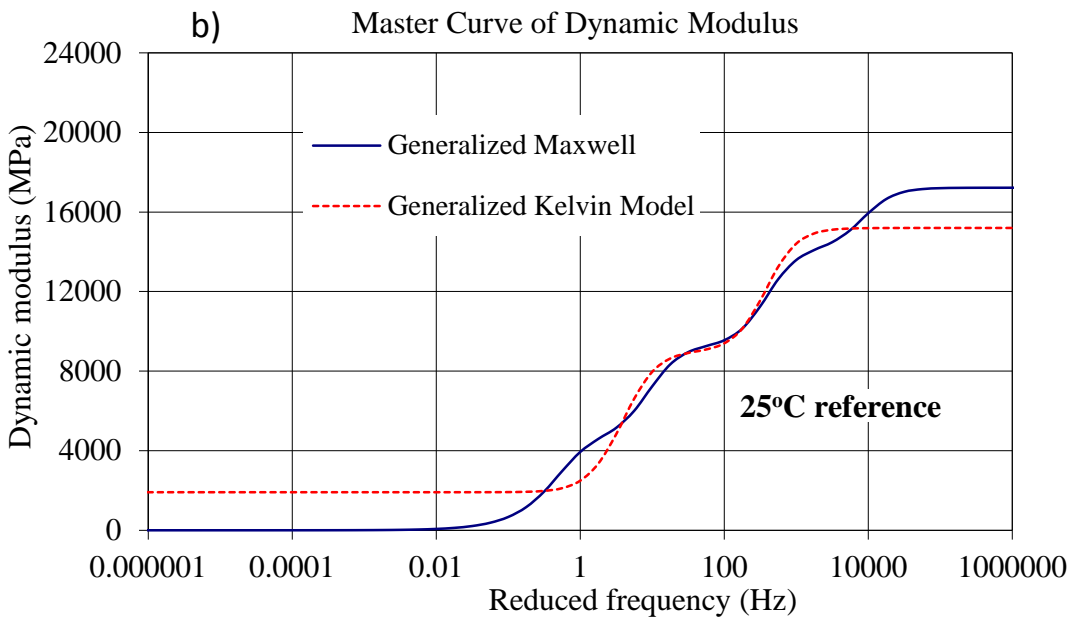
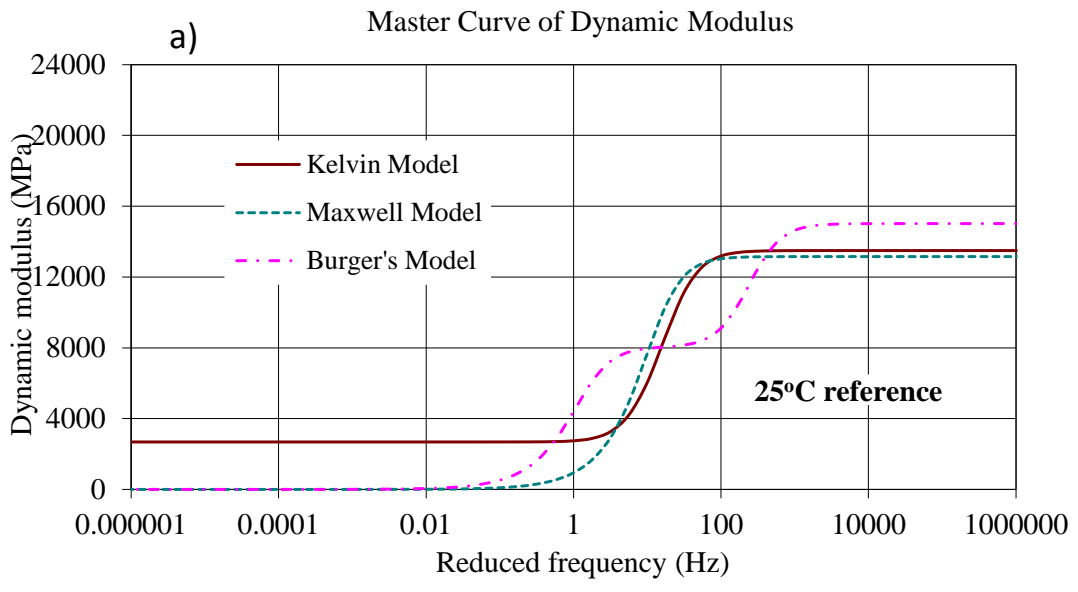


**Figure 3. Master curves of dynamic modulus by mechanical models.**

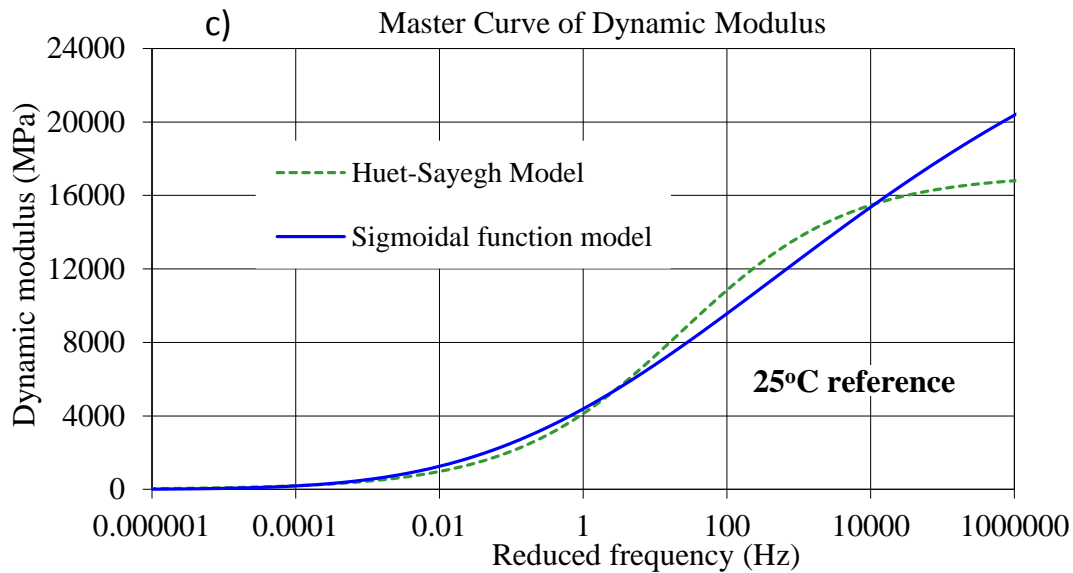


**Figure 3. Master curves of dynamic modulus by mechanical models (continued).**

However, the generalized Maxwell model and generalized Kelvin model are unable to produce very smooth fitted master curves (frequency on the logarithmic scale) from laboratory test data (see their “oscillations” in Figure 3b). On the other hand, the Huet-Sayegh model and sigmoidal function can produce smoother master curves (see Figure 3c). The mechanical model provides the physical meaning needed to describe the material viscoelastic behavior rather than a mathematical function only, and thus Xu and Solaimanian (2008) recommended the Huet-Sayegh model as the standard used to describe the master curve of the dynamic modulus. However, the ultimate purpose of the material model is to simulate the structural responses for numerical solution. The generalized Maxwell model and generalized Kelvin model in the exponential Prony series have the advantage of providing numerical integration and the differential needed to achieve improved accuracy and computation speed; thus, they have been widely adopted in the commercial finite element (FE) software, which includes ANSYS and ABAQUS. Currently there are no definitions of inputs for the Huet-Sayegh model in the numerical solution including the FE software; however, one method is to convert the model into a Prony series for inputs. As is the case in the Huet-Sayegh model, the mathematical sigmoidal function is not defined as capable of achieving direct material model inputs for numerical solutions. The Mechanistic-Empirical Pavement Design

Guide (MEPDG) funded by NCHRP (Project 31A) put together by the Applied Research Associates (ARA) along with several other consultants (Glover and Mallela, 2009) uses the sigmoidal function to approximate the dynamic and material viscoelastic behaviors as discussed previously. Therefore, in this research, the generalized Maxwell model of the Prony series representation is adopted to simulate the viscoelastic behavior of materials.

### 1.1.2 Damping Models

Damping consists of: material damping, structural damping, and fluid viscous damping for energy dissipation (Puthanpurayil et al. 2011). Damping models can be both frequency dependent and independent or viscous and non-viscous. The Rayleigh damping model, one of the frequency-dependent and viscous models to date, is still the most popular model employed in structural dynamic analysis (Puthanpurayil et al. 2011):

$$[C] = \alpha[M] + \beta[K] \quad (1-8)$$

where  $[C]$  is damping matrix,  $[M]$  is mass matrix, and  $[K]$  is stiffness matrix, and  $\alpha$  and  $\beta$  are model parameters.

One of the advantages of this model is that the damping matrix can be directly estimated according to material mass and stiffness without performing sophisticated material testing. The main issue with this model lies in its strong dependence on the frequency of structures such that the model parameters (i.e.,  $\alpha$  and  $\beta$ ) are evaluated as a function of the frequency (Puthanpurayil et al. 2011). However, the Rayleigh damping model has been often used to represent damping at small strain levels, whereas material models are primarily considered linear (Park and Hashash 2004). In this dissertation research, the base, subbase and soil materials are considered linear elastic under the FWD loading for a very short period. In addition, because no laboratory testing for material characterization was conducted in this research, the Rayleigh damping model was adopted in this research as presented in Chapter 3 and Chapter 4.

Saouma et al. modified the Rayleigh damping model to be dependent on stiffness matrix only for simulating the radiation damping for soil-structural interaction as follows:

$$C = \frac{\xi}{\pi f} [K] \quad (1-9)$$

where  $\xi$  is a damping factor for frequency  $f$ , and  $[K]$  is stiffness matrix.

Very often the symmetric mass and stiffness matrices are used; therefore, the Rayleigh model yields a symmetric matrix. However, Kim et al. (2013) estimated a non-symmetric format of damping matrices for multi-degrees-of-freedom structures.

Other frequency dependent models besides the Rayleigh damping model have also been studied, including those proposed by Bagley and Torvik (1983), Lesieutre and Mingori (1990), McTavish and Hughes (1993), and Adhikari and Woodhouse (2001).

More recent research on other damping models for use in structures and materials includes the following examples: Hussein and Frazier (2010) considered both proportional damping (stiffness and mass proportional damping) and general damping (damping nonzero) for modeling the band structure of phononic crystals. Tileylioglu et al. (2011) studied damping models by adjusting to the translational and rotational vibration modes for a shallow foundation structure. Gottlieb and Habib (2011) proposed a quadratic and cubic nonlinear damping model for governing the dynamics of a chaotic spherical pendulum to update the linear model. Labonnote et al. (2013) proposed a hysteretic damping model as decomposed to the shear part and bending part as applied to the Timoshenko timber beams. Dvornik et al. (2013) modeled the anisotropic properties of damping, where they assumed that the anisotropy of damping is given by an order of magnitude reduction of the component along the symmetry axis of the damping matrix as applied to the magnetic nanoelements. Pisanò and Jeremić (2014) simulated soil damping based on a simple visco-elastic-plastic model. Boumediene et al. (2014) used a generalized Maxwell based viscoelastic model to predict the passive damping of a sandwich structure. Sun et al. (2014) developed a thermoelastic damping in a symmetric trilayered circular plate, and validated for a thin plate structure.

### **1.1.3 Multilayer Systems with Viscoelastic Properties**

Viscoelasticity is the characterization of material deformation where the stress is dependent on strain rate or time. Under a constant loading, the deformation of materials may increase continuously due to creep behavior; while under a constant strain, the stress

of materials may reduce continuously due to stress relaxation. Multilayer systems or composites that demonstrate viscoelastic properties exist everywhere in life at variable scales. Examples include the human skin and tissues, the multilayer molecular structure of polymers (Tronto et al. 2013), and multilayer pavement structures, among others. Figure 4a shows a multilayer memory foam mattress, in which the viscoelastic properties must be designed properly to achieve optimum sleep comfort. Figure 4b shows the multilayer structure of the arterial wall of the human heart (Hossain et al. 2012), where the viscoelastic properties affect blood flow and cardiac health. Flexible pavement structure is a large-scale multilayer structure, which typically consists of an asphalt concrete (AC) top layer, then the base and sub-layers, and finally, the soil foundation. The AC is a typical viscoelastic and viscoplastic material (Xu and Solaimanian 2009). AC rutting or permanent deformation and fatigue cracking are related to its viscoelastic properties. Rutting causes traffic noise, rough road conditions, and hydroplaning that results in vehicular accidents. Therefore, it is important to understand the viscoelastic properties of multilayer systems.

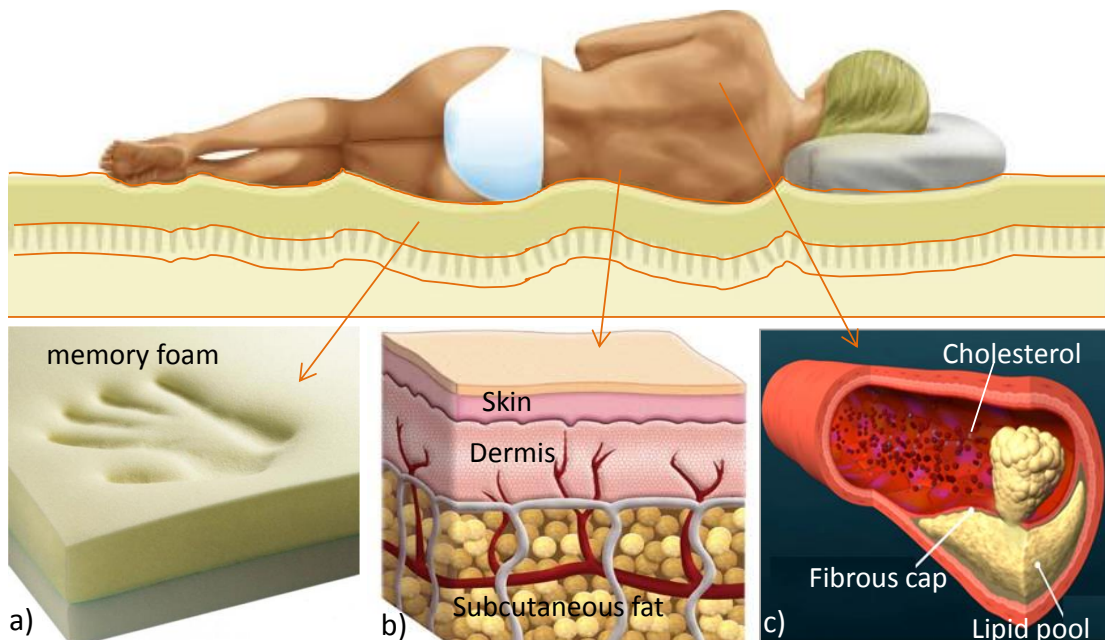


**Figure 4. Multilayer systems: a foam memory mattress (www.sleep-matters.co.uk), human skin, and heart arterial wall (Hossain et al. 2012).**

### 1.1.4 FWD Nondestructive Test

Nondestructive testing (NDT) has been used extensively as a means for evaluating the material properties of the multilayer structure. In particular, the Falling weight deflectometer (FWDs) has been widely used for pavement structure evaluation over the past 30 years. Generally, the FWDs are used to measure pavement deflections with multiple deflection sensors in response to a dynamic load in stationary mode. Examples of deflection sensors include geophones (e.g., used by Dynatest FWDs) and seismometers (e.g., used by KUAB FWDs). Since 1994, most FWDs have been sold with 7, 9 or 10 deflection sensors. Deflection sensor spacings often follow guidance from the Federal Highway Administration's Long Term Pavement Performance (LTPP) program (see Figure 5). The FWD dynamic load is meant to emulate traffic loading. FWD data are used (usually just the peak values of the deflection and load pulses) to evaluate the structural capacity of pavements for research, design, rehabilitation, and pavement management purposes.

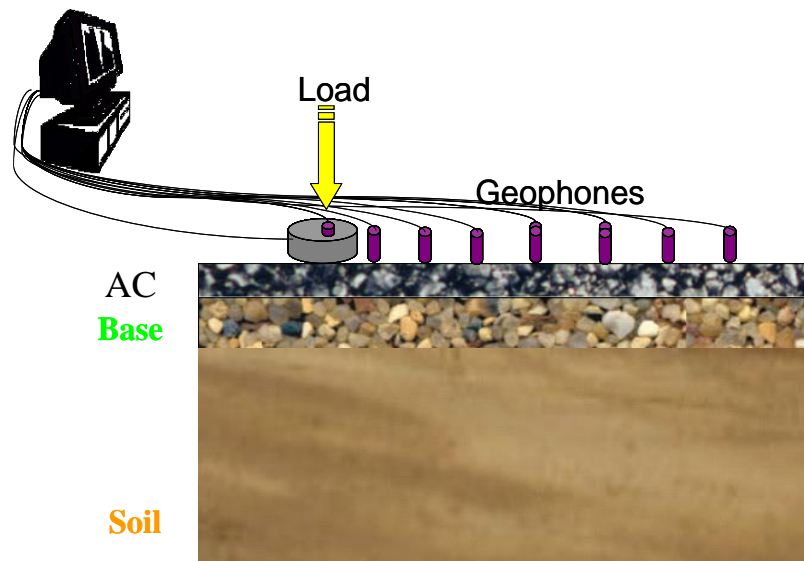


**Figure 5. FWD Load Platen and Sensor Offsets.**

Based on a survey in 2008, there were 82 FWDs (mainly made by Dynatest, KUAB, and JILS) owned by 45 State Highway Administrations (SHAs) (Alavi et al. 2008). Though not included in this survey, there is a comparable number of FWDs

owned by private companies, institutes, and other agencies, as projected from the FWD ownership documented in the European COST 336 (European Commission 1998).

Figure 6 shows examples of FWDs made by KUAB, JILS, and Dynatest. These FWDs have different physical configurations for applying load pulses (weights, static preload, drop heights, load platen, etc.) and different technologies of geophones to collect deflection measurements. Commonly used load levels are 6,000, 9,000, 12,000, and either 16,000 or 18,000 pounds for highway applications.



**Figure 6. Examples of FWDs from KUAB, JILS, and Dynatest.**

The shapes and amplitudes of FWD deflection pulses are different when applying different load times due to the dynamic effects for 0.025 ms and 0.05 ms of each recorded data point (Molenaar 2005). Figure 7 shows one example of the applied FWD loading and measured deflection time histories. The FWD pulses contain approximately 120 ms

of time history data (varies from one vendor to another) with non-zero tails due to drift. The drift is largely due to errors in the digital integration of response time history caused by the assumption of zero velocity just prior to the rise.

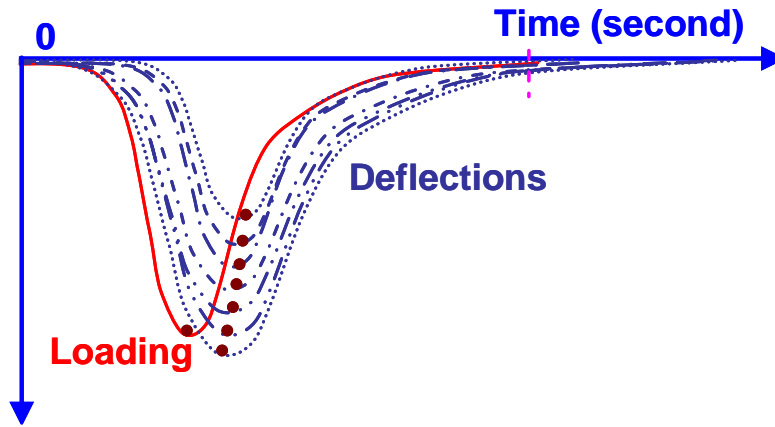


**Figure 7. Time Histories of FWD Load and Deflection.**

Generally, only the maxima or peak values of the load and deflection pulses are stored due to the common usage of FWD static backcalculation. Most FWD static analysis tools can be used to backcalculate a single modulus value for each pavement layer for use in design. Backcalculated AC layer moduli are often normalized to a reference temperature (e.g., 70 °F) with adjustment techniques such the BELLS models (Lukanen et al. 2000). FWD time histories data are not commonly used, and the availability and application of FWD dynamic backcalculation methodologies are limited.

### **1.1.5 Pavement Design Methods with Moduli Inputs**

Even though the AASHTO (American Association of State Highway and Transportation Officials) 1993 pavement analysis and design method was implemented more than two decades ago, it is still vastly used for engineering designs in the United States. The 1993 AASHTO *Guide* (AASHTO 1993) is an empirical pavement design method. In this method the layer elastic modulus is correlated to the structural number (SN) which is a determinant factor for the pavement service life.

More recently, the 2004 Mechanistic Empirical Pavement Design Guide (MEPDG (Glover and Mallela 2009) has been used and is gaining popularity. MEPDG is a mechanistic-empirical method, where pavement responses are calculated based on the

mechanistic model and then the pavement performance is predicted using statistical empirical models.

Both design methods have been using the FWD backcalculation results of layer moduli as material inputs for the pavement overlay design and performance predictions. In the following sections the review is based on the MEPDG (the public version 1.100) as presented in the September 2009 final report (Glover and Mallela 2009).

#### **1.1.5.1 Material parameters input**

In the MEPDG methodology Level 1 design (the highest level of accuracy), the dynamic modulus master curve is the principal material input for AC layers and the resilient modulus is the principal material input for unbound layers. For rehabilitation designs, the backcalculated layer moduli can be used as the inputs for the unbound layers. However, it is not possible to directly input any backcalculated moduli for existing AC layers.

The MEPDG Level 1 inputs for new AC materials are the laboratory-measured dynamic modulus values at several user-defined temperatures and frequencies. The input screen (see Figure 8) permits either direct tabular input of dynamic modulus values or the import/export of dynamic modulus values stored in an external tab-delimited text file. For Level 2 and 3 inputs, the AC modulus is calculated by a regression equation that uses binder properties and mixture volumetric and gradation properties to predict dynamic modulus at analysis temperatures and loading frequencies (Witczak 2004).

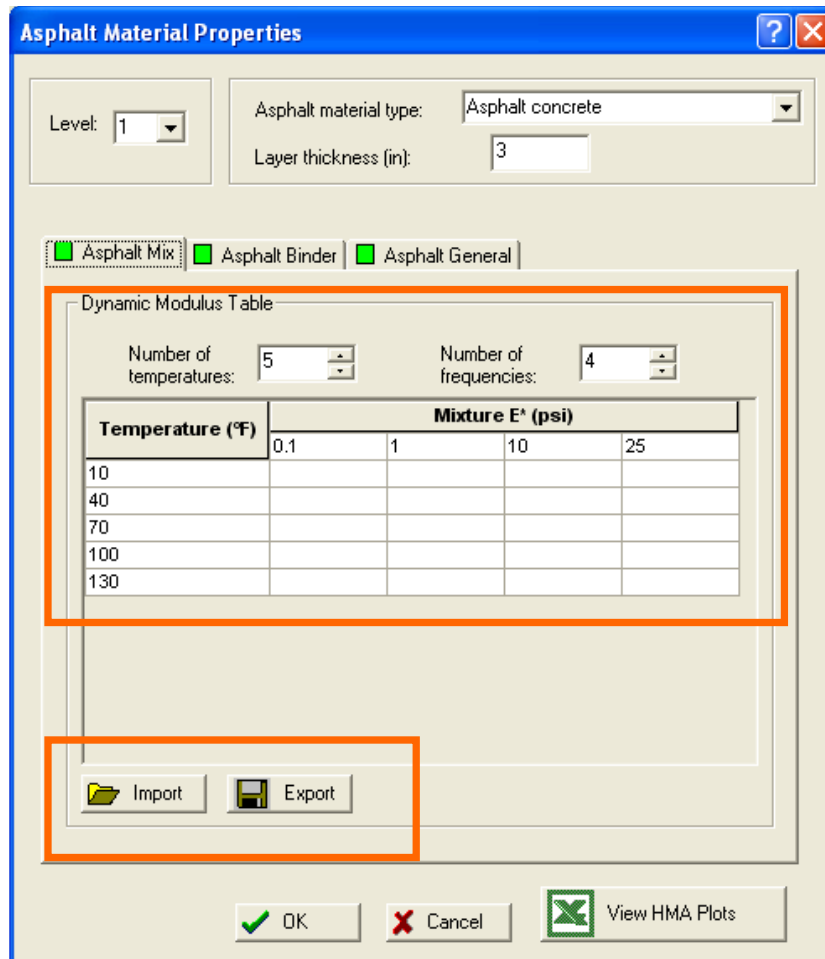


**Figure 8. Master curve input (Level 1) of AC materials in MEPDG with import/export facilities**

The inability to input directly any backcalculated modulus (e.g., from static backcalculation) for existing AC materials at any input level of the MEPDG severely constrains the usage of FWD test data in rehabilitation designs. On the other hand, the MEPDG does allow more flexibility for the direct input of layer moduli for unbound materials at Level 2. The user may enter either (see Figure 9): (a) a single laboratory-measured resilient modulus value for the expected in-place stress state at an appropriate reference condition (generally optimum moisture and in place compacted density) with the Enhanced Integrated Climatic Model (EICM) providing adjustments for climate effects (i.e., site equilibrium moisture conditions, freeze/thaw effects, etc.); (b) one single representative design value, with no EICM adjustments; or (c) 12 monthly representative

design values with no EICM adjustments. The representative design values for the latter two options could be based on historical records or they could be backcalculated from FWD data with the usual field-to-laboratory correction.

Level 1 inputs for unbound materials in new construction projects are the three  $k$  parameters for the stress-dependent resilient modulus model, although Level 1 is not yet calibrated. Level 1 input of unbound material stiffness is not available for rehabilitation projects.

The screenshot shows the 'Unbound Layer - Layer #2' dialog box. At the top, 'Unbound Material' is set to 'A-1-a' and 'Thickness(in)' is 8. There are checkboxes for 'Strength Properties' and 'ICM'. Under 'Input Level', 'Level 2' is selected. Under 'Analysis Type', 'ICM Calculated Modulus' is selected. Under 'User Input Modulus', 'Representative value (design value)' is selected. In the 'Material Property' section, 'Modulus (psi)' is selected, and the 'Modulus (input) (psi)' field is highlighted with a red box and contains the value 40000. Other material property options include CBR, R-Value, Layer Coefficient - ai, Penetration DCP (rr), and Based upon PI and Gradation. There are buttons for 'View Equation', 'Calculate >>', 'AASHTO Classification', and 'Unified Classification'. At the bottom are 'OK' and 'Cancel' buttons.

**Figure 9. Layer Modulus input (level 2) of unbound materials in MEPDG.**

To summarize the material inputs to MEPDG,

Table 1 lists input options for new AC or existing AC, and unbound materials at all three levels for both new construction and rehabilitation.

**Table 1. Materials modulus inputs in MEPDG at different levels**

| <i>Level</i> | <i>New AC</i>  | <i>Existing AC</i>   | <i>Unbound materials</i>  |
|--------------|--|--|---|
| 1            | Laboratory-measured $ E^* $ data at various temperatures and loading rates.  | Same as Level 3.   | Three parameter model stress-dependent resilient modulus model <sup>1</sup>   |
| 2            | Predicted from Witczak $ E^* $ equation as a function of binder viscosity and mixture volumetric and gradation properties. | Same as Level 3.   | (a) A representative value at reference conditions (with adjustment by EICM);<br>(b) a single seasonally averaged annual design value (no EICM adjustment); or<br>(c) 12 seasonal design values (no EICM adjustment) <sup>2</sup> |
| 3            | Predicted from Witczak $ E^* $ equation as a function of binder viscosity and mixture volumetric and gradation properties. | Predicted from Witczak $ E^* $ equation as a function of estimated binder viscosity and mixture volumetric and gradation properties of existing AC, with damage reduction an empirical function of overall pavement condition. | Default value as a function of soil class.  |

<sup>1</sup>Level 1 input of unbound materials is not available for rehabilitation designs in the current MEPDG version.

<sup>2</sup>Resilient modulus at Level 2 can also be defined via correlations with other material parameters such as California Bearing Ratio (CBR).

### 1.1.5.2 Building master curve based on time-temperature superposition

The Level 1 inputs for AC mixtures in the MEPDG are the laboratory-measured dynamic modulus at various temperatures and loading rates (see Figure 8). The values at each temperature fall along distinct lines with low temperatures and shorter loading times giving higher  $|E^*|$  values and high temperatures with longer loading times giving lower values. These individual line segments at each temperature can then be shifted based on the time-temperature superposition principle to produce the complete master curve. To shift a master curve segment to a reference temperature, a shift factor can be applied for each segment corresponding to a given test temperature to obtain the reduced frequency:

$$\alpha_T = \frac{f_{T_r}}{f_T} \quad (1-10)$$

where  $\alpha_T$  is the shift factor as function of temperature;  $f_T$  is frequency at test temperature  $T$ ; and  $f_{T_r}$  is the reduced frequency at the reference temperature  $T_r$  (e.g., 70 °F).

$\alpha_T$  could be determined according to the WLF temperature-time superposition rule (Williams et al. 1955):

$$\log_{10}(\alpha_T) = \frac{-\gamma_1(T-T_r)}{\gamma_2+T-T_r}$$

where  $\gamma_1, \gamma_2$  are model parameters.

$$\alpha_T = \frac{t}{t_r} \quad (1-11)$$

where  $\alpha_T$  is the shift factor as a function of temperature;  $T$  is temperature;  $T_r$  is the reference temperature (e.g., 70 °F);  $t$  is time of loading;  $t_r$  is reduced time of loading at reference temperature.

Figure 10 shows an example of the shifting process. Before shifting, each line segment consists of dynamic moduli at different loading times for a given temperature. Data at temperatures below the reference temperature are shifted to the left while data at temperatures above the reference temperature are shifted to the right, yielding the smooth master curve shown in the lower part of the Figure.

The mathematical model of sigmoidal function ( $\log|E^*| = \delta + \frac{\alpha}{1+e^{\beta+\gamma\log(t_r)}}$ ) has often been used to fit the dynamic modulus master curve (Witczak, 2004).

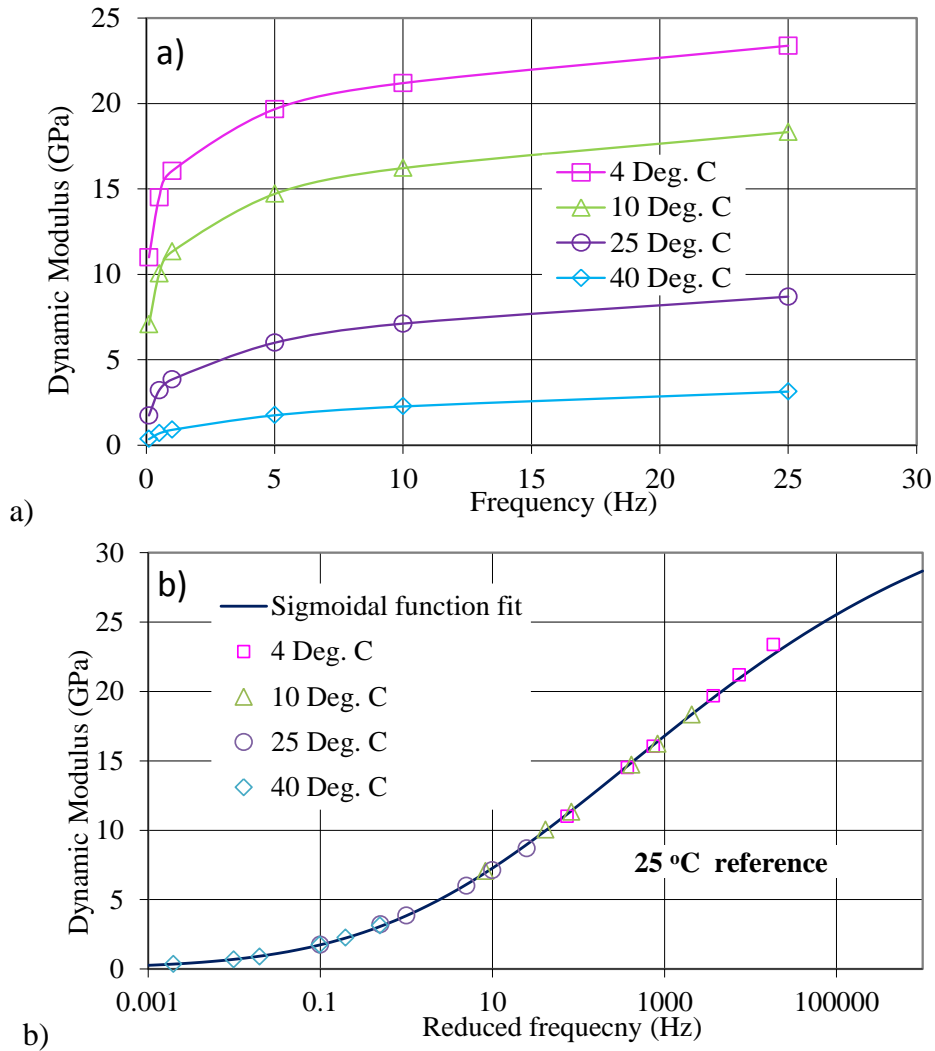


**Figure 10. Time-temperature superposition of AC master curves: a) laboratory tests; b) master curve fit (Xu 2007).**

Note that Figure 10 is for laboratory test results rather than FWD measurements; FWD tests usually are not performed over such a wide range of temperatures and frequencies in practice. Ideally, if the FWD dynamic backcalculation method can produce “unshifted” master curve segments, these segments can then serve as Level 1 inputs of new AC materials (i.e., undamaged) and existing AC materials (i.e., damaged master curve) to the MEPDG for use in the pavement response computation.

### 1.1.5.3 Response model

In the current MEPDG, the response simulation of viscoelastic behavior of AC material is based on a quasi-static method (dynamic inertia effect is ignored). At a reduced frequency based on the traffic speed and temperature, the corresponding dynamic modulus value (see Figure 11) is used as input for the linear elastic multilayer analysis program to calculate the pavement response.

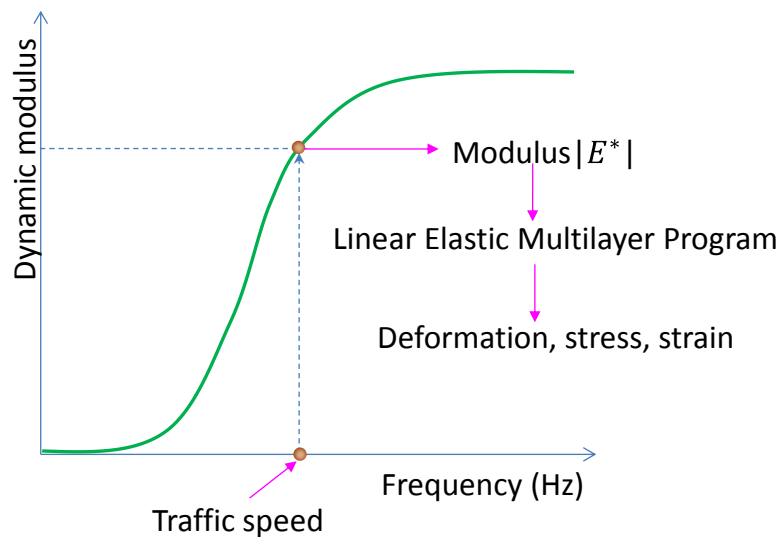


**Figure 11. Master curve of dynamic modulus.**

### 1.1.6 Multilayer Property Backcalculation

#### 1.1.6.1 General principles of backcalculation- a two-stage approach

Backcalculation has been extensively researched. Figure 12 shows an example of the endpoint of a static backcalculation pavement layer elastic moduli using FWD tests, in which the deflections measured from seven FWD geophones are in close agreement with the predictions using the converged layer moduli values.

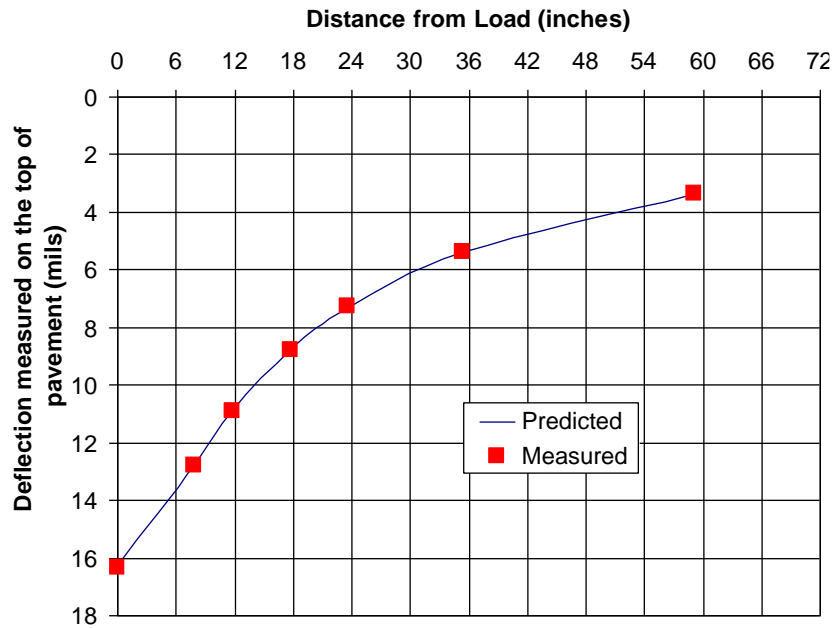


**Figure 12. Measured and Predicted FWD Deflection Bowl for Backcalculation.**

Backcalculation of pavement moduli is an iterative process, generally it involves two-stages: 1) simulate the pavement responses under the FWD plate loading for a given set of layer moduli; 2) adjust the layer moduli using various mathematical algorithms by reducing the difference between measured and simulated responses as shown in Figure 13.

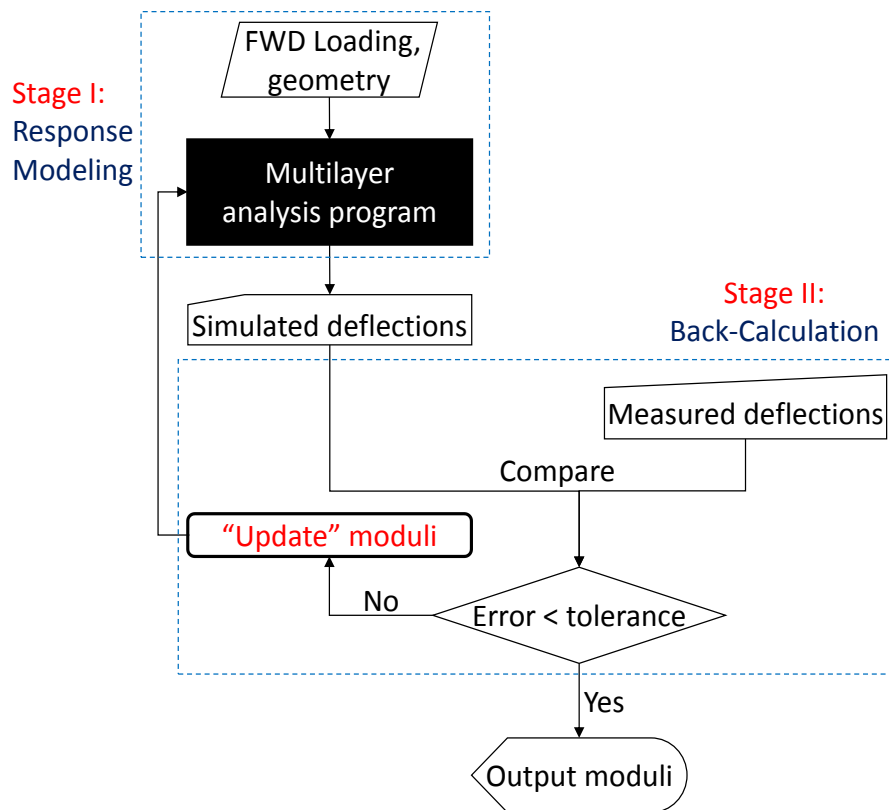


**Figure 13. Two-step approach of FWD backcalculation.**

### 1.1.6.2 Inverse approach for multilayer systems in science & engineering

The two-stage method has been widely used in different science and engineering disciplines for analyzing the multilayer system with some examples listed in the following sources:

- Catheline et al. (2004): visco-elastic (VE) properties of membrane
- Brigham et al. (2007): fluid properties
- Szeri (2007), Zhao et al. (2009) : VE properties of biomaterials
- Araújo et al. (2009): VE properties of sandwich structure
- Giavazzi et al. (2010) : VE properties of human skin
- Sims et al. (2010): VE properties of subcutaneous fats, ANSYS forward plus MATLAB inverse

### 1.1.6.3 Commonly used response models of flexible pavements

The methodologies and associated computer programs for simulating multilayer pavement responses include multi-layer elastic theory (e.g., BISAR and ELSYM5), finite element methods (e.g., ILLIPAVE, MICHPAVE), and semi-analytical techniques (Ji et al. 2006). General purpose commercial finite element codes (e.g., ABAQUS and ANSYS) can also be employed. Most existing programs are based on the assumption of static loading and linear elastic material properties (see Table 2), although some programs have considered the dynamic response (see Table 3). The VEROAD program developed at the Delft University of Technology (Hopman 1996) treats the AC as a linear viscoelastic material. A more detailed discussion and review will be presented in Chapter 3.

**Table 2. Examples of static forward analysis software for flexible pavements**

| <i>Program or Method</i> | <i>Author(s)</i>               | <i>Features</i>               | <i>Analysis Method</i>         |
|--------------------------|--------------------------------|-------------------------------|--------------------------------|
| ELSYM 5                  | UC Berkeley                    | Linear elastic                | Analytical multilayer analysis |
| BISAR                    | Shell Global Inc.              | Linear elastic                | Analytical multilayer analysis |
| Everstress               | Washington DOT                 | Linear elastic                | Analytical multilayer analysis |
| ILLIPAVE                 | University of Illinois         | Elastic+stress-dependent soil | Finite element                 |
| TTI PAVE                 | Texas Transportation Institute | Elastic+Mohr-Columbia model   | Finite element                 |
| MichPAVE                 | Michigan State University      | Elastic+stress-dependent soil | Finite element                 |
| SAPSI-M                  | Chatti and Yun                 | Damped elastic                | Analytical + Finite element    |
| VEROAD                   | Hopman                         | Static viscoelastic           | Analytical multilayer analysis |
| CAPA-3D                  | Scarpas                        | Material damages              | Finite element                 |

**Table 3. Examples of dynamic forward analysis for flexible pavements**

| <i>Program or Method</i> | <i>Author(s)</i> | <i>Features</i>                   | <i>Analysis Method</i>                                 |
|--------------------------|------------------|-----------------------------------|--|
| AXIDIN                   | Antunes (1991)   | Dynamic elastic                   | Two-dimensional finite element method                  |
| PUNCH                    | Kausel (1989)    | Dynamic elastic                   | Explicit, closed-form solution for the Green functions |
| UTFWIBM                  | Roesset (1987)   | Dynamic elastic                   | Fourier superposition                                  |
| SCALPOT                  | Magnuson (1998)  | Dynamic elastic                   | Haskell-Thompson transfer matrix approach              |
| SAPSI                    | Chen (1987)      | Dynamic elastic                   | Multilayer linear elastic system with Green's function |
| ViscoWave                | Lee (2013)       | Dynamic viscoelastic (no damping) | Analytical multilayer analysis                         |
| 3D-Move Analysis         | UNR (2013)       | Viscoelastic, damping             | Continuum-based finite-layer                           |

#### 1.1.6.4 Commonly used optimization algorithms for multilayer systems

For the 2<sup>nd</sup> step of the backcalculation procedure, commonly used optimization algorithms include at least the following:

- Newton-Raphson method (Harichandran et al., 1993),
- Hooke-Jeeves pattern search ( used in the MODULUS program),
- System identification method (Wang and Lytton, 1993),
- Kalman filter method (Choi and Pestana., 2006),
- Non-linear least square method (Sivaneswaran et al., 1991),
- Probabilistic method ( Hadidi and Gucunski, 2010), and
- Neural network models (Meier et al. 1997).

In these inverse computations, the deflections are simulated using the multilayer analysis program. Then backcalculation was performed based on the values of deflection outputs to update the material properties. The deflections with the new material parameters were simulated again and compared with measurements. Iterations continue until reaching an acceptable small deflection difference between the simulations and measurements.

Figure 14 shows an artificial neural network (ANN) method for backcalculation, where a large database of deflections with various structures (e.g., layer thickness) and material properties is given, and then the neural network method (with three layers of input, hidden, and output ones) is applied for backcalculation (Sharma and Das 2008).

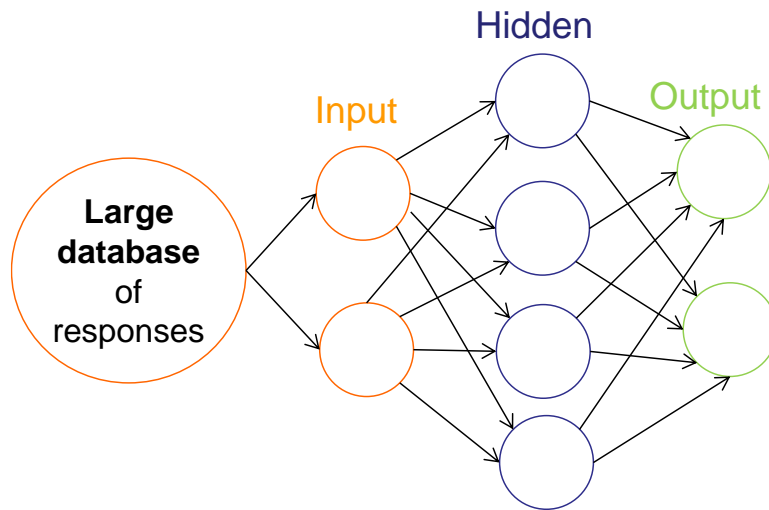


**Figure 14. Artificial neural network method.**

The inputs for the Kalman filter method include the initial values for the material properties and the measured deflections. A weighted error-covariance matrix is computed first; then, the Kalman gain is computed to order to iterate and update the property values and the error-covariance matrix (Choi and Pestana 2006). Iterations continue until achieving an acceptable error.

#### **1.1.6.5 Static FWD backcalculation programs**

Most existing backcalculation programs or methodologies are based on the assumption of linear elastic material properties and static loading conditions (i.e., peak load and deflections). Popular programs include MODULUS, EVERCALC, MODCOMP, ELMOD, etc. Table 4 summarizes some static linear elastic backcalculation programs.

**Table 4. Examples of static backcalculation programs for flexible pavements.**

| <i>Software/method</i> | <i>Authors/Sources</i>              | <i>Pavement Analysis</i> | <i>Optimization Algorithm</i>                                     |
|------------------------|-------------------------------------|--------------------------|---|
| MichPave               | Michigan State University           | Linear Multi-layer       | Newton  |
| EVERCALC               | Washington DOT                      | Linear Multi-layer       | Gauss-Newton algorithm  |
| MODULUS                | Texas Transportation Institute      | Linear Multi-layer       | Database with calculated moduli for all moduli combination search |
| MODTAG                 | Cornell University/<br>Virginia DOT | Linear Multi-layer       | Newton  |
| ELMOD 6                | Dynatest                            | FEM/Linear Multi-layer   | Equivalent thickness method                                       |

#### 1.1.6.6 Dynamic or static viscoelastic FWD backcalculation research

Some FWD backcalculation programs model the entire dynamic response under the FWD loading, and a few treat the AC as a linear viscoelastic material. Table 5 summarizes examples of dynamic backcalculation programs.

**Table 5. Examples of dynamic backcalculation programs for flexible pavements.**

| <i>Software/method</i> | <i>Authors/Sources</i>                 | <i>Pavement Analysis</i>           | <i>Material Property</i>      |
|------------------------|--|------------------------------------|-------------------------------|
| FWD-DYN                | Foinquinos, Roesset, and Stokoe (1993) | Fourier superposition              | Elastic moduli                |
| BKGREEN                | Kang (1998)                            | Discrete Green functions           | Elastic moduli                |
| SSSM-BACK              | Wang (1993)                            | Semi-analytical                    | Elastic moduli                |
| DYNA-BACK              | Chatti (2003)                          | SAPSI Program                      | Elastic moduli, damping ratio |
| SSSM-SIM               | Ji, et al (2006)                       | Semi-analytical                    | Elastic moduli, damping ratio |
| PDAP                   | Magnuson and Lytton (1993)             | SCALPOT (transfer matrix approach) | AC creep compliance           |

Except for the programs listed in Table 5, other research pertaining to dynamic backcalculation as found in the literature includes the following:

- Uzan (1994) backcalculated the linear dynamic properties of AC layer, using the UTFWIBM program for computing pavement response and the least square optimization method for backcalculating the elastic moduli.
- Liang and Zhu (1998) used the dynamic analysis to backcalculate the fatigue parameters of the AC mixture.

- Scarpas and Blaauwendraad (2001) used the spectral element method to simulate the pavement dynamic response and backcalculate the complex modulus of AC materials with the Burgers model.
- Fernando and Liu (2002) coupled the system identification method into the FWD-DYN program for determining pavement moduli and damping ratios.
- Loizos and Scarps (2005) used a linear dynamic finite element program (AXIDEN and CAPA 3D) for computing pavement response and a forward method for backcalculating pavement elastic moduli.
- Hadidi and Gucunski (2010) used the ABAQUS software to simulate pavement responses and a probabilistic approach to backcalculate elastic moduli.
- Broutin and Theillout (2010) used the FE software CESAR-LCPC for determining the dynamic pavement response with the global Rayleigh damping, and the PREDIWARE software with the Gauss Newton algorithm for backcalculating the material elastic moduli and damping ratios.
- Kutay et al. (2011) used the quasi-static approach to emulate the viscoelastic behavior and backcalculate the master curve of dynamic modulus  $|E^*|$  with the mathematical sigmoidal function. It is a static back-calculation approach.

The differences between predicted and measured deflection time histories will be minimized by varying material property values until achieving an acceptable error tolerance. This process is called optimization. During this procedure, the time series data will be down sampled to reduce the number of data points to be used in this procedure. The error tolerance will be the weighted summation of differences between predicted and measured deflection time histories at down sampled data points of all sensors.

Few of the existing backcalculation methods or programs consider AC materials as viscoelastic (e.g., Chatti et al. 2004). Some backcalculation methods produce creep compliance of AC materials (e.g., Magnuson et al. 1991; Uzan 1994). Magnuson et al. (2001) used a generalized power function to characterize the creep compliance of AC materials. This material model (power function) is relatively simple with a few material parameters. However, this function is not a physical model, nor can it effectively describe

the upper bound and shape of the creep compliance and the master curve of dynamic moduli according to laboratory test results (e.g., Schwartz et al. 2002; Liao 2007), as shown in Figure 15. The upper bound is the portion of a master curve at low reduced frequencies or high reduced times; while the lower bound is that at the high reduced frequencies or low reduced times.

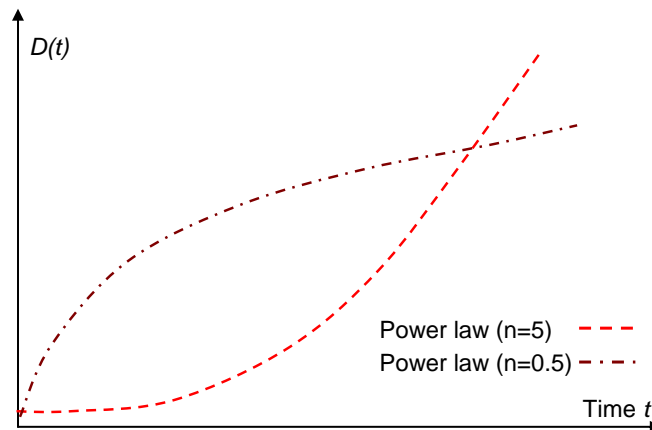
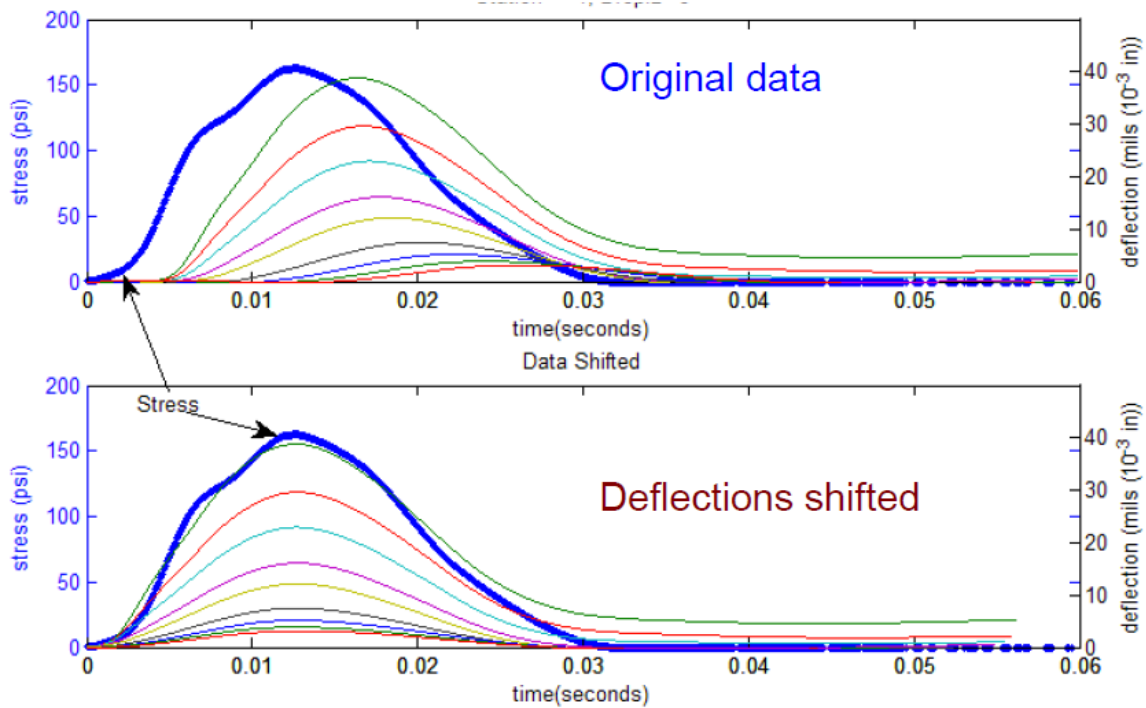


**Figure 15. Creep compliance by power law.**

Scarpas and Zhu (2001), and Scarpas et al. (2002) used the spectral element method and the four-parameter Burger model to inverse the viscoelasticity. However, this method with spectral element method has not been validated with sufficient data sets and implemented into a practical application. Meanwhile, experimental and modeling results indicate that the four-parameter model is unable to fully represent the viscoelastic behavior at a wide range of reduced frequency or time such as that of dynamic moduli (see Figure 3a).

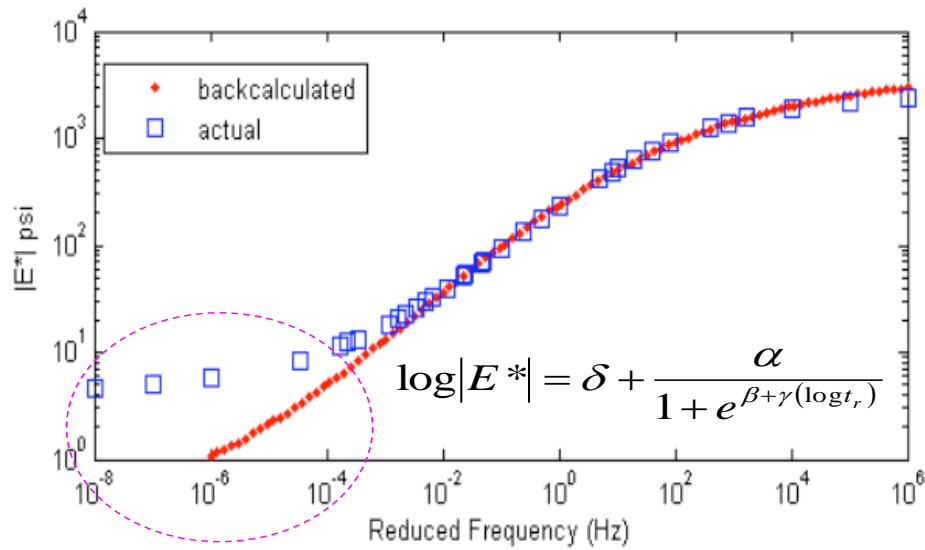
E. Kutay of Michigan State University has utilized an FHWA grant, DTFH61-11-C-00026: “Enhanced Analysis of Falling Weight Deflectometer Data for use with Mechanistic - Empirical Flexible Pavement Design and Analysis and Recommendations for Improvements to Falling Weight Deflectometer” to study the backcalculation of dynamic modulus of a master curve (Kutay et al. 2011),. Kutay et al. (2011) backcalculated the master curve of dynamic moduli  $|E^*|$  (absolute value of complex modulus  $E^*$ ) using a simplified procedure that modeled the pavement response using a linear-elastic analysis program at each time point. The dynamic loading effect has not

been accounted for; rather the time delay of deflections from loading due to wave propagation is shifted manually as shown in Figure 16a. Some discrepancy between true values and backcalculated ones appeared, especially for  $|E^*|$  at the lower reduced frequency range as seen Figure 16b. More recent results presented a genetic algorithm for inverse analysis of viscoelastic properties with the forward response analysis based on a viscoelastic multilayer program (Varma et al. 2013) as shown in Figure 16c.

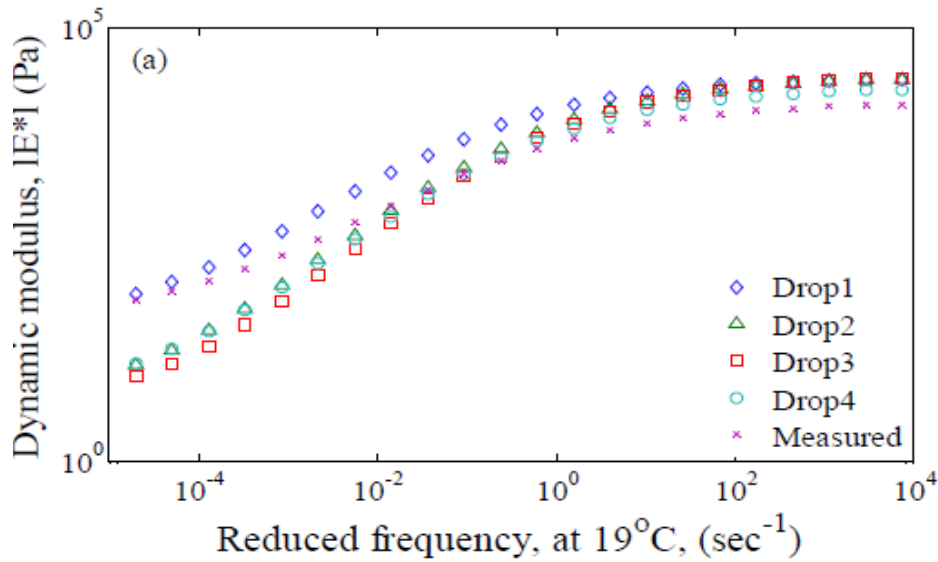


(a) Manual time shift to eliminate the dynamic loading effect (Kutay et al. 2011)

Figure 16. Backcalculation of dynamic moduli master curve  $|E^*|$ .



(b) Backcalculation results of dynamic moduli master curve (Kutay et al. 2011)



(c) Backcalculation results of dynamic moduli master curve using genetic algorithm (Varma et al. 2013)

Figure 16. Backcalculation of dynamic moduli master curve  $|E^*|$  (continued).

## 1.2 Research Problems

Based on the literature review above, existing gaps in research may be summarized as follows:

- Most existing backcalculation programs and methods for multilayer pavement systems produce only the elastic properties of AC material based on either a static or dynamic simulation method; in contrast, the national MEPDG (mechanistic empirical pavement design guide) Level I design uses the dynamic modulus (material viscoelasticity dependent) as the material input for the AC material, and thus a more advanced backcalculation method is needed for the current pavement analysis and design;
- Some methods backcalculate the viscoelastic material properties, but are based primarily on a static simulation method and the simplified material model (e.g., the four parameter Burger model, and 3-parameter power-law based mathematical model), which cannot capture the material's behavior fully;
- For most existing pavement backcalculation, the analytical multilayer analysis programs are used for response modeling, which offers a fast computation speed but is unable to account for more complex situations, such as including the material nonlinearity, time dependency, and temperature profile to emulate in-service conditions; therefore, a more advanced forward response model must be developed in order to consider the dynamic and viscoelastic properties of materials;
- Most existing inverse methods of the multilayer systems are based on a two-stage approach: a forward computation is conducted based on certain programs, and then at the second stage, the inverse algorithm is applied using the response outputs calculated from the first stage of response modeling without direct interactions with the PDEs (partial differential equations) of the first stage. This method may not be sufficiently fast and accurate enough for larger scale material model parameters inversion. For example, for a viscoelastic material model with 14 model parameters (seven elastic moduli and another seven viscosity elements), the two-stage method requires 14 forward computations in order to determine the

gradients  $g_i$  based on the finite difference method in order to achieve a good accuracy, as follows:

$$g_i = \frac{\partial u}{\partial X_i} = \frac{u(X_i + \Delta X_i) - u(X_i)}{\Delta X_i} \text{ for } i = 1, 2, 3 \dots 14 \quad (1-12)$$

where  $u$  is deflection;  $X$  is the material property of the elastic modulus and viscosity, and  $\Delta X$  is a small variation of  $X$ .

- When using an artificial neural network or pattern search method, a large database of deflections, which vary in structure and material properties, is usually required. This becomes impractical when material nonlinearity and time dependency occur; furthermore, the computation time for the forward response modeling is expensive (e.g., very extensive sensitivity analysis is required to cover numerous cases).

### 1.3 Research Objective

The objective of this dissertation research was to develop a computational method for inverse computing dynamic moduli of multilayer systems with applications to flexible pavements under FWD tests, in order to advance existing backcalculation methods and foster understanding of material behaviors and structural responses.

The methodology developed was based on the Lagrangian function, which integrates the two-stage approach into one Lagrangian variation system for larger scale material model parameters. A dynamic viscoelastic-damping coupled model was also developed for the forward response modeling.

### 1.4 Research Scope

The dissertation covers the following contents, divided into five chapters:

Chapter 1 includes the background, literature review, and research problems and objectives.

Chapter 2 develops a finite element model for forward response modeling of the multilayer structure, plus the Newton-Raphson method for inverse computing layer

elastic moduli based on a two-stage approach. The temperature profile of the AC layer based on the AASHTO 1993 pavement design method (AASHTO 1993) is considered, even though most existing backcalculation methods treat temperature as a constant. The inverse method developed in this research also helps to address the common issue of a no-unique inverse solution by estimating appropriate moduli seed values. The static elastic model also serves as a foundation for more advanced numerical method developments as discussed in Chapters 3 and 4.

Chapter 3 develops a finite element model and numerical solution method for modeling the dynamic viscoelastic response of pavement structure under loading pulse. Compared to most existing response modeling, typically static or dynamic elastic modeling, the method developed here has a dynamic-viscoelastic-damping coupled model that has been demonstrated to be an enhanced model for emulating the structural response more accurately through FWD test data. The model serves as the forward computation module for the inverse computation method developed in Chapter 4.

Chapter 4 develops a Lagrangian optimization method for inverting the dynamic moduli and viscoelastic properties of multilayer systems with implementations to flexible pavement structures under FWD tests. Compared to the often used two-stage inverse approach, this method has improved computation speed and accuracy. The model was also implemented in several FWD field tests to invert the dynamic moduli, where the same test section was considered in variable seasons.

Chapter 5 provides a brief conclusion of the main findings and discusses future research.

Independent computer coding written in FORTRAN was also developed for all of the numerical computations discussed in Chapters 2, 3 and 4. Thus, the dissertation research products also have a great potential for industry applications.

## **Chapter 2: A Finite-element Model and Newton-Raphson Method for Inverting Elastic Moduli<sup>1</sup>**

This chapter develops a finite element model and a Newton-Raphson based numerical method to inverse compute the layer elastic moduli (e.g.,  $|E^*|$  of asphalt layer and elastic moduli of unbound layers) in flexible pavements. Compared to most existing back-calculation approaches, the new method can account for temperature profile and associated modulus variation. The modulus seed values are estimated based on an empirical method, which helps address the common issue of no-unique solutions. The model developed will serve as a basic foundation for the dynamic viscoelastic model as discussed in Chapter 3.

A finite element model is developed to simulate the static elastic pavement responses. A Newton-Raphson iteration procedure was proposed to inverse compute the multilayer moduli. As a two-stage approach, it calculates the pavement responses first and then inverse computes layer elastic moduli using response output values. A computer code written in FORTRAN was developed for the numerical computation. The empirical area method was adopted to estimate the seed values; furthermore, an average engineering error of 1.77%, 10.83%, 8.99%, and 1.08% was achieved for the inversed moduli of asphalt concrete, base, subbase, and soil, respectively, based on the Monte Carlo simulation of 5,000 datasets that were used for validation. This indicates that the two-stage approach method was accurate enough for inverse computing the elastic layer moduli of pavement structure, dealing with a relatively simple material model with a small number of model parameters. The method was also able to inverse compute the modulus variation of the top asphalt layer due to temperature profile, with an average error of 4.45% attained for three examples in cold, regular and hot weather conditions.

1. *Modified from: Q. Xu, and J.A. Prozzi (2014) A finite-element and Newton-Raphson method for inverse computing multilayer moduli, Finite Elements in Analysis and Design 81:57-68. Prozzi's contribution included reviewing and offering advice.*

## 2.1 Background

The falling weight deflectometer (FWD) method has been widely used for highway and airport pavement structure evaluation (Alavi et al. 2008). Using FWD, a dynamic load is applied on a circular plate sitting on the top of pavement structure. The displacements on the surface of pavement structure are measured using several geophones with certain spacing (Alavi et al. 2008) as shown in Figure 17. For example, seven geophones are used to measure displacements at the distances of 0, 8 inches (20.3 cm), 12 inches (30.5 cm), 24 inches (61.0 cm), 36 inches (91.4 cm), 48 inches (121.9 cm), and 60 inches (152.4 cm). The FWD data, only peak values of displacements and load pulses, are commonly used to evaluate the structural capacity of pavements.

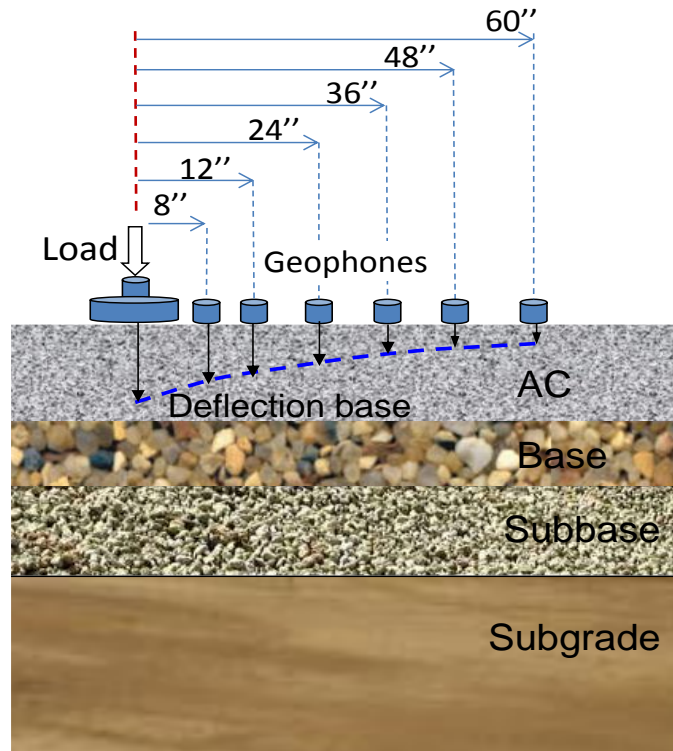


**Figure 17. FWD test and displacement basin.**

As is often the case for rehabilitation design purposes, the FWD loading and measured displacement basin of peak values are also used to inverse compute (or backcalculate) the material properties, typically the layer elastic moduli (Alavi et al. 2008).

Back-calculating pavement layer elastic moduli primarily involves two stages: I) simulate pavement responses of displacements under the FWD loading; and II) compute layer elastic moduli using the mathematical inverse algorithm by minimizing the displacement difference between simulated results from Step I and FWD measurements (also called “observations”). This topic has been extensively studied with popular programs including EverCalc developed by the Washington Department of Transportation (DOT) (Sivaneswaran et al. 2001), MODULUS developed by the Texas Transportation Institute (Michalak and Scullion 1995), MODCOMP 5 originally developed by Cornell University with a DOS version and then updated by Virginia DOT with a Windows version, ELMOD developed by Dynatest Consulting Inc. (Dynatest, 2010), and MichiBack developed by Michigan State University (Harichandran et al. 1993). For these programs, Step I for simulating pavement response is based on the analytical multilayer elastic program. Other analytical approaches, such as the Vlasov or modified Vlasov models (Liang and Zhu1998), are also used for pavement response modeling during backcalculation. The well-known multilayer elastic analysis programs include ELSYM5, originally developed by the University of California at Berkeley and later adapted to microcomputers by Kopperman et al. (1986), BISAR developed by the Shell Global (Shell Inc. 1998), and Everstress developed by the University of Washington and the Washington DOT (Sivaneswaran et al. 2001), etc. These multilayer elastic analysis programs are unable to account for complex and variable boundary and loading conditions such as spatial variation of temperatures and nonlinear material properties. In comparison, the finite element (FE) models could account for more complex boundary and loading conditions, and material properties. For Step II, a variety of algorithms have been studied, including the Kalman filter method (Choi and Pestana 2006), Newton method (Sivanesaran et al. 2001), neural network (Meier et al. 1997; Saltan and Sezgin 2007), least square (Sivaneswaran et al. 1991), and system identification (Wang and Lytton 1993), data mining (Saltan et al. 2011), co-variance matrix adaptation evolution strategy (Gopalakrishnan and Manik 2010), Powell hybrid algorithm (Al-Khoury et al. 2001), and the Ritz-vectors based method (Dong et al. 2002),

etc. Poisson's ratio values of pavement materials are relatively stable and, for typical ranges, usually have a very small effect on displacements (Huang 2003); hence, they are usually assumed as constants rather than being backcalculated. In this paper, Poisson's ratio values are adopted from the literature and not backcalculated.

Backcalculation of layer moduli, as a mathematical computation procedure, is regarded as an "art work" as it may achieve multiple moduli results all with acceptable numerical accuracy (modeled responses *vs.* observations) – the very common non-unique solution problem.

Accordingly, the goal of this research was to develop a numerical methodology and solution to inverse compute the elastic moduli of a multilayer pavement structure, which could help improve the engineering accuracy (differences between inverted moduli and true values) by addressing the non-unique solution problem. Meanwhile, a simple temperature profile model also accounted for the AC material. A finite element model with infinite elements for the infinite half-spaces of boundaries was developed to simulate pavement responses. Consequently, a Newton-Raphson iteration procedure was proposed to inverse compute the layer elastic moduli, where the finite difference method was used to compute the gradient tensor. A computer code in FORTRAN language was developed for the numerical solution.

## **2.2 Finite Element Model Development for Pavement Analysis**

### **2.2.1 Axisymmetric Model**

FWD vertical loading is applied on a circular plate sitting on the surface of pavement. The pavement structure (highway, airport, and parking lot) under the FWD circular loading can be assumed as an axisymmetric body on the semi-infinite half-space of soil foundation at the bottom, with infinite half-spaces at the outer edges. This assumption is rational as: 1) the multilayer structure body is continuous; 2) material properties are considered homogeneous; 3) the soil foundation has infinite depth; and 4) the dimension size of the multilayer is much larger than the FWD loading area (e.g., the

parking lot size compared to the 15 cm-radius of the FWD loading plate). Therefore, it has been a common practice to assume the axisymmetric model under the circular FWD or vehicle loading for calculating pavement responses by using the multilayer analysis programs (Huang 2003).

### 2.2.1.1 Stress Equilibrium

The stress equilibrium for the static solid state can be expressed as follows in a constitutive relation:

$$\nabla \cdot \nabla(\mathbf{C}\mathbf{u}) + \mathbf{b} = 0 \quad (2-1)$$

where  $\mathbf{u}$  is displacement;  $\mathbf{b}$  is body force;  $\mathbf{C}$  is elasticity tensor;  $\nabla \cdot \nabla$  is the Laplacian operator.

For a three-dimensional (3-D) solid in a cylindrical coordinate system  $r - \theta - z$ , the stress-equilibrium equation with components can be decomposed to the following (Sadd 2009):

$$\frac{\partial \sigma_{rr}}{\partial r} + \frac{1}{r} \frac{\partial \sigma_{r\theta}}{\partial \theta} + \frac{\partial \sigma_{rz}}{\partial z} + \frac{1}{r} (\sigma_{rr} - \sigma_{\theta\theta}) + b_r = 0 \quad (2-2)-a$$

$$\frac{\partial \sigma_{r\theta}}{\partial r} + \frac{1}{r} \frac{\partial \sigma_{\theta\theta}}{\partial \theta} + \frac{\partial \sigma_{\theta z}}{\partial z} + \frac{2}{r} \sigma_{r\theta} + b_\theta = 0 \quad (2-2)-b$$

$$\frac{\partial \sigma_{rz}}{\partial r} + \frac{1}{r} \frac{\partial \sigma_{\theta z}}{\partial \theta} + \frac{\partial \sigma_{zz}}{\partial z} + \frac{1}{r} \sigma_{rz} + b_z = 0 \quad (2-2)-c$$

where  $r$  is radius (horizontal);  $\theta$  is angle;  $z$  is depth (vertical);  $\sigma_{rr}$  is normal stress on the  $r$  direction;  $\sigma_{zz}$  is normal stress on the  $z$  direction;  $\sigma_{\theta\theta}$  is normal stress on the  $\theta$  direction;  $\sigma_{zr}$  is shear stress on the  $z - r$  plane pointing on  $r$  direction;  $\sigma_{r\theta}$  is shear stress on the  $r - \theta$  plane pointing on  $\theta$  direction;  $\sigma_{\theta r}$  is shear stress on the  $r - \theta$  plane pointing on  $r$  direction,  $\sigma_{\theta r} = \sigma_{r\theta}$ ;  $\sigma_{z\theta}$  is shear stress on the  $z - \theta$  plane pointing on  $\theta$  direction;  $\sigma_{\theta z}$  is shear stress on the  $z - \theta$  plane pointing on  $z$  direction,  $\sigma_{\theta z} = \sigma_{z\theta}$ ;  $b_r$  is body force on the  $r$  direction,  $b_r = 0$ ;  $b_z$  is body force on the  $z$  direction; and  $b_\theta$  is body force on the  $\theta$  direction,  $b_\theta = 0$ .

According to the axisymmetry, shear stresses of  $\theta_{z\theta}, \theta_{\theta z}$  and  $\theta_{r\theta}, \theta_{\theta r}$  are dismissed; the deformation on the  $\theta$  direction is dismissed ( $u_{\theta\theta} = 0$ ), and  $\sigma_{\theta\theta}$  is independent of  $\theta$  ( $\frac{\partial \sigma_{\theta\theta}}{\partial \theta} = 0$ ). The new stress equilibrium illustration is shown in Figure 18, and the stress equilibrium equation can be reduced to the following:

$$\frac{\partial \sigma_{rr}}{\partial r} + \frac{\partial \sigma_{rz}}{\partial z} + \frac{1}{r}(\sigma_{rr} - \sigma_{\theta\theta}) + b_r = 0 \quad (2-3)-a$$

$$\frac{\partial \sigma_{rz}}{\partial r} + \frac{\partial \sigma_{zz}}{\partial z} + \frac{1}{r}\sigma_{rz} + b_z = 0 \quad (2-3)-b$$

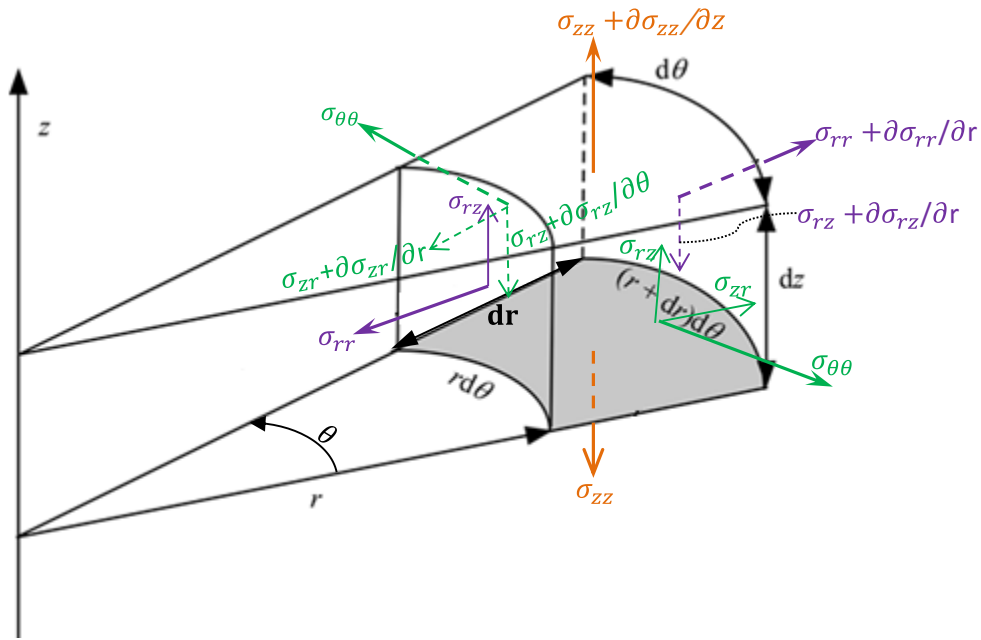


**Figure 18. Axisymmetric model stress state of solid.**

For the axisymmetric problem, the displacement on the  $\theta$  direction is zero, and thus the displacement vector is expressed as follows:

$$\mathbf{u} = \begin{bmatrix} u_r \\ u_z \end{bmatrix} \quad (2-4)$$

where  $\mathbf{u}$  is displacement vector;  $u_r$  is the displacement on the  $r$  direction; and  $u_z$  is the displacement on the  $z$  direction.

The strains can be expressed as follows (Sadd 2009):

$$\varepsilon_{rr} = \frac{\partial u_r}{\partial r} \quad (2-5)\text{-a}$$

$$\varepsilon_{zz} = \frac{\partial u_z}{\partial z} \quad (2-5)\text{-b}$$

$$\varepsilon_{\theta\theta} = \frac{u_r}{r} \quad (2-5)\text{-c}$$

$$\gamma_{rz} = \frac{\partial u_r}{\partial z} + \frac{\partial u_z}{\partial r} \quad (2-5)\text{-d}$$

where  $\varepsilon_{rr}$  is normal strain on the r direction;  $\varepsilon_{zz}$  is normal strain on the z direction;  $\varepsilon_{\theta\theta}$  is normal strain on the  $\theta$  direction, and  $\gamma_{zr}$  is shear strain on the z – r plane pointing on r direction,  $\gamma_{zr} = \gamma_{rz}$ . Note that the shear strains of  $\gamma_{z\theta}, \gamma_{\theta z}, \gamma_{r\theta}, \gamma_{\theta r}$  are dismissed for the axisymmetric problem.

### 2.2.1.2 State Equation

The potential energy or the virtual work is the sum of internal strain energy, body force work, and external energy produced by the FWD loading as follows:

$$\Pi(\mathbf{u}) = \frac{1}{2} \int_{\Omega} \mathbf{C} \nabla \mathbf{u} : \nabla \mathbf{u} d\Omega + \int_{\Omega} \mathbf{b} \cdot \mathbf{u} d\Omega - \int_{\partial\Omega} \mathbf{f} \cdot \mathbf{u} ds \quad (2-6)$$

where  $\Pi(\mathbf{u})$  is energy with respect to  $\mathbf{u}$ ;  $\mathbf{b}$  is body force;  $\mathbf{C}$  is elasticity tensor, and  $\nabla$  is derivative operator.

For the axisymmetric problem in the finite element formulation, the derivative operator  $\nabla$  is expressed as a 4 (row) by 2 (column) matrix in the following form:

$$\nabla = \begin{bmatrix} \frac{\partial}{\partial r} & 0 \\ 0 & \frac{\partial}{\partial z} \\ \frac{1}{r} & 0 \\ \frac{\partial}{\partial z} & \frac{\partial}{\partial r} \end{bmatrix} \quad (2-7)$$

For the axisymmetric problem the elasticity tensor  $\mathbf{C}$  can be expressed as follows (Saddi 2009):

$$\mathbf{C} = \frac{E}{(1+\nu)(1-2\nu)} \begin{bmatrix} 1-\nu & \nu & \nu & 0 \\ \nu & 1-\nu & \nu & 0 \\ \nu & \nu & 1-\nu & 0 \\ 0 & 0 & 0 & 0.5(1-2\nu) \end{bmatrix} \quad (2-8)$$

where  $E$  is Young modulus and  $\nu$  is Poisson's ratio. Using the Ritz method (Cook et al. 2002), applying the variation with respect to the displacement variable  $u$  and zero energy, a weak form of the stone equation is obtained as follows:

$$\int_{\Omega} \mathbf{C} \nabla \mathbf{u} : \nabla \hat{\mathbf{u}} d\Omega + \int_{\Omega} \mathbf{b} \cdot \hat{\mathbf{u}} d\Omega - \int_{\partial\Omega_4} f \cdot \hat{\mathbf{u}} ds = 0 \quad (2-9)$$

By numerically solving the weak form of the state equation, the displacement  $\mathbf{u}$  can be determined as will be discussed later.

### 2.2.1.3 Boundary Conditions

#### *Natural boundary condition*

The FWD loading is applied on the boundary of  $\partial\Omega_4$  (see Figure 19) with a radius of 15 cm (5.9 inch). The natural boundary condition for loading is expressed as follows:

$$\boldsymbol{\sigma} \cdot \mathbf{n} ds = f \text{ on } \partial\Omega_4 \quad (2-10)$$

where  $\mathbf{n}$  is the normal direction;  $s$  is surface unit, and  $f$  is FWD loading pressure on the vertical direction.

#### *Essential boundary condition*

The essential boundary conditions for the constrained displacements on boundaries are expressed as follows (see Figure 19):

$$u_r = 0 \text{ on } \partial^2\Omega_1 \quad (2-11)\text{-a}$$

$$u_r = 0 \text{ on } \partial\Omega_2 \cup \partial\Omega_3 \quad (2-11)\text{-b}$$

$$u_z = 0 \text{ on } \partial\Omega_3 \quad (2-11)\text{-c}$$

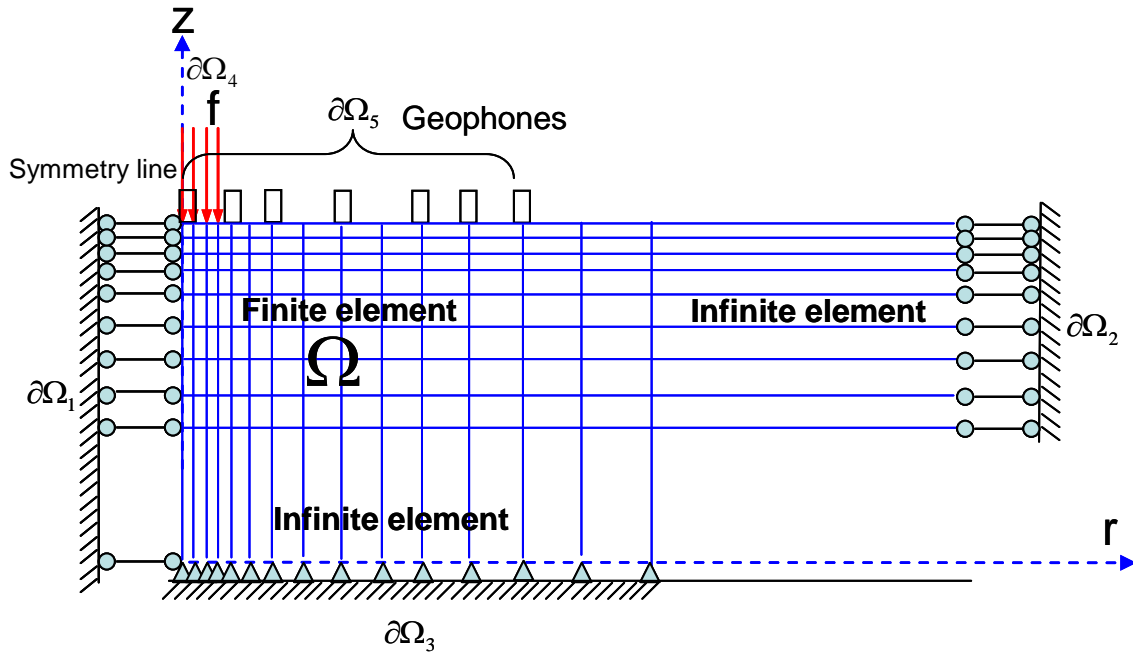


**Figure 19. Axisymmetric FE model under FWD loading.**

### 2.2.2 Temperature Profile and Modulus Variation

The mechanical behavior and modulus of the top AC layer is temperature dependent (Huang 2003), while the modulus of the unbound materials (base/subbase and soil) can be regarded as constants (Huang 2003). In the FE model, the temperature profile and associated modulus variation of the AC layer is accounted for. According to the AASHTO 1993 design method, the AC modulus is temperature dependent as follows (AASHTO 1993):

$$E(T) = \frac{E(T_r)}{10^{-0.0002175(T_r^{1.886} - T^{1.886})}} \quad (2-12)$$

where,  $E(T)$  = modulus at temperature  $T$ ;  $T_r$  = reference temperature, e.g. 70 °F.

In the FE model, the temperature values are read in at different depths, and then the modulus at that depth and element is calibrated according to the above equation.

### 2.2.3 Numerical Solution

The finite element (FE) method is used to solve the PDE controlled state equation for determining the displacement variable,  $\mathbf{u}$ , and then the simplified Newton-Raphson

inverse procedure is proposed to backcalculate the layer elastic moduli. A computer program written in FORTRAN coding was developed for the entire numerical solution of FE model and inverse computation.

### 2.2.3.1 Finite elements

The two-dimensional (2-D) finite element model for the axisymmetric problem was built as shown in Figure 19. The 8-node isoparametric ring element (Felippa 2011) was adopted to simulate the main body of the axisymmetric domain as shown in Figure 20a. The infinite elements were used to simulate the infinite half-spaces of boundaries on the further right side along the radial direction (Figure 20b) and the soil foundation along the depth direction (Figure 20c).

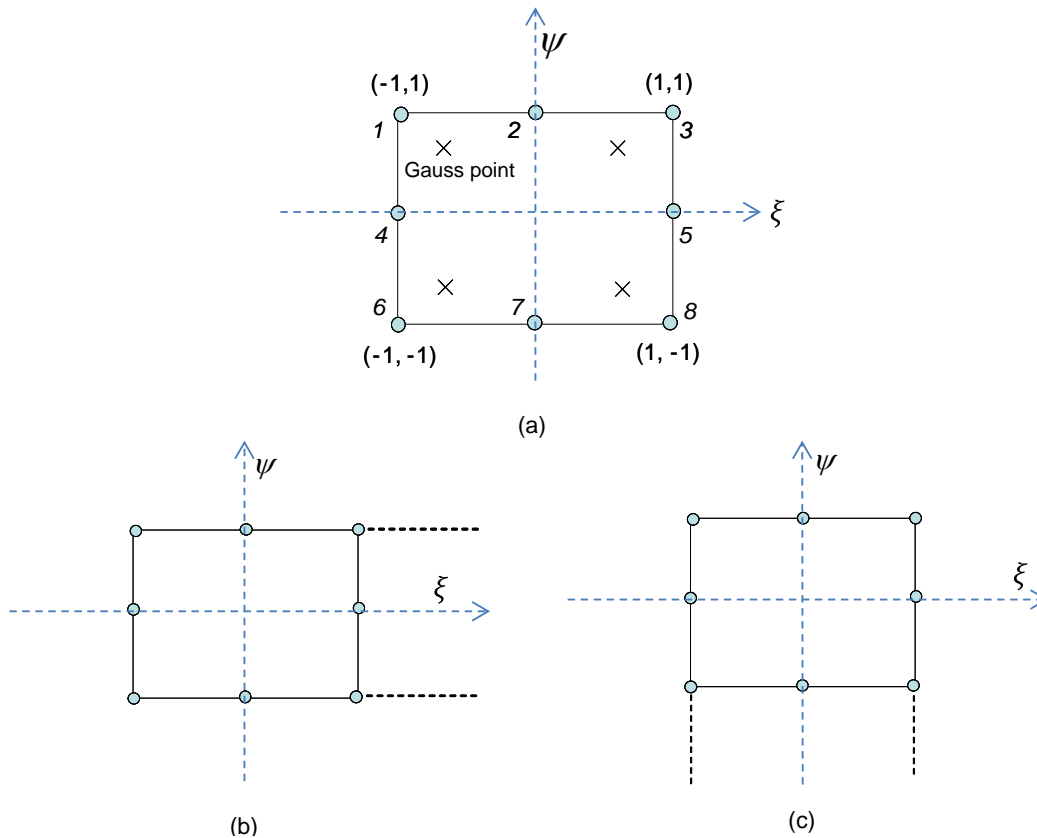


**Figure 20. Isoparametric finite and infinite elements at the local coordinates (a) finite elements for the domain body; (b) infinite element for the right side; and (c) infinite element for the infinite half-space of soil.**

The two-times polynomial shape function was used for the 8-node ring element as follows:

$$\phi_1 = -\frac{1}{4}(1 - \xi)(1 - \psi)(1 + \xi + \psi) \quad (2-13)\text{-a}$$

$$\phi_2 = -\frac{1}{4}(1 + \xi)(1 - \psi)(1 - \xi + \psi) \quad (2-13)\text{-b}$$

$$\phi_3 = -\frac{1}{4}(1 + \xi)(1 + \psi)(1 - \xi - \psi) \quad (2-13)\text{-c}$$

$$\phi_4 = -\frac{1}{4}(1 - \xi)(1 + \psi)(1 + \xi - \psi) \quad (2-13)\text{-d}$$

$$\phi_5 = \frac{1}{2}(1 - \xi)(1 - \psi)(1 + \xi) \quad (2-13)\text{-e}$$

$$\phi_6 = \frac{1}{2}(1 + \xi)(1 - \psi)(1 - \psi) \quad (2-13)\text{-f}$$

$$\phi_7 = \frac{1}{2}(1 + \xi)(1 + \psi)(1 - \xi) \quad (2-13)\text{-g}$$

$$\phi_8 = \frac{1}{2}(1 - \xi)(1 + \psi)(1 - \psi) \quad (2-13)\text{-h}$$

where  $(\xi, \psi)$  is local coordinates.

The four Gauss points of each element are taken at  $\left(\frac{1}{\sqrt{3}}, \frac{1}{\sqrt{3}}\right), \left(-\frac{1}{\sqrt{3}}, \frac{1}{\sqrt{3}}\right), \left(\frac{1}{\sqrt{3}}, -\frac{1}{\sqrt{3}}\right), \left(-\frac{1}{\sqrt{3}}, -\frac{1}{\sqrt{3}}\right)$  as seen in Figure 20 (a).

### 2.2.3.2 Infinite elements

Bettess's model (Bettess 1980) was adopted for simulating the infinite half-spaces, with the shape function expressed as follows:

$$\phi_i^{inf} = f_i(\xi, \psi)\phi_i \quad (2-14)$$

where  $\phi_i(\xi, \psi)$  is the shape function of finite elements, and  $f_i(\xi, \psi)$  is the decay function.

Here an exponential form for the decay function was used (Bettess 1980):

At the positive direction (Figure 20b):

$$f_i(\xi, \psi) = e^{\frac{\xi_i - \xi}{L}} \quad (2-15)$$

At the negative direction (Figure 20c):

$$f_i(\xi, \psi) = e^{\frac{\psi - \psi_i}{L}} \quad (2-16)$$

where  $L$  is length to determine the severity of the decay.

The derivatives of the infinite element shape function for the right side of the model can be expressed as follows:

$$\frac{\partial \phi_i^{\text{inf}}}{\xi} = \frac{\partial \phi_i}{\partial \xi} f_i + \phi_i \frac{\partial f_i}{\partial \xi} \quad (2-17)\text{-a}$$

$$\frac{\partial \phi_i^{\text{inf}}}{\psi} = \frac{\partial \phi_i}{\partial \psi} f_i \quad (2-17)\text{-b}$$

For the bottom side of the model:

$$\frac{\partial \phi_i^{\text{inf}}}{\xi} = \frac{\partial \phi_i}{\partial \xi} f_i \quad (2-18)\text{-a}$$

$$\frac{\partial \phi_i^{\text{inf}}}{\psi} = \frac{\partial \phi_i}{\partial \psi} f_i + \phi_i \frac{\partial f_i}{\partial \psi} \quad (2-18)\text{-b}$$

### 2.2.3.3 FE solution of displacements

The displacements  $u$  and  $\hat{u}$  (variation of  $u$ ) in the state Equation 2-9) are discretized as follows:

$$u = \sum_{i=1}^n \phi_i u_i \quad (2-19)\text{-a}$$

$$\hat{u} = \sum_{i=1}^n \phi_i \hat{u}_i \quad (2-19)\text{-b}$$

where  $u_i$  and  $\hat{u}_i$  are the displacements of the  $i^{\text{th}}$  node,  $i = 1, 2 \dots 8$ ;  $n$  is node number of a single element,  $n = 8$ .

The strain vector is determined as follows:

$$\varepsilon = \nabla u = \sum_{i=1}^n u_i \nabla \phi_i = \mathbf{B}u \quad (2-20)$$

where  $\mathbf{B} = \nabla \phi$ , strain-displacement matrix.

For an element of axisymmetry domain, applying the derivative operator to the shape function matrix  $\boldsymbol{\phi}$ , the strain-displacement matrix  $\mathbf{B}$  ( $4 \times 16$ ) can be determined as follows:

$$\mathbf{B} = \begin{bmatrix} \frac{\partial \phi_1}{\partial r} & 0 & \frac{\partial \phi_2}{\partial r} & 0 & \dots & \frac{\partial \phi_8}{\partial r} & 0 \\ 0 & \frac{\partial \phi_1}{\partial z} & 0 & \frac{\partial \phi_2}{\partial z} & \dots & 0 & \frac{\partial \phi_8}{\partial z} \\ \frac{\phi_1}{r} & 0 & \frac{\phi_2}{r} & 0 & \dots & \frac{\phi_8}{r} & 0 \\ \frac{\partial \phi_1}{\partial z} & \frac{\partial \phi_1}{\partial r} & \frac{\partial \phi_2}{\partial z} & \frac{\partial \phi_2}{\partial r} & \dots & \frac{\partial \phi_8}{\partial z} & \frac{\partial \phi_8}{\partial r} \end{bmatrix} \quad (2-21)$$

When substituting the discretized  $u$  and  $\hat{u}$  into the weak form of state equation (Equation 2-9), the following weak form can be obtained:

$$\int_{\Omega} \mathbf{B}u \cdot \mathbf{B}\hat{u}d\Omega + \int_{\Omega} \mathbf{b} \cdot \boldsymbol{\phi}\hat{u}d\Omega - \int_{\partial\Omega_4} f \cdot \boldsymbol{\phi}_{\Gamma}\hat{u}ds = 0 \quad (2-22)$$

$$\int_{\Omega} \mathbf{B}^T u \mathbf{B}\hat{u}d\Omega + \int_{\Omega} \boldsymbol{\phi}^T \mathbf{b}\hat{u}d\Omega - \int_{\partial\Omega_4} \boldsymbol{\phi}_{\Gamma}^T f \hat{u}ds = 0 \quad \forall \hat{u} \quad (2-23)$$

Dismiss the arbitrary term  $\hat{u}$  on both sides

$$\int_{\Omega} \mathbf{B}^T \mathbf{C} \mathbf{B} u d\Omega = - \int_{\Omega} \boldsymbol{\phi}^T \mathbf{b} d\Omega + \int_{\partial\Omega_4} \boldsymbol{\phi}_{\Gamma}^T f ds \quad (2-24)$$

The stiffness matrix is as follows:

$$\mathbf{K} = \int_{\Omega} \mathbf{B}^T \mathbf{C} \mathbf{B} d\Omega \quad (2-25)$$

Let  $\mathbf{K}^e$  be the stiffness matrix for each element. For a numerical solution,  $\mathbf{K}^e$  can be discretized with Gauss points as follows:

$$\mathbf{K}^e = \sum_{k=1}^{n_G} \sum_{l=1}^{n_G} w_k w_l \mathbf{B}^T(\xi_k, \psi_l) \mathbf{C} \mathbf{B}(\xi_k, \psi_l) 2\pi r(\xi_k, \psi_l) J_{\Omega}(\xi_k, \psi_l) \quad (2-26)$$

where  $w_k, w_l$  are weight function ( $w_k = w_l = 1$  in this model);  $n_G$  is number of Gauss points at each direction,  $n_G = 2$ , and  $J_{\Omega}(\xi_k, \psi_l)$  is the determinant of Jacob's function on the local coordinate of  $(\xi_k, \psi_l)$ .

The Jacob determinant is presented as follows:

$$J_{\Omega(\xi_k, \psi_k)} = \det \left[ \frac{\partial}{\partial \xi}, \frac{\partial}{\partial \psi} \right]^T = \det \begin{bmatrix} \frac{\partial r}{\partial \xi} & \frac{\partial z}{\partial \xi} \\ \frac{\partial r}{\partial \psi} & \frac{\partial z}{\partial \psi} \end{bmatrix} = \frac{\partial r}{\partial \xi} \frac{\partial z}{\partial \psi} - \frac{\partial z}{\partial \xi} \frac{\partial r}{\partial \psi} \quad (2-27)$$

The body-force term  $\int_{\Omega} \boldsymbol{\phi}^T \mathbf{b} d\Omega$  is discretized with Gauss points for the numerical solution as follows:

$$\int_{\Omega} \boldsymbol{\phi}^T \mathbf{b} d\Omega = \sum_{k=1}^{n_G} \sum_{l=1}^{n_G} 2\pi r(\xi_k, \psi_l) w_k w_l \boldsymbol{\phi}^T(\xi_k, \psi_l) b(\xi_k, \psi_l) J_{\Omega}(\xi_k, \psi_l) \quad (2-28)$$

The external force term  $\int_{\partial\Omega_4} \boldsymbol{\phi}^T f ds$  is discretized with Gauss points for the numerical solution as follows:

$$\int_{\partial\Omega_4} \boldsymbol{\phi}^T f ds = \sum_{l=1}^{n_G} 2\pi r(\xi_k, \psi_l) w_k(\xi_k) f(\xi_k) J_{\Gamma}(\xi_k) \quad (2-29)$$

The loading vector is formed as follows:

$$\mathfrak{R} = - \int_{\Omega} \boldsymbol{\phi}^T \mathbf{b} d\Omega + \int_{\partial\Omega_4} \boldsymbol{\phi}^T f ds \quad (2-30)$$

By assembling the stiffness matrix of each element to the global domain, the global linear system is achieved as follows:

$$\mathbf{K}u = \mathfrak{R} \quad (2-31)$$

where  $\mathbf{K}$  is the global stiffness matrix;  $\mathfrak{R}$  is the global loading vector.

The stiffness matrix  $\mathbf{K}$  is positive definite, and the matrix can be banded by gathering only the non-zero terms to reduce the data storage space and accelerate the computation speed. In order to minimize the bandwidth size, the element numbers and nodes were aligned with an increasing order along the radius direction as shown in Figure 21 for an example of a four-element domain. The  $\mathbf{K}$  matrix was then decomposed to the upper and lower triangular matrixes ( $\mathbf{L}$  and  $\mathbf{U}$ , respectively) following the  $\mathbf{LU}$  factorization rule, and thus the linear system of Equation (2-31) can be re-expressed as follows:

$$\mathbf{L}\mathbf{U}u = \mathfrak{R} \quad (2-32)$$

Consequently, the linear system was solved following two steps in sequence for finding  $y$  vector and then  $u$  displacement vector:

$$\begin{cases} \mathbf{L}y = \mathfrak{R} \\ \mathbf{U}u = y \end{cases} \quad (2-33)$$

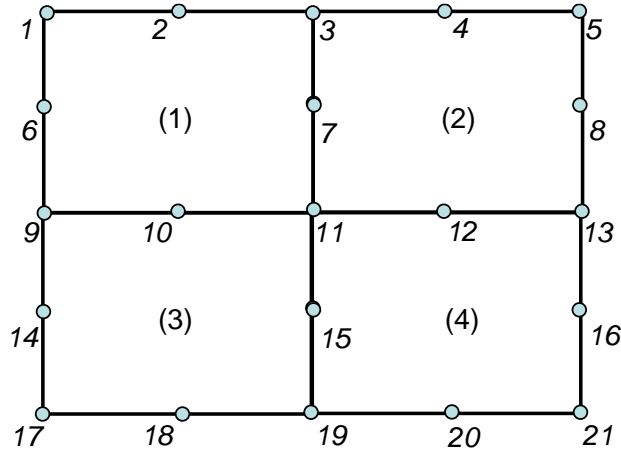


**Figure 21. Sketch example of finite elements and nodes.**

## 2.3 Newton-Raphson Inverse Algorithm

An inverse computation procedure based on the Newton-Raphson method is proposed as follows. As compared to other existing methods discussed earlier (Sivaneswaran et al. 1991, Wang and Lytton 1993, Meier et al. 1997, Al-Khoury et al. 2001, Dong et al. 2002, Choi et al. 2006, Saltan and Sezgin 2007, Gopalakrishnan and Manik 2010, Saltan et al. 2011), the proposed method uses the developed FE model to simulate pavement responses, and a Newton-Raphson method with empirically estimated moduli as initial seed values for the inversion computation. In addition, the temperature profile of AC layer can be accounted for.

### 2.3.1 Guess initial moduli seed values

The initial moduli seed values could be any positive values within a fairly wide range. However, as mentioned earlier a variety of inversed moduli results may be obtained—all with acceptable numerical accuracies but with different engineering accuracy. Therefore, initial seed values that penalize or constrain the initial moduli seed value ranges according to engineering judgment are recommended to improve the

engineering accuracy of inverse computation. The Long Term Pavement Performance program (LTPP) database has provided massive amounts of information for pavement structures and material properties including the layer elastic moduli (FHWA 2010). LTPP is based on a comprehensive 20-year study of in-service pavements, monitoring more than 2,400 asphalt and Portland cement concrete pavement test sections across the U.S. and Canada. Table 6 summarizes the moduli value range resulted from the LTPP program for a four-layer pavement structure with the AC as the surface layer, crushed stone as the base layer, gravel material as the subbase layer, and soil as the subgrade. These moduli ranges represent variable properties of pavement materials. The moduli seed values and inverted layer moduli are constrained within these ranges in this study.

**Table 6 Layer moduli range (in MPa) from LTPP program**

| Layer   | Min | Max   |
|---------|-----|-------|
| AC      | 700 | 25000 |
| Base    | 100 | 1500  |
| Subbase | 50  | 750   |
| Soil    | 35  | 450   |

Here the empirical “area method” (Stubstad et al. 2006) is evaluated to estimate the initial moduli seed values for the AC layer. The area method is used to roughly estimate the layer moduli of a pavement structure according to the FWD measured displacement and geophone distances (Stubstad et al. 2006), following the “area concept” proposed in the AASHTO 1993 pavement design guide (AASHTO 1993). The “area” is used to characterize the displacement basin, and the area method is described as follows.

The Boussinesq’s analytical solution (Boussinesq 1885) is used to compute displacement  $u$  on the top of earth or soil foundation—an infinite half-space structure, under a circular loading as follows:

$$u = \frac{(1+\nu)f}{E} \left( 1 - 2\nu + \frac{2vd}{\sqrt{R_a^2+d^2}} - \frac{d^3}{(R_a^2+d^2)^{1.5}} \right) \quad (2-34)$$

where  $\nu$  is Poisson’s ratio of soil;  $f$  is peak FWD loading pressure;  $R_a$  is FWD loading area radius, and  $d$  is FWD geophone distance to the loading center.

The composite modulus of the multilayer pavement structure can be derived from the Boussinesq's equation where  $\nu=0.5$  and  $d=0$  as follows (AASHTO 1993):

$$E_{com} = \frac{1.5Raf}{u_0} \quad (2-35)$$

Then, according to the area method, the modulus of AC layer can be empirically estimated as a function of the composite modulus and “area” factors relating to the geophone distances and displacements (Stubstad et al. 2006):

$$E_{AC} = \frac{E_{com}AF_{AC} \times k_3^{\frac{1}{AF_{AC}}}}{k_3^2} \quad (2-36)-a$$

$$AF_{AC} = \frac{k_2 - 1}{k_2 - \frac{A_{12}}{k_1}}^{1.35} \quad (2-36)-b$$

$$A_{12} = 2 \left( 2 + \frac{3u_8}{u_0} + \frac{u_{12}}{u_0} \right) \quad (2-36)-c$$

where  $AF_{AC}$  is an area factor;  $A_{12}$  is the “area” beneath the first 12 inches (305 mm) of the displacement basin;  $k_2$  is 1.752;  $k_3$  is the ratio of AC layer thickness to loading plate diameter;  $u_0$  is FWD peak displacements measured on the distance of 0;  $u_8$  is FWD peak displacements measured on the distance of 8 inches (203 mm);  $u_{12}$  is FWD peak displacements measured on the distance of 12 inches (305 mm).

### 2.3.2 Inverse computing layer elastic moduli

With the estimated initial moduli seed values as material parameter inputs, the FE simulation was performed to determine pavement displacements as discussed earlier. The FE numerical solution is further detailed later.

The Newton-Raphson method was used to iterate and update the seed moduli until the numerical accuracy criterion (the difference between simulated deflections and measurements or observations) is satisfied. The iteration goal is to minimize the displacement difference between observations (or measurements) and FE modeling results.

The gradient tensor for the inverse computation is defined as follows:

$$g = \begin{bmatrix} \frac{\partial u_1}{\partial E_1} & \frac{\partial u_1}{\partial E_2} & \dots & \frac{\partial u_1}{\partial E_n} \\ \dots & \dots & \dots & \dots \\ \frac{\partial u_m}{\partial E_1} & \frac{\partial u_m}{\partial E_2} & \dots & \frac{\partial u_m}{\partial E_n} \end{bmatrix} \quad (2-37)$$

where  $u_i$  is the deflection at the  $i^{th}$  geophone location ( $i = 1,2,3 \dots m$ );  $E_j$  is the modulus of the  $j^{th}$  layer ( $j = 1,2,3 \dots n$ ).

Figure 22 shows the schematic relationship between calculated displacement and assumed modulus, or deflection curve. The displacements represent the deflections on the surface of the pavement structure at those geophone locations (e.g., 7). Each modulus at each geophone location corresponds to one deflection curve. Here the gradient of the  $i^{th}$  geophone location and the  $j^{th}$  layer moduli at the  $k^{th}$  iteration step is calculated using the finite difference method (FDM) as follows (see Figure 22):

$$g_{i,j}^k = \frac{u_i^k - u_i^{k-1}}{\log(E_j^k) - \log(E_j^{k-1})} \quad (2-38)$$

where  $u_i^k$  is modeled displacement on the  $i^{th}$  geophone and the  $k^{th}$  iteration step;  $E_j^k$  is the inversed moduli of the  $j^{th}$  layer on the  $k^{th}$  iteration step, and the logarithmic scale is applied to moduli for improving numerical stability.

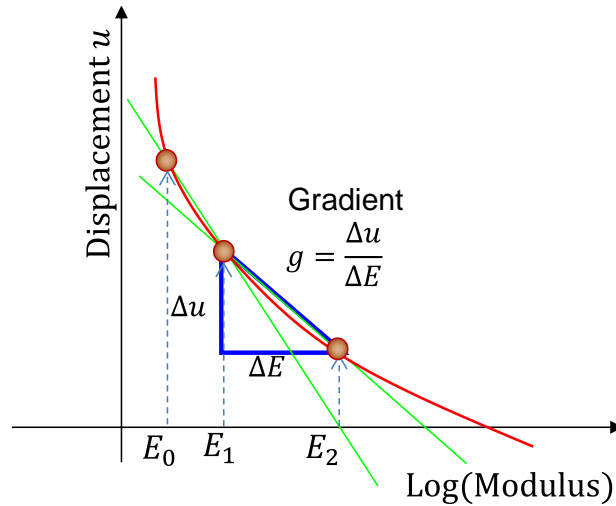


**Figure 22. Gradient calculation.**

Consequently, the moduli variation vector at the  $k^{th}$  iteration step can be determined as follows according to the Newton-Raphson method:

$$\bar{g}\Delta E_k = \alpha_k(u_{obs} - u_{simu.}) \quad (2-39)$$

If the geophone sensor number is the same as that of the layer moduli number, the moduli variation can be determined as follows:

$$\Delta E_k = \alpha_k \bar{g}^{-1}(u_{obs} - u_{simu.}) \quad (2-40)$$

If the geophone sensor number is unequal to that of the layer moduli number, the moduli variation can be determined as follows:

$$\bar{g}^T \bar{g} \Delta E_k = \bar{g}^T \alpha_k (u_{obs} - u_{simu.}) \quad (2-41)$$

$$\Delta E_k = \alpha_k (\bar{g}^T \bar{g})^{-1} \bar{g}^T (u_{obs} - u_{simu.}) \quad (2-42)$$

where,  $\alpha_k$  is the step length;  $\bar{g}$  is the gradient tensor;  $u_{obs}$  is measured deflection vector containing all deflection values measured at those geophone locations;  $u_{simu.}$  is simulated deflection vector at the  $k^{th}$  iteration on those geophone locations.

Afterwards, the modulus vector at the  $k^{th}$  iteration step  $E_k$  is determined as follows:

$$E_k = E_{k-1} + \Delta E_k \quad (2-43)$$

where  $E_{k-1}$  is the modulus vector at the  $(k - 1)^{th}$  iteration step.

Here an error, the root of mean square (*RMS*) value, is used to evaluate the goodness of fit for the simulated displacements as compared to measurements:

$$RMS = \sqrt{\sum_i^m \left( \frac{u_{i,obs} - u_{i,simu.}}{u_{i,obs}} \right)^2} / m \quad (2-44)$$

where  $u_{i,obs}$  is the measured displacements on the pavement surface of the  $i^{th}$  geophone;  $u_{i,simu.}$  is the FE modeled displacement on the pavement surface of the  $i^{th}$  geophone location;  $m$  is total number of geophones, i.e., 7 in this project.

The inverse iteration continues until the *RMS* value is less or equal to the numerical target (e.g., 3%).

### 2.3.3 Computer coding for numerical solution

At each iteration step, pavement displacements are computed, and the Newton-Raphson inversion is performed to compute the layer elastic moduli. A computer code in FORTRAN language was developed for the entire numerical computation. Two main FORTRAIN modules were designed for the core computations: 1) the FE modeling; and 2) the Newton-Raphson inverse computing. Figure 23 presents the flow chart for the computation procedure. The inputs include the pavement structure parameters of layer thicknesses and material Poisson's ratio values, the guessed initial moduli seed values, and the FWD loading. Typical Poisson's ratio values were used in this study, i.e. 0.35, 0.35, 0.40, and 0.45 for AC, base, subbase, and soil, respectively (Huang 2003). FWD measured displacement data were added as observations. Consequently, FE modeling was performed to compute the pavement responses of displacements, followed by the Newton-Raphson inverse computation to determine the layer moduli. This procedure repeats, and the moduli values were updated until the numerical error became acceptable (e.g.  $RMS < 3\%$ ).

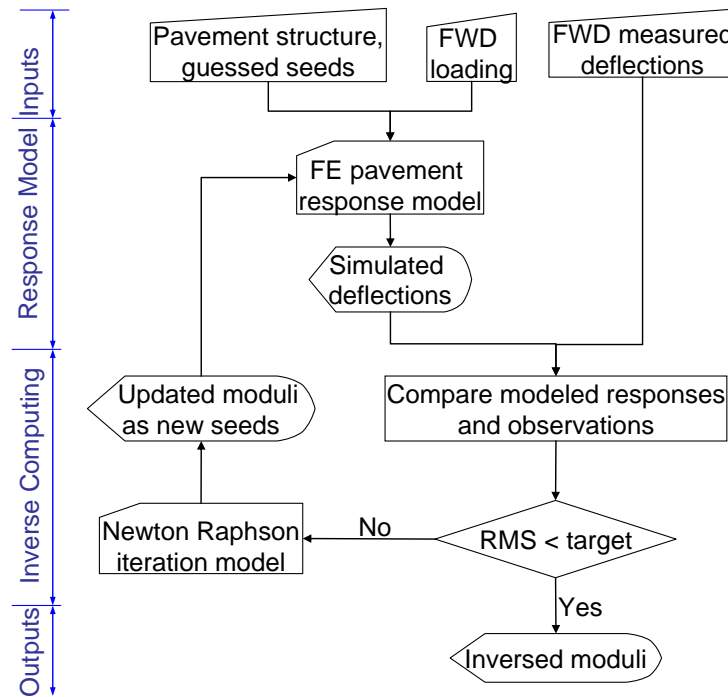


Figure 23. Flow chart for the numerical computation procedure.

## 2.4 Validation Method

To validate the proposed method and numerical solution, typical pavement structures and layer moduli were designed. A Monte-Carlo simulation approach was also employed for validation.

A typical four-layer pavement structure was used for validation (based on LTPP data), named Case I as shown in Table 7. Case II uses half size of the AC layer thickness of Case I to study the effects of AC layer thickness. Case III and Case IV use lower moduli for subbase while higher moduli for soil, with the same and half size of AC layer thickness of Case I, respectively. Case III and IV are designed to study the effects of the moduli of subbase and soil.

**Table 7 Pavement structure layer thickness/moduli values**

|                | <b>Case I</b> | <b>Case II</b> | <b>Case III</b> | <b>Case IV</b> |
|----------------|---------------|----------------|-----------------|----------------|
| <b>HMA</b>     | 15cm/2500MPa  | 7.5cm/2500MPa  | 15cm/2500MPa    | 7.5cm/2500MPa  |
| <b>Base</b>    | 25cm/350MPa   | 25cm/350MPa    | 25cm/350MPa     | 25cm/350MPa    |
| <b>Subbase</b> | 15cm/150MPa   | 15cm/150MPa    | 15cm/75MPa      | 15cm/75MPa     |
| <b>Soil</b>    | 50MPa         | 50MPa          | 200MPa          | 200MPa         |

To validate the accuracy, a Monte-Carlo simulation approach was used and a large dataset of moduli for Case I pavement structure was randomly generated for validation. These included 5,000 randomly generated moduli values for each of the AC, base, subbase, and soil layer. These moduli values were assumed to follow a normal distribution, with a coefficient of variance of 30%, as shown in Figure 24. A very small portion of moduli values fell beyond the LTPP program range and were thus filtered out.

Note that in this study, laboratory testing of pavement materials was not performed to validate the inversion results due to following reasons. The laboratory testing conditions were very different than the in-situ situations including the loading frequency and material confined conditions used in the FE simulation. Meanwhile, the sample preparation from field via coring is destructive for highway systems and very costly. Therefore, rather than using the laboratory validation, a theoretical validation procedure was used. Two validations were conducted as follows:

1) Validation of the FE simulated responses: the well-known ELSYM5 multilayer analytical program was used for validation.

2) Validation of the inversed moduli: first, with the inputs of randomly generated true moduli values, the pavement displacements can be calculated as the “observations.” Then the true moduli values are completely “forgotten.” Consequently, based on the “observations.” the numerical inversion is performed to determine the inversed moduli. Finally, the inversed moduli are compared with the true moduli values to verify the engineering accuracy.

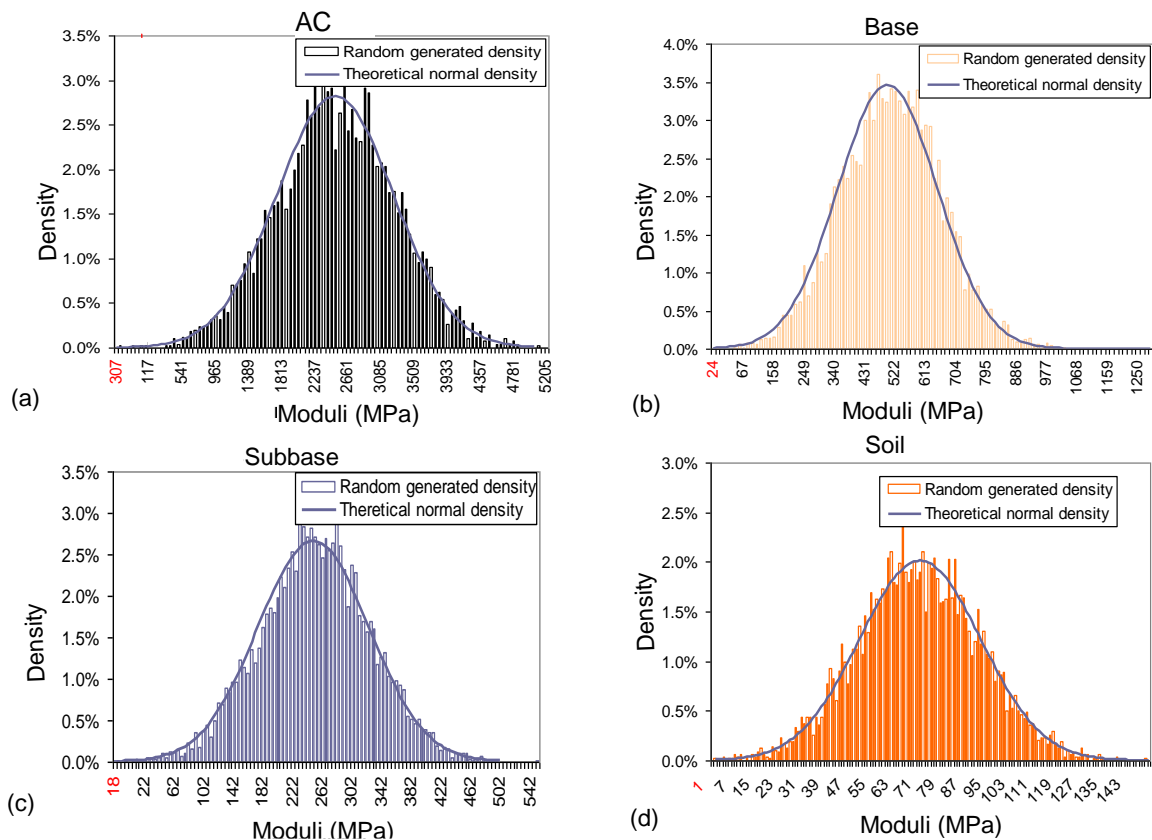


**Figure 24. Probability density of randomly generated moduli in normal-distribution: (a) AC; (b) Base; (c) Subbase, and (d) Soil.**

## **2.5 Results and Analyses**

The FE modeled response results were validated by commercial software, and then the inversed moduli results were validated and the results are discussed in the following subsections.

### **2.5.1 FE Model Validation**

Figure 25a-d present the FE modeled vertical displacements for the pavement structures of Case I to IV, respectively. Results show that Case III and IV have lower displacement values due to their higher soil moduli as compared to that of Case I and II. Case II has the largest displacement value due to its lowest AC thickness and soil moduli.

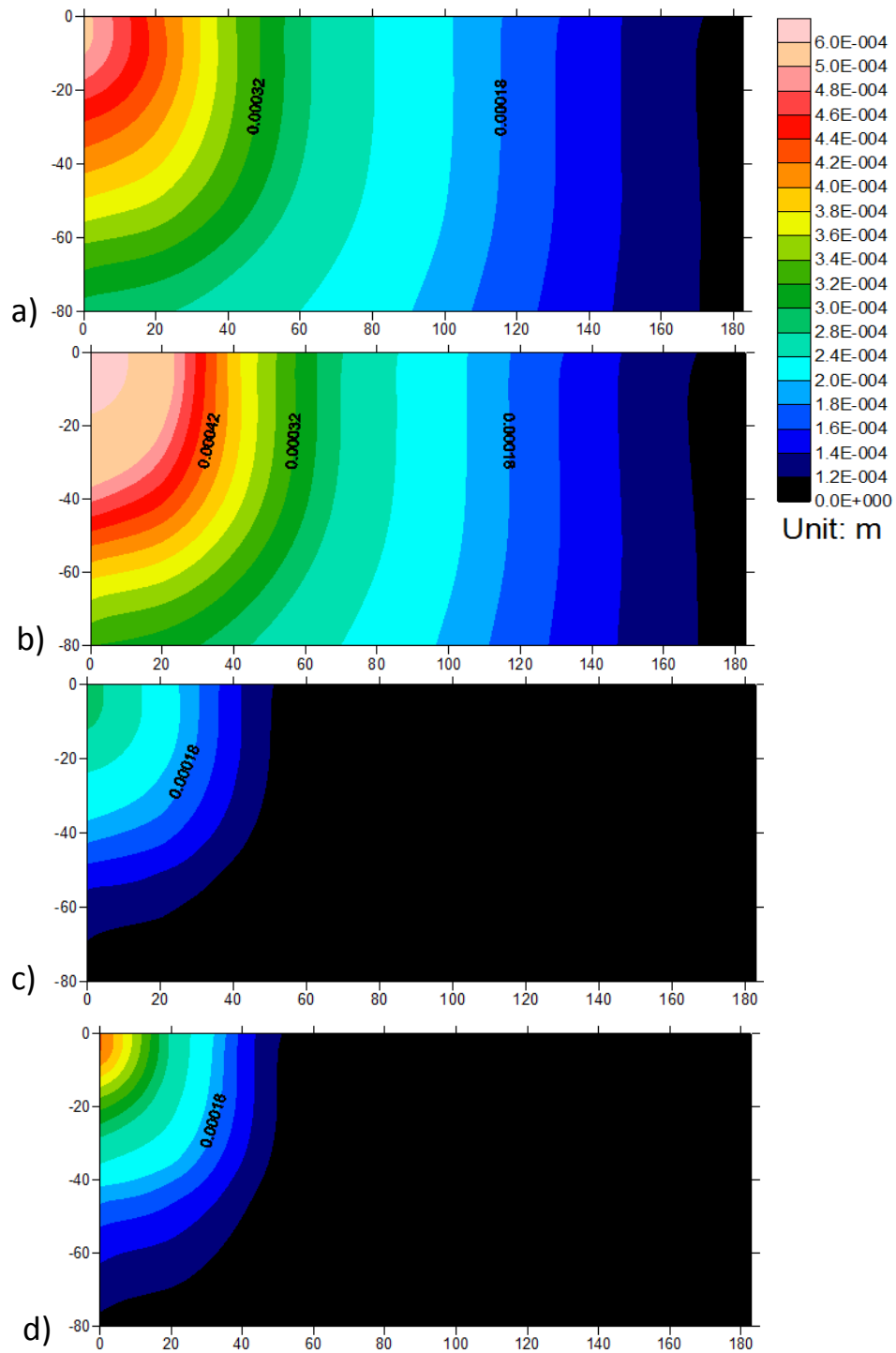


**Figure 25. Pavement displacements simulated by the developed FE model and computer coding for a) Case I, b) Case II, c) Case III, and d) Case IV.**

## 2.5.2 Inversion Results and analyses

### 2.5.2.1 Simulated responses compared to true values

Figure 26 presents the simulated deflections using inverted material moduli vs. the true values (modeled values using true material moduli), indicating a very close match.

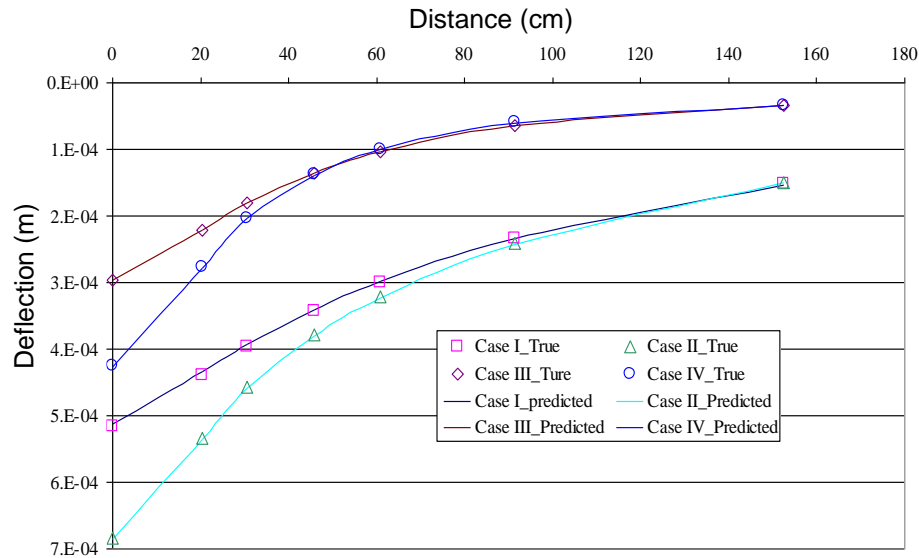


Figure 26. Pavement displacement basin predictions vs. true values.

### 2.5.2.2 Comparison with popular commercial software

The inverted results of layer moduli were compared with that of other available commercial software.

Figure 25 presents backcalculation results of a four-layer pavement structure as compared to that from popular commercial software being used in the industry, including the MichBack (by Michigan State), MODULUS (by Texas Transportation Institute), and EVERCALC (by the University of Washington). This one-case study indicates that this dissertation's developed method (Xu's) and the MichBack had the best accuracy. EVERCALC followed by MODULUS, which had the lowest accuracy among these four programs.

|                  | AC  | Base | Subbase | Subgrade |
|------------------|-----|------|---------|----------|
| Seeds (ksi)      | 100 | 500  | 7       | 3        |
| True Value (ksi) | 500 | 45   | 15      | 7.5      |
| Thickness (inch) | 6   | 10   | 6       | $\infty$ |

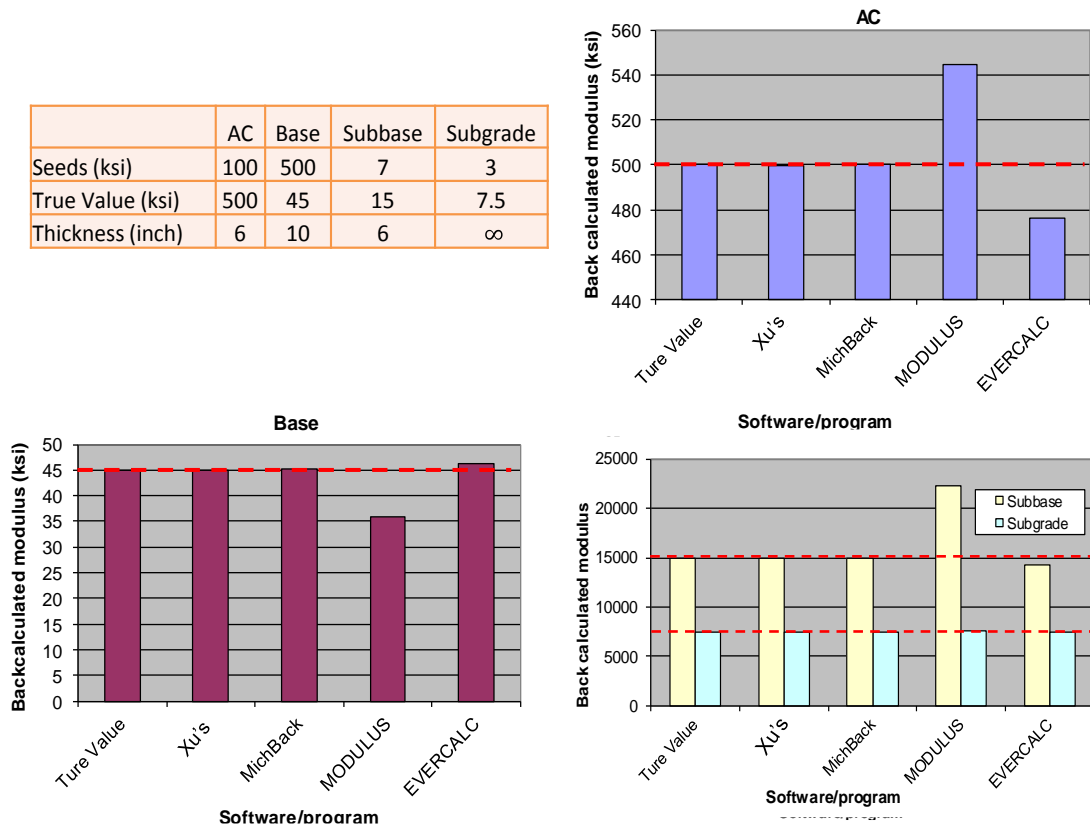


**Figure 27. Comparison with other commercial software.**

### 2.5.2.3 Effect of iteration steps

Figure 28 shows the inversed moduli on different iteration steps. It shows that inversed moduli will usually gradually approach the true values with the increase of iteration steps, though in some cases (e.g., for the AC moduli), and it may also reverse the search direction first and then come back to approach the true value. It was also noted that the inverted moduli values always show the same sign (will either be lower or higher than true values for all iteration steps), indicating a stable convergence using this numerical procedure.

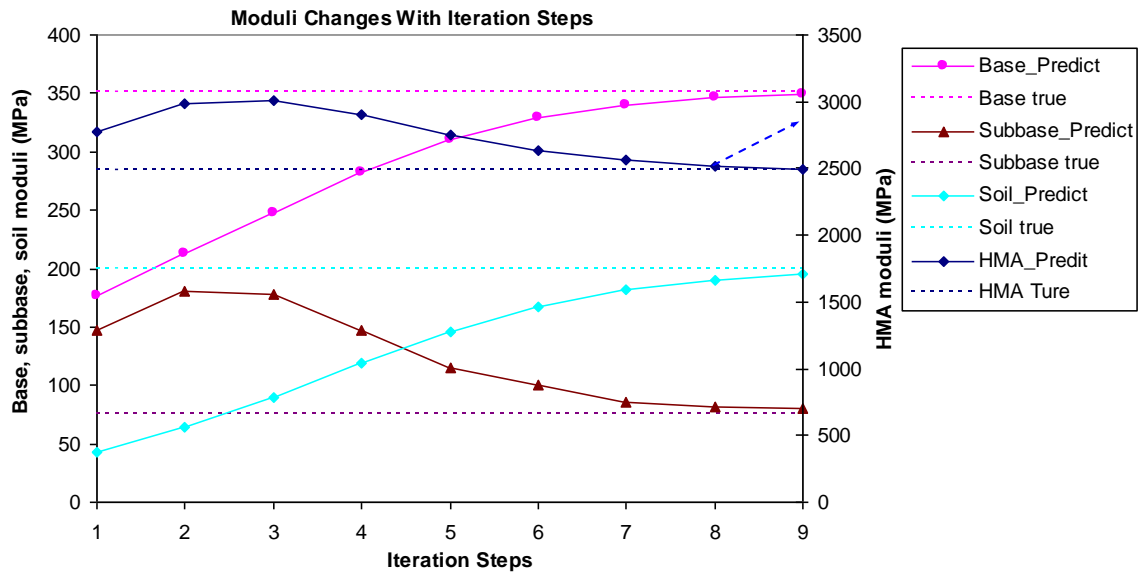


**Figure 28. Inversed moduli with iteration steps.**

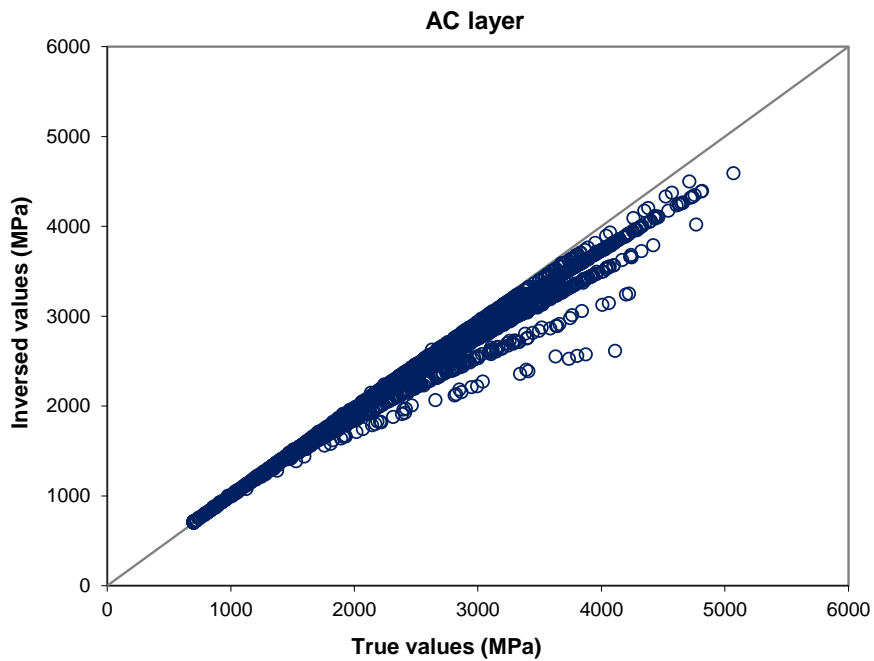
#### 2.5.2.4 Effects of initial moduli seed values

Figure 29a, b, and c represent inverted moduli using random moduli as seed values (e.g., low-bounded values of the LTPP program’s range), for the area method estimated moduli, and inversed moduli using area-method estimated moduli as seed values, respectively. Figure 30 shows the inversed moduli of base, subbase, and soil, using random initial moduli seed values

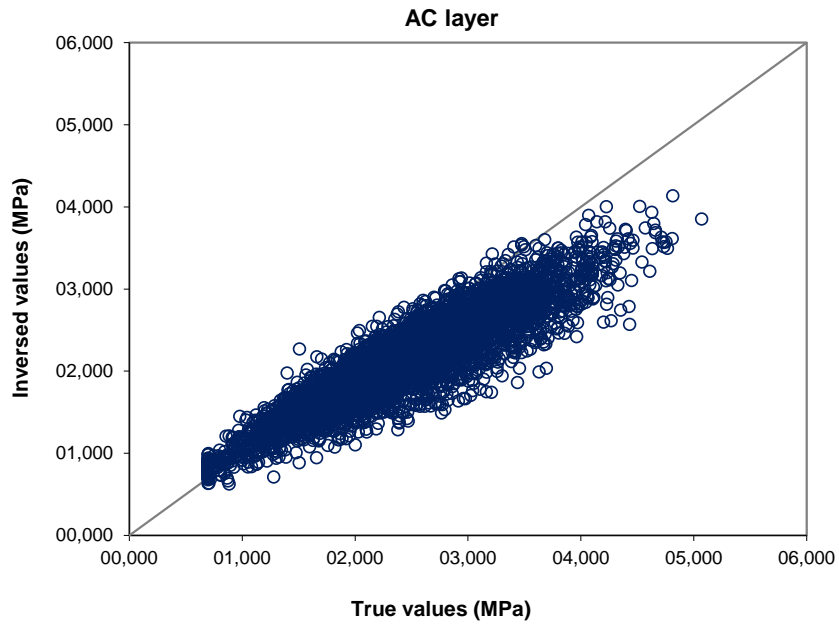
Table 8 summarizes the statistics of engineering error (differences of percentages between inversed moduli and true values).

These case studies indicate that moduli seed values play a critical role in engineering accuracy for the AC layer moduli. This is due to AC moduli’s relatively large variation and their significant effects on pavement displacements. However, results show that numerical accuracy is not sensitive to moduli seed values. For example, the *RMS* is 2.12% and 2.22% for the inversed results using the random moduli values as seeds and using the area-method estimated moduli as seeds, respectively. Figure 29 results indicate that the inverted AC moduli with the area-method-estimated moduli as seeds have the highest engineering accuracy. For example, it has an engineering error

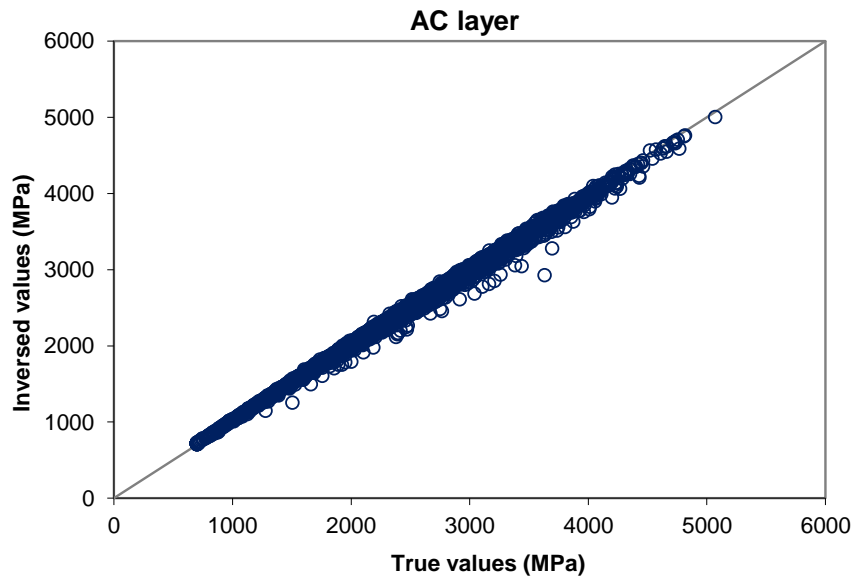
(difference of percentage) of only 1.77%, apparently lower than 16.69% and 5.55% resulting from the area method and the inversion results using random moduli seeds, respectively. Results also indicate that the inverted moduli of the unbound materials (base, subbase and soil) are much less sensitive to the moduli seed values as compared to that of AC layer, which might be due to their smaller variations and less significant effects on pavement displacements.



(a) inversed moduli using random seed values  
Figure 29. Inversed moduli vs. true values of AC.



**(b) area-method estimated moduli**



**(c) inversed moduli using area-method estimated moduli as seeds.**

**Figure 29. Inversed moduli vs. true values of AC (continued).**

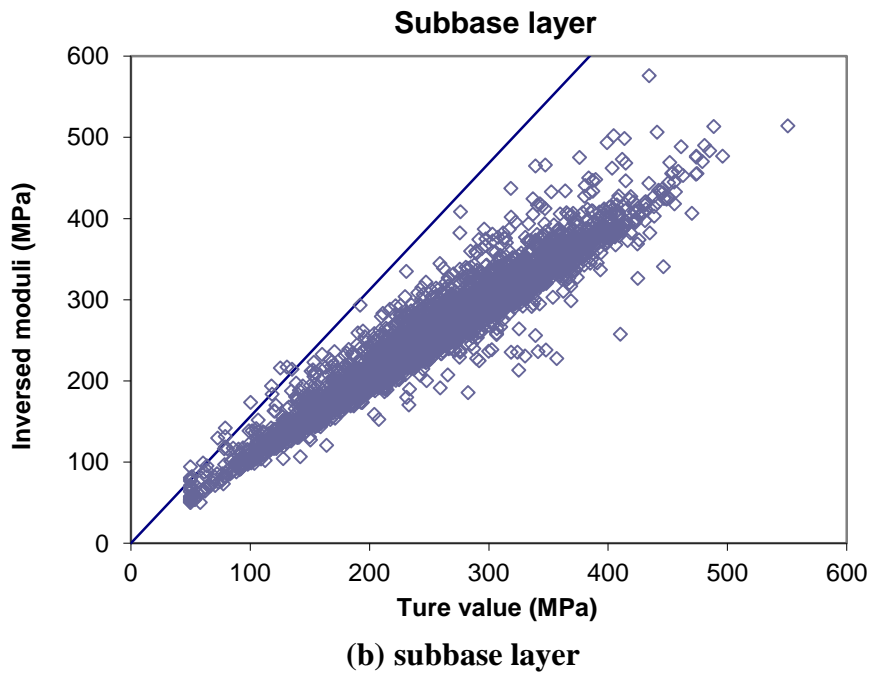
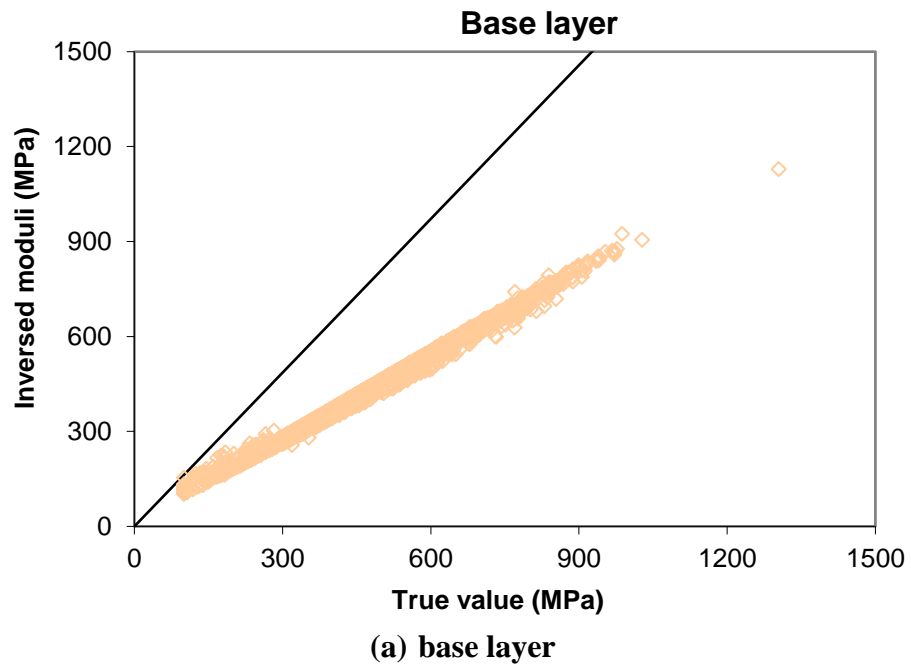
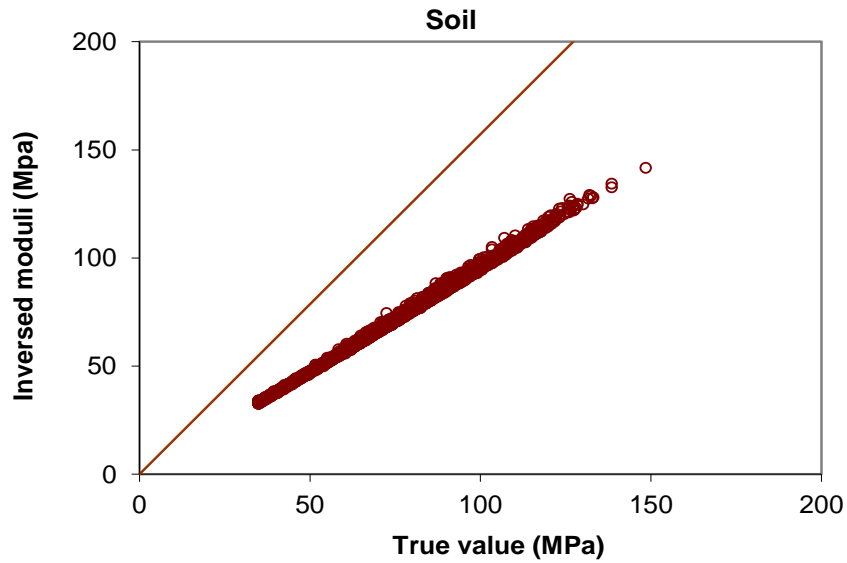


**Figure 30. Inversed moduli vs. true values using random seed values.**



(c) soil

Figure 30. Inversed moduli vs. true values using random seed values (continued).

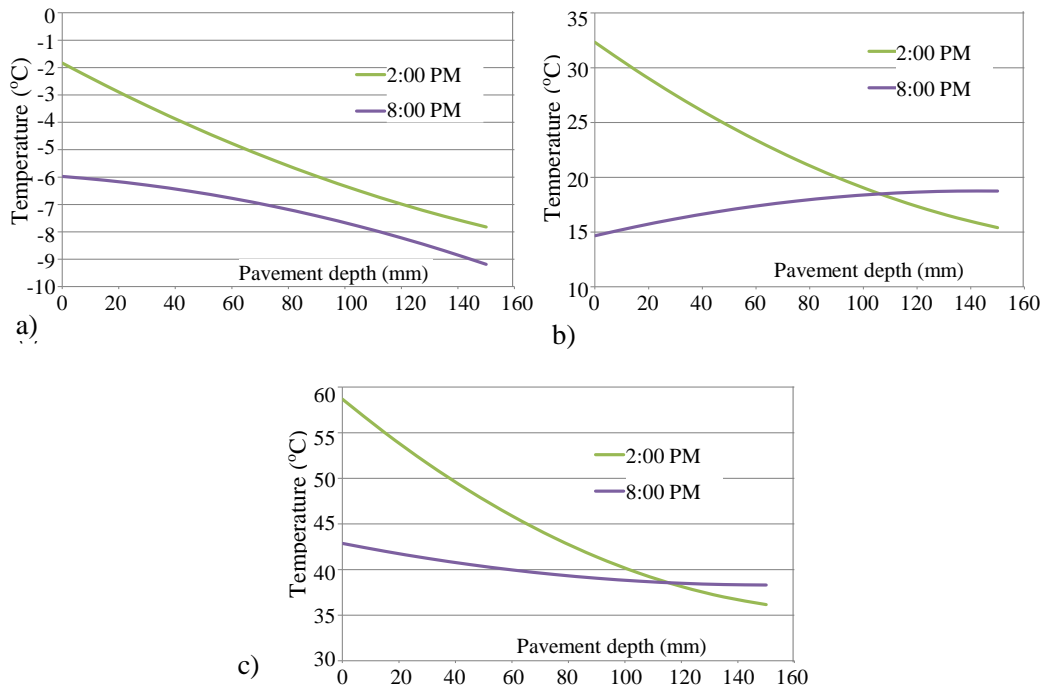
**Table 8 Average engineering error of inversed moduli**

| Method                             | Moduli error |
|------------------------------------|--------------|
| HMA - area-method estimated moduli | 16.69%       |
| HMA - random seeds                 | 5.55%        |
| HMA - area-method modulus as seeds | 1.77%        |
| Base - random seeds                | 10.12%       |
| Subbase - random seeds             | 8.98%        |
| Soil - random seeds                | 1.32%        |

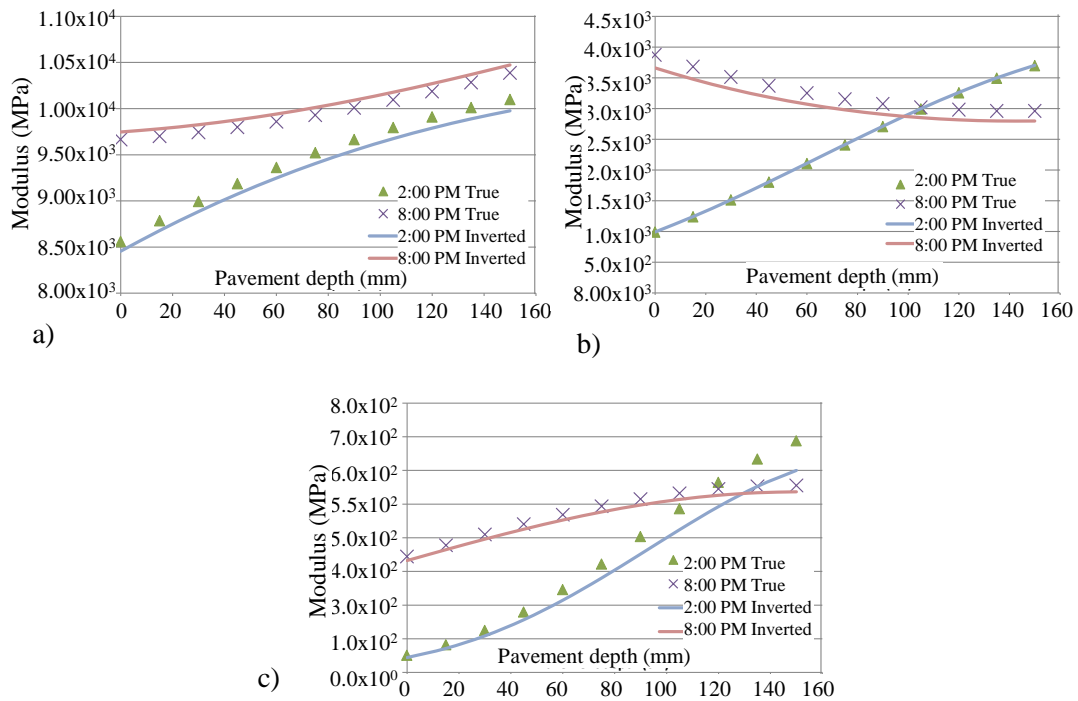
### 2.5.2.5 Moduli profile as temperature dependent

To account for the temperature profile effects, three examples with three weather conditions were implemented for the Case I structure: 1) cold weather, 2) regular weather, and 3) hot weather. The temperature profile data of AC layers at 2:00 PM and 8:00 PM of each example were extracted and estimated from the LTPP data (FHWA 2012) at the Montana State site (cold weather), the Delaware State site (regular weather), and the Arizona State site (hot weather) as shown in Figure 31. The temperature ranges are from -9.2°C to -1.8°C, 14.7°C to 32.3°C, and 36.2°C to 58.7°C for the cold, regular, and hot weather, respectively. The hot weather had the highest temperature variation (22.5°C difference at 2:00 PM), then the regular weather (16.9°C difference at 2:00 PM), and the cold weather had the lowest temperature variation (6.0°C difference at 2:00 PM).

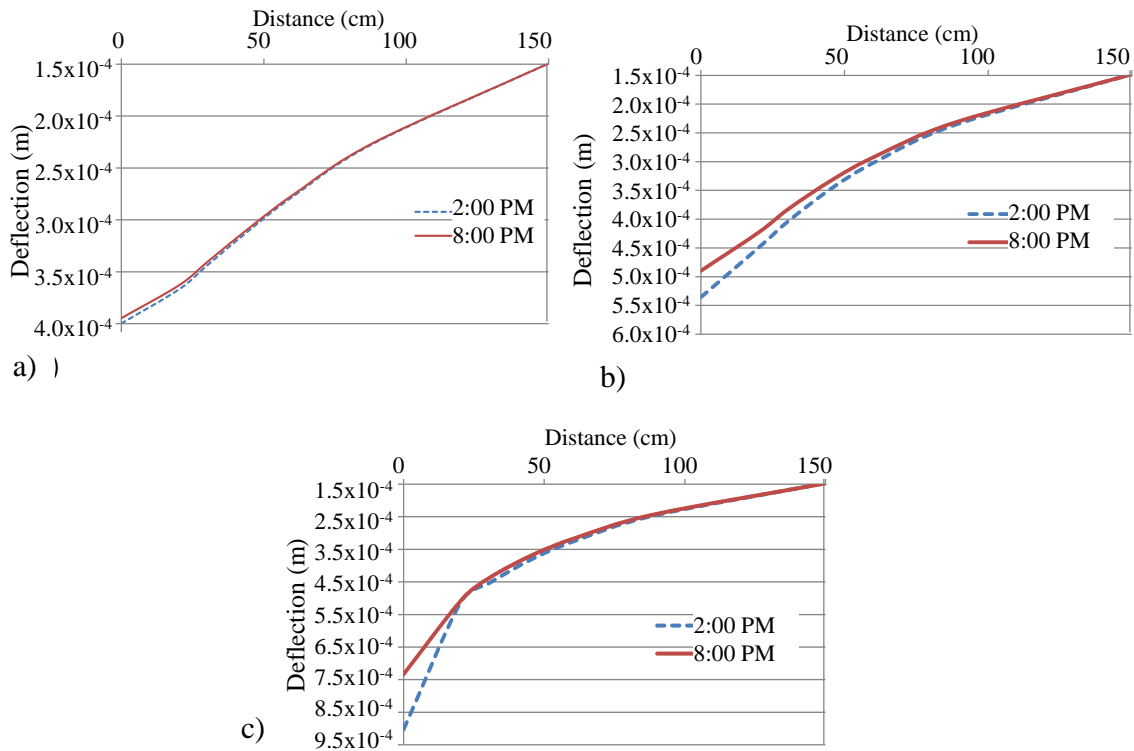
Figure 32 shows the inversed moduli profile of AC as compared to the true values. Results indicate that inverted moduli values could match true values with an average error of 4.45%. For the cold weather the inversed moduli were a little over-predicted while for the regular weather they were a little under-predicted at 8:00 PM. Figure 33 shows the simulated deflections on the surface of top AC layer. Results indicate that deflection at 2:00 PM was lower than that at 8:00 PM primarily at the zero or close distances, and this difference decreased with the increase of distance until two deflections merged together. This observation could be explained by temperature variations at different times, while at far distances deflections were primarily dependent on the moduli of underneath layers, which are considered temperature independent. The hot weather condition had the highest deflection values and deflection differences between 2:00 PM and 8:00 PM, then the regular weather, and cold weather due to their temperature values and variations along depths.



**Figure 31. Temperature profile of AC layer at 2:00 PM and 8:00 PM: a) cold weather; b) normal weather; c) hot weather.**



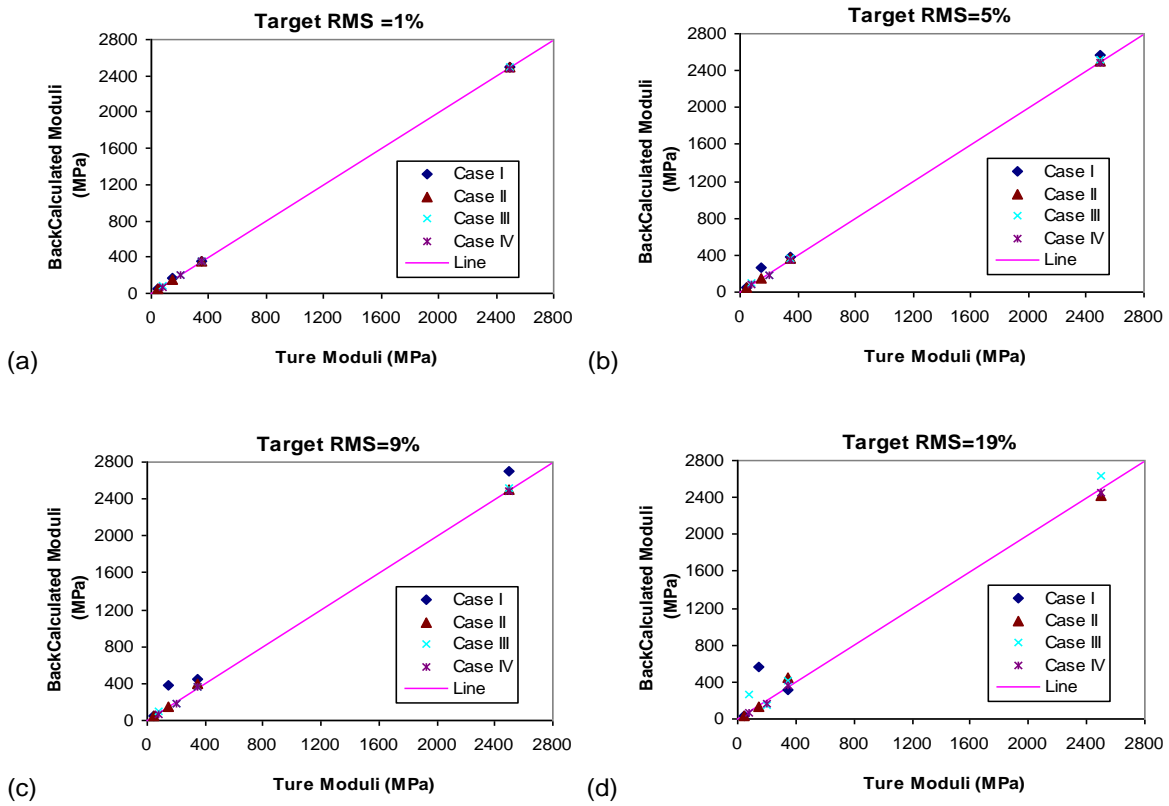
**Figure 32. Inversed AC moduli profile vs true values: a) cold weather; b) normal weather; c) hot weather.**



**Figure 33. Simulated deflections: a) cold weather; b) normal weather; c) hot weather.**

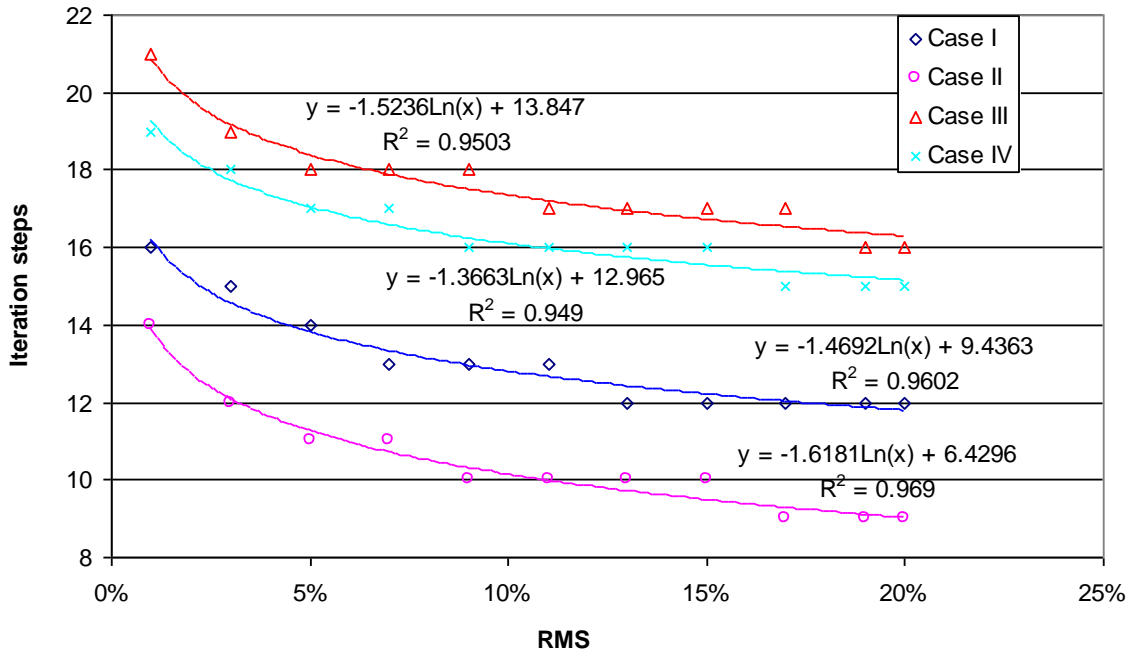
### 2.5.2.6 Effect of Root Mean Square

Figure 33 shows the modeled displacement basin as compared to the observations on the last iteration step (with an *RMS* of 3%), indicating a very close match and reasonable numerical accuracy. Different *RMS* targets were used for the numerical inversion, i.e., 1%, 5%, 9%, and 19%. Figure 34 shows the inversed moduli as compared to the true values using different *RMS* targets. Results indicate that a lower *RMS* target results in improved engineering accuracy and vice versa.



**Figure 34. Inversed moduli vs. true values with different RMS targets.**

Figure 35 shows the final iteration steps versus *RMS* targets. As expected the iteration steps generally decrease with the increase of *RMS* target value, but the effect of *RMS* target is less significant when its value gets relatively high (e.g., 7% or higher). Based on these results, an *RMS* target of 5% or a lower value would be recommended for engineering applications when using this numerical method.



**Figure 35. Final iteration steps vs. RMS.**

## 2.6 Summary

In this research a numerical method and procedure was developed to inverse compute the elastic moduli of the multilayer structure. A static elastic FE model with infinite-elements for the infinite half-spaces of boundaries was developed to model pavement response. Consequently, a Newton-Raphson iteration procedure is proposed to inverse compute the layer moduli, where the gradient tensor is calculated using finite difference method. The empirical area method was used to estimate the initial moduli seed values for the AC layer as a penalization or constraint. The entire numerical computation was coded in FORTRAN language for the numerical solution. Monte Carlo simulations from 5,000 randomly generated moduli values for each layer of a four-layer pavement structure were used as true values for validation purposes. Results indicate that the developed numerical approach has a relatively stable convergence. A 5% or lower value of *RMS* target is recommended for the engineering application when using this method. The moduli seed values seem to have very small effects on the numerical accuracy (modeled responses versus observations or measurements). However, the

moduli seed values play a critical role in the engineering accuracy (inverted moduli versus true values) for the inverted moduli of AC layer. With these 5,000 randomly generated moduli values for each layer, an engineering error of 1.77% for the inverted moduli of AC layer was achieved. The inverted moduli of unbound materials (base, subbase, and soil) were much less sensitive to the initial moduli seed values as compared to that of the AC layer. This has helped address the common issue in multilayer system backcalculation—no unique solution especially for AC material. Using the random moduli seed values, an engineering error of 10.83%, 8.99%, and 1.08% were observed for the inverted moduli of base, subbase, and soil, respectively. The computational method could also inverse compute the modulus variation of AC layers due to temperature profile with an average error of 4.45% attained for three examples.

The finite element model serves as part of the basic foundations for the proposed numerical solution method of the dynamic viscoelastic response modeling as discussed in the next chapter.

### **Chapter 3: A Time-domain Finite Element Method for Dynamic Viscoelastic Solution of Layered-half-space Responses under Loading Pulse**

Analytical solutions and numerical methods have more often been studied to compute multilayer structural responses using (dynamic) elastic models. This chapter develops a dynamic viscoelastic model and Galerkin-based time-domain finite element (FE) method to simulate the layered half-space responses under loading pulses. The model and numerical methods serve as one of the core computation modules of the inverse computation, as will be discussed in Chapter 4.

The time-temperature dependent material viscoelasticity is modeled by the generalized Maxwell model. A combined Houbolt, central finite difference (FD) and forward FD method was proposed in this research for time discretization of acceleration and velocity to reduce the time-step length. A computer code written in FORTRAN language was developed for the numerical computation and validated using analytical solution and numerical modeling. Compared to most existing computer methods, the developed approach presents a more comprehensive model: 1) it has captured the coupled effects of material viscoelastic behavior, dynamic loading, and system damping; 2) it is also able to model two environmentally-associated critical conditions: temperature profile and space-dependency of moduli. The model was implemented for a layered flexible pavement structure on soil foundation under vehicle and plate loadings, where the top asphalt layer is modeled as viscoelastic, and unbound materials are considered damped elastic. An experimental plate loading test was designed for evaluation. Results find that a dynamic-viscoelastic model that considers damping could more accurately emulate structural responses. Temperature variation of a single layer could significantly affect response values. Displacement, velocity and acceleration, and stress and strain were also analyzed to foster understanding of the structural dynamic response and material viscoelastic deformation. The developed method could serve as a potential means to enhance structural analysis, which can also be used for other laminate or disk structures

at different length and time scales, thereby fostering understanding of material deformation and structural responses.

### **3.1. Background**

The soil or earth is a semi-infinite half-space. When a layered structure is built on a soil foundation it becomes a layered half-space such as the pavement system used for highways, airport runways, and parking lots to sustain vehicle loading. As shown in Figure 36, a layered half-space of pavement structure on soil sample usually consists of three or four layers: asphalt concrete (AC) or Portland cement concrete as the surface course, base layer (e.g., aggregate and stabilized base), subbase layer (e.g., gravel material), and soil foundation (semi-infinite half-space). The layered structure with an AC surface course is called *a flexible pavement system*, which is implemented for model validation and analysis in this research. The vehicle tire contact area could be approximated as a circular for pavement analysis and design (Huang 2003, AASHTO 1993, and ARA 2004). The plate loading tests were used to evaluate the structural capacity. In this test a circular plate is placed on the surface of the soil or layered structure and a mass was dropped to hit the plate, which produced a loading pulse within a short time period (e.g., 0.1 second or less) (see Figure 36). Among these plate loading tests, the falling weight deflectometer (FWD) test is a popular one emulating the vehicle loading effect, where several geophones are also placed at various distances to record the deflection responses (see Figure 36).

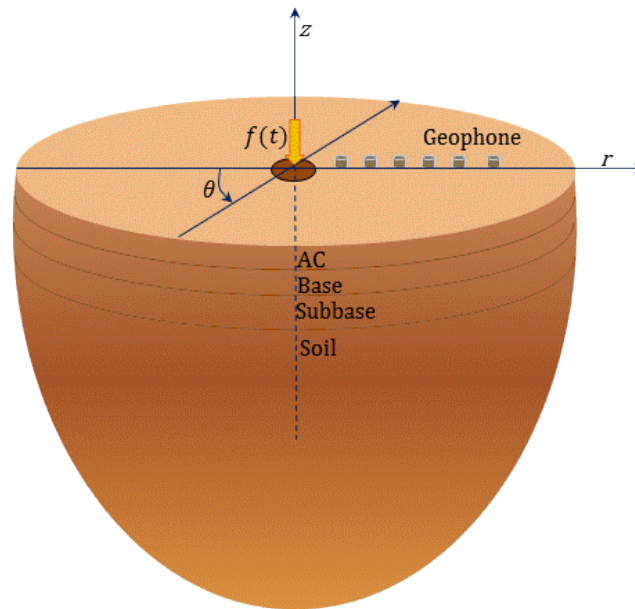


**Figure 36. A layered half-space of flexible pavement structure on soil under circular loading.**

Understanding structural response of the layered half-space under external loading is a key for risk assessment (e.g., deformations under seismic loading) and structural design. Multiple models and computer methods have been developed or employed to simulate responses of deflection, stress, and strain for the (layered) half-space. These models and research progress are reviewed and summarized as follows:

i) **Analytical approaches for half-space and layered half-space.** Boussinesq's solution (Boussinesq 1885) has been used to calculate responses of an elastic half-space (e.g., soil) under a static point loading. Lamb (Lamb 1905) might be the first researcher to develop a formulation for the surface motion of homogeneous elastic half-space under a point pulse. Extensive research has attempted to solve Lamb's problem, including the most recent publication by Kausel (2012), who derived a complete set of exact explicit formulas for the suddenly applied point loads. Miller and Pursey (1954) derived a solution for the harmonic uniform circular load applied to the elastic half-space. The elastic solution of a layered half-space could also be extended to a viscoelastic hysteretic medium using the complex moduli as inputs by Foinquinos (1995). Foinquinos and

Roësset (2000) further provided solutions for vertical loading applied to the elastic layered half-space (e.g., pavement structure).

Among analytical approaches, the most widely used methodology is the multilayer analysis program. The method is based on linear elasticity theory for an axisymmetric multilayer structure with semi-infinite half-space using Hankel transforms. Samples of well-known multilayer analysis programs include ELSYM 5, which was originally developed by the University of California at Berkeley and later adapted to microcomputers by Kopperman et al. (1986); BISAR developed by Shell Global Inc. (1998); and Everstress developed by the University of Washington (2001). However, these multilayer analysis programs can account only for the static loading and linear elastic material property. Researchers have endeavored to extend this solution for applying to more complex conditions. For example, Pan and Han (2005) derived the functionally graded elastic multilayered half-space under static loading mode. Consequently Pan's group created the MultiSmart3D program, which can divide a single layer into multi sub-layers and assign various elastic modulus values at depth. Levenberg (2013) analyzed the pavement responses to subsurface deformations based on layered elastic theory with a distorted bottom boundary condition. The AC is a typical viscoelastic or viscoplastic material. AC is highly temperature- and time- dependent (Xu and Solaimanian 2008, 2009), and thus, the linear elasticity theory may not be accurate enough to capture its material behavior under dynamic loading. Consequently, some researchers have extended the multilayer analytical methods by accounting for the material's viscoelastic behavior or dynamic loading effects or both. Hopman (1996) and Kim (2011) developed the viscoelastic solutions of the multilayer structure under a static loading mode. Most recently Lee (2013) developed a dynamic viscoelastic analysis program called ViscoWave based on the Laplace and Hankel transforms, as extended from the layered linear elastic approach. However, the damping effect was not taken into account (Lee 2013). Figure 37 briefly illustrates these developments of analytical approaches for solutions of the half-space and layered half-space.

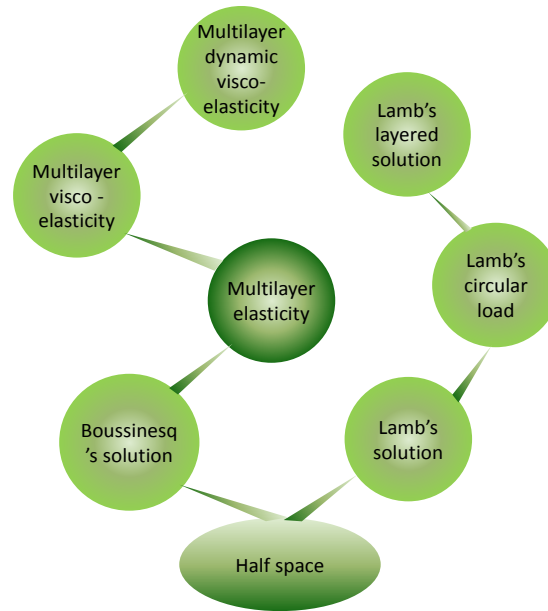


**Figure 37. Analytical solutions of (layered) half space.**

ii) **Numerical methods.** Different numerical algorithms have been used for response modeling of the layered half-space structure including the finite element (FE) method, spectral element method (Al-Khoury et al. 2001), and boundary element method (Birgisson et al. 1997). In comparison to the multilayer analysis programs, the FE modeling could account for more complex conditions including the variable boundary and loading conditions, and advanced material models. Dave et al. (2011) developed a functionally graded FE model to account for the non-homogeneous viscoelastic material property under a static loading pattern. Researchers have also developed FE computer programs for pavement response analysis, and samples include MICHPAVE developed by Michigan State University (Harichandran and Baladi 2000), ILLI-PAVE developed by the University of Illinois at Urbana Champaign in 2001 (Ramirez 2001), and TTI-PAVE developed by the Texas Transportation Institute (2009). These FE programs are primarily used to simulate the static loading and linear elastic material properties, but some of them have accounted for the stress-dependency of soil's resilient modulus (e.g., ILLI-PAVE, MICHPAVE). TTI-PAVE incorporated the Mohr-Coulomb yield criterion to account for material plastic failure under super heavy loading. Scarpas et al. (1997) developed the CAPA-3D FE software for modeling infrastructure materials, which could also perform

pavement analysis. It has accounted for some nonlinear material behaviors as well as coupling effects of heat transfer, oxygen diffusion, and moisture interaction. For example, Mo et al. (2008) used the CAPA-3D FE software to simulate the tire-pavement contact stresses using the viscoelastic material model with a static loading mode.

Using the commercial FE software packages, extensive existing research has modeled the linear, nonlinear, static, and dynamic behaviors of the flexible pavement structure. Some examples include the followings: Blab and Harvey (2002) simulated the pavement response using the static viscoelastic model; Uddin and Garza (2004) simulated the dynamic response of a flexible pavement under FWD loading using the LS-DYNA software; Kim (2007) simulated the flexible pavement responses considering the stress-dependent behavior of soil foundation through ABAQUS; Yoo (2007) built a three-dimensional (3-D) FE model for the dynamic and viscoelastic analysis of flexible pavement, where two tire-pavement configurations were considered; Al-Qadi et al. (2009) modeled the creep behavior of AC material under a static loading history using the FE method with ABAQUS; Howard and Warren (2009) simulated the stationary transient loading and nonlinear stress dependency of subgrade and crushed stone; Wang and Al-Qadi (2009) simulated dynamic responses of pavement structure considering the 3-D tire-pavement contact stress distributions as implemented in ABAQUS; Cao et al. (2013) simulated the elastic dynamic response of a pavement structure, considering the vehicle-pavement coupling effect in ABAQUS.

iii) **Combined and other methods.** Chatti and Yun (1996) developed a damped elastic model based on the combined analytical and FE algorithm. Ayadi et al. (2012) developed a dynamic semi-analytical and FE model to simulate pavement deflections under the FWD loading. Kausel and Park (2006) derived dynamic elastic responses of the layered half-space in time domain based on the thin layer method. Sun et al. (2013) proposed a high-order thin layer method for modeling viscoelastic wave propagation in the stratified media. Most recently in 2013, the University of Nevada at Reno developed the 3-D Move Analysis Software (2013) based on the finite layer method using Fourier transforms for each layer whereby 3-D vehicle contact stress distributions were generated

from moving loading (Siddharthan et al. 1998, 2000, and 2002). The material model input for the AC layer is the mathematical sigmoidal function of dynamic modulus, but phase angle is a user input option to determine a damping ratio for dynamic analysis. Chaillat and Bonnet (2013) proposed a multiple formulation for the solution of elastic dynamic half-space of soil using Green's tensor.

Analytical and numerical methods for modeling viscoelastic and/or dynamic behaviors have also been developed for other uniform solids or composite media. Some examples are reviewed as follows. Shaw et al. (1994) solved a quasi-static stress problem for a linear viscoelastic solid using the FE method for space-domain discretization and semi-discrete estimations. Makris (1995) examined a convolution integral analytical solution for time domain analysis of the viscoelastic model of a soil body. Guénette and Fortin (1995) proposed a mixed FE method to compute the viscoelastic flow of benchmark problems. Shaw and Whiteman (2000) proposed a space-time Galerkin FE discretization method for solving the linear quasistatic compressible viscoelasticity problem based on the elliptic partial differential equation. Kim and Paulino (2002) proposed a framework for a generalized isoparametric formulation using the graded FE method, which can possess spatially varying material properties. Qin et al. (2010) developed an algorithm to simulate the static viscoelastic response of a single body under the moving loading pattern. Timonin (2013) proposed a finite-layer method for the linear elastic stress-strain analysis of layered composites, where each particular layer is considered a constituent of the entire laminate structure; the nonlinear geometry was also considered.

### **3.2. Research Motivation and Significance**

First, most existing computer methods and programs of layered half-space, such as those mentioned above, have primarily considered limited aspects—either the dynamic effect, the elastic or viscoelastic behavior of material, or both, but without considering the damping effect, e.g., the analytical solution developed by Lee (2013). Therefore, a more comprehensive model and computer method considering the dynamic loading effect,

material's viscoelastic behavior, and the system damping effect may more accurately capture the coupled effects of loading and material behavior. As discussed earlier, different modeling approaches including static or dynamic, and elastic or viscoelastic models were used to simulate the multilayer's structural responses. Many of these approaches have been validated via laboratory and in-situ tests, according to existing research. Qin (2010) used the multilayer linear elastic analysis program to simulate FWD peak deflections and validated the simulation results through field measured responses. Al-Qadi (2009) simulated the static viscoelastic responses of a flexible pavement under vehicle loading, and validated it using in-situ measurements at the loading position. Cao et al. (2013) performed an elastic dynamic finite element modeling and validated it through experimental data. However, the laboratory and field validations could produce biased results since the laboratory testing conditions on small specimens could be very different from those in field conditions. For example, the indirect tensile test on a 10-cm-diameter specimen is used to determine the resilient modulus (ASTM D7369 -11), which may not exactly represent the in-situ stress-strain state of a solid confined in a large pavement structure under vehicle loading. Meanwhile, validations of linear elastic modeling are based only on the peak response values without considering time history (Qin 2010), arguing that the time history effect could be ignored within such a short loading period. In addition, field validations with stress-strain gauge instruments are usually applied to a single location often at the loading position, which doesn't account for the geometry effect at multiple distances to loading. Therefore, considering this single location vs. multiple locations for loading dilemma, the question arises: which modeling approach is indeed more accurate for simulating structural responses under a short-time periodic loading?

Secondly, the in-service situations of the layered half-space are indeed more complex than theoretical assumptions often used in existing modeling studies, such as uniform temperature and moisture distributions along the layer depth. Temperatures of AC material and moisture contents of soil foundation are well known as two critical factors affecting material properties and associated structural responses. A higher

temperature induces more stress relaxation or higher creep deformation (Xu 2007). Variable moisture contents cause variable material properties at different depths of the soil foundation (Nazarian et al. 1987, Aouad 1993). Analytical approaches, including multilayer analysis programs, have difficulty capturing these variable conditions. The powerful FE software such as ANSYS does not provide a user input for space dependency of elastic moduli (e.g., users may need to build a large number of model bodies in order to assign variable modulus values as space dependent and then “glue” all of them). Therefore, a numerical method such as an FE solution considering space dependency would be a promising option for simulating these environmentally associated effects on structural responses.

Lastly, an enhanced model is essential for improving structural analysis and design methods. For example, the current national *Mechanistic-Empirical Pavement Design Guide* (MEPDG) funded by the National Cooperative Highway Research Program (NCHRP) and carried out by the Applied Research Associates (ARA) along with several consultants used the dynamic modulus as a material parameter input of AC for Level 1 (the highest) structural design, which was verified in the final report (Glover and Mallela 2009). It accounts for the frequency and temperature effects on material’s viscoelastic behavior. However, in the response analysis, a modulus value corresponding to the frequency was attained and then used as a material parameter input for the static-elastic multilayer analysis program (Glover and Mallela 2009). Therefore, this approximation method is still based on a static elastic analysis in nature, and it may under- or over- estimate response values.

The enhanced model and computer method could also be used for other laminate or disk structures at different length and time scales for response analysis considering the elastic or viscoelastic, static or dynamic properties.

Accordingly, the objective of this chapter is to develop a time-domain FE model and computer method for dynamic viscoelastic solution of layered-half-space responses under the loading pulses. The damping effect temperature profile, and space dependency of moduli were also taken into account. A computer program written in FORTRAN was

developed for the numerical computation. The computer code and FE simulation results were validated by analytical solution for the linear elastic model and by numerical modeling for the dynamic and viscoelastic models. The model is implemented to a flexible pavement structure on soil foundation under both FWD and vehicle loadings. Structural responses of deflections, velocity and acceleration, and stress and strain were analyzed to foster understanding of structural dynamic responses and material viscoelastic deformation. The model developed in this research can serve as a potential means to advance current pavement analysis methods. The developed model and computer method could also be used for other laminate and disk structures at different length and time scales. The developed model presented in this chapter will serve as one module of the inverse method developed in the next chapter.

### **3.3. Model Development**

#### **3.3.1 Model domain and governing state equation**

The half-space and layered half-space under circular loading can be treated as a semi-infinite axisymmetric body (see Figure 38) because: 1) the structure is continuous with isotropic material property assumed; 2) the soil foundation (earth) has infinite depth; and 3) the dimension size of the loading area (e.g., a 15-cm radius of the FWD loading plate) is much smaller compared to the model size (e.g., a parking lot of 2,000 m<sup>2</sup>). It has been a common practice to regard the layered half-space under vehicle and FWD loading as an axisymmetric model for analysis and design (Huang 2003, AASHTO 1993, ARA 2004). The multilayer elastic analysis programs discussed earlier are also based on this assumption (Kopperman et al. 1986, Shell 1989, Sivaneswaran et al. 2001).

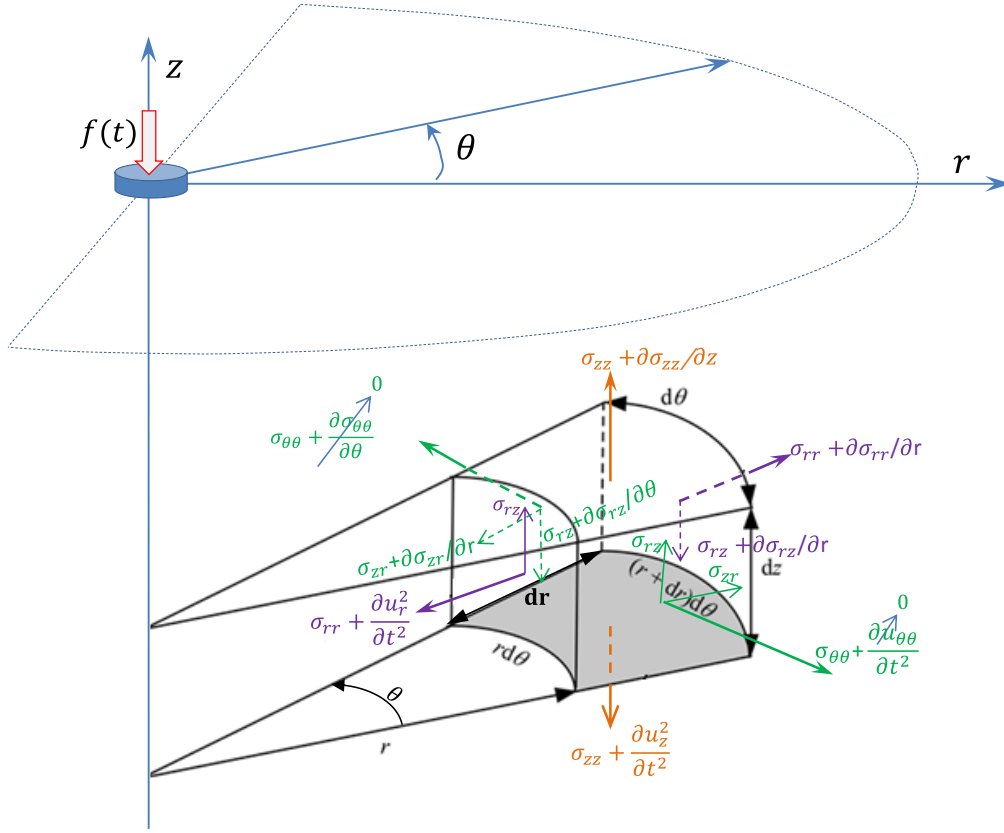


**Figure 38. Dynamic stress state of the axisymmetric model in the  $r - z - \theta$  coordinate.**

Figure 39 presents the FE model domain and boundary conditions for a layered structure under a dynamic loading pulse. A finite but relatively large model size is used to simulate the semi-infinite half-space. The layer interfaces are considered fully bonded, as commonly found in flexible pavement structures (Huang 2003).

The strong form of the governing state equation is formed as follows:

$$\nabla \cdot \boldsymbol{\sigma} + b = c \frac{\partial \mathbf{u}(t)}{\partial t} + \rho \frac{\partial^2 \mathbf{u}(t)}{\partial t^2} \text{ on } \Omega \times \text{on } t_d] \quad (3-1)\text{-a}$$

$$\boldsymbol{\sigma} \cdot \mathbf{n} ds = f(t) \text{ on } \partial\Omega_4 \times [0, t_d] \quad (3-1)\text{-b}$$

$$u_r = 0 \text{ on } \partial^2\Omega_1 \times [0, t_d] \quad (3-1)\text{-c}$$

$$u_r = 0 \text{ on } \partial\Omega_2 \times [0, t_d] \quad (3-1)\text{-d}$$

$$u_z = 0 \text{ on } \partial\Omega_3 \times [0, t_d] \quad (3-1)\text{-e}$$

where equation (a) is the stress equilibrium considering dynamic inertia and damping in a continuum form,  $\sigma$  is stress tensor,  $u$  is displacement,  $b$  is body force,  $\rho$  is material density,  $c$  is damping, and  $t$  is time variable,  $\Omega \in \mathbb{R}^3$  is a 3-D space domain,  $[0, t_d]$  is a time domain with a period of  $t_d$ ; equation (b) is the natural boundary condition,  $f(t)$  is dynamic loading time history at the vertical direction,  $n$  is the normal direction unit to the surface  $s$ , and  $\Omega_4$  is the loading area; equation (c) is the essential boundary condition applied to the axisymmetric line  $\partial^2\Omega_1$ ; equation (d) is the essential boundary condition applied on the far field, the outside area  $\partial\Omega_2$ ; and equation (e) is the essential boundary condition at the bottom area of soil foundation  $\partial\Omega_3$ .

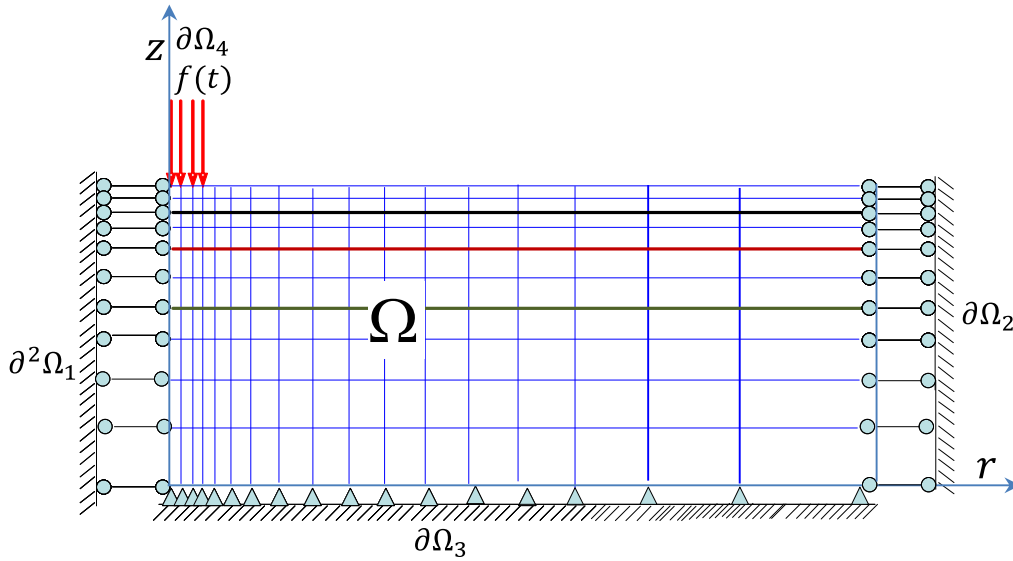


**Figure 39. Finite element model and boundary conditions on the  $r - z$  plane ( $\Omega$  are  $\mathbb{R}^3$  space domains of the layered-half-space).**

According to the axisymmetry of a cylindrical coordinate system  $r - z - \theta$  (see Figure 38), the shear stresses and displacements at the angular direction are dismissed, and normal stress at the angular direction is independent of angle  $\theta$  such that  $\frac{\partial \sigma_{\theta\theta}}{\partial \theta} = 0$ . Thus, the stress-equilibrium can be decomposed to the  $r$  and  $z$  directions in a reduced form as follows (Slaughter 2002):

$$\frac{\partial \sigma_{rr}}{\partial r} + \frac{\partial \sigma_{rz}}{\partial z} + \frac{1}{r}(\sigma_{rr} - \sigma_{\theta\theta}) + b_r = c \frac{\partial u_r}{\partial t} + \rho \frac{\partial u_r^2}{\partial t^2} \quad (3-2) \text{-a}$$

$$\frac{\partial \sigma_{rz}}{\partial r} + \frac{\partial \sigma_{zz}}{\partial z} + \frac{1}{r} \sigma_{rz} + b_z = c \frac{\partial u_z}{\partial t} + \rho \frac{\partial u_z^2}{\partial t^2} \quad (3-2)-b$$

where  $r, z, \theta$  are radius, depth, and angle, respectively;  $\sigma_{rr}, \sigma_{zz}$ , and  $\sigma_{\theta\theta}$  are normal stress at the  $r, z$ , and  $\theta$  direction, respectively;  $\sigma_{rz}$  and  $\sigma_{zr}$  are shear stresses on the  $z - r$  plane,  $\sigma_{rz} = \sigma_{zr}$ ;  $b_r$  and  $b_z$  are body forces at the  $r$  and  $z$  direction,  $b_r = 0$ ; and  $u_r$  and  $u_z$  are displacements at  $r$  and  $z$  direction, respectively.

### 3.3.2 Material model

No material damages occur as assumed for modeling the responses of the layered half-space under a relatively small loading within a short period. If material damages such as permanent deformation and cracking occur, the viscoplastic or fracture models will be needed which is not studied in this dissertation. The material viscoelasticity was modeled by the generalized Maxwell model. The base/subbase and soil layer were considered elastic, and the space dependency of the elastic moduli were accounted for (see Figure 40). Damping was also considered for elastic materials. Figure 40 shows the material model of a pavement structure in a one-dimensional (1-D) mode.

The relaxation modulus  $E(t)$  in the Prony series for the generalized Maxwell model can be expressed as a function of reduced time  $t$  as follows:

$$E(t) = E_\infty + \sum_{i=1}^N E_i e^{-\frac{E_i}{\eta_i} t} = E_\infty + \sum_{i=1}^N E_i e^{-\frac{t}{\tau_i}} \quad (3-3)$$

where  $E_\infty$  is Young's modulus at infinite time ( $t = \infty$ );  $E_i$  is Young's modulus of the  $i^{th}$  spring element for  $i = 1, 2 \dots N$ ;  $\eta_i$  is viscosity of the  $i^{th}$  dashpot element for  $i = 1, 2 \dots N$ ;  $N$  is the spring-dashpot parallel term number in series, and  $\tau_i$  is the retarded time,  $\tau_i = \frac{\eta_i}{E_i}$ .

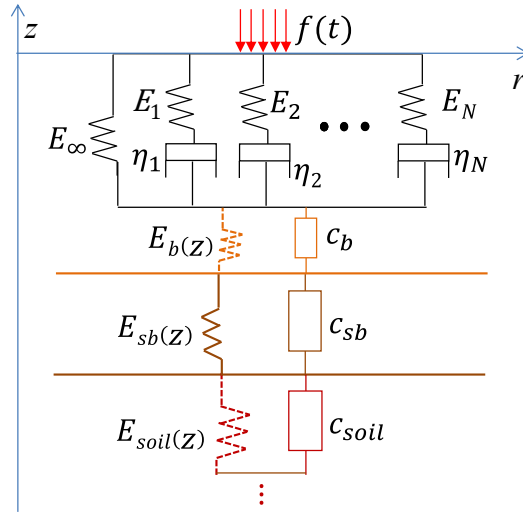


**Figure 40. Material models of the multilayer structure in a 1-D mode ( $E$  is elastic modulus,  $\eta$  is viscosity, and  $c$  is damping).**

The temperature effect of viscoelastic material could be converted to a reduced time using the temperature-time superposition rule (Christensen 1982). Pellinen (2001) developed a technique to shift temperature effect to the reduced time, where the shift factor  $\alpha_T$  can be fitted to a two times polynomial function of temperature. More generally  $\alpha_T$  could be determined according to the WLF temperature-time superposition rule (Williams et al. 1955):

$$\log_{10}(\alpha_T) = \frac{-\gamma_1(T-T_0)}{\gamma_2+T-T_0} \quad (3-4)$$

where  $\gamma_1, \gamma_2$  are model parameters;  $T$  is temperature, and  $T_0$  is the reference temperature, e.g., 25 °C.

In this research Equation (3-3) was modified as follows to consider temperature effect:

$$E(t, T, T_0) = E_\infty + \sum_{i=1}^N E_i e^{-\frac{E_i}{\eta_i} \alpha_T t} \quad (3-5)$$

Likewise, the shear and bulk relaxation moduli in the Prony series can be expressed as follows:

$$G(t) = G_\infty + \sum_{i=1}^N G_i e^{-\frac{G_i}{\eta_{gi}} \alpha_T t} \quad (3-6)-a$$

$$K(t) = K_{\infty} + \sum_{i=1}^N K_i e^{-\frac{K_i}{\eta_{ki}} \alpha_T t} \quad (3-6)-b$$

where  $G_{\infty}$  is shear modulus at infinite time ( $t=\infty$ );  $G_i$  is shear modulus of the  $i^{th}$  spring element for  $i = 1, 2 \dots N$ ;  $\eta_{Gi}$  is shear viscosity of the  $i^{th}$  dashpot element for  $i = 1, 2 \dots N$ ;  $K_{\infty}$  is bulk modulus at infinite time ( $t=\infty$ );  $K_i$  is bulk modulus of the  $i^{th}$  spring element for  $i = 1, 2 \dots N$ ;  $\eta_{Ki}$  is bulk viscosity of the  $i^{th}$  dashpot element for  $i = 1, 2 \dots N$ .

Multiple damping models exist as discussed in section 1.1.2 with details. Among these models, the Rayleigh damping model is still the most popular one to date for simulating structural dynamic response. One of the advantages of this model is that the damping matrix can be directly estimated as a function of material mass and stiffness without performing sophisticated material testing (Chopra 2001, Cook et al. 2002):

$$\mathbf{C} = \alpha \mathbf{M} + \beta \mathbf{K} \quad (3-7)$$

where  $\mathbf{C}$  is the damping matrix;  $\alpha, \beta$  are Rayleigh coefficients;  $\mathbf{M}$  is mass matrix, and  $\mathbf{K}$  is the stiffness matrix.

The Rayleigh coefficient  $\alpha$  and  $\beta$  can be determined as follows (Chopra 2001, Cook et al. 2002):

$$\alpha = \frac{2\xi \omega_1 \omega_2}{\omega_1 + \omega_2} \quad (3-8)-a$$

$$\beta = \frac{2\xi}{\omega_1 + \omega_2} \quad (3-8)-b$$

where  $\omega_1$  and  $\omega_2$  are frequency interests of the range;  $\xi$  is damping ratio.

One main issue of this model is its strong dependence on the frequency (Puthanpurayil et al. 2011). However, the Rayleigh damping model has been often used to represent damping at small strain levels, whereas material models are primarily considered linear (Park and Hashash 2004). Without material characterization, the Rayleigh damping model was therefore adopted for modeling the base/subbase and soils in this research.

### 3.3.3 Stress-strain constitutive relations

For the three-dimensional (3-D) model domain, the stress tensor  $\boldsymbol{\sigma}$  is a sum of two terms — deviatoric stress and hydrostatic stress — as follows (Sadd 2005):

$$\boldsymbol{\sigma} = \mathbf{S} + \frac{1}{3}\text{tr}(\boldsymbol{\sigma})\mathbf{I} = \mathbf{S} + \sigma_h\mathbf{I} \quad (3-9)$$

where  $\mathbf{S}$  is the deviatoric stress tensor;  $\text{tr}(\cdot)$  is the trace;  $\sigma_h$  is the hydrostatic stress scalar; and  $\mathbf{I}$  is an identity matrix.

Likewise the strain tensor  $\boldsymbol{\varepsilon}$  in the 3-D space domain is a sum of deviatoric strain and hydrostatic strain as follows (Sadd 2005):

$$\boldsymbol{\varepsilon} = \mathbf{e} + \frac{1}{3}\text{tr}(\boldsymbol{\varepsilon})\mathbf{I} = \mathbf{e} + \varepsilon_h\mathbf{I} = \frac{1}{2}[\nabla\mathbf{u} + \nabla\mathbf{u}^T] + \frac{1}{3}\nabla \cdot \mathbf{u} \quad (3-10)$$

where  $\boldsymbol{\varepsilon}$  is the total strain tensor ( $\boldsymbol{\varepsilon} = \frac{1}{2}[\nabla\mathbf{u} + \nabla\mathbf{u}^T]$ ),  $\mathbf{e}$  is the deviatoric strain tensor; and  $\varepsilon_h$  is the hydrostatic strain scalar ( $\varepsilon_h = \frac{1}{3}\nabla \cdot \mathbf{u}$ ).

The deviatoric strain tensor can be attained by subtracting the hydrostatic strain term from the total strain tensor as follows:

$$\mathbf{e} = \frac{1}{2}[\nabla\mathbf{u} + \nabla\mathbf{u}^T] - \frac{1}{3}\nabla \cdot \mathbf{u} \quad (3-11)$$

For the linear elastic materials, the stress-strain constitutive relationship in a 3-D space domain is expressed as follows (Sadd 2005):

$$\boldsymbol{\sigma} = 2\mu\boldsymbol{\varepsilon} + \lambda\text{tr}(\boldsymbol{\varepsilon})\mathbf{I} \quad (3-12)$$

where  $\mu$  is the 1st Lamé's parameter,  $\mu = G$ ;  $G$  is shear modulus;  $\lambda$  is the 2nd Lamé's parameter,  $\lambda = K - \frac{2}{3}G$ , and  $K$  is bulk modulus.

Substituting Equations (3-10) and (3-11) into Equation (3-12), the following stress-displacement relationship for the 3-D space domain of the elastic unbound materials are attained as follows:

$$\boldsymbol{\sigma} = 2G\left(\frac{1}{2}[\nabla\mathbf{u} + \nabla\mathbf{u}^T] - \frac{1}{3}\nabla \cdot \mathbf{u}\right) + 3K\left(\frac{1}{3}\nabla \cdot \mathbf{u}\right) \quad (3-13)$$

In Equation (3-13) replace  $G$  with  $G(t - \tau)$  and  $k$  with  $K(t - \tau)$  and then integrate with the time domain of  $[0, t_d]$  to arrive at the the stress-displacement constitutive relationship for the viscoelastic material in a 3-D space domain as follows:

$$\boldsymbol{\sigma}(t) = 2 \int_0^t G(t - \tau) \frac{\partial \left( \frac{1}{2} [\nabla \mathbf{u}(\tau) + \nabla \mathbf{u}(\tau)^T] - \frac{1}{3} \nabla \cdot \mathbf{u}(\tau) \right)}{\partial \tau} d\tau + 3 \mathbf{I} \int_0^t K(t - \tau) \frac{\partial \left( \frac{1}{3} \nabla \cdot \mathbf{u}(\tau) \right)}{\partial \tau} d\tau \quad (3-14)$$

where the time-dependent stress tensor  $\boldsymbol{\sigma}(t)$  is decomposed to two components, deviatoric stress tensor  $\mathbf{S}(t)$  and hydrostatic stress scalar  $\sigma_h(t)$ , and will be used for the numerical solution later:

$$\mathbf{S}(t) = 2 \int_0^t G(t - \tau) \frac{\partial \left( \frac{1}{2} [\nabla \mathbf{u}(\tau) + \nabla \mathbf{u}(\tau)^T] - \frac{1}{3} \nabla \cdot \mathbf{u}(\tau) \right)}{\partial \tau} d\tau \quad (3-15)$$

$$\sigma_h(t) = 3 \int_0^t K(t - \tau) \frac{\partial \left( \frac{1}{3} \nabla \cdot \mathbf{u}(\tau) \right)}{\partial \tau} d\tau \quad (3-16)$$

### 3.3.4 Weak form of state equation

Based on the Galerkin method (Ern and Guermond 2004), applying a test function  $\mathbf{p}(t)$  on both sides of the strong form (Equation (3-1)-a), and then integrating with the space and time domains will result in a weak form as follows:

$$\int_0^{t_d} \int_{\Omega} (\nabla \cdot \boldsymbol{\sigma}) \cdot \mathbf{p}(t) d\Omega dt + \int_0^{t_d} \int_{\Omega} \mathbf{b} \cdot \mathbf{p}(t) d\Omega dt - \int_0^{t_d} \int_{\Omega} c \frac{\partial \mathbf{u}(t)}{\partial t} \cdot \mathbf{p}(t) d\Omega dt - \int_0^{t_d} \int_{\Omega} \rho \frac{\partial^2 \mathbf{u}(t)}{\partial t^2} \cdot \mathbf{p}(t) d\Omega dt = 0 \quad \in \Omega \times [0, t_d] \quad (3-17)$$

According to Green's function  $(\nabla \cdot \boldsymbol{\sigma}) \cdot \mathbf{p}(t) d\Omega = (\boldsymbol{\sigma} \cdot \mathbf{n} ds) \cdot \mathbf{p}(t) - \boldsymbol{\sigma} : \nabla \mathbf{p}(t)$  and the natural boundary condition  $(\boldsymbol{\sigma} \cdot \mathbf{n} ds = f(t))$ , the weak form can be re-expressed as follows:

$$\int_0^{t_d} \int_{\Omega} \boldsymbol{\sigma} : \nabla \mathbf{p}(t) d\Omega dt - \int_0^{t_d} \int_{\Omega} \mathbf{b} \cdot \mathbf{p}(t) d\Omega dt + \int_0^{t_d} \int_{\Omega} c \frac{\partial \mathbf{u}(t)}{\partial t} \cdot \mathbf{p}(t) d\Omega dt + \int_0^{t_d} \int_{\Omega} \rho \frac{\partial^2 \mathbf{u}(t)}{\partial t^2} \cdot \mathbf{p}(t) d\Omega dt - \int_0^{t_d} \int_{\partial \Omega_4} f(t) \cdot \mathbf{p}(t) ds dt = 0 \quad \in \Omega \times [0, t_d] \quad (3-18)$$

Substituting Equation (3-14) into Equation (3-17) the final weak form can be shown as:

$$\int_0^{t_d} \int_{\Omega} \left[ 2 \int_0^t G(t-\tau) \frac{\partial \left( \frac{1}{2} [\nabla \mathbf{u}(t) + \nabla \mathbf{u}(\tau)^T] - \frac{1}{3} \nabla \cdot \mathbf{u}(t) \right)}{\partial \tau} d\tau + 3 \mathbf{I} \int_0^t K(t-\tau) \frac{\partial \left( \frac{1}{3} \nabla \cdot \mathbf{u}(t) \right)}{\partial \tau} d\tau \right] : \nabla \mathbf{p}(t) d\Omega dt + \left[ \int_0^{t_d} \int_{\Omega} c \frac{\partial \mathbf{u}(t)}{\partial t} \cdot \mathbf{p}(t) d\Omega dt + \int_0^{t_d} \int_{\Omega} \rho \frac{\partial^2 \mathbf{u}(t)}{\partial t^2} \cdot \mathbf{p}(t) d\Omega dt \right] = \left[ \int_0^{t_d} \int_{\partial \Omega_4} f(t) \cdot \mathbf{p}(t) ds dt + \int_0^{t_d} \int_{\Omega} b \cdot \mathbf{p}(t) d\Omega dt \right] \in \Omega \times [0, t_d] \quad (3-19)$$

### 3.4. Numerical Solution Method

#### 3.4.1 Finite element and shape function

The eight-node isoparametric “ring” element was used for the axisymmetric FE model domain as shown in Figure 41. The ring element is a two-dimensional quadratic element physically, but it integrates for a 3-D space domain of the volume, and the hoop stress and hoop strain in the  $\theta$  direction are also computed (see Figure 38). Four Gauss points within one element were set at the local coordinates of:  $(\xi, \psi) = \left( \frac{1}{\sqrt{3}}, \frac{1}{\sqrt{3}} \right), \left( -\frac{1}{\sqrt{3}}, \frac{1}{\sqrt{3}} \right), \left( \frac{1}{\sqrt{3}}, -\frac{1}{\sqrt{3}} \right), \left( -\frac{1}{\sqrt{3}}, -\frac{1}{\sqrt{3}} \right)$  as seen in Figure Figure 41a.

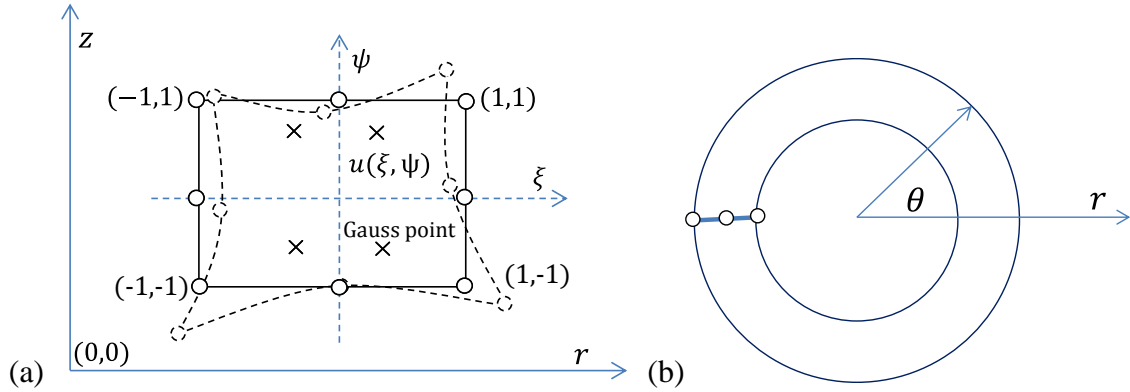


**Figure 41. Eight-node isoparametric ring element: (a) on the global  $r - z$  plane and local  $\psi - \xi$  plane with undeformed and deformed shapes; (b) on the global  $r - \theta$  plane.**

Displacement and test function are formulated as a function of those values at eight FE nodes for a single element via the shape function  $\Phi$  as:

$$\mathbf{u} = \Phi \mathbf{u} \quad (3-20)\text{-a}$$

$$\mathbf{p} = \Phi \mathbf{p} \quad (3-20)\text{-b}$$

where  $u, p$  are displacement and test function vectors (dimension of 16, for eight FE nodes of an element and two directions for each node),  $u^e = [u_1^r, u_1^z, u_2^r, u_2^z \dots \dots u_8^r, u_8^z]^T$ , and  $p^e = [p_1^r, p_1^z, p_2^r, p_2^z \dots \dots p_8^r, p_8^z]^T$ ; while  $\Phi$  is a 2-by-16 matrix of shape function.

The two-times polynomial function is used, which can achieve fairly high accuracy for an eight-node quadratic element (Cooke et al. 2001). The shape function matrix for an element is expressed as:

$$\Phi = \begin{bmatrix} \phi_1 & 0 & \phi_2 & 0 & \phi_3 & 0 & \phi_4 & 0 & \phi_5 & 0 & \phi_6 & 0 & \phi_7 & 0 & \phi_8 & 0 \\ 0 & \phi_1 & 0 & \phi_2 & 0 & \phi_3 & 0 & \phi_4 & 0 & \phi_5 & 0 & \phi_6 & 0 & \phi_7 & 0 & \phi_8 \end{bmatrix}^T \quad (3-21)$$

where

$$\begin{aligned} \phi_1 &= -\frac{1}{4}(1-\xi)(1-\psi)(1+\xi+\psi) \\ \phi_2 &= -\frac{1}{4}(1+\xi)(1-\psi)(1-\xi+\psi) \\ \phi_3 &= -\frac{1}{4}(1+\xi)(1+\psi)(1-\xi-\psi) \\ \phi_4 &= -\frac{1}{4}(1-\xi)(1+\psi)(1+\xi-\psi) \\ \phi_5 &= \frac{1}{2}(1-\xi)(1-\psi)(1+\xi) \\ \phi_6 &= \frac{1}{2}(1+\xi)(1-\psi)(1-\psi) \\ \phi_7 &= \frac{1}{2}(1+\xi)(1+\psi)(1-\xi) \\ \phi_8 &= \frac{1}{2}(1-\xi)(1+\psi)(1-\psi) \end{aligned} \quad (3-22)$$

### 3.4.2 FE formulation

First, the displacement  $\mathbf{u}(t)$  and test function  $\mathbf{p}(t)$  are replaced by the column vectors of  $u(t)$  and  $p(t)$  at FE nodes for each time  $t$ . The stress and strain tensors  $\boldsymbol{\sigma}$  and  $\boldsymbol{\varepsilon}$  (3-by-3 matrices) are manipulated to be 4-by-1 vectors with the non-zero terms:  $\boldsymbol{\sigma} = [\sigma_{rr}, \sigma_{zz}, \sigma_{\theta\theta}, \sigma_{rz}]^T$  and  $\boldsymbol{\varepsilon} = \nabla u = [\varepsilon_{rr} \quad \varepsilon_{zz} \quad \varepsilon_{\theta\theta} \quad \gamma_{rz}]^T$ .

The strain-displacement operator  $\nabla$  (a 4-by-2 matrix) for the axisymmetric model in the FE formulation is expressed as follows:

$$\nabla = \begin{bmatrix} \frac{\partial}{\partial r} & 0 \\ 0 & \frac{\partial}{\partial z} \\ \frac{1}{r} & 0 \\ \frac{\partial}{\partial z} & \frac{\partial}{\partial r} \end{bmatrix} \quad (3-23)$$

The hydrostatic strain is also manipulated as a 4-by-1 vector with the fourth zero-term added, and defined as:

$$\varepsilon_h = \nabla_h u = \frac{1}{3} [\varepsilon_{rr} + \varepsilon_{zz} + \varepsilon_{\theta\theta} \quad \varepsilon_{rr} + \varepsilon_{zz} + \varepsilon_{\theta\theta} \quad \varepsilon_{rr} + \varepsilon_{zz} + \varepsilon_{\theta\theta} \quad 0]^T \quad (3-24)$$

where  $\nabla_h$  is the hydrostatic strain-displacement operator (4-by-2 matrix) in the FE formulation, defined as follows:

$$\nabla_h = \frac{1}{3} \begin{bmatrix} \frac{\partial}{\partial r} + \frac{1}{r} & \frac{\partial}{\partial z} \\ \frac{\partial}{\partial r} + \frac{1}{r} & \frac{\partial}{\partial z} \\ \frac{\partial}{\partial r} + \frac{1}{r} & \frac{\partial}{\partial z} \\ 0 & 0 \end{bmatrix} \quad (3-25)$$

Now one starts the FE solution. Substitute Equation (3-20) into Equations (3-15) and (3-16) to form the FE formulations of the deviatoric and hydrostatic stress terms (in 4-by-1 vector forms):

$$S(t) = 2 \int_0^t G(t - \tau) \frac{\partial(\nabla \Phi u(\tau) - \nabla_h \Phi u(\tau))}{\partial \tau} d\tau = 2 \int_0^t (\nabla \Phi - \nabla_h \Phi) G(t - \tau) \frac{\partial u(\tau)}{\partial \tau} d\tau \quad (3-26)$$

$$\sigma_h(t) = 3 \int_0^t K(t - \tau) \frac{\partial(\nabla_h \Phi u(\tau))}{\partial \tau} d\tau = 3 \int_0^t K(t - \tau) \nabla_h \Phi \frac{\partial(u(\tau))}{\partial \tau} d\tau \quad (3-27)$$

Substitute Equation (3-20) into Equation (3-19) to form the weak form of the governing state equation in the FE formulation:

$$\begin{aligned} & \left[ \int_0^{t_d} \int_{\Omega} \int_0^t 2G(t - \tau) (\nabla \Phi - \nabla_h \Phi) \frac{\partial u(\tau)}{\partial \tau} d\tau \cdot (\nabla \Phi) p(t) d\Omega dt + 3 \int_0^t K(t - \right. \\ & \left. \tau) \nabla_h \Phi \frac{\partial(u(\tau))}{\partial \tau} d\tau \cdot (\nabla \Phi) p(t) d\Omega dt \right] + \left[ \int_0^{t_d} \int_{\Omega} c \Phi \frac{\partial u(t)}{\partial t} \cdot \Phi p(t) d\Omega dt + \int_0^{t_d} \int_{\Omega} \rho \Phi \frac{\partial^2 u(\tau)}{\partial t^2} \cdot \right. \\ & \left. \Phi p(t) d\Omega dt \right] = \left[ \int_0^{t_d} \int_{\partial\Omega_4} f(t) \cdot \Phi p(t) ds dt + \int_0^{t_d} \int_{\Omega} b \cdot \Phi p(t) d\Omega dt \right] \end{aligned} \quad (3-28)$$

It can be rearranged as follows:

$$\begin{aligned} & \left[ 2 \int_0^{t_d} \int_{\Omega} \int_0^t \mathbf{B}^T G(t - \tau) (\mathbf{B} - \mathbf{B}_h) \frac{\partial u(\tau)}{\partial \tau} d\tau p(t) d\Omega dt + 3 \int_0^{t_d} \int_{\Omega} \int_0^t \mathbf{B}^T K(t - \right. \\ & \left. \tau) \mathbf{B}_h \frac{\partial(u(\tau))}{\partial \tau} d\tau p(t) d\Omega dt \right] + \left[ \int_0^{t_d} \int_{\Omega} \Phi^T c \Phi \frac{\partial u(t)}{\partial t} p(t) d\Omega dt + \right. \\ & \left. \int_0^{t_d} \int_{\Omega} \Phi^T \rho \Phi \frac{\partial^2 u(t)}{\partial t^2} p(t) d\Omega dt \right] = \left[ \int_0^{t_d} \int_{\partial\Omega_4} \Phi^T f(t) p(t) ds dt + \int_0^{t_d} \int_{\Omega} \Phi^T b p(t) d\Omega dt \right] \end{aligned} \quad (3-29)$$

where  $\mathbf{B} = \frac{1}{2}[\nabla\boldsymbol{\Phi} + \nabla\boldsymbol{\Phi}^T] = \nabla\boldsymbol{\Phi}$ , is the strain-displacement matrix (a 4-by-16 matrix for one element);  $\mathbf{B}_h = \nabla_h\boldsymbol{\Phi}$ , is defined as the hydrostatic strain-displacement matrix (a 4-by-16 matrix for one element);  $\boldsymbol{\Phi}_r^T$  is the transposed shape function to be used for discretization of loading on the surface area.

Equation (3-29) is subjected to  $\forall p(t) \in \Omega \times [0, t_d]$ , and thus, the  $p(t)$  can be dismissed on both sides of the equation  $\forall t \in [0, t_d]$ . The following weak form of the governing state equation satisfies:

$$\left[ 2 \int_{\Omega} \int_0^t \mathbf{B}^T G(t-\tau)(\mathbf{B} - \mathbf{B}_h) \frac{\partial u(\tau)}{\partial \tau} d\tau d\Omega + 3 \int_{\Omega} \int_0^t \mathbf{B}^T K(t-\tau)\mathbf{B}_h \frac{\partial(u(\tau))}{\partial \tau} d\tau d\Omega \right] + \left[ \left( \int_{\Omega} \boldsymbol{\Phi}^T c \boldsymbol{\Phi} d\Omega \right) \frac{\partial u(t)}{\partial t} + \left( \int_{\Omega} \boldsymbol{\Phi}^T \rho \boldsymbol{\Phi} d\Omega \right) \frac{\partial^2 u(t)}{\partial t^2} \right] = \left[ \int_{\partial\Omega_4} \boldsymbol{\Phi}_r^T f(t) ds + \int_{\Omega} \boldsymbol{\Phi}^T b d\Omega \right] \quad \forall t \in [0, t_d] \quad (3-30)$$

Here the relaxation modulus term is defined as follows:

$$\mathbf{R}(t-\tau) = 2\mathbf{B}^T G(t-\tau)(\mathbf{B} - \mathbf{B}_h) + 3\mathbf{B}^T K(t-\tau)\mathbf{B}_h \quad (3-31)$$

Thus, Equation (3-30) can be reduced to a simplified format as a final weak form of the governing state equation, which can be used for the numerical solution as discussed later:

$$\int_{\Omega} \int_0^t \mathbf{R}(t-\tau) \frac{\partial(u(\tau))}{\partial \tau} d\tau d\Omega + \mathbf{C} \frac{\partial u(t)}{\partial t} + \mathbf{M} \frac{\partial^2 u(t)}{\partial t^2} = \mathfrak{R} \quad (3-32)$$

where  $\mathbf{M}$  is mass matrix that  $\mathbf{M} = \int_{\Omega} \boldsymbol{\Phi}^T \rho \boldsymbol{\Phi} d\Omega$ ;  $\mathbf{C} = \int_{\Omega} \boldsymbol{\Phi}^T c \boldsymbol{\Phi} d\Omega$  is damping matrix to be determined from Equation (3-7); and  $\mathfrak{R}$  is load vector that  $\mathfrak{R} = \int_{\partial\Omega_4} \boldsymbol{\Phi}_r^T f(t) ds + \int_{\Omega} \boldsymbol{\Phi}^T b d\Omega$ .

### 3.4.3 Time discretization

The integration with time  $t \in [0, t_d]$  is discretized to finite time steps as illustrated in Figure 42. The forward computation starts at zero and ends at  $t_d$  with a total  $n$  time steps. The response calculated at the current time step  $k$  is dependent on those determined at previous time steps for  $k = 1, 2, 3 \dots \dots k-1$  to consider the ‘‘memory’’ effect of material viscoelasticity.

Different algorithms have been developed for the discretization of time steps, which include the forward Finite Difference Method (FDM), backward FDM, central FDM, the Houbolt method, the Wilson  $\theta$  method, and the Newmark method, etc. The Houbolt method has the advantage that computation results are less dependent on time step length (Bathe 1996), and thus is chosen herein in order to save computation time. As results, a relatively great step length (i.e., 0.001 second) could achieve accurate results. The acceleration and velocity at the time step  $k$  can be written as follows following the Houbolt method:

$$\ddot{u}(k) = \frac{2u(k+1) - 5u(k) + 4u(k-1) - u(k-2)}{\Delta t^2} \quad (3-33)\text{-a}$$

$$\dot{u}(k) = \frac{11u(k+1) - 18u(k) + 9u(k-1) - 2u(k-2)}{6\Delta t} \quad (3-33)\text{-b}$$

where  $u(i)$  is displacement at the  $i^{th}$  time step for  $i = k - 2, k - 1, k$  and  $k + 1$ .

The first order differential or gradient  $\frac{\partial u(\tau)}{\partial \tau}$  term at the sub-time of  $\tau \in [0, t]$  in Equation (3-32) for the viscoelastic solution is discretized rather using the forward FDM method, since it could accurately estimate the gradient value in a more simplified form than the Houbolt method (see Figure 42):

$$\frac{\partial(u(\tau))}{\partial \tau} = \lim_{\Delta \tau \rightarrow 0} \frac{u(\tau + \Delta \tau) - u(\tau)}{\Delta \tau} \approx \frac{u(j+1) - u(j)}{t_{j+1} - t_j} \quad (3-34)$$

where  $u(\tau)$  is displacement at the sub-time  $\tau \in [t_j, t_{j+1}]$  for  $j = 1, 2 \dots k$ .

With time discretization, substitute Equation (3-33) and Equation (3-34) into Equation (3-32), to form the time-discretized weak form, for an explicit solution at the current time step  $k$ :

$$\int_{\Omega} \sum_{j=1}^k \int_{t_{j-1}}^{t_j} R(t - \tau) d\tau d\Omega \frac{u(j+1) - u(j)}{\Delta t} + \mathbf{C} \frac{11u(k+1) - 18u(k) + 9u(k-1) - 2u(k-2)}{6\Delta t} + \mathbf{M} \frac{2u(k+1) - 5u(k) + 4u(k-1) - u(k-2)}{\Delta t^2} = \mathfrak{R} \quad (3-35)$$

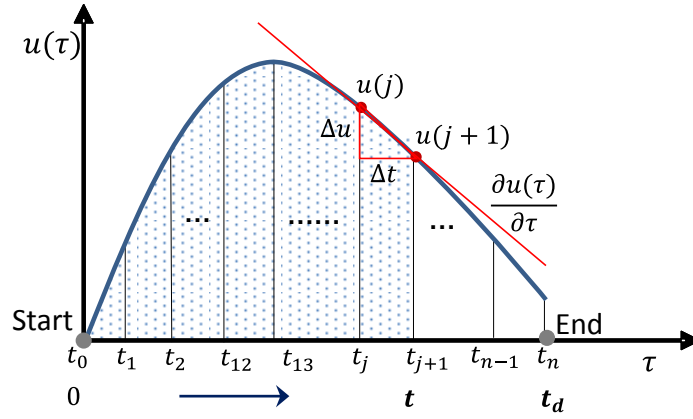


**Figure 42. Time discretization.**

### 3.4.4 Viscoelastic stiffness matrix

Here the “viscoelastic stiffness matrix” of AC material at the sub-time step  $j = 1, 2, 3, \dots, k$  is defined as follows for numerical computation use:

$$J(j) = \int_{\Omega_{AC}} \int_{t_{j-1}}^{t_j} R(t - \tau) d\tau d\Omega \quad (3-36)$$

The derivation of viscoelastic stiffness matrix is detailed in the following. Substitute Equation (3-31) into Equation (3-36) to re-express  $J(j)$  as follows:

$$J(j) = 2 \int_{\Omega_{AC}} \int_{t_{j-1}}^{t_j} \mathbf{B}^T G(t - \tau) (\mathbf{B} - \mathbf{B}_h) d\tau d\Omega + 3 \int_{\Omega_{AC}} \int_{t_{j-1}}^{t_j} \mathbf{B}^T K(t - \tau) \mathbf{B}_h d\tau d\Omega \quad (3-37)$$

where  $J(j)$  consists of two components, named deviatoric viscoelastic stiffness matrix  $J_d(j)$  and hydrostatic viscoelastic stiffness matrix  $J_h(j)$ , respectively:

$$J_d(j) = 2 \int_{\Omega_{AC}} \int_{t_{j-1}}^{t_j} \mathbf{B}^T G(t - \tau) (\mathbf{B} - \mathbf{B}_h) d\tau d\Omega \quad (3-38)$$

$$J_h(j) = 3 \int_{\Omega_{AC}} \int_{t_{j-1}}^{t_j} \mathbf{B}^T K(t - \tau) \mathbf{B}_h d\tau d\Omega \quad (3-39)$$

Substitute the relaxation modulus forms of Equation (3-6) into Equation (3-38) to derive the deviatoric viscoelastic stiffness matrix as follows:

$$J_d(j) = 2 \int_{\Omega_{AC}} \int_{t_{j-1}}^{t_j} \mathbf{B}^T \left[ G_0 + \sum_i^N G_i e^{-\frac{G_i}{\eta_i}(t-\tau)} \right] [\mathbf{B} - \mathbf{B}_h] d\tau d\Omega \quad (3-40)$$

After the integration of sub-time step  $[t_{j-1}, t_j]$ ,  $J_d(j)$  can be re-derived and re-arranged as follows:

$$J_d(j) = 2 \int_{\Omega_{AC}} \int_{t_{j-1}}^{t_j} \mathbf{B}^T G_0 [\mathbf{B} - \mathbf{B}_h] dt d\Omega + 2 \int_{\Omega_{AC}} \int_{t_{j-1}}^{t_j} \mathbf{B}^T \sum_i^N \eta_{Gi} [\mathbf{B} - \mathbf{B}_h] d e^{-\frac{G_i}{\eta_{Gi}}(t-\tau)} d\Omega = 2 \int_{\Omega_{AC}} \mathbf{B}^T \left[ G_0 \Delta t + \sum_i^N \eta_{Gi} \left( e^{-\frac{G_i}{\eta_{Gi}}(t-t_j)} - e^{-\frac{G_i}{\eta_{Gi}}(t-t_{j-1})} \right) \right] [\mathbf{B} - \mathbf{B}_h]^T d\Omega \quad (3-41)$$

Substitute Equation (3-6)-b into Equation (3-39) for deriving the hydrostatic viscoelastic stiffness matrix at the sub-time step  $j$  as follows:

$$J_h(j) = 3 \int_{\Omega_{AC}} \int_{t_{k-1}}^{t_k} \mathbf{B}^T \left[ K_0 + \sum_i^N K_i e^{-\frac{K_i}{\eta_i}(t-\tau)} \right] \mathbf{B}_h d\tau d\Omega \quad (3-42)$$

$J_h(j)$  can be re-derived and rearranged as follows after the integration of the sub-time step  $[t_{j-1}, t_j]$ :

$$J_h(j) = 3 \int_{\Omega_{AC}} \mathbf{B}^T K_0 \mathbf{B}_h \Delta t d\Omega + 3 \int_{\Omega_{ac}} \mathbf{B}^T \sum_i^N \eta_{Ki} \left[ e^{-\frac{K_i}{\eta_{Ki}}(t-t_j)} - e^{-\frac{K_i}{\eta_{Ki}}(t-t_{j-1})} \right] \mathbf{B}_h d\Omega = 3 \int_{\Omega_{AC}} \mathbf{B}^T \left[ K_0 \Delta t + \sum_i^N \eta_{Ki} \left( e^{-\frac{K_i}{\eta_{Ki}}(t-t_j)} - e^{-\frac{K_i}{\eta_{Ki}}(t-t_{j-1})} \right) \right] \mathbf{B}_h d\Omega \quad (3-43)$$

### 3.4.5 Formulation of global linear system

Substitute the viscoelastic stiffness matrix of Equation (3-36) into Equation (3-35) to reach the final time-discretized weak form as follows:

$$\sum_{j=1}^k \mathbf{J}(j) \frac{u^{(j+1)} - u^{(j)}}{\Delta t} + \mathbf{C} \frac{11u^{(k+1)} - 18u^{(k)} + 9u^{(k-1)} - 2u^{(k-2)}}{62t} + \mathbf{M} \frac{2u^{(k+1)} - 5u^{(k)} + 4u^{(k-1)} - u^{(k-2)}}{\Delta t^2} = \mathfrak{R} \quad (3-44)$$

where  $u^{(k)}$  is displacement at the  $k^{th}$  time step for  $k = 1, 2, 3 \dots n$ ;  $u^{(j)}$  is displacement at the  $j^{th}$  sub-time step or time  $t_j$  for  $j = 1, 2, 3 \dots k$ .

Equation (3-44) can then be rearranged as follows:

$$\left[ \frac{\mathbf{J}(k+1)}{\Delta t} + \frac{11\mathbf{C}}{6t} + \frac{2\mathbf{M}}{\Delta t^2} \right] u^{(k+1)} = \mathfrak{R} + \mathbf{J}(k) \frac{u^{(k)}}{\Delta t} - \sum_{j=1}^{k-1} \mathbf{J}(j) \frac{u^{(j+1)} - u^{(j)}}{\Delta t} + \mathbf{C} \frac{18u^{(k)} - 9u^{(k-1)} + 2u^{(k-2)}}{6\Delta t} + \mathbf{M} \frac{5u^{(k)} - 4u^{(k-1)} + u^{(k-2)}}{\Delta t^2} \quad (3-45)$$

Thus, the linear system for the solution of dynamic viscoelastic displacements at the time step  $(k+1)$  is formed:

$$\mathbf{K}_{dve} u^{(k+1)} = \mathfrak{R}_{dve} \quad (3-46)$$

where  $\mathbf{K}_{\text{dve}}$  is the dynamic viscoelastic stiffness matrix, a  $2n$ -by- $2n$  matrix with  $n$  as the total node number of the pavement structure (two directions for each node), and for the zones of unbound materials, the elements of  $\mathbf{K}_{\text{dve}}$  are zeroed;  $\mathfrak{R}_{\text{dve}}$  is the dynamic viscoelastic load vector, a  $2n$ -by-1 vector.

$$\mathbf{K}_{\text{dve}} = \frac{J(k+1)}{\Delta t} + \frac{11\mathbf{C}}{6t} + \frac{2\mathbf{M}}{\Delta t^2} \quad (3-47)$$

$$\mathfrak{R}_{\text{dve}} = \mathfrak{R} + \mathbf{J}(k) \frac{u(k)}{\Delta t} - \sum_{j=1}^{k-1} \mathbf{J}(j) \frac{u(j+1)-u(j)}{\Delta t} + \mathbf{C} \frac{18u(k)-9u(k-1)+2u(k-2)}{6\Delta t} + \mathbf{M} \frac{5u(k)-4u(k-1)+u(k-2)}{\Delta t^2} \quad (3-48)$$

Combining the formulations of dynamic viscoelastic and dynamic elastic with damping models, the global dynamic viscoelastic linear system of the entire pavement structure can be formed as follows:

$$\mathbf{K}u(t) = \mathfrak{R}_{\text{dve}} \quad (3-49)$$

where  $\mathbf{K}$  is the global stiffness matrix, which can be expressed as follows:

$$\mathbf{K} = \mathbf{K}_{\text{E}} + \left[ \frac{J(k+1)}{\Delta t} + \frac{11\mathbf{C}}{6\Delta t} + \frac{2\mathbf{M}}{\Delta t^2} \right] \quad (3-50)$$

$\mathbf{K}_{\text{E}}$  is the global elastic stiffness matrix of the elastic layers, a  $2n$ -by- $2n$  matrix.

The global elastic stiffness matrix is calculated by integration as  $\mathbf{K}_{\text{E}} = \int \mathbf{B}^T \mathbf{C} \mathbf{B} d\Omega$  (Cook et al. 2001).  $\mathbf{C}$  is the fourth-order elasticity tensor of the axisymmetric model (Sadd 2005) as follows:

$$\mathbf{C} = \frac{E}{(1+\nu)(1-2\nu)} \begin{bmatrix} 1-\nu & \nu & \nu & 0 \\ \nu & 1-\nu & \nu & 0 \\ \nu & \nu & 1-\nu & 0 \\ 0 & 0 & 0 & 0.5(1-2\nu) \end{bmatrix} \quad (3-51)$$

where  $E$  is Young's modulus;  $\nu$  is Poisson's ratio.

### 3.4.6 Space discretization

The volume differential of an element is calculated as follows:

$$d\Omega = 2\pi r(\xi_k, \psi_l) dr dz = 2\pi r(\xi_k, \psi_l) J_{\Omega}(\xi_k, \psi_l) \quad (3-52)$$

where  $r(\xi_k, \psi_l)$  is global radial coordinate of the Gauss point at the local coordinate of  $(\xi_k, \psi_l)$  for that element, and  $k = 1,2$  and  $l = 1,2$  for two Gauss points at each direction;

$J_\Omega(\xi_k, \psi_l)$  is determinant of Jacob's function,  $J_{\Omega(\xi_k, \psi_k)} = \det \begin{bmatrix} \frac{\partial r}{\partial \xi} & \frac{\partial z}{\partial \xi} \\ \frac{\partial r}{\partial \psi} & \frac{\partial z}{\partial \psi} \end{bmatrix}$  (equivalent to the area of that element).

The elastic stiffness matrix of an element,  $\mathbf{k}_E^e$  can be discretized to four Gauss points as follows:

$$\mathbf{K}_E^e = \sum_{k=1}^{n_G} \sum_{l=1}^{n_G} w_k w_l \mathbf{B}^T(\xi_k, \psi_l) C \mathbf{B}(\xi_k, \psi_l) 2\pi r(\xi_k, \psi_l) J_\Omega(\xi_k, \psi_l) \quad (3-53)$$

where  $\mathbf{B}$  is the strain-displacement matrix, a 4-by-16 matrix for one element;  $C$  is the fourth order elasticity tensor;  $w_m$  is a weight function at the radial direction and is set as 1 in this model;  $w_l$  is a weight function at the depth direction and is set as 1;  $n_G$  is the number of Gauss points at each direction of  $r$  and  $z$ ,  $n_G = 2$ .

The deviatoric viscoelastic stiffness matrix  $\mathbf{J}_d^e(k)$ , a 16-by-16 matrix for one element, can be discretized to the four Gauss points as follows:

$$\begin{aligned} \mathbf{J}_d^e(j) = & \sum_{k=1}^{n_G} \sum_{l=1}^{n_G} w_k w_l \Delta t 2\pi r(\xi_k, \psi_l) J_\Omega(\xi_k, \psi_l) \mathbf{B}^T(\xi_k, \psi_l) G_0 [\mathbf{B}(\xi_k, \psi_l) - \\ & \mathbf{B}_h(\xi_k, \psi_l)] + \sum_{k=1}^{n_G} \sum_{l=1}^{n_G} \sum_i^N w_k w_l 2\pi r(\xi_k, \psi_l) J_\Omega(\xi_k, \psi_l) \mathbf{B}(\xi_k, \psi_l)^T \eta_{Gi} \left[ e^{-\frac{G_i}{\eta_{Gi}}(t-t_j)} - \right. \\ & \left. e^{-\frac{G_i}{\eta_{Gi}}(t-t_{j-1})} \right] [\mathbf{B}(\xi_k, \psi_l) - \mathbf{B}_h(\xi_k, \psi_l)] \end{aligned} \quad (3-54)$$

Likewise, the hydrastatic viscoelastic stiffness matrix  $\mathbf{J}_h^e(k)$ , a 16-by-16 matrix for one element, can be discretized to the four Gauss points as follows:

$$\begin{aligned} \mathbf{J}_h^e(j) = & \sum_{k=1}^{n_G} \sum_{l=1}^{n_G} w_k w_l \Delta t \mathbf{B}^T(\xi_k, \psi_l) K_0 \mathbf{B}_h(\xi_k, \psi_l) 2\pi r(\xi_k, \psi_l) J_\Omega(\xi_k, \psi_l) + \\ & \sum_{k=1}^{n_G} \sum_{l=1}^{n_G} \sum_i^N w_k w_l \mathbf{B}^T(\xi_k, \psi_l) \eta_{Ki} \left[ e^{-\frac{K_i}{\eta_{Ki}}(t-t_j)} - \right. \\ & \left. e^{-\frac{K_i}{\eta_{Ki}}(t-t_{j-1})} \right] \mathbf{B}_h(\xi_k, \psi_l) 2\pi r(\xi_k, \psi_l) J_\Omega(\xi_k, \psi_l) \end{aligned} \quad (3-55)$$

The mass matrix of each element can be discretized to the four Gauss points as follows:

$$\mathbf{M}^e = \sum_{k=1}^{n_G} \sum_{l=1}^{n_G} w_k w_l \mathbf{\Phi}^T(\xi_k, \psi_l) \rho(\xi_k, \psi_l) \mathbf{\Phi}(\xi_k, \psi_l) 2\pi r(\xi_k, \psi_l) J_\Omega(\xi_k, \psi_l) \quad (3-56)$$

The damping matrix of each element can be discretized to the four Gauss points following the Rayleigh damping model as follows:

$$\mathbf{C}^e = \alpha \sum_{k=1}^{n_G} \sum_{l=1}^{n_G} w_k w_l 2\pi r(\xi_k, \psi_l) \mathbf{\Phi}^T(\xi_k, \psi_l) \rho(\xi_k, \psi_l) \mathbf{\Phi}(\xi_k, \psi_l) J_\Omega(\xi_k, \psi_l) + \beta \sum_{k=1}^{n_G} \sum_{l=1}^{n_G} w_m w_l 2\pi r(\xi_m, \psi_l) \mathbf{B}^T(\xi_m, \psi_l) \mathbf{C} \mathbf{B}(\xi_m, \psi_l) J_\Omega(\xi_m, \psi_l) \quad (3-57)$$

The load vector  $\mathfrak{R}$  for one element can be discretized to the two Gauss points for external loading (only at the depth direction) and the four Gauss points for the body force term as follows:

$$\mathfrak{R}^e = \sum_{k=1}^{n_G} w_k \mathbf{\Phi}_F^T(\xi_k) f(\xi_k) J_{\partial\Omega_4}(\xi_k) + \sum_{k=1}^{n_G} \sum_{l=1}^{n_G} 2\pi w_k w_l \mathbf{\Phi}^T(\xi_k, \psi_l) b(\xi_k, \psi_l) r(\xi_k, \psi_l) J_\Omega(\xi_k, \psi_l) \quad (3-58)$$

where  $J_{\partial\Omega_4}(\xi_k)$  is the determinant of the Jacobin function for the loading area  $\partial\Omega_4$ .

Finally, the global stiffness matrix and load vector are formed by assembling that of each element (just add up all values at the same node number).

### 3.4.7 Solution of global linear system

The stiffness matrix  $\mathbf{K} > 0$  (positive definite), and thus  $\mathbf{K}$  can be banded in order to reduce the storage space and to improve computation speed. To minimize the bandwidth of the a stiffness matrix, the nodes are assigned in an incremental order along the radial direction (from left to right) and then the depth direction (from top to bottom) as shown in Figure 43a. This method results in the smallest bandwidth. Figure 43b presents the FE mesh produced by the ANSYS-14.5 software, where the node number seems randomly assigned.

There are total  $n_r$  rows of elements and total  $n$  FE nodes. The band matrix has a significantly reduced dimension size of  $n_b$ -by- $2n$  ( $n_b$  is the band width). The bandwidth is dependent on the element numbers in both directions as follows:

$$n_b = n_d(n_m + 1) \quad (3-59)$$

where  $n_d$  is degrees of freedom,  $n_d = 2$ ;  $n_m$  is the maximum node number difference within one element that  $n_m = n_1 + n_2 + 2$ ;  $n_1$  is the total node number of one ‘‘row’’

along the  $r$  direction on the top or bottom of elements (see Figure 43);  $n_2$  is the total node number of one “row” along the  $r$  direction at the center of elements (see Figure 43). For example, a model with total of 1,583 nodes has a full stiffness-matrix size of 3,166-by-3,166, and banded-matrix size of 310-by-3,166.

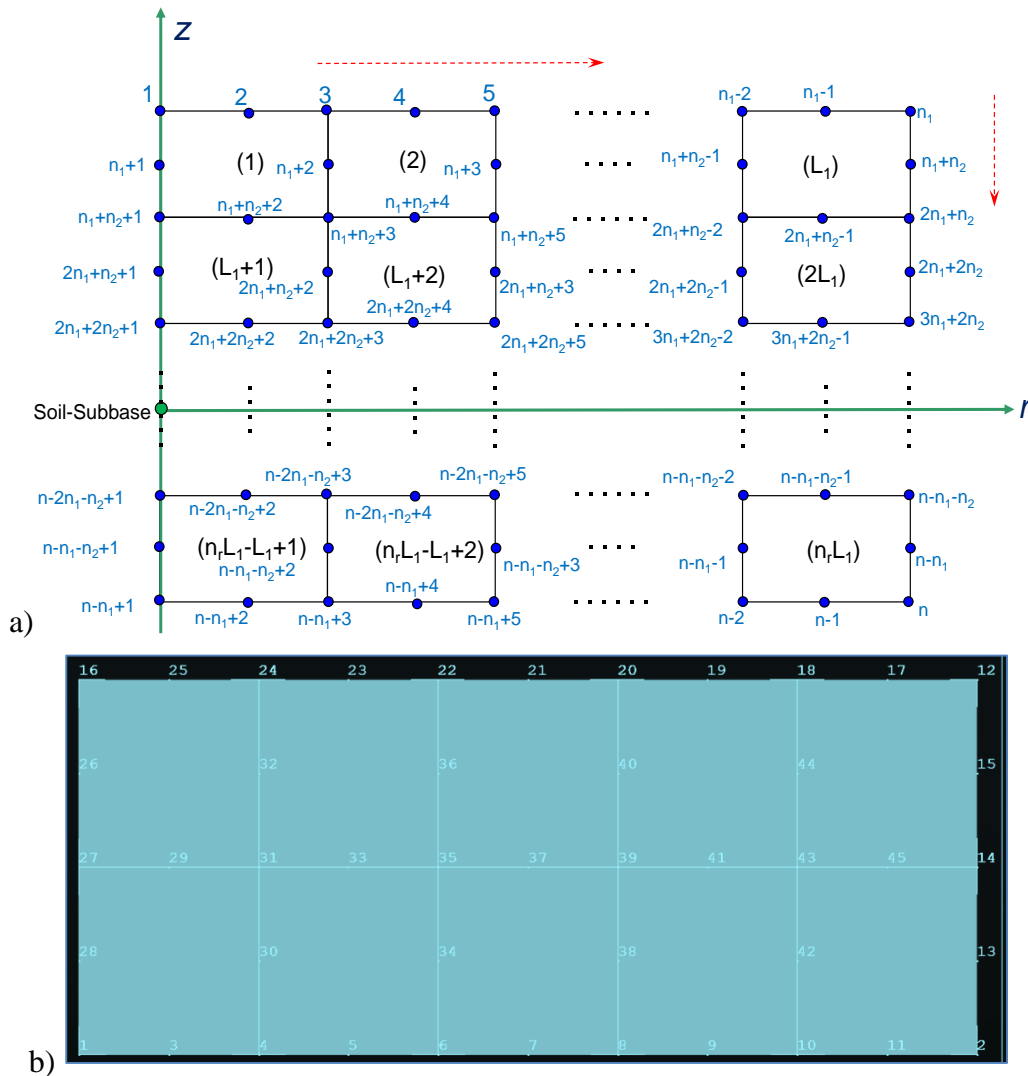


**Figure 43. Finite element diagram: a) Method in this research (arrows show the element and node number assignment direction as from left to right and from top to bottom); b) FE mesh produced by ANSYS-14.5 software.**

The factorization method with banded matrix is used for solving the global linear system. The banded stiffness matrix,  $\mathbf{K}_{dve}$ , is decomposed to the upper and lower triangular matrices following the factorization method as follows (see Figure 44):

$$\mathbf{k} = \mathbf{LU} \quad (3-60)$$

where  $\mathbf{U}$  is the upper triangular matrix; and  $\mathbf{L}$  is the lower triangular matrix.

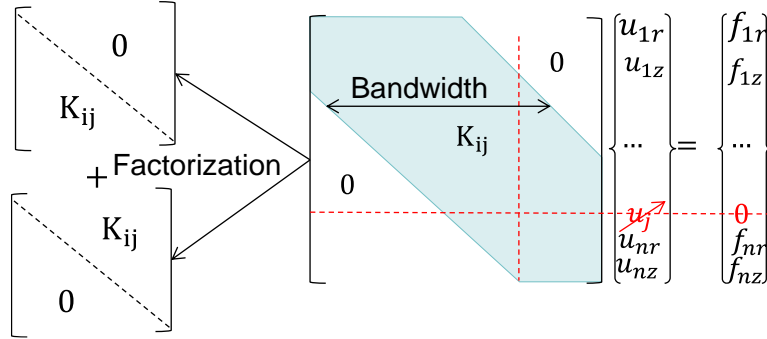


**Figure 44. Linear system in the matrix-vector format.**

Then the global linear system can be rearranged as follows:

$$\mathbf{LU}u = \mathfrak{R}_{dve} \quad (3-61)$$

Following the factorization method (Hardy et al. 1980), the linear system is solved following two steps in sequence for finding first the  $y$  vector and then the  $u$  displacement vector:

$$\mathbf{L}y = \mathfrak{R}_{dve} \quad (3-62)\text{-a}$$

$$\mathbf{U}u = y \quad (3-62)\text{-b}$$

As the  $\mathbf{K}$  matrix is symmetric positive definite, the  $\mathbf{U}$  matrix is equivalent to the conjugate transpose matrix of  $\mathbf{L}$  as  $\mathbf{L}^*$ .

Given the initial deflection as zero at time  $t_0$  and the loading function, the displacement vector  $u(t)$  at each time step can be determined by one solution of this linear system. The  $n$  total time steps require total  $n$  solutions of the linear system.

At time zero, there are no external force and associated acceleration and displacement. Therefore, Equation (3-49) is subjected to the initial conditions of:

$$f(0) = 0 \quad (3-63)\text{-a}$$

$$u(0) = 0 \quad (3-63)\text{-b}$$

$$\ddot{u}(0) = 0 \quad (3-63)\text{-c}$$

Calculating  $u(1)$  requires  $u(-2)$  and  $u(-1)$  as inputs which are unknown according to Equation (3-49) using the Houbolt method. Therefore, the central FDM method is proposed here to solve these unknown inputs. According to Central FDM and the initial conditions, the following equations satisfy to calculate  $\dot{u}(0)$ ,  $u(-1)$  and  $u(1)$ :

$$0 = \frac{1}{\Delta t^2} [u(-1) + u(1)] \quad (3-64)$$

$$\dot{u}(0) = \frac{1}{20t} [u(1) - u(-1)] \quad (3-65)$$

$$\left[ (\mathbf{K}_E - \mathbf{K}_{ve}) + \frac{J^{(1)}}{\Delta t} + \frac{\mathbf{M}}{\Delta t^2} + \frac{\mathbf{C}}{2\Delta t} \right] u(1) = \mathfrak{R}(0) - \left( \frac{\mathbf{M}}{\Delta t^2} - \frac{\mathbf{C}}{2\Delta t} \right) u(-1) \quad (3-66)$$

Since the second time step ( $k = 2$ ), the Houbolt method is resumed for solving  $u(k)$  at  $k = 2, 3, 4 \dots n$  following Equation (3-49).

After calculations of displacements of all nodes, the strain and then stress responses can be solved following Equation (3-10) and then Equation (3-13).

### 3.4.8 Computer code development

A computer code written in the FORTRAN computer language was developed to implement the numerical computation procedure detailed above. Figure 45 shows the flow chart for the computer coding.

The inputs contain the material model parameters, the loading time history, and pavement structure geometry. The model geometry is meshed accordingly with model and element size defined by users following Figure 43. The elastic stiffness matrices of  $\mathbf{K}_E$  and  $\mathbf{K}_{ve}$  are formed. Consequently, the FE computation starts at the initial time step  $k = 1$  ( $u(0) = 0$  is given). At each time step the viscoelastic stiffness matrix and the global stiffness matrix are formed. Then boundary conditions are applied, and the load vector is built. The global linear system is formed and the response is solved. This computation continues until the time step reaches the last one.

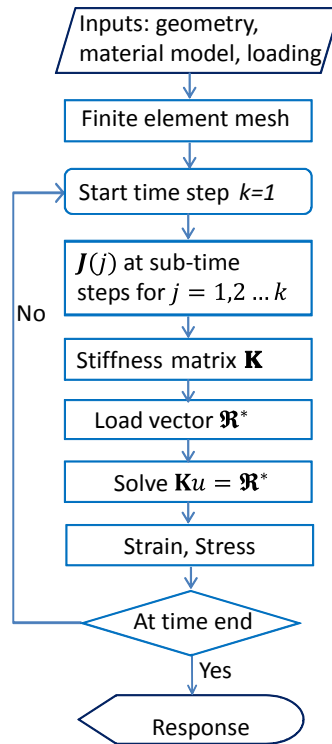


**Figure 45. Flowchart of the developed computer coding for the dynamic viscoelastic FE solution.**

### 3.5. Experimental Design

The model and computer method discussed above is implemented to a flexible pavement structure on soil foundation. A field plate loading test using FWD was designed and performed in the State of Florida for new construction projects. The fresh pavement was selected in order to avoid the influence of material damages such as fatigue cracking. The test was performed shortly after finishing compaction at the pavement temperature of 104°F (40°C). The state report provided the layer thicknesses. The pavement structure consists of an AC layer (11.18 cm), a granular base (17.78 cm), and a subbase course (30.48 cm) on the subgrade. A peak loading value of 9,000 pounds (40,034 N) was set as half of a standard single axle loading of a vehicle (AASHTO 1993, ARA 2004). The circular loading plate has a radius of 5.9 inches (15 cm). Seven geophones were used to collect deflection pulses at distances of 0, 8, 12, 18, 24, 36, and 60 inches (0, 20.32, 30.48, 45.72, 60.96, 91.44, and 152.40 cm). Figure 46a plots the

measured FWD loading and deflection time histories, which start from zero and rise to peaks, and then drop to zero. As seen in Figure 46a, the loading-time path has some “noises” at the beginning stage and a rest time after the major loading curve, but its major curve is fairly smooth.

The time-domain loading  $f(t)$  is converted to frequency domain ( $F(s) = \int_0^{\infty} f(t)e^{-st} dt$ ). Figure 46 (b) plots the Fast Fourier Transformed (FFT) results in decibels ( $dB = 20 \log_{10} \frac{|F(s)|}{|F_0|}$ ,  $|F_0|$  is the peak  $|F(s)|$ ). Results indicate that the vast majority of energy occurs before a frequency of 78.3 Hz as seen from the small-scaled  $|F(s)|$  vs. frequency curve, and at frequencies greater than 200 Hz, the energy is relatively negligible. No obvious pitches of frequency domain were observed, which may be explained by the following: 1) for this input signal of loading pulse, an un-symmetric output pulse can be expected (Ayre 1976), and 2) insufficient resonances are found, which relate to the layer depth, material stiffness, input signal, and damping property (Oppenheim et al. 1975). A softer material with higher damping suppresses resonance when waves rebound back at the interface. For example, the first deflection peak occurs 0.0056 seconds behind the peak loading with a resonance frequency estimated at 178.57 Hz ( $1/0.0056$ ). However, at that frequency there is insufficient energy to “excite” the resonance (see Figure 46b).

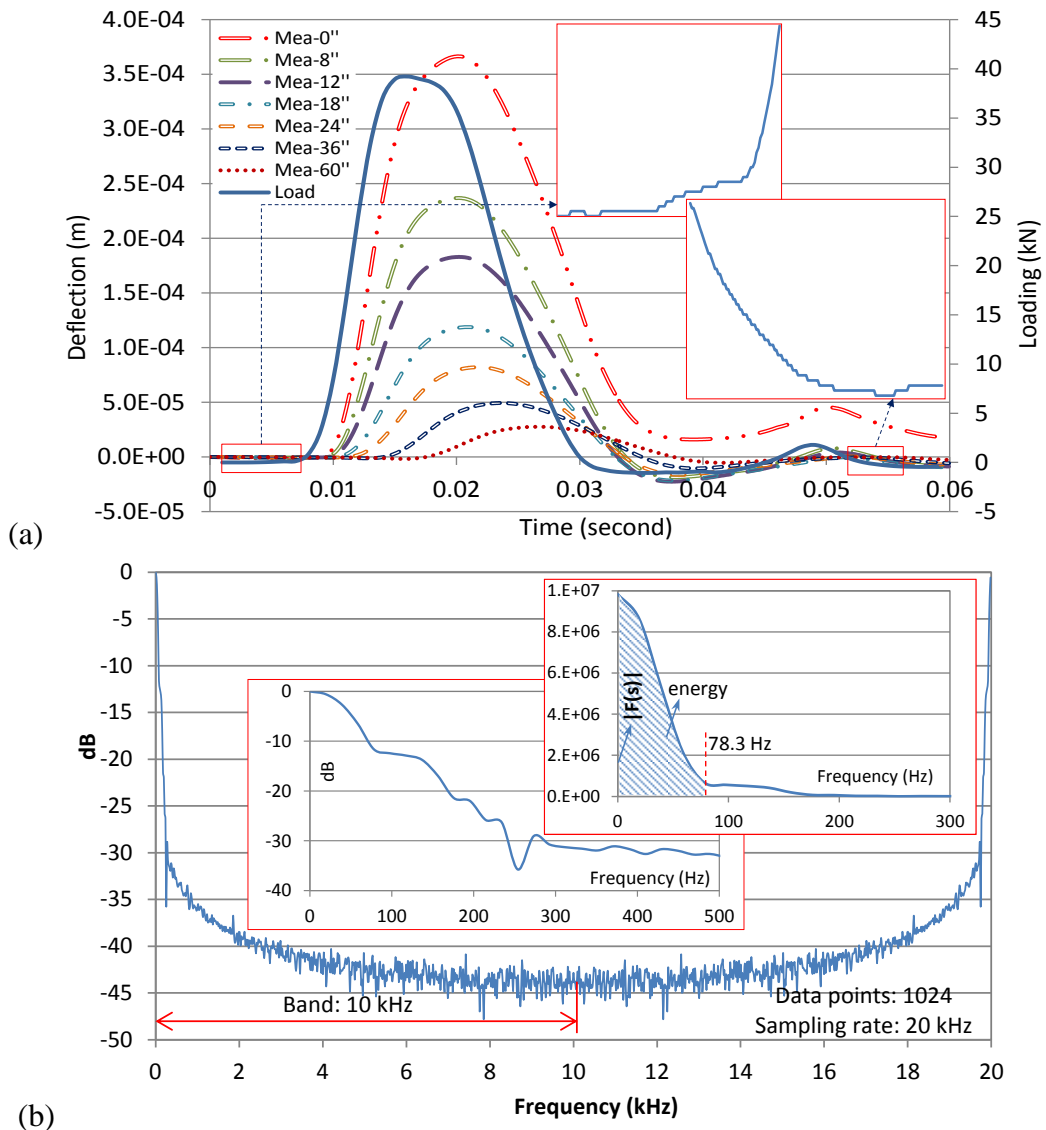


**Figure 46. (a) Time-domain FWD loading and deflection histories; (b) FFT transformed frequency-domain spectrum of loading pulse.**

### 3.6. Results and Analysis

#### 3.6.1 Model validations

##### 3.6.1.1 Pavement structure and material properties

The same pavement structure for the FWD testing is used for model validation. The top AC layer is considered viscoelastic. The MEPDG software (ARA 2004) Level 1 design proposed the stress-dependent elastic moduli model — 3 —  $k$  model — for

unbound materials, but this model has not yet been validated for user application in the software. Other research has considered the stress dependency of unbound material moduli (Kim 2007). According to common pavement analyses and design methods (Huang 2003, AASHTO 1993, ARA 2004), the unbound materials could be considered linear elastic for response modeling. In this research, the stress dependency of moduli for a short-period of loading time is not taken into account. Rather, two improvements are proposed: 1) the frequency-dependent viscous damping is added (in contrast to the dynamic viscoelastic analytical model developed by Lee 2013), and its effect will be discussed later; 2) the space dependency of moduli at depth (caused by moisture variation) is incorporated. The depth-dependent elastic moduli and damping are assigned to the base, subbase, and soil, and named  $E_b(z)$ ,  $E_{sb}(z)$ ,  $E_{soil}(z)$  and  $c_b$ ,  $c_{sb}$ ,  $c_{soil}$ , respectively (see **Figure 40**).

Figure 47 presents the model parameters including the given layer thickness, material density and Young’s moduli, which are default values falling within the regular range of the national Long-Term Pavement Performance (LTPP) database (FHWA 2012). The relaxation modulus of AC material is attained from a laboratory test on one SuperPave mixture. Note that these properties may not represent the true values, but they do not jeopardize the theoretical validation as discussed in the following.

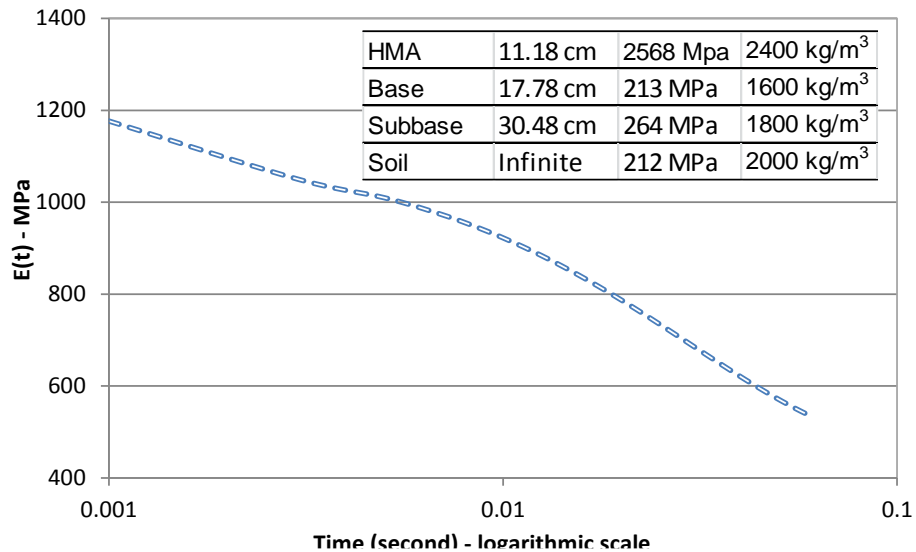


**Figure 47. Pavement structure and material properties – trial values.**

The Poisson's ratio of AC material can be temperature-dependent. Lee (1976) attained the Poisson's ratios of 0.24 at 10 °C and 0.46 at 42 °C based on laboratory tests on a few samples. Kassem et al. (2013) showed that AC's Poisson's ratio increases with time under the direct tensile testing, with slight changes only at the beginning and then remains constant under compressive relaxation testing. Within a very short period of loading time, temperature variation is negligible, and therefore, constant Poisson's ratios of 0.35, 0.40, 0.45, and 0.45 are used for AC, base, subbase, and soil, respectively (Huang 2003). This assumption has also been made by many other pavement modeling (Al-Qadi et al. 2009).

The shear and bulk relaxation moduli are not measured at the laboratory and actually no protocol is available to specify this testing on AC material. Therefore, the shear and bulk relaxation moduli could be determined as follows (Christensen 1982):

$$G(s) = \frac{E(s)}{2(1+\nu(s))} \quad (3-67)\text{-a}$$

$$K(s) = \frac{E(s)}{3(1-2\nu(s))} \quad (3-67)\text{-b}$$

where  $\nu(s)$  is Poisson's ratio and  $s$  is the Laplace transform term. As  $\nu(s)$  is regarded constant in this model,  $G(t)$  and  $K(t)$  could be calculated using the same equation by replacing  $s$  term with time term  $t$  (Christensen 1982).

### 3.6.1.2 FE model

To determine the finite model and element sizes, first the FE linear elastic simulation results were compared with those calculated by the well-known multilayer analysis program — ELSYM5 (Kopperman et al. 1986), until achieving almost identical results at multiple locations with multiple modulus and geometry inputs. Consequently, a sensitivity analysis was conducted: 1) the simulated deflections showed minimum changes when increasing the element and model size for the dynamic viscoelastic modeling; and 2) the stress wave propagation did not “hit” the boundaries at the end of the loading time (e.g., the compressive wave propagated 52.5 meters in the AC material for a loading period of 0.05 seconds at an estimated speed of 1,050 m/s [ $V = \sqrt{E/\rho}$ ]).

The sensitivity analysis of element size was also performed by using variable element size. As a result, an element size of 5.58 cm and node distance of 2.79 cm for an 8-node element at the loading zone and geophone positions resulted in almost identical deflection results as that of an element size of 1 cm and node distance of 5 mm. Therefore, a node distance of 2.79 cm was used for those critical regions. Graded meshes are used, and at far fields the mesh size is coarse. The model has a dimension size of 168.64 m (radius)  $\times$  147.71 m (depth). It consists of a total eight-node element number of 492 and node number of 1,583 with a half-bandwidth of 255. Existing research studies typically used a smaller model size for pavement structure (e.g., 3.05 m by 4.57 m as used by Howard and Warren (2009) for higher computing efficiency purpose). However, this study illustrates that a larger model size is essential for greater numerical accuracy in modeling the dynamic problem in order to avoid the “rebound” of stress waves at boundaries. Komvopoulos and Yang’s (2006) research also indicated that it is necessary to avoid the effects of dilatational waves after they have been detected from the artificially meshed boundaries.

A verification of time step length was also conducted. A time step length of 0.001 second (total 59 time steps) was reduced to 0.00005 second (total 1180 time steps, the smallest time step length from most FWD test data). Results indicate that the peak deflection was reduced 2.3% for the first sensor location on the surface of pavement while deflections at other sensor locations are almost identical, but computation time was increased 19 times. To consider the computation efficiency, a time step length of 0.001 second was adopted, which will also be used in the inverse computation module as discussed in Chapter 4.

### **3.6.1.3 Validation results**

Figure 48 presents simulated peak deflections at those seven geophones (various distances) as compared to the ELSYSM 5 analytical solutions for the linear elastic model. The results show an almost identical match. Various Young’s modulus values, geometry sizes, and loading magnitudes were used and all achieved very close matches to the

ELSYM 5 calculation results. The initial model and element sizes were determined from this validation.

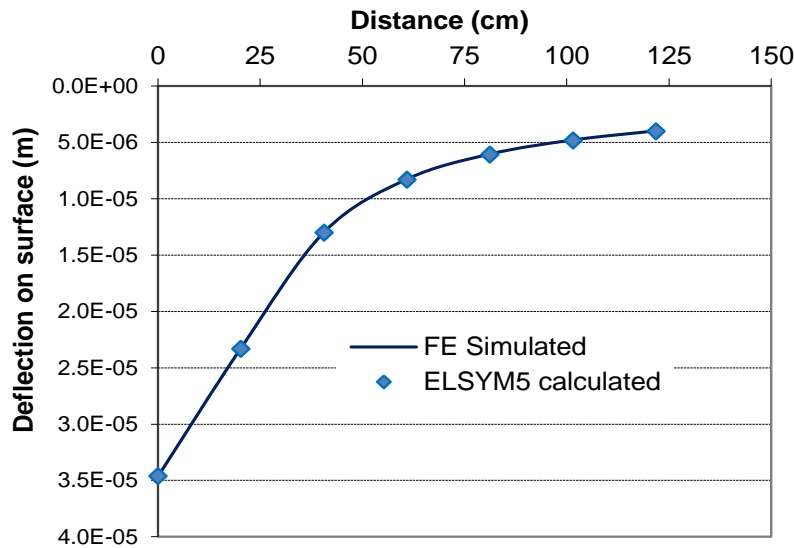
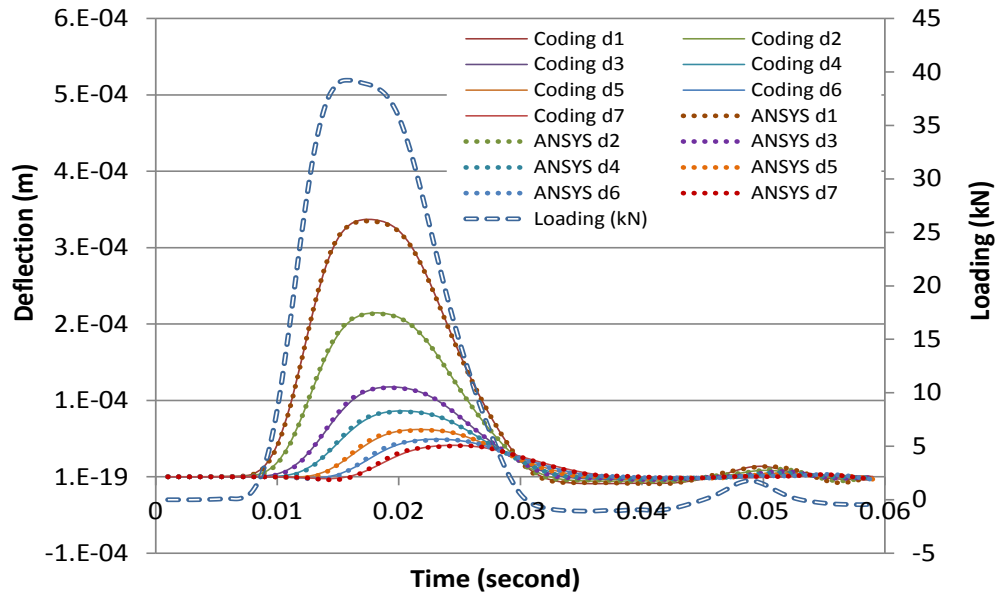
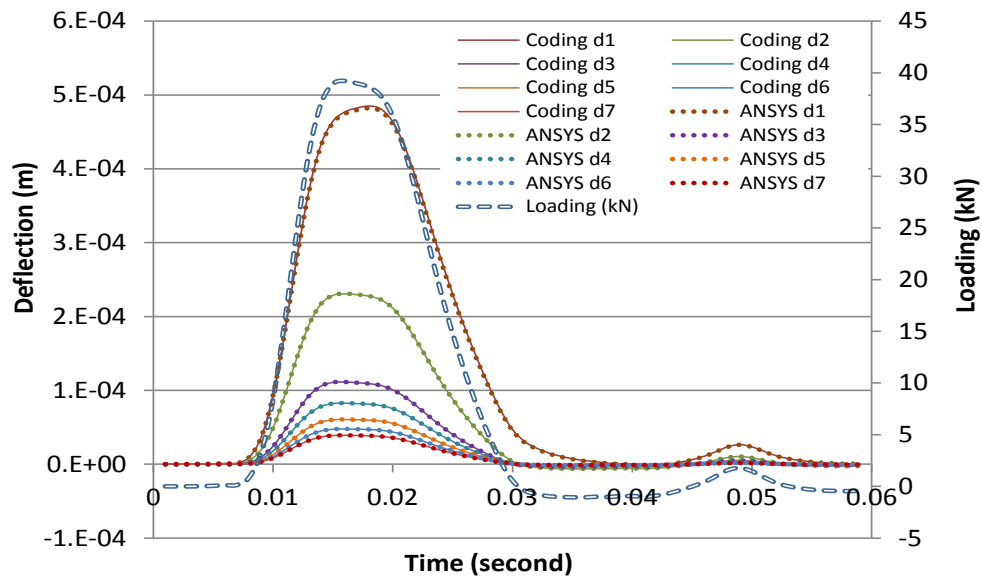


**Figure 48. FE simulated peak deflections vs. ELSYM 5 calculations of a static elastic model.**

Consequently, the commercial ANSYS software Version 14.5 (2013) was used for validation, employing exactly the same model as that of the developed FE method (i.e., exactly the same mesh and model sizes, node number and coordinate, loading pattern and time steps, material models, and boundary conditions). Figure 49 plots the coding of modeled results and ANSYS simulations together for the dynamic elastic, static viscoelastic, and dynamic viscoelastic models at FE node distances of 0.00, 22.11 cm, 43.42 cm, 57.63 cm, 78.95 cm, 100.26 cm, and 121.58 cm, respectively. From these graphs, it is difficult to visually identify any obvious differences. However, some minor gaps exist at or before the peaks (i.e., gaps at the peak of distance zero of the dynamic viscoelastic model, see Figure 49c). The minor difference may be explained by the different algorithms used for each specific aspect. For example, the space discretization of Gaussian point locations used in ANSYS are unknown to users, and ANSYS uses the Newmark algorithm for time step discretization rather than the Houbolt method adopted in this research.



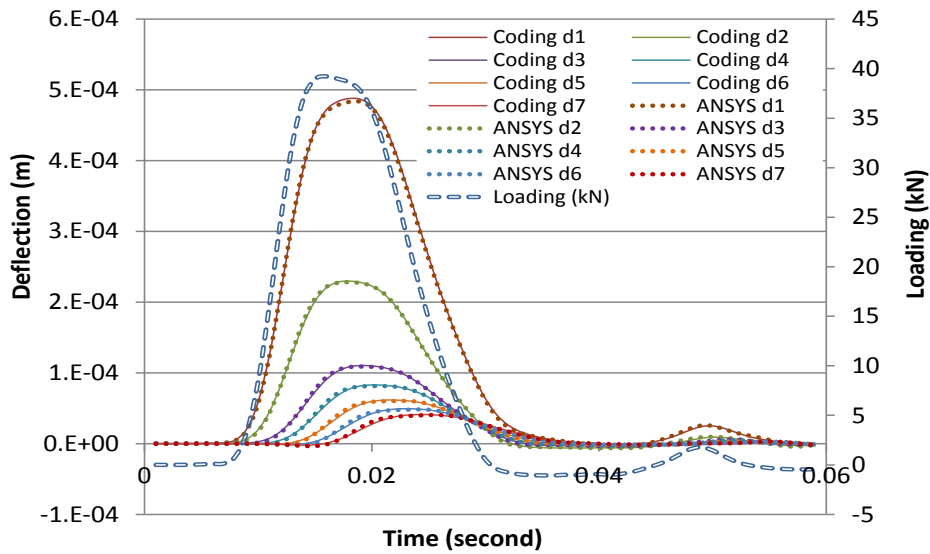
(a) dynamic elastic model



(b) static viscoelastic model

**Figure 49. Coding modeled results vs. ANSYS simulations.**

(Note: “Coding di” is the coding modeled deflection at the  $i^{th}$  distance, “ANSYS di” is ANSYS simulated deflection at the  $i^{th}$  distance)



(c) dynamic viscoelastic model

Figure 49. Coding modeled results vs. ANSYS simulations (continued)

### 3.6.2 Simulations of FWD testing

#### 3.6.2.1 Deflections

Since material parameters such as elastic moduli are unknown, different material model values within reasonable ranges based on the LTPP database (FHWA 2012) were tried in order to achieve simulation results closer to the measurements. Damping ratios of pavement materials are usually less than 10% as indicated by Seed (1984). According to the literature review (by Seed et al. 1984; Zhong et al. 2002), it is reasonable to assume damping ratio values between 0 and 10% for regular pavement materials. Using a frequency range determined from the FWD loading spectrum analysis and following Equation (3-7), the Rayleigh damping model parameters were determined. Table 9 presents the final material model parameters. Some other researchers reported Rayleigh damping coefficients. Ju and Ni (2007) used the Rayleigh coefficients of  $\beta \in [3.17 \times 10^{-4}, 1.54 \times 10^{-3}]$  for soil. It was found that simulation results are very sensitive to  $\beta$  but not sensitive to  $\alpha$ , as the determinant of stiffness matrix (for  $\beta\mathbf{K}$ ) is far larger than that of the mass matrix (for  $\alpha\mathbf{M}$ ).

Simulation results indicate that only the dynamic viscoelastic model considering damping could achieve very close match for measurements at all seven geophones.

**Table 9. Material model parameters**  
**(a) AC - generalized Maxwell model parameters**

|                |          |          |          |          |          |          |          |
|----------------|----------|----------|----------|----------|----------|----------|----------|
| Moduli (MPa)   | 2.56E+03 | 1.76E+03 | 3.04E+03 | 3.63E+03 | 3.28E+03 | 6.19E-06 | 4.14E-03 |
| $\eta$ (MPa.s) | 1.53E+00 | 1.62E-05 | 2.27E-09 | 1.91E-01 | 3.06E-03 | 7.68E-10 | 1.91E-08 |

**(b) Unbound materials model parameters**

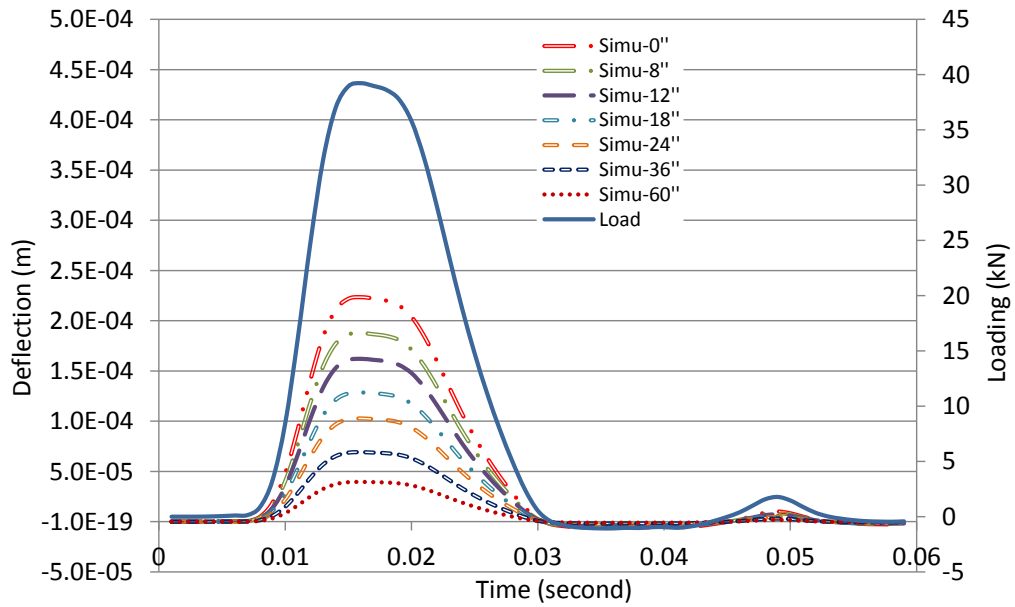
| Layer                           | Base     | Subbase  | Soil     |
|---------------------------------|----------|----------|----------|
| Moduli (MPa)                    | 300      | 230      | 175      |
| Rayleigh damping $\alpha$ (1/s) | 3.20E-04 | 6.19E-04 | 1.52E-03 |
| Rayleigh damping $\beta$ (s)    | 5.14     | 7.02     | 6.03     |

**(c) Density and Poisson's ratio**

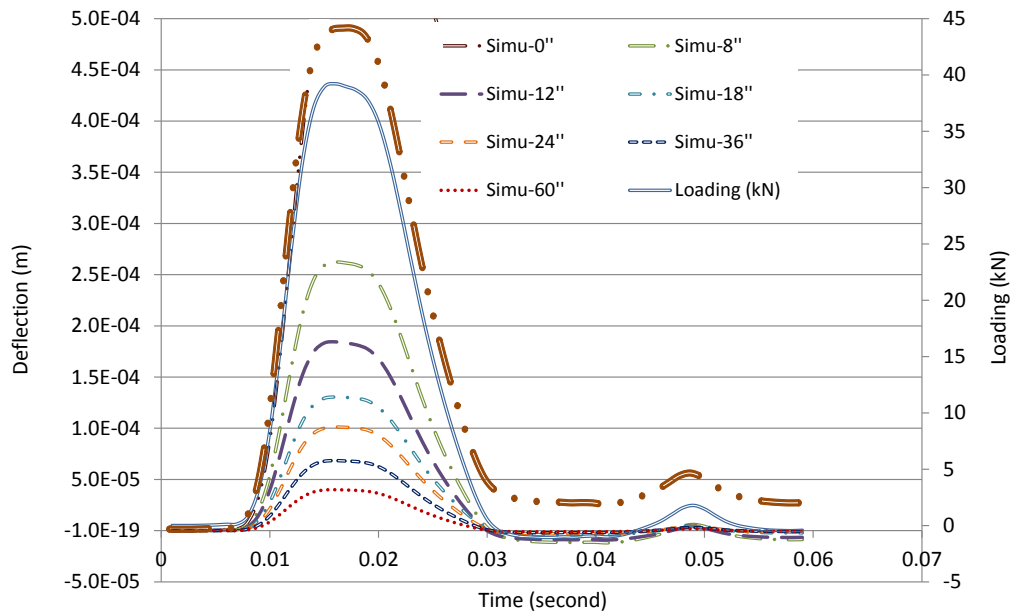
| Layer                        | HMA  | Base | Subbase | Soil |
|------------------------------|------|------|---------|------|
| Density (kg/m <sup>3</sup> ) | 2400 | 1900 | 1800    | 1600 |
| Poisson's ratio              | 0.35 | 0.35 | 0.35    | 0.40 |

Figure 50 presents simulated results of deflections for the static elastic model vs. static viscoelastic model: both nullify the dynamic inertia and Rayleigh damping. Figure 51 presents dynamic elastic model with damping vs. dynamic elastic model without damping: both nullify all dashpots and leave only the elastic springs in the generalized Maxwell model (see Figure 40).

Figure 50 clearly shows that the static elastic model has significantly lower deflection values than the static viscoelastic model, primarily at the loading position. However, one should note that for the static elastic model all dashpots are annulled and the material elastic modulus equals to the sum of those for springs. Results also show that compared to the dynamic elastic model (Figure 50b vs. Figure 51), the static viscoelastic model produces higher deflections, which also remain positive during the “rest” time after the major loading curve. This clearly indicates the contribution of material’s creep behavior of viscosity. However, at far fields (e.g., 60 inches or 152.4 cm) their differences are minor because deflections at that distance are vastly dependent on the moduli of unbound layers such as soil foundation (Huang 2003). Figure 51 indicates that without considering damping, a time offset exists when compared to results where damping is factored in. Compared to the static elastic model, the dynamic elastic model’s deflection value is slightly lower due to lost kinetic energy (Figure 50a vs. Figure 51).



(a) Static elastic



(b) static viscoelastic modeled deflections

Figure 50. Static modeled deflections.

Note: Simu-0": simulated deflection at 0-inch distance, and so on; Mea-0": FWD measured deflection at 0-inch distance, and so on.

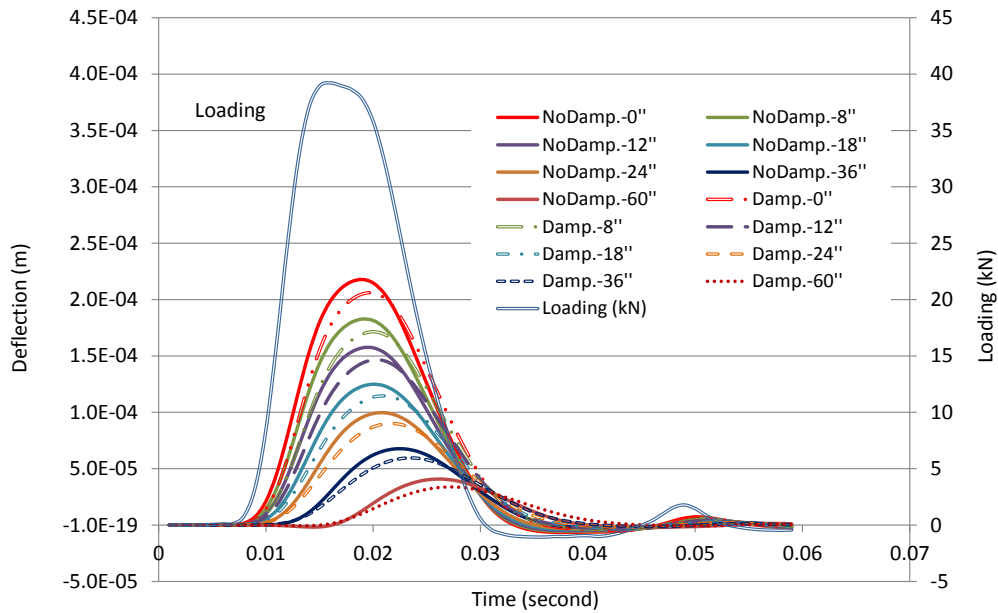
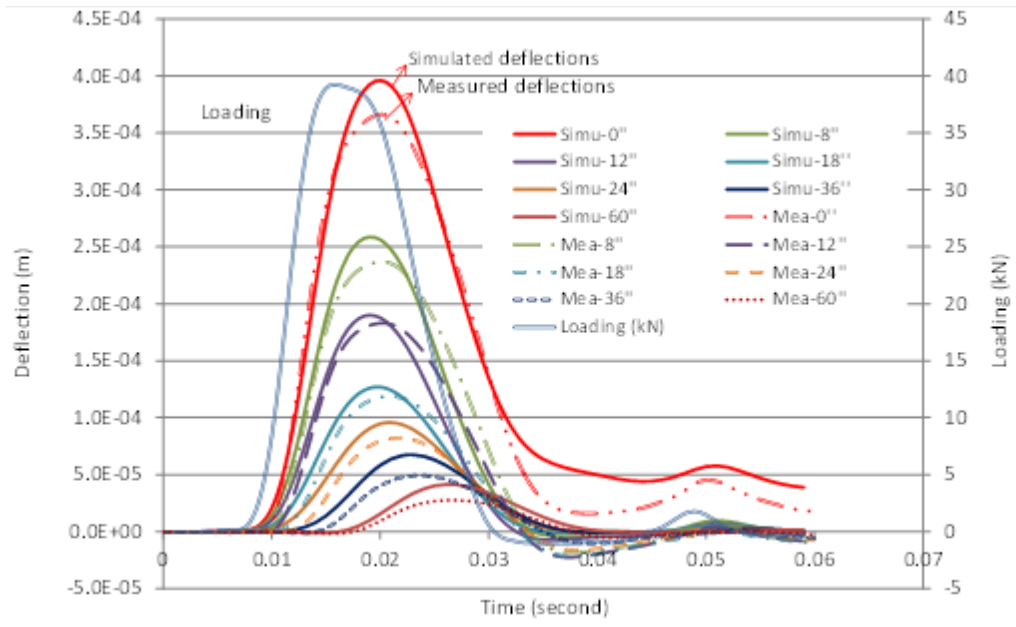
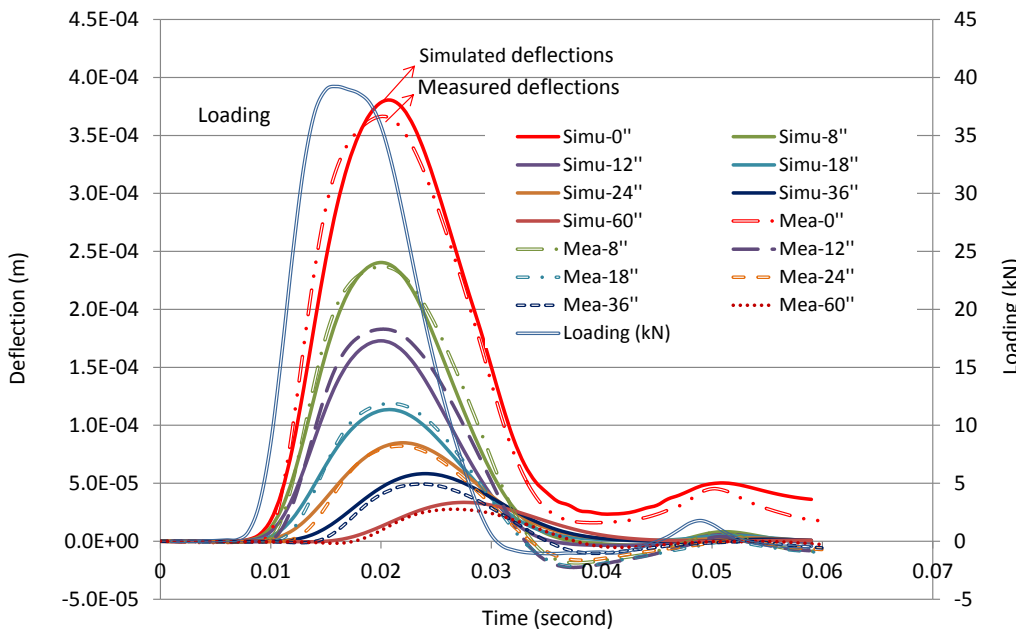


**Figure 51. Dynamic elastic modeled deflections with and without damping.**

Figure 52 presents the dynamic viscoelastic simulations as compared to the FWD measured deflections without and with considering damping, respectively. Again, without considering the damping effect of materials, it clearly shows that simulations always have a time offset (i.e., 0.003 seconds behind for the peaking deflection) and gapping as compared to measurements (see Figure 52a). Ayadi et al. (2012) also confirmed the damping effect on each pavement layer. Figure 52b indicates a fairly good match of simulation results to measurements, indicating that both structural dynamic response and material viscoelastic behavior contribute to material deformations.



(a)



(b)

**Figure 52. Dynamic viscoelastic model simulation results vs. measurements: (a) without considering damping; (b) with consideration of damping.**

Figure 53 presents the contour of displacement at the depth or  $z$  direction at 0.023 seconds. Results indicate that the largest deflection (negative to the  $z$  direction) always appears on the surface under loading. A small “up” deflection (positive to the  $z$  direction and opposite to the vertical loading direction) appears on or close to the surface area and

quickly propagates to far fields with time indicating a small resonance of waves rebounded from the layer interfaces.

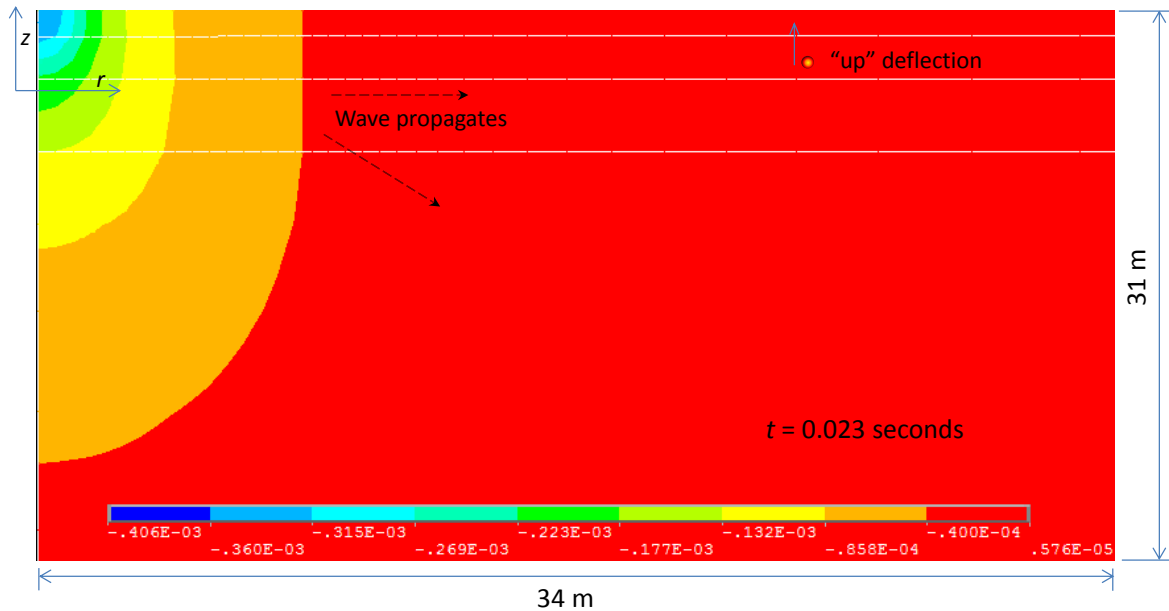


**Figure 53. Vertical displacement ( $t = 0.023$  second).**

### 3.6.2.2 Velocity and acceleration

Figure 54 and Figure 55 plot the velocity and acceleration contours at the last time step ( $t = 0.059$  s), respectively. Figure 56 plots the vertical velocity and acceleration on the top of AC at a distance of 0 and 15 meters. Results show that the velocity (absolute value) follows the tangent of the displacement pattern. First it increases and then decreases to zero at the peak-displacement time, and then repeats this pattern in a reversed direction. Meanwhile the acceleration follows the tangent of velocity. The peak velocity at 0.013 seconds corresponds to the zero acceleration. Apparently at a further distance (e.g., 15 m, Figure 56) the acceleration and velocity drop significantly when displacement magnitude starts becoming “flatter.”

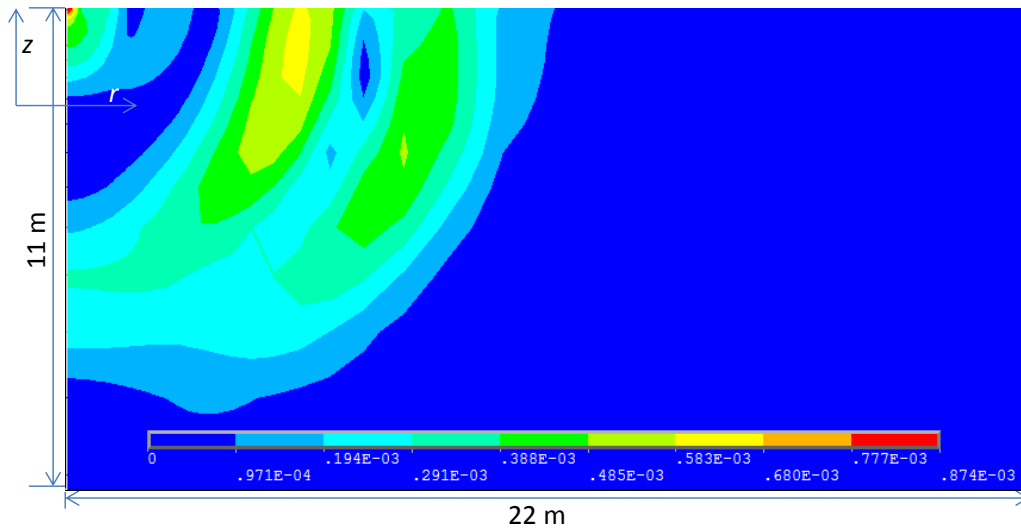


**Figure 54. Velocity (m/s) of depth direction at the end of time period (0.059 second).**

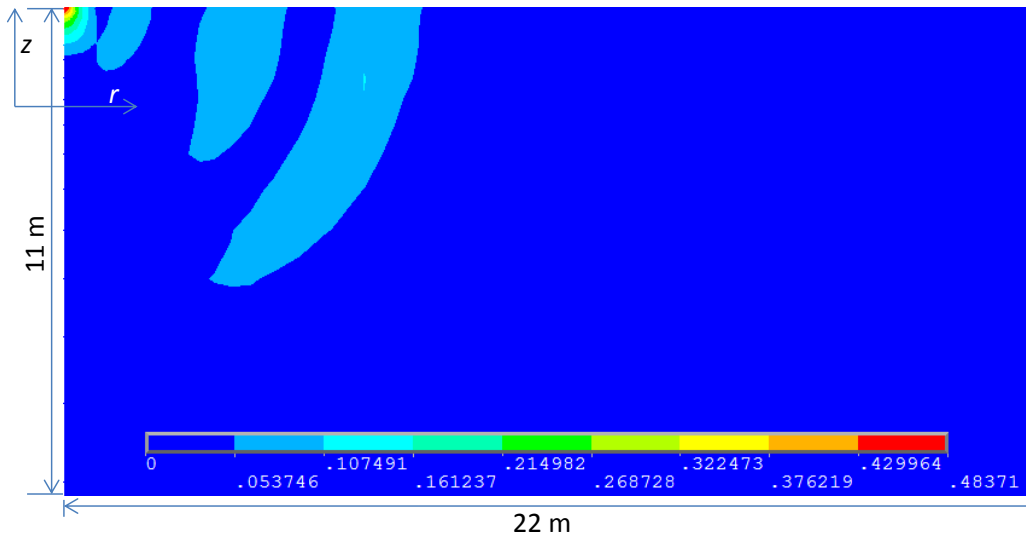


**Figure 55. Acceleration (m/s<sup>2</sup>) of depth direction at the end of time period (0.059 second)**

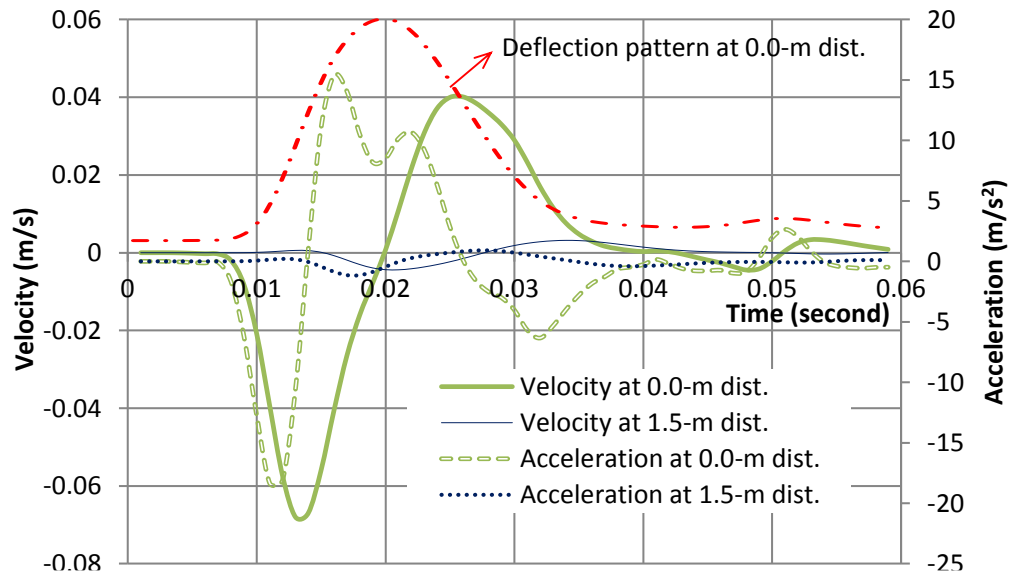


**Figure 56. Simulations of velocity and acceleration on the top of AC of depth direction for distances of 0 m and 1.5 m from loading.**

### 3.6.2.3 First principal stress

In pavement design, the tensile stress of the AC layer and associated cracking is one of the major concerns. Figure 57 presents the contour of the first principal stress of the AC layer at time length. It shows that the maximum tensile stress mostly appears at the bottom of the AC layer at the loading center during the major loading time, and vanishes after the loading is dropped when stress waves are propagated to far fields.

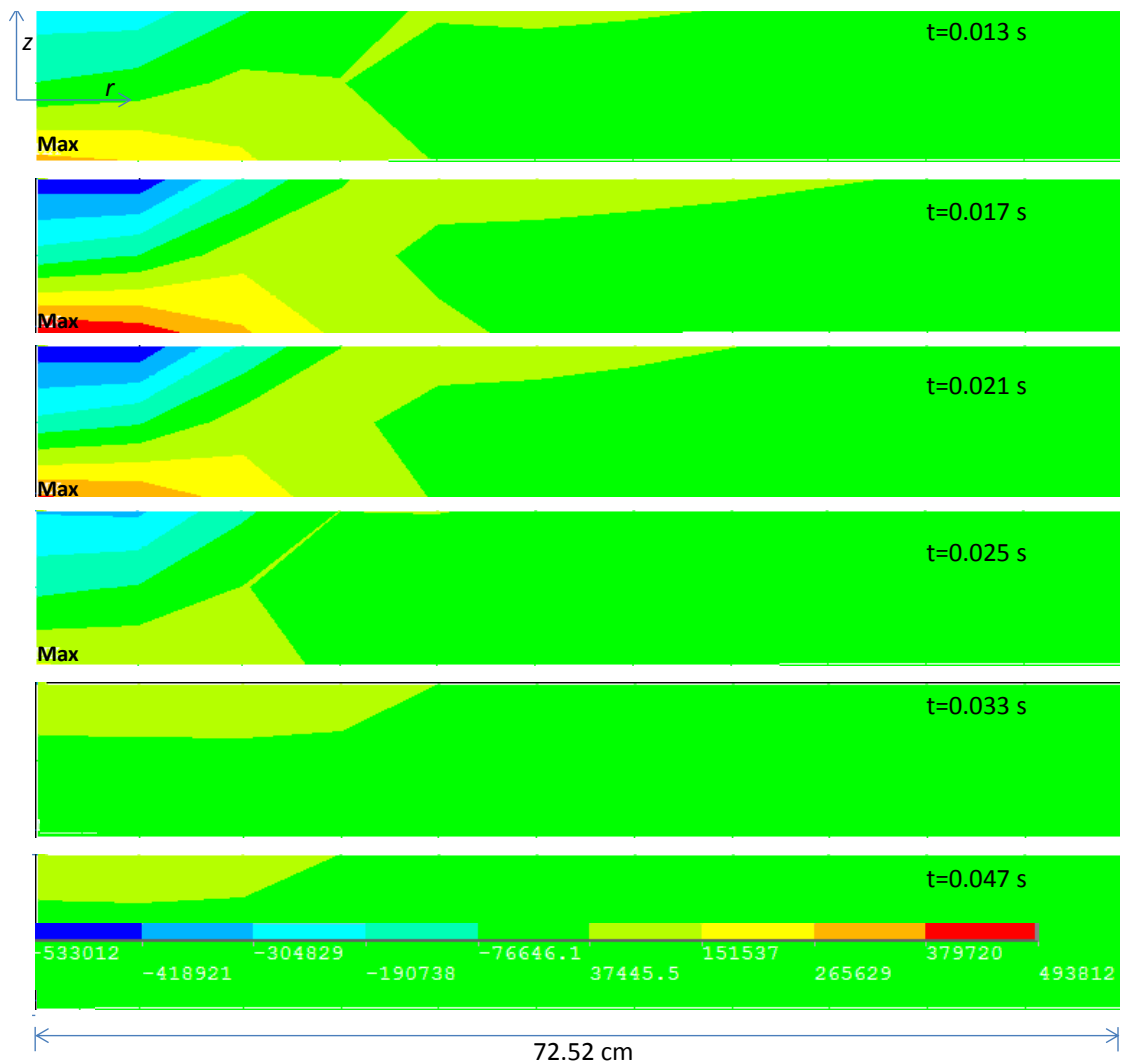


**Figure 57. First principal stress of AC layer at time length (MPa).**

### 3.6.3 Simulations of vehicle loading

#### 3.6.3.1 Deflections

FWD loading pattern could be very similar to or somehow different from the vehicle loading pattern depending on the pavement structure and vehicles. Huang (2003) suggested simulating the vehicle loading pulse using a sin-based function (i. e.,  $f(t) = A_0 \sin^2\left(\frac{\pi t}{t_d}\right)$ ). Figure 58 presents one vehicle loading pulse emulated from Huhtala's measurement (1986), and simulated deflection responses as applied to the same pavement structure with the same material properties presented above. The vehicle loading has

amplitude of 40 kN, half of a standard vehicle single axle loading (80 kN), the same as that of the FWD loading. As compared to the FWD loading pulse, it produces higher peak deflections (i.e., 15.6% higher at the loading position), but shorter time offsets of deflections to loading. This phenomenon could be explained by the loading patterns since FWD loading takes about 0.01 second to rise from zero to the peak value, while vehicle loading takes about 0.02 seconds. The fast ramping of loading consumes more kinetic energy due to dynamic inertia and damping effect, while a slower ramping of loading or a longer loading time produces higher deflections due to the AC material's creep behavior. As with the FWD modeling results, deflections primarily at the loading position remain positive when loading is dropping to zero, and will slowly drop to zero if given sufficient "rest" time.

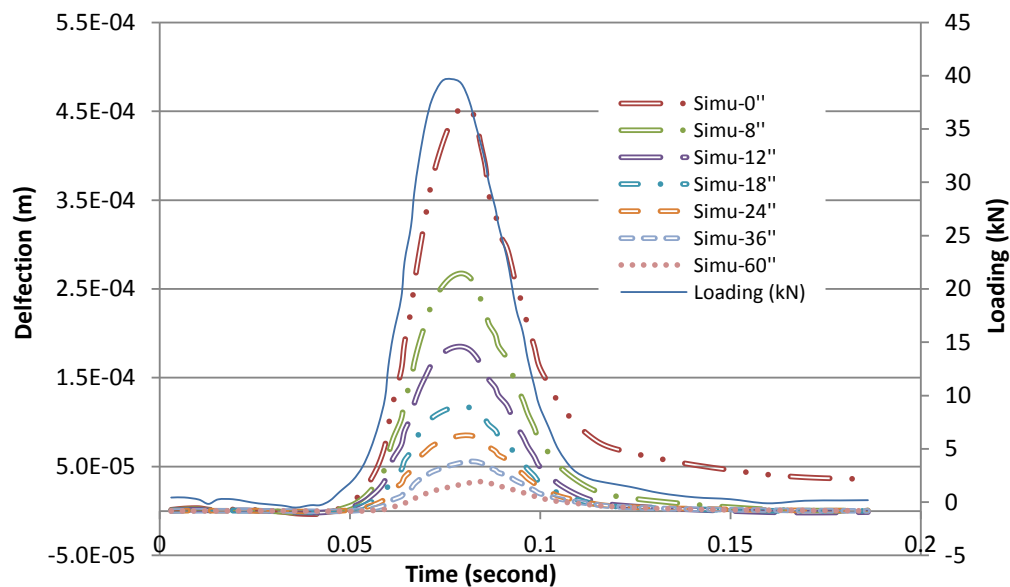


**Figure 58. Vehicle loading pulse and simulated dynamic viscoelastic deflections.**

### 3.6.3.2 Stress and strain

Figure 59 presents the radial stress of pavement structure profile under the loading center at a few time steps. Results clearly show that the vast majority of radial stresses occur within the AC layer primarily due to its much higher material modulus than those of other layers. Max values appear at the bottom and on the top of the AC layer from

opposite directions, and they change from tension/compression (bottom/top) to compression/tension (bottom/top) with time increase.

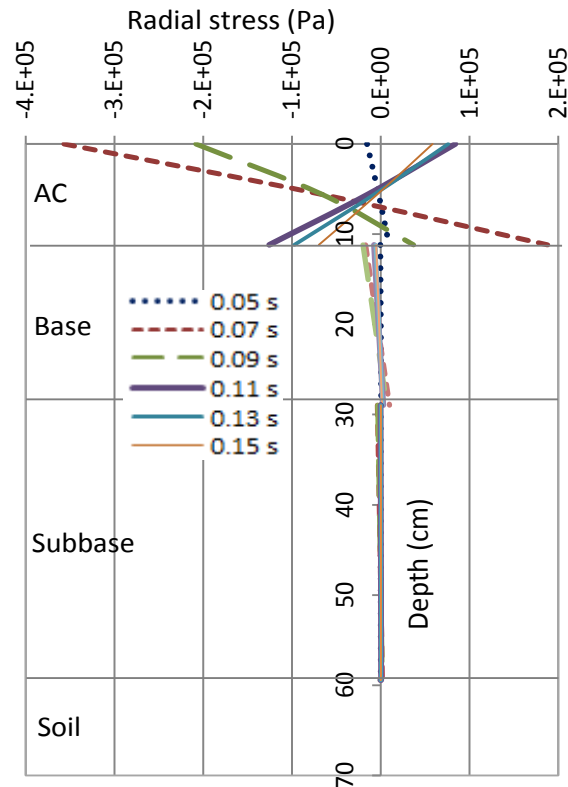


**Figure 59. Radial stress profile of pavement structure (dynamic viscoelastic model).**

**Figure 60** and **Figure 61** plot the radial stress and radial strain of the AC layer at time length for the dynamic elastic model and dynamic viscoelastic model, respectively. As the radial stress is dependent on both the radial strain and hoop strain (i.e.,  $\sigma_{rr} = \frac{E}{(1+\nu)(1-2\nu)} [(1-\nu)\epsilon_{rr} + \nu\epsilon_{zz} + \nu\epsilon_{\theta\theta}]$ ), it is not surprising to see that the direction of radial stress could be opposite to that of the radial stain, such as those observed at the middle position of the AC layer. Results show that the viscoelastic property has significantly changed the stress-strain patterns: 1) radial stress reaches the peak and then drops to zero, and reaches the second peak on the opposite direction, and then returns back to zero again (see **Figure 61**); 2) the first peak radial stress appears in advance of the peak loading, which may be explained by the stress relaxation, and 3) the dynamic viscoelastic model produces obviously lower peak radial stress but higher peak radial

strain than that of the dynamic elastic model, due to its stress relaxation and creep deformation, respectively. This has clearly shown the influence of material viscoelasticity on structural responses.

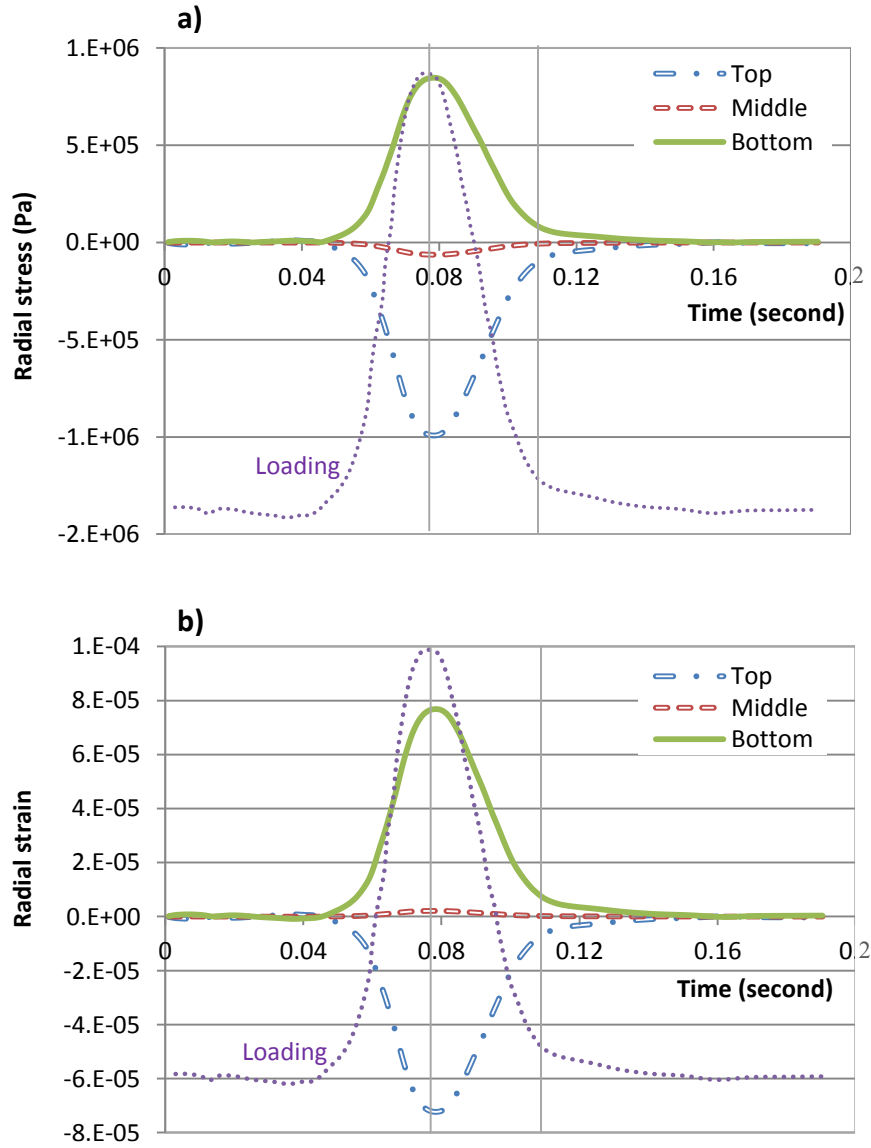


**Figure 60. Simulated radial stress and strain of AC layer using dynamic elastic model.**

Note: positive values mean tension, and negative values mean compression.

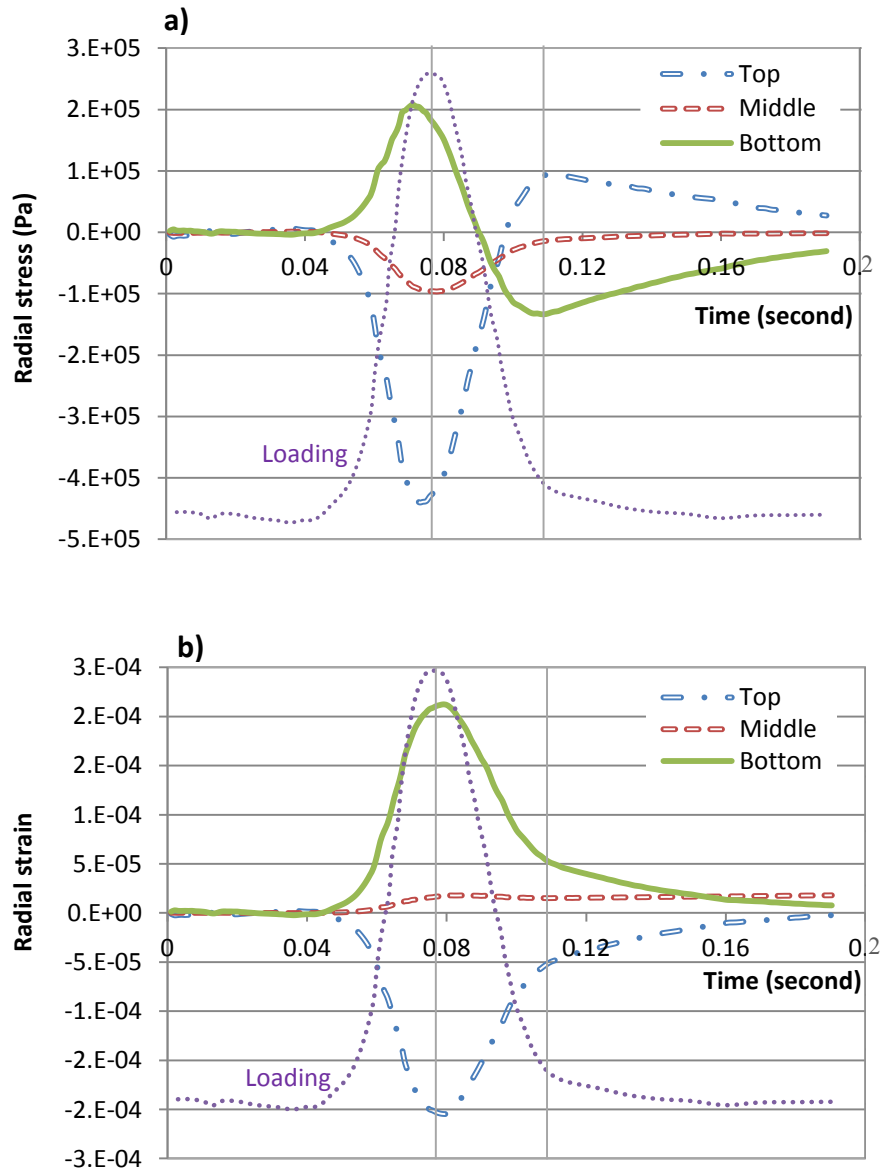


**Figure 61. Simulated radial stress and strain of AC layer using dynamic viscoelastic model.**

Note: positive values mean tension, and negative values mean compression.

### 3.6.4 Temperature and moduli profiles

Using the same pavement structure, material properties, and loading input presented in Section 3.6.2 as the control model, a temperature profile with  $T \in [25.5^\circ\text{C}, 55.5^\circ\text{C}]$  according to the LTPP database (FHWA 2012) is applied to the AC layer (see Figure 62). The majority of pavement depths have lower temperature values

than the uniform control temperature of 40°C. The WLF model (parameters attained from Xu 2007) induces a variable temperature-time superposition shift factor. Simulation results indicate that deflections primarily at the positions under loading or nearby have decreased (e.g., the peak deflection at the loading position decreases 11.85%). This is obviously due to AC material's temperature-dependency of viscoelasticity.

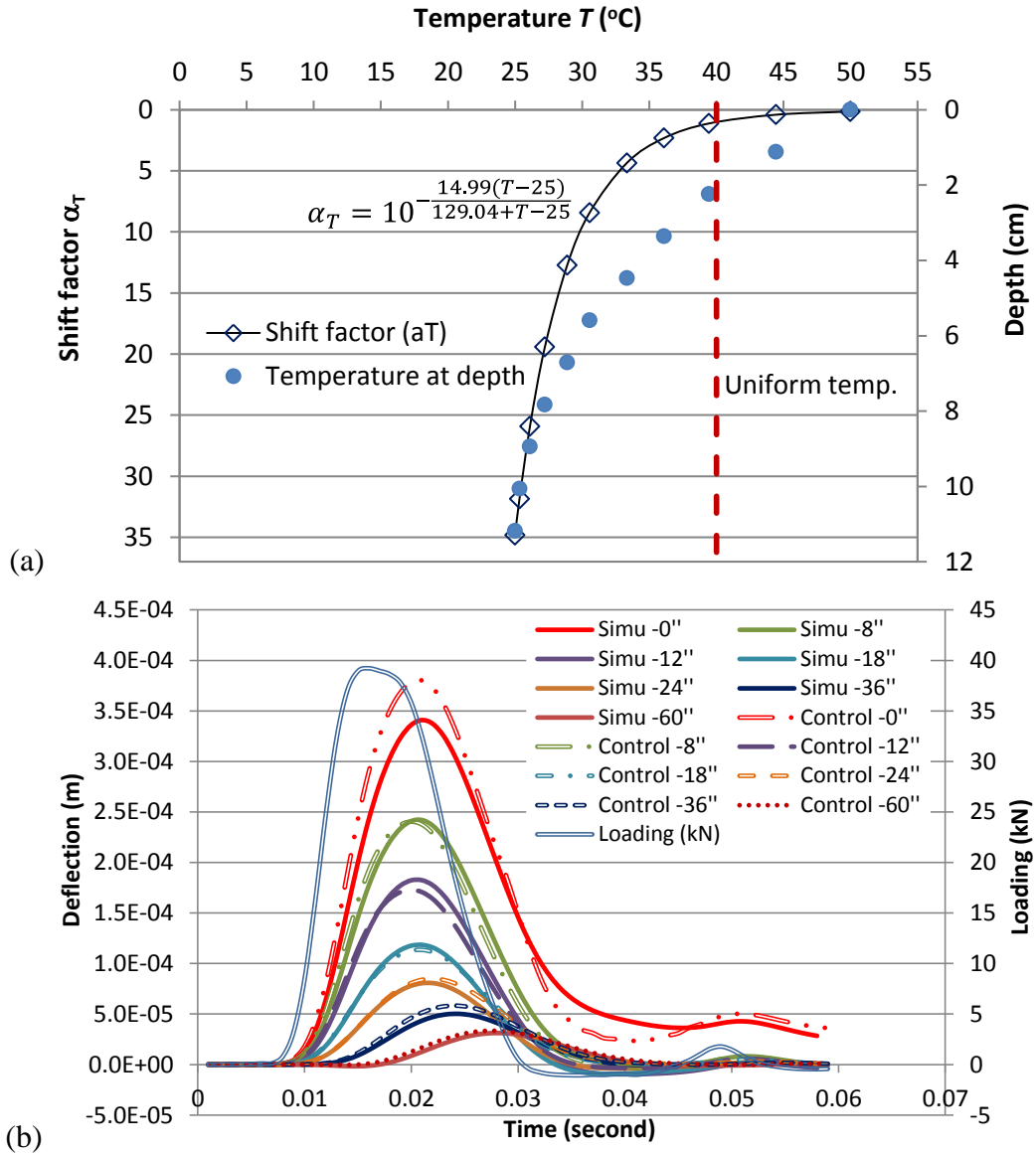
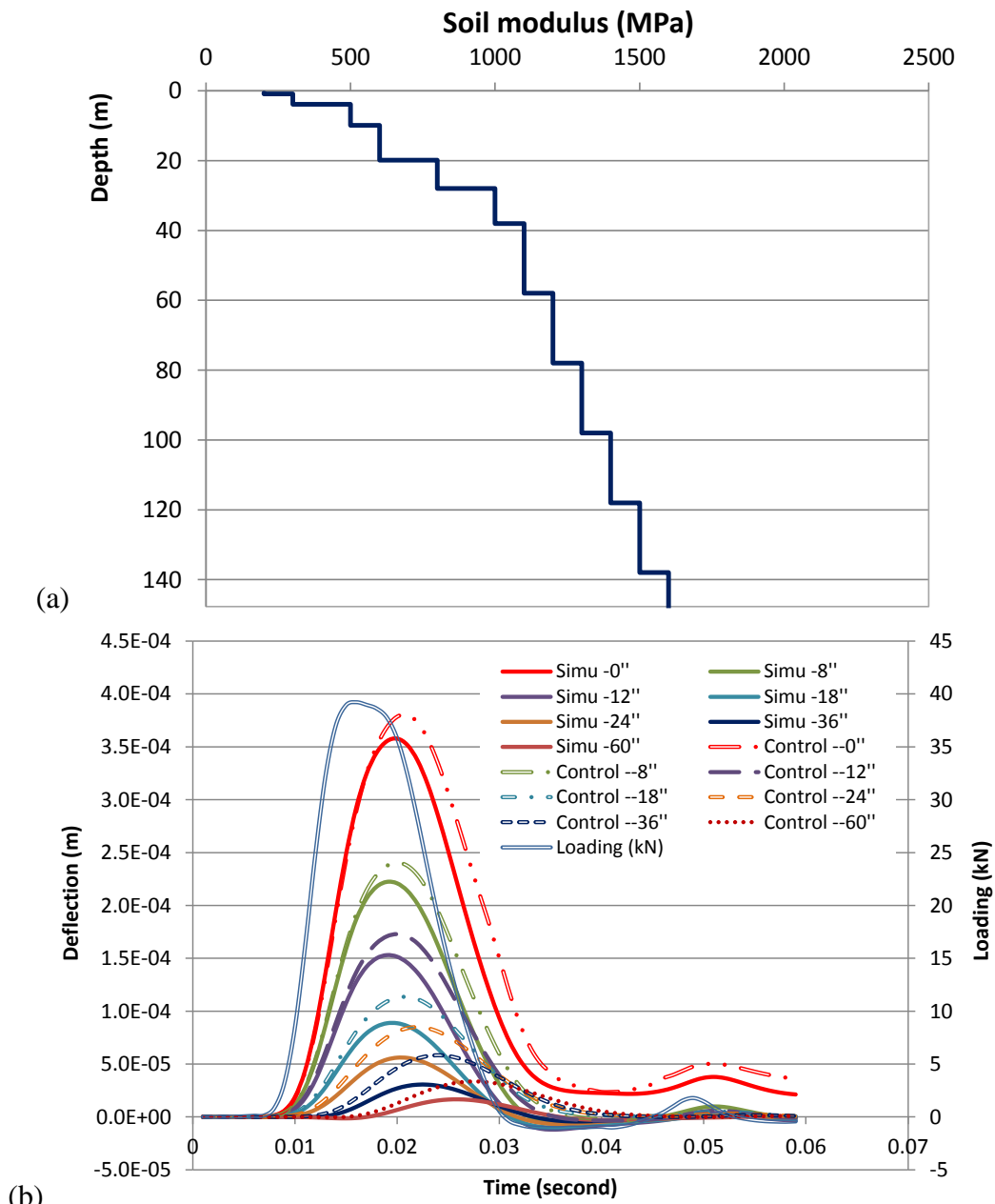


Figure 62. (a) Temperature profile of AC layer and  $\alpha_T$ ; and (b) simulated deflections vs. control ones at the reference temperature of 40 °C.

Figure 63 presents a case study for variable moduli profile of soil foundation. The soil moduli may increase with depth (Nazarian et al. 1987; Aouad 1993) due to the moisture variation at depth or bedrock. As estimated from the Spectrum Analysis of Surface Waves (SASW) measured wave velocities at depth (Aouad 1993), the modulus of soil in this case is varying from 200 MPa (the control uniform value) to 1,500 MPa with a depth of 147.12 meters (see Figure 63a). As results, simulated deflections at all seven geophone distances were reduced (see Figure 63b), since the support becomes stronger at deeper depth. Note that the contribution of moduli increase has also been “compensated” by the influence of deeper depth, thus a lesser reduction of deflections as compared to that of moduli values is observed.



**Figure 63. (a) Moduli profile of soil foundation and (b) simulated deflections.**

### 3.7. Summary

This chapter developed a time-domain finite element (FE) model and Galerkin-based numerical solution method for simulating dynamic viscoelastic responses of the layered half-space under loading pulses. A computer code written in FORTRAN was developed for the numerical computation and validated by analytical solutions and

numerical modeling. It was implemented to a flexible pavement structure on soil foundation under both the FWD and vehicle loadings. The AC layer was modeled by the generalized Maxwell model, and unbound materials (base, subbase, and soil) were considered damped and elastic.

- As compared to most existing computer methods for the (layered) half-space, the developed approach represents a more comprehensive model, accounting for the coupled dynamic loading, damping effects, and material's viscoelastic behavior over time. The model was implemented into a flexible pavement structure on soil foundation. Results indicated that a dynamic viscoelastic model that includes damping could better simulate the measurements than the dynamic elastic or dynamic viscoelastic model, which does not include damping, which has often been the practice up until now. Dynamic inertia primarily contributes to the time offset, and the damping further adds up this effect and “reduces” deflection value. The material viscoelastic behavior can also significantly contribute to the deflection magnitudes and shapes or patterns.
- A combined Houbolt central and forward finite differences method is proposed for time discretization of velocity and acceleration which reduces the time-step length while achieving numerical accuracy. The global layered stiffness matrix considering coupled dynamic and damping, and viscoelastic properties was formulated in this research and stored in a banded format for solving the global linear system with the factorization method, which saves storage space and computer speed.
- The developed model and computer method is also able to simulate two critical environment-associated conditions: 1) the temperature profile at depth; and 2) the space dependency of moduli profile at depth. Results have shown that these variable properties could significantly affect structural response values.
- Displacement, velocity and acceleration, and stress and strain are computed and analyzed, which fosters understanding of a layered infrastructure and its structural dynamic response and material viscoelastic deformation.

- The developed model and computer method could serve as a potential means to advance structural analysis and design methodology. For example, it may be used as a computation module to help improve the MEPDG method for pavement structure analysis, which calculates responses based on a static elastic approach to approximate the dynamic viscoelastic problem.
- It could also be used for other laminate and disk structures at different time and length scales.

The developed dynamic viscoelastic solution is used as a module for the inverse computation, and it is a primary topic of discussion in the next chapter.

## **Chapter 4: A Lagrangian Optimization Method for Inverting Dynamic Moduli of Multilayer Systems**

This chapter developed a Lagrangian optimization and numerical solution method to invert the material dynamic moduli of multilayers for application to flexible pavements under FWD testing. The developed forward response model in Chapter 3 serves as one module of the inverse computation. The Lagrangian function was formed as a cost function (objective function plus regularization term) constrained by the partial differential equation (PDE) governing state equation. The generalized Maxwell model simulates the time-dependent material viscoelasticity under a dynamic loading resource. The first- and second-order state, adjoint, and decision equations of the Lagrangian were formed to compute the response (see Chapter 3), test function, gradient vector, and Hessian matrix. Given gradient and Hessian inputs, the Armijo rule was modified for finding a stable step length for inverting material model parameters. A time-domain finite element method was developed for numerical solutions of PDEs, and unique mathematical derivations were formulated to solve this specific dynamic viscoelastic inverse problem for the multilayer systems. A computer code written in FORTRAN language was developed to implement the entire numerical computation. Compared to most existing “two-stage” inverse approaches used for multilayer systems, the proposed and now developed method successfully integrated inverse computation and forward modeling into one Lagrangian function: 1) it improves numerical accuracy and computation speed by deriving both the precise gradient and Hessian; and 2) it can more reliably invert a larger scale of model parameters. The numerical method was implemented to a multilayer pavement structure under the falling weight deflectometer test. With measurement inputs of loading pulse and deflection time history, the frequency-dependent dynamic moduli master curve and material viscoelastic properties were inverted and validated. The method was implemented to a few field tests including one site with FWD measurements conducted 10 times for the four seasons throughout the same year.

## 4.1. Background

Dynamic modulus  $E^*$  is the ratio of stress over strain under vibratory conditions (i.e.,  $E^* = \frac{\sigma_0 \sin(t\omega + \delta)}{\epsilon_0 \sin(t\omega)}$ ).  $E^*$  is a characterization of material viscoelastic (VE) property, which can decompose into the storage modulus (the real or elastic part) plus the loss modulus (the imaginary or viscous part) as  $E^* = E' + iE''$ . For viscoelastic materials, stress and deformation rate are dependent on time and temperature (Xu and Solaimanian 2009; Motamed et al. 2013). Multilayer systems displaying the VE property exist widely in the contexts of engineering and human life at different length scales, including human tissues such as the skin (Cobb 2004) and arterial walls (Gu et al. 2013), polymer-based high-molecular structures (Tronto et al. 2013), memory foams, multilayer circuits, multilayer pavements with polymer-modified asphalt concrete (AC) surface, and airplane multilayer bodies with polymer-coated surfaces as shown in Figure 64.

The material properties, including the elastic modulus and VE property, play a crucial role in a subject's deformation, response, performance, and risks. For example, VE plaques cause blockages of arterial lumen (Hossain et al. 2012). Infrastructure pavements with AC typically exhibit rutting or permanent deformation and fatigue cracking under repeated loading, which are dependent on the material's VE property (Xu and Solaimanian 2009). Pavement rutting is one of the main causes of hydroplaning-associated traffic accidents (see Figure 64-e). In order to safely perform material and structural design of multilayer systems, a complete understanding of dynamic VE properties is important.

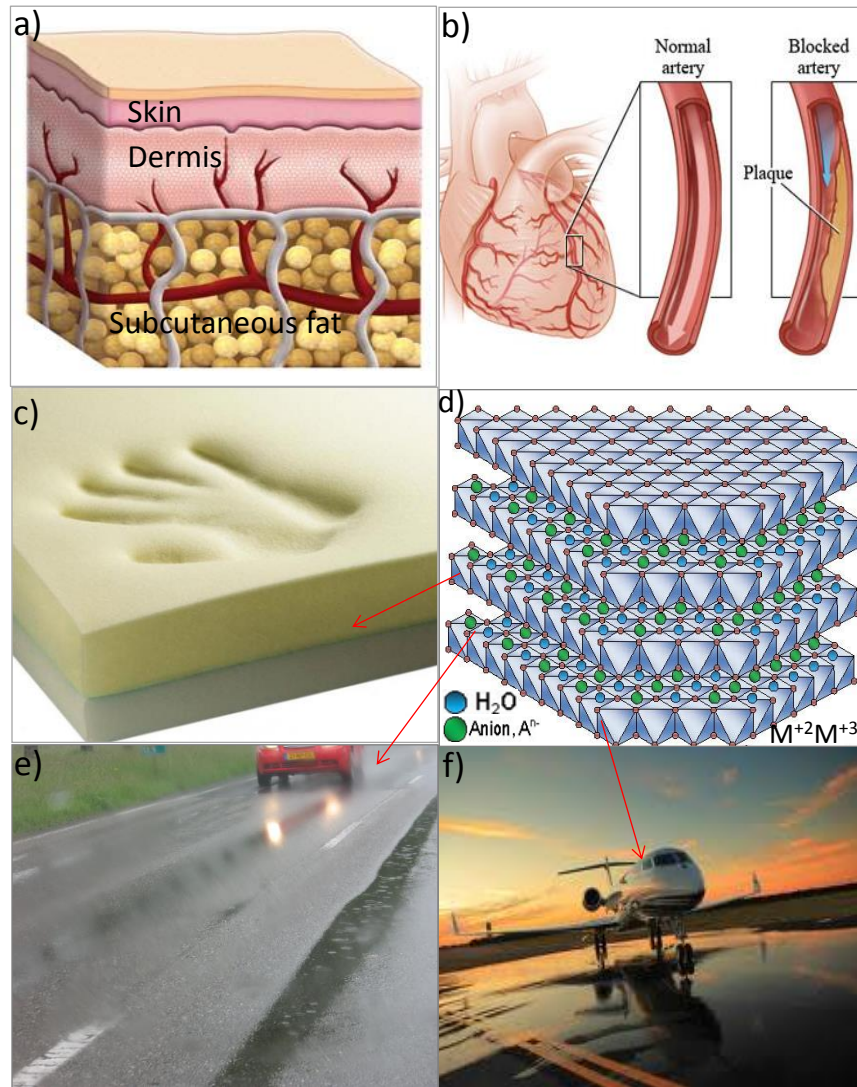


**Figure 64. Viscoelastic multilayer systems at variable length scale: a) human layered tissues (Cobb 2004); b) a heart's artery wall (Xiong et al. 2013); c) a memory foam mattress (<http://thememory-foam-mattress.blogspot.com/>); d) a layered polymer molecular structure (Tronto et al. 2013); e) polymer-modified-asphalt pavement (Courtesy of M. M. Minderhoud); f) an airplane with polymer modified multilayer coating was landing on a multilayer airport runway (Courtesy of Tanner Wugange).**

To monitor health conditions, nondestructive tests have been employed to measure responses by applying a loading source. Inverse computations using the response data collected from such tests can predict or estimate material properties—including dynamic moduli and VE properties—without directly measuring them. More often the

inverse computations generally involve two steps: 1) simulating structural responses (e.g., deflections on the surface) under a load to emulate nondestructive tests; and then 2) minimizing the error function of the differences between response simulations and measurements—or observations—using a mathematical optimization algorithm to estimate appropriate material properties. Here, this is referred to as a two-stage approach.

Inverse computations of multilayer systems have been studied in engineering and science including biology and the polymer materials sciences. Catheline et al. (2004) used the wave-propagation-based experimental data with an inverse method to estimate the VE properties of a membrane. Brigham et al. (2007) used the SMARS approach (a combination of a classical random search algorithm plus the neural networks-based method) to invert the VE material properties of solids immersed in fluids. Lei and Szeri (2007) and Zhao et al. (2009) developed a two-stage approach to invert the material hyperelastic and VE properties of biomaterials, where the forward responses were computed using ABAQUS and the inverse computation was based on the Levenberg-Marquardt algorithm embedded in MATLAB. Araújo et al. (2009) used a gradient-based optimization technique with the Gauss-Newton algorithm (presented by Herskovits et al. 2004) and a minimizing error function (based on the difference between experimental vibration data and finite element (FE) modeling results) to invert the linear VE properties of a sandwiched structure. Sims et al. (2010) used an inverse FE method to determine the VE properties of subcutaneous fat by combining ANSYS (for forward computations) and MATLAB (for the inversion of the nonlinear least square fit rooting algorithm). Giavazzi et al. (2010) inverted the VE skin parameters with the FSQP (Feasible Sequential Quadratic Programming) algorithm coupling FE modeling for response computations (method presented by Yuung-Hwa et al. 2006). Araújo et al. (2010) studied a constrained minimization problem, in which gradient-based optimization techniques were employed to invert the five-parameter-based VE fractional derivative models.

Within the multilayer pavements on roads, parking lots, and airports, researchers have widely studied inverse computation—or backcalculation—of material properties. Often, plate-load tests—such as the falling weight deflectometer (FWD) testing, in which

a load is dropped onto the subject's surface—are performed to collect data of loading pulse and deflections. Most of these backcalculation studies have focused on the elastic moduli of the layers, which is an essential parameter for structural analysis and design. Various optimization algorithms have been developed or implemented, including the Newton-Raphson method (Harichandran et al. 1993), the system identification method (Wang and Lytton 1993), the Kalman filter method (Choi and Pestana 2006), the non-linear least square method (Sivaneswaran et al. 1991), the probabilistic method, (Hadidi and Gucunski 2010), and neural network model (Meier et al. 1997), among others. Some backcalculation programs have accounted for the dynamic loading effects of backcalculating materials' elastic moduli (Foinquinos et al. 1993, Wang 1993, Uzan 1994, Kang 1998), and some have accounted for the damping property (Fernando and Liu 2002, Loizos and Scarps 2005, Broutin and Theillout 2010). Magnuson et al. (1991), Magnuson and Lytton (1993), and Uzan (1994) backcalculated creep compliance of AC material using a mathematical power function with three model parameters. Liang and Zhu (1998) used the dynamic analysis to backcalculate the fatigue parameters of the AC material. Scarpas and Blaauwendraad (2002) backcalculated the complex modulus of AC materials using the four-parameter Burgers model. More recently, Kutay et al. (2011) backcalculated the master curve of the “dynamic modulus” (the absolute values only) using the five-parameter mathematical sigmoidal function model and a linear elastic analysis to approximate dynamic loading effects. Levenberg (2012) used the min-max optimum approach for inverse computation of a two-parameter VE model—elastic modulus combined with viscosity for the pavement structure. Varma et al. (2013) presented a genetic algorithm for inverse analysis of VE properties of asphalt mixture.

Base on this study's thorough literature review, the research problems are summarized as follows:

i) Typically, a two-stage approach—response forward modeling and then inverse computation—is used for inverse computation of multilayer material properties, including those discussed above—the FE modeling and MATLAB inverse combined method developed by Zhao et al. (2009) to invert the VE properties of biomaterials. In

inverse computation, the gradient of an objective function with respect to inverse parameters is often calculated. Xu and Prozzi (2014) developed a two-stage approach to invert the temperature-dependent moduli of multilayers, where the responses were modeled using the forward FE method, and then the gradient was estimated using the modeled responses for each material model parameter, as follows:

$$\mathbf{g}_i = \frac{\partial u}{\partial E_i} = \frac{u(E_i + \Delta E_i) - u(E_i)}{\Delta E_i} \quad (4-1)$$

where  $u$  and  $\hat{u}$  are simulated and observed deflection responses, and  $\Delta E_i$  is modulus variation. In this method, the tangent  $g_i$  is approximated based on the modeled response results, which may reduce the numerical accuracy. Meanwhile, for each material model parameter—such as the elastic moduli of each layer material—one forward response model is required, which is more computationally expensive than the method developed in this research.

ii) For the inverse computation of layered structures such as pavements, the simplified material model is often used, including examples discussed earlier—e.g., the mathematical power law and sigmoidal functions and the four-parameter Burgers model. The mathematical power law model and sigmoidal function may offer a good fit to the experimental data, but it lacks sufficient details to describe the physical behaviors. The Burgers model—in a relatively simple format with limited model parameters—is unable to represent the full creep compliance and dynamic modulus master curve at a wider range of reduced frequency or temperature (Xu and Solaimanian 2009).

iii) The model conditions might be simplified. For example, although modeling of the layered structure under applied loading is a dynamic viscoelastic problem, either the material nonlinear behavior or the dynamic loading effects are approximated using the linear elastic approaches for some examples discussed above (e.g., Kutay et al. 2011).

iv) The VE property of a material exhibits more complex time-dependent behavior than typical functions with small selections of model parameters (e.g. the four-parameter Burgers model). Therefore, an advanced physical model is needed to describe

the material behavior. With an increased number of model parameters, the process of computation becomes more numerically expensive when using conventional two-stage approaches. Additionally, the two-stage approach may result in reduced accuracy, as numerical approximation is often used to compute the gradient (Xu and Prozzi 2014).

Accordingly, the objective of this research was to develop a Lagrangian-based optimization method and numerical solution to invert the dynamic moduli of materials within a layered system. The developed method integrated the forward modeling and inverse computation into one Lagrangian function, and mathematical formulations of gradient and Hessian on the PDEs were derived. The generalized Maxwell model in Prony series was employed to model material VE behavior, and other material components are considered elastic with damping. The developed model and numerical solution method was implemented to highway pavement structures under the falling weight deflectometer (FWD) tests. The developed method is expected to invert the material's dynamic moduli and VE property with relatively larger model parameters, thereby improving numerical accuracy and computation speed compared to the other methods discussed above.

## **4.2. Inverse Problem and Lagrangian Function**

### **4.2.1 Model Domain**

The model domain of the multilayer system for the forward and inverse problem is presented in Figure 65. On one surface area a loading source was applied for time  $t \in [0, t_d]$  where  $t_d$  is the loading period, and responses in time were measured at variable distances (e.g., displacements).

The VE property was modeled by the generalized Maxwell model made up of a parallel spring and dashpot series (see Figure 65), where the stress of the dashpot is dependent on strain rate ( $\sigma(t) = \eta \frac{\partial \varepsilon}{\partial t}$ ). The relaxation modulus and that of the shear and bulk ones for VE materials in Prony series are expressed as follows (Christensen 1982):

$$E(t) = E_\infty + \sum_{i=1}^N E_i e^{-\frac{E_i}{\eta_i} t} \quad (4-2)-a$$

$$G(t) = G_\infty + \sum_{i=1}^N G_i e^{-\frac{G_i}{\eta_{Gi}} t} \quad (4-2)-b$$

$$K(t) = K_\infty + \sum_{i=1}^N K_i e^{-\frac{K_i}{\eta_{Ki}} t} \quad (4-2)-c$$

where  $E_\infty$ ,  $G_\infty$  and  $K_\infty$  are Young's, shear and bulk modulus at the infinite time of  $t = \infty$ ;  $E_i$ ,  $G_i$  and  $K_i$  are the Young's, shear modulus and bulk modulus of the  $i^{th}$  spring element for  $i = 1, 2 \dots N$  where  $N$  is the total term number of spring-dashpot series;  $\eta_i$ ,  $\eta_{Gi}$  and  $\eta_{Ki}$  are viscosity, shear and bulk viscosity of the  $i^{th}$  dashpot element.

For other materials in this multilayer system under dynamic loading, their material properties are modeled by the damped elastic model.

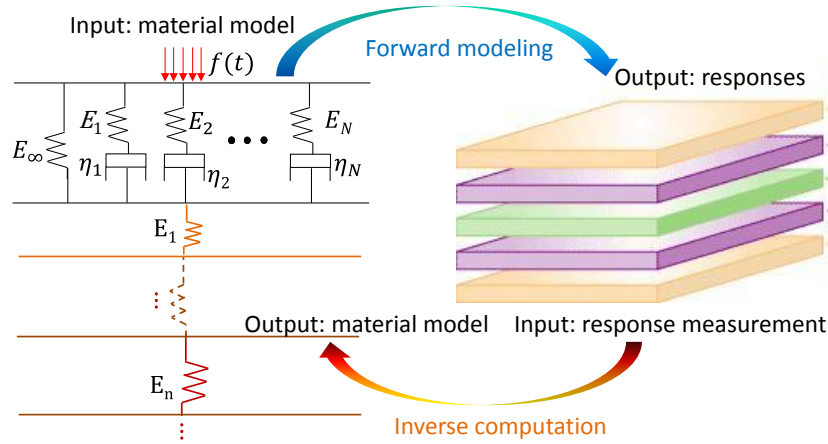


**Figure 65. Multilayer system forward and inverse computation.**

According to the stress equilibrium, the strong form of the governing state equation of the model domain can be formed as follows:

$$\nabla \cdot \boldsymbol{\sigma} + b = c \frac{\partial \mathbf{u}(t)}{\partial t} + \rho \frac{\partial^2 \mathbf{u}(t)}{\partial t^2} \quad \mathbf{u}(t) \in H^1 (\Omega \text{ in } \mathbb{R}^3 \times t \in [0, t_d]) \quad (4-3)$$

where  $b$  is the body force,  $c$  is damping of structural system and materials,  $\rho$  is material density,  $\boldsymbol{\sigma}$  is stress tensor,  $\mathbf{u}(t)$  is displacement response at time  $t$ ;  $H^1$  is a Sobolev space,  $\Omega \in \mathbb{R}^3$  is a three-dimensional (3-D) space domain and  $t \in [0, t_d]$  is the time domain.

According to the material viscoelasticity, the stress tensile  $\boldsymbol{\sigma}(t)$  can be expressed as follows (Christensen 1982):

$$\boldsymbol{\sigma}(t) = 2 \int_0^t G(t - \tau) \frac{\partial \mathbf{e}(\tau)}{\partial \tau} d\tau + 3\mathbf{I} \int_0^t K(t - \tau) \frac{\partial \varepsilon_h(\tau)}{\partial \tau} d\tau \quad (4-4)$$

where  $\mathbf{e}(\tau)$  is the deviatoric strain tensor;  $\varepsilon_h(\tau)$  is the hydrostatic strain scalar at time variable  $\tau$ ; and  $\mathbf{I}$  is the identity matrix;  $G(t - \tau)$  is the shear relaxation modulus; and  $K(t - \tau)$  is the bulk relaxation modulus. The governing state equation is subjected to the natural boundary condition or “force” equilibrium at the loading surface as follows (see Figure 65):

$$\boldsymbol{\sigma} \cdot \mathbf{n} ds = f(t) \text{ on } \partial\Omega_4 \times [0, t_d] \quad (4-5)$$

The essential boundary conditions satisfy the following (see Figure 65):

$$u = \hat{u}_i(t) \text{ on } \partial\Omega_i \times [0, t_d] \quad (4-6)$$

where  $\hat{u}_i(t)$  is the displacement on the  $i^{th}$  boundary area  $\partial\Omega_i$ .

The response outputs can be defined as:

$$u = \hat{u}_5(t) \text{ on } \partial\Omega_5 \times [0, t_d] \quad (4-7)$$

where  $\hat{u}(t)$  is the displacement response outputs in the area of  $\partial\Omega_5$ .

Following the Galerkin method, by applying a test function on both sides of the governing state equation and then integrating with time and space domains, the weak form of the governing state equation can be formed as follows:

$$\int_0^{t_d} \int_{\Omega} \boldsymbol{\sigma} : \nabla \mathbf{p}(t) d\Omega dt + \left[ \int_0^{t_d} \int_{\Omega} c \frac{\partial \mathbf{u}(t)}{\partial t} \cdot \mathbf{p}(t) d\Omega dt + \int_0^{t_d} \int_{\Omega} \rho \frac{\partial^2 \mathbf{u}(t)}{\partial t^2} \cdot \mathbf{p}(t) d\Omega dt \right] - \left[ \int_0^{t_d} \int_{\partial\Omega_4} f(t) \cdot \mathbf{p}(t) ds dt + \int_0^{t_d} \int_{\Omega} b \cdot \mathbf{p}(t) d\Omega dt \right] = 0 \quad (4-8)$$

#### 4.2.2 Inverse Problem

The inverse problem is formed as follows: 1) the given information includes the observed or measured loading source and response pulses in time; 2) the unknown information for inversion are the material model parameters of each layer of the

multilayer system; and 3) given the initial estimated material properties as seeds, the inverse computation—an iterative procedure—is conducted to estimate material properties including the VE properties and the elastic moduli of each layer (see Figure 65).

### 4.2.3 Cost Function

Inverse computation is an iteration procedure used to determine the optimal material model parameters, applied at each iteration step in order to find the material properties that minimize the differences between response observations and the modeling results. The objective function (a scalar) is defined as follows:

$$f(m) := \frac{1}{2} \int_0^{t_d} \int_{\partial\Omega_5} (\mathbf{u} - \mathbf{u}_{obs})^2 ds dt \quad \mathbf{u} \in H^1(\Omega \times [0, t_d]) \quad (4-9)$$

where  $\mathbf{u}$  is a simulated response (e.g., displacement);  $\mathbf{u}_{obs}$  is observation at the surface area of  $\partial\Omega_5$  (see Figure 65);  $H^1$  is a Sobolev space of functions vanishing on  $\partial\Omega$  with square integrable derivatives. Multiple solutions may exist (Xu and Prozzi 2014); thus, here a regularization term is proposed to penalize or limit the range of material properties. The cost function is formed as a sum of the objective function plus the regularization term:

$$J(m) := \frac{1}{2} \int_0^{t_d} \int_{\partial\Omega_5} (\mathbf{u} - \mathbf{u}_{obs})^2 ds dt + \frac{\gamma}{2} \int_{\Omega} (1 - \chi_{(m_1^*, m_2^*)}^m) (m - m^*)^2 d\Omega \quad \mathbf{u}, m \in H^1(\Omega \times [0, t_d]) \quad (4-10)$$

where  $\gamma$  is a regularization parameter;  $m$  is the material model parameter function;  $m^*$  is the material model parameter range for penalization, and  $m^* = (m_1^*, m_2^*)$ , which is estimated based on engineering practice (see Table 6 presented in Chapter 2);  $\chi_{(m_1^*, m_2^*)}^m$  is an identity function defined as follows:

$$\chi_{(m_1^*, m_2^*)}^m = \begin{cases} 1 & \forall m \in (m_1^*, m_2^*) \\ 0 & \text{otherwise} \end{cases} \quad (4-11)$$

#### 4.2.4 Lagrangian Function

The cost function is subjected to the governing state equation as a PDE constraint. According to the Lagrangian theory, the Lagrangian function can be formed as a sum of the cost function and governing state equation weak form, which is used to find the stationary point for inverse computing material model parameter  $m$ :

$$\begin{aligned} \mathcal{L}(\mathbf{u}, \mathbf{p}, m) := & \frac{1}{2} \int_0^{t_d} \int_{\partial\Omega_5} (\mathbf{u} - \mathbf{u}_{obs})^2 d\Omega dt + \frac{\gamma}{2} \int_{\Omega} (1 - \chi_{(m_1^*, m_2^*)}^m) (m - m^*)^2 d\Omega + \\ & \left[ \int_0^{t_d} \int_{\Omega} \boldsymbol{\sigma} : \nabla \mathbf{p}(t) d\Omega dt + \left( \int_0^{t_d} \int_{\Omega} c \frac{\partial \mathbf{u}(t)}{\partial t} \cdot \mathbf{p}(t) d\Omega dt + \int_0^{t_d} \int_{\Omega} \rho \frac{\partial^2 \mathbf{u}(t)}{\partial t^2} \cdot \mathbf{p}(t) d\Omega dt \right) - \right. \\ & \left. \left( \int_0^{t_d} \int_{\partial\Omega_4} f(t) \cdot \mathbf{p}(t) ds dt + \int_0^{t_d} \int_{\Omega} b \cdot \mathbf{p}(t) d\Omega dt \right) \right] \in \Omega \times [0, t_d] \end{aligned} \quad (4-12)$$

where  $\mathbf{u}$  (displacement),  $p$  (test function), and  $m$  are three “independent” variables of the Lagrangian function.  $\mathbf{p}$  may also be called as Lagrangian multiplier.

### 4.3. Inverse Computation Method

#### 4.3.1 Optimality Conditions

To find material parameter  $m$  using the Lagrangian function, the optimality conditions shall be satisfied for the inverse procedure. Here, both the first order necessary and second order sufficient conditions were imposed for optimality (Nocedal and Wright 2006):

First order necessary condition (also called Karush–Kuhn–Tucker [KKT] condition) states: Suppose that  $m$  is a local minimizer and  $\mathcal{L}$  is continuously differentiable in an open neighborhood of  $m$  then, the gradient is zero ( $\nabla \mathcal{L}(m) = 0$ ).

Second order sufficient condition states: Suppose that the Hessian matrix ( $\nabla^2 \mathcal{L}$ ) is continuous in an open neighborhood of  $m$ ; if  $\nabla \mathcal{L}(m) = 0$  and  $\nabla^2 \mathcal{L}(m)$  is positive definite, then  $m$  is a strict local minimizer of  $\mathcal{L}$ .

The first order necessary condition finds the stationary point, including those local stationary points where the tangents are ideally zero. The second order sufficient condition is to assure that the stationary point is the strict local minimum.

## 4.3.2 Inverse procedures

### 4.3.2.1 Framework

The inverse computation is an iterative procedure in which the material model parameters are updated at each iteration step as an evolving procedure until reaching an optimal point at which the numerical error (the difference between response observations and modeling results) is small enough.

Figure 66 shows the flow chart of the numerical inverse computation procedures. The inputs include the model geometry, loading sources, and initial guessed material model seeds. Responses (e.g., deflections) are computed given the initial conditions. The root mean squared value (*RMS*) of deflection difference between measurements and simulations is calculated as follows:

$$RMS = \sqrt{\frac{\sum_{i=1}^N \sum_{j=1}^L \left( \frac{u_{ij} - u_{obs,ij}}{u_{obs,ij}} \right)^2}{LN}} \quad (4-13)$$

where  $u_{ij}$  is the response values at the  $i^{th}$  time step (total  $N$ ) and  $j^{th}$  location (total  $L$ ).

If the *RMS* is lower than the allowable error limit (e.g., 5%) then the iteration stops and outputs the material model parameters as the inverse computed ones; otherwise, the iteration continues. The gradient vector and then the Hessian matrix are computed. Given gradient and Hessian values, the inverse search direction and step length are determined as will be discussed later. Then the material model parameter values are updated as follows:

$$m_k = m_{k-1} + \alpha_k \tilde{m}_k \quad (4-14)$$

where  $m_{k-1}$ ,  $m_k$  is the material model parameter computed at the  $(k-1)^{th}$  and  $k^{th}$  iteration step and the initial value  $m_0$  could be any estimated value (e.g.,  $m^*$ );  $\tilde{m}_k$  is the search direction at the  $k^{th}$  iteration step; and  $\alpha_k$  is the step length at the  $k^{th}$  iteration step as used to adjust the search direction value.

Given the updated material model parameters at the  $k^{th}$  iteration step, the  $RMS$  can be recomputed, and the iteration continues until  $RMS$  is lower than the permitted error when the updated material model parameters are considered acceptable inverse results.

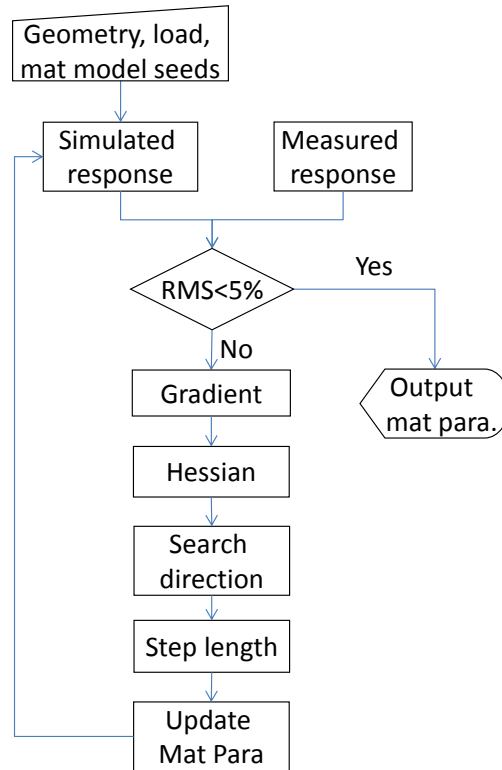


**Figure 66. Flow chart for the numerical inverse computation**

Figure 67 demonstrates an example of an objective function  $f(x, y) = x^2 - y^2$   $\forall x \in (-10, 10) \times y \in (-10, 10)$  used to find the optimal point (target). The minimum values of the objective function occur at the boundaries, but they are not the inverting targets. Searching begins at a lower boundary, involving six iteration steps until arriving at the “target.” At each iteration step of this inverse computation, three key elements are computed including the gradient  $\mathbf{g}$  (to satisfy the first order necessary condition), search direction  $\tilde{m}$  and step length  $\alpha_k$ . The Hessian matrix  $\mathbf{H}$ , the second order differential of Lagrangian with respect to material model parameter  $m$ , may also be calculated to improve the convergence speed.

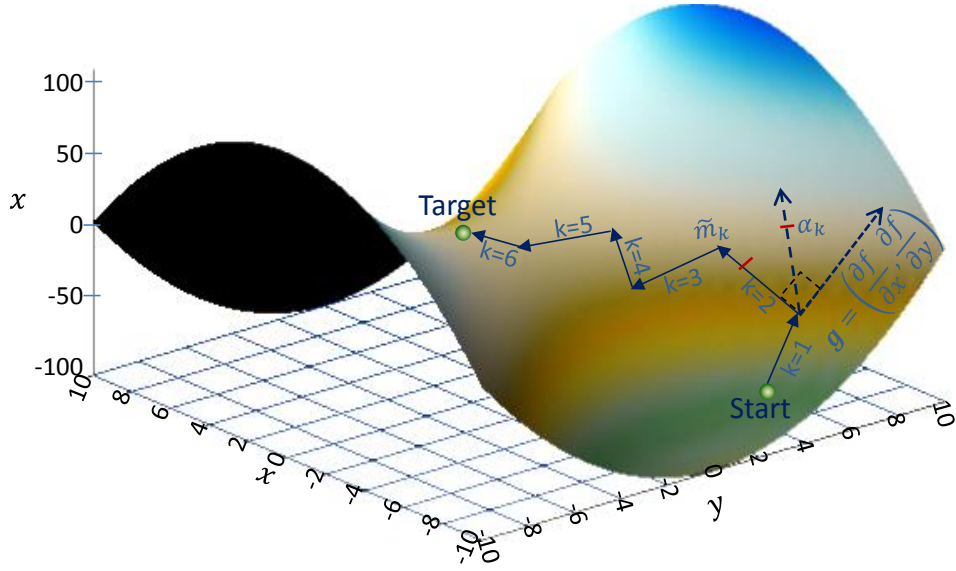


Figure 67. Inverse computation illustration (plotted using Surfer® software).

#### 4.3.2.2 Calculation of Gradient and Hessian

The computation of the gradient vector involves three steps: 1) find deflection  $u$ ; 2) find test function  $p$ ; and then, 3) calculate the gradient vector given  $u$  and  $p$ .

Applying the first order variation of Lagrangian with respect to test function  $\mathbf{p}$  and zeroing it, the deflection  $u$  could be computed by the following equation:

$$\frac{\partial \mathcal{L}(\hat{\mathbf{p}})}{\partial \mathbf{p}} = \int_0^{t_d} \int_{\Omega} \boldsymbol{\sigma} : \nabla \hat{\mathbf{p}} d\Omega dt + \int_0^{t_d} \int_{\Omega} b \cdot \hat{\mathbf{p}} d\Omega dt + \int_0^{t_d} \int_{\Omega} c \frac{\partial \mathbf{u}(t)}{\partial t} \cdot \hat{\mathbf{p}} d\Omega dt + \int_0^{t_d} \int_{\Omega} \rho \frac{\partial^2 \mathbf{u}}{\partial t^2} \cdot \hat{\mathbf{p}} d\Omega dt - \int_0^{t_d} \int_{\partial \Omega_4} f \cdot \hat{\mathbf{p}} ds dt = 0 \quad (4-15)$$

where,  $\hat{\mathbf{p}}$  is variation of test function  $\mathbf{p}$ ,  $\nabla \hat{\mathbf{p}} \in \Omega \times [0, t_d]$ .

Applying the first order variation of Lagrangian with respect to variable  $\mathbf{u}$  and zeroing it, and given the computed  $\mathbf{u}$  above, the test function  $\mathbf{p}$  could be computed by the following equation:

$$\frac{\partial \mathcal{L}(\hat{\mathbf{u}})}{\partial \mathbf{u}} = \int_0^{t_d} \int_{\Omega} (\mathbf{u} - \mathbf{u}_{obs}) \cdot \hat{\mathbf{u}} d\Omega dt + \int_0^{t_d} \int_{\Omega} \frac{\partial \boldsymbol{\sigma}}{\partial \mathbf{u}} \hat{\mathbf{u}} : \nabla \mathbf{p} d\Omega dt + \int_0^{t_d} \frac{\partial}{\partial \mathbf{u}} \left[ \int_{\Omega} c \frac{\partial \mathbf{u}(t)}{\partial t} \cdot \mathbf{p} d\Omega \right] \hat{\mathbf{u}} dt + \int_0^{t_d} \frac{\partial}{\partial \mathbf{u}} \left[ \int_{\Omega} \rho \frac{\partial^2 \mathbf{u}}{\partial t^2} \cdot \mathbf{p} d\Omega \right] \hat{\mathbf{u}} dt = 0 \quad (4-16)$$

where  $\hat{\mathbf{u}}$  is variation of response variable  $\mathbf{u}$ ,  $\nabla \hat{\mathbf{u}} \in \Omega \times [0, t_d]$ .

Given that  $\mathbf{u}$  and  $\mathbf{p}$  have been determined, the gradient  $\mathbf{g}$  could be calculated by applying the first order differential to the Lagrangian with respect to material parameter  $m$  by the following equation:

$$\int_{\Omega} \mathbf{g} \cdot \hat{\mathbf{m}} d\Omega = \frac{\partial \mathcal{L}(\hat{\mathbf{u}}, \hat{\mathbf{p}})}{\partial m} = \gamma \int_{\Omega} (m - m^*) \cdot \hat{\mathbf{m}} d\Omega + \int_0^{t_d} \int_{\Omega} \frac{\partial \sigma}{\partial m} \cdot \hat{\mathbf{m}} \cdot \nabla \mathbf{p} d\Omega dt + \frac{\partial}{\partial m} \int_0^{t_d} \int_{\Omega} c \frac{\partial \mathbf{u}(t)}{\partial t} \cdot \hat{\mathbf{m}} \cdot \mathbf{p}(t) d\Omega dt \quad (4-17)$$

where,  $\hat{\mathbf{m}}$  is a variation of  $\mathbf{m}$ ,  $\forall \hat{\mathbf{m}} \in \Omega \times [0, t_d]$ ; in this case  $\chi_{(m_1^*, m_2^*)}^m = 0$ , the same for all of the following mathematical derivations. Thus, the strong form of the gradient is written as follows:

$$\mathbf{g} = \gamma(m - m^*) + \int_0^{t_d} \frac{\partial \sigma}{\partial m} \cdot \nabla \mathbf{p} dt + \frac{\partial}{\partial m} \int_0^{t_d} c \frac{\partial \mathbf{u}(t)}{\partial t} \cdot \mathbf{p}(t) dt \quad (4-18)$$

where the third term of damping is dependent on the elastic stiffness according to the Rayleigh damping model ( $\mathbf{C} = \alpha \mathbf{M} + \beta \mathbf{K}$ ).

Finding the Hessian matrix also involves three computation steps with three equilibrium equations: 1) an incremental state equation to determine incremental response of displacement  $\tilde{\mathbf{u}}$ , 2) an incremental adjoint equation to determine incremental test function  $\tilde{\mathbf{p}}$ , and 3) an incremental decision or control equation to determine the Hessian matrix given  $\tilde{\mathbf{u}}$  and  $\tilde{\mathbf{p}}$ .

Applying the second order variation of Lagrangian with respect to  $\partial^2 \mathbf{p}$ ,  $\partial \mathbf{p} \partial \mathbf{u}$ , and  $\partial \mathbf{p} \partial m$ , sum and then zero, the incremental deflection  $\tilde{\mathbf{u}}$  can be computed by the following equation:

$$\frac{\partial \mathcal{L}(\hat{\mathbf{p}})(\hat{\mathbf{p}})}{\partial^2 \mathbf{p}} + \frac{\partial \mathcal{L}(\hat{\mathbf{p}})(\tilde{\mathbf{u}})}{\partial \mathbf{p} \partial \mathbf{u}} + \frac{\partial \mathcal{L}(\hat{\mathbf{p}})(\tilde{m})}{\partial \mathbf{p} \partial m} = 0 \quad (4-19)$$

Given  $\tilde{\mathbf{u}}$  and applying the second order variation of Lagrangian with respect to  $\partial \mathbf{u} \partial \mathbf{p}$ ,  $\partial^2 \mathbf{u}$ , and  $\partial \mathbf{u} \partial m$ , sum and then zero, the incremental test function  $\tilde{\mathbf{p}}$  can be computed by the following equation:

$$\frac{\partial \mathcal{L}(\hat{\mathbf{u}})(\tilde{\mathbf{p}})}{\partial \mathbf{u} \partial \mathbf{p}} + \frac{\partial \mathcal{L}(\hat{\mathbf{u}})(\tilde{\mathbf{u}})}{\partial^2 \mathbf{u}} + \frac{\partial \mathcal{L}(\hat{\mathbf{u}})(\tilde{m})}{\partial \mathbf{u} \partial m} = 0 \quad (4-20)$$

Given  $\tilde{u}$  and  $\tilde{p}$  values, and applying the second order variation of Lagrangian with respect to  $\partial m \partial \mathbf{p}$ ,  $\partial m \partial \mathbf{u}$ , and  $\partial^2 m$ , the Hessian matrix could be computed by the following equilibrium:

$$\mathbf{H}(\hat{\mathbf{m}}, \tilde{\mathbf{m}}) = \frac{\partial \mathcal{L}(\hat{\mathbf{m}})(\tilde{\mathbf{p}})}{\partial m \partial \mathbf{p}} + \frac{\partial \mathcal{L}(\hat{\mathbf{m}})(\tilde{\mathbf{u}})}{\partial m \partial \mathbf{u}} + \frac{\partial \mathcal{L}(\tilde{\mathbf{m}})}{\partial^2 m} \quad (4-21)$$

#### 4.3.2.3 Determining Search Direction and Step Length

Given the initial material property seed values (e.g., the elastic modulus  $E_i$  and viscosity of  $\eta_i$  of viscoelastic layers as detailed in Equation (4-2), and moduli of elastic layers, the gradient and Hessian matrix are computed above. Then according to Newton's method (derived from the Taylor's theorem), the search direction  $\tilde{\mathbf{m}}_k$  at the iteration step of  $k$  is determined as follows:

$$\tilde{\mathbf{m}}_k = -\mathbf{H}_k(\mathbf{m})^{-1} \mathbf{g}_k(\mathbf{m}) \quad (4-22)$$

where  $\mathbf{H}_k(\mathbf{m})$  is the Hessian matrix, and  $\mathbf{g}_k(\mathbf{m})$  is gradient computed at the  $k^{\text{th}}$  iteration step.

The Wolfe conditions are proposed for performing the inexact line search in an efficient way to compute an acceptable search direction and step length. The Wolfe conditions are as follows (Wolfe 1969):

$$(i) \ u(m_{k+1}) - u(m_k) \leq c_1 \alpha_k \tilde{\mathbf{m}}_k^T \mathbf{g}_k \quad (4-23)\text{-a}$$

$$(ii) \ \tilde{\mathbf{m}}_k^T \mathbf{g}_{k+1} \geq c_2 \tilde{\mathbf{m}}_k^T \mathbf{g}_k \quad (4-23)\text{-b}$$

where  $\mathbf{u}_{k+1}$ ,  $\mathbf{u}_k$  are displacement vectors at the  $(k+1)^{\text{th}}$  and  $k^{\text{th}}$  iteration step, respectively;  $\mathbf{g}_{k+1}$ ,  $\mathbf{g}_k$  are gradient vectors at the  $(k+1)^{\text{th}}$  and  $k^{\text{th}}$  iteration step, respectively;  $\tilde{\mathbf{m}}_k$ ,  $\tilde{\mathbf{m}}_k^T$  are search direction vectors and its transpose;  $c_1, c_2$  are two constants for numerical practice, i.e.,  $0 < c_1 < c_2 < 1$ .

Inequality (i) in Equation (4-23) is known as the Armijo rule, and inequality (ii) in Equation (4-23) is known as the curvature condition. The Armijo rule is to ensure that the step length  $\alpha_k$  decreases the parameter value sufficiently, and the inequality (ii) is to

ensure that the gradient has been reduced sufficiently (Nocedal and Wright 2006). In particular, if the two inequalities hold when the cosine of the angle between  $\tilde{\mathbf{m}}_k$  and the gradient  $\mathbf{g}_k$  ( $\text{Cos}(\theta) = \frac{\mathbf{g}_k^T \tilde{\mathbf{m}}_k}{\|\mathbf{g}_k\| \|\tilde{\mathbf{m}}_k\|}$ ) is bounded away from zero, the gradient  $\mathbf{g}_k \rightarrow 0$  (Nocedal and Wright 2006).  $c_1$  value is usually set quite small while  $c_2$  value is much bigger. Nocedal and Wright (2006) gives example values of  $c_1 = 10^{-4}$ , and  $c_2 = 0.9$  for the Newton or quasi-Newton method, and 0.1 for the conjugate gradient method.

To maintain a descent search direction,  $\tilde{\mathbf{m}}_k^T \mathbf{g}_k < 0$  satisfies. The inequality (ii) of Equation (4-23) can be modified as a strong Wolfe condition on curvature as follows:

$$|\tilde{\mathbf{m}}_k^T \mathbf{g}_{k+1}| \leq |c_2 \tilde{\mathbf{m}}_k^T \mathbf{g}_k| \quad (4-24)$$

The step length is used to constrain the “diversion” (overestimated or underestimated search direction) toward a more stable inverse computation. Here a modified Armijo rule is proposed to determine the step length as follows:

$$\frac{\|u - u_{obs}\|}{\alpha_k \tilde{\mathbf{m}}_k^T \mathbf{g}_k} \leq c_1 \quad (4-25)$$

where  $u$  is simulated displacement response;  $u_{obs}$  is measured displacement; and  $c_1$  is a parameter. The initial step length is set as  $\alpha_k$ , here  $\alpha_k$  is proportional to  $1/(u - u_{obs})^2$ . Then at each iteration step, it is reduced to half until this inequality is satisfied.

### 4.3.3 Computation Time

To calculate the gradient, the Lagrangian optimization method always involves four linear system solutions (two for gradient vector, and another two for Hessian matrix). When dealing with relatively large-scale model parameters such as a viscoelastic inverse problem with 18 model parameters, the two-stage approach involves 18 linear system solutions to calculate 18 gradient values in order to achieve good accuracy. Table 10 presents the computation time in contrast. The developed method could significantly improve the computation speed when dealing with large scale inverse problems. However, the Lagrangian optimization method involves much more complex mathematical derivations and requires relatively expensive numerical solutions for the

linear system(s). When dealing with simpler inverse problems with a small model parameter number, the two-stage method is sufficient and accurate enough as the analytical solution can be used for very fast computation of the forward responses instead.

**Table 10. Computation time comparison**

| Inverse Problem | Elastic Problem    |                          | Viscoelastic Problem |                          |
|-----------------|--------------------|--------------------------|----------------------|--------------------------|
|                 | Two-stage approach | Langrangian optimization | Two-stage approach   | Langrangian optimization |
| Linear systems  | 4                  | 4                        | 18                   | 4                        |
| Time steps      | 1                  | 1                        | 25                   | 25                       |
| Total time      | 4                  | 4                        | 450                  | 100                      |

#### 4.4. Numerical Solution Method

The numerical solution involves computations of gradient vector, Hessian matrix, search direction and step length, and lastly, material model properties. The numerical solution developed is based on a time-domain finite element (FE) method. Unique mathematical derivations and solutions of this specific dynamic viscoelastic multilayer system inverse problem are developed and detailed in the following way.

##### 4.4.1 Lagrangian Weak Form

Firstly, the Lagrangian form is re-expressed in a weak form for numerical computation purposes. As discussed in Chapter 3, viscoelastic stress can be expressed as follows:

$$\boldsymbol{\sigma}(t) = \mathbf{R}(t - \tau) \frac{\partial \mathbf{u}(t)}{\partial t} \quad (4-26)$$

where  $\mathbf{R}(t - \tau)$  is the relaxation modulus such that:

$$\mathbf{R}(t - \tau) := 2 \int_0^t G(t - \tau) \left( \frac{1}{2} [\boldsymbol{\nabla} + \boldsymbol{\nabla}^T] - \frac{1}{3} \boldsymbol{\nabla} \cdot \right) d\tau + 3\mathbf{I} \int_0^t K(t - \tau) \left( \frac{1}{3} \boldsymbol{\nabla} \cdot \right) d\tau \quad (4-27)$$

where  $G(t - \tau)$  and  $K(t - \tau)$  are the shear and bulk relaxation modulus, respectively.

Substitute Equation (4-26) into the Langrangian function (4-12), and discretize the displacement and test function ( $\mathbf{u} = \boldsymbol{\Phi} \mathbf{u}$ ;  $\mathbf{p} = \boldsymbol{\Phi} \mathbf{p}$ , where  $\boldsymbol{\Phi}$  is the shape function matrix); then, the Lagrangian weak form can re-expressed as follows:

$$\begin{aligned} \mathcal{L} = & \frac{1}{2} \int_0^{t_d} \int_{\partial\Omega_s} (\boldsymbol{\Phi}u - \boldsymbol{\Phi}u_{obs})^2 ds dt + \frac{\gamma}{2} \int_{\Omega} (1 - \chi_{(m_1^*, m_2^*)}^m) (m - m^*)^2 d\Omega + \\ & \int_0^{t_d} \int_{\Omega} \int_0^t R(t - \tau) \frac{\partial(u(\tau))}{\partial\tau} d\tau p(t) d\Omega dt + \left[ \int_0^{t_d} \mathbf{C} \frac{\partial u(t)}{\partial t} p(t) dt + \int_0^{t_d} \mathbf{M} \frac{\partial^2 u(t)}{\partial t^2} \cdot p(t) dt \right] - \\ & \left[ \int_0^{t_d} \int_{\partial\Omega_4} \boldsymbol{\Phi}_{\Gamma}^T f(t) p(t) ds dt + \int_0^{t_d} \int_{\Omega} \boldsymbol{\Phi}^T b p(t) d\Omega dt \right] \in \Omega \times [0, t_d] \end{aligned} \quad (4-28)$$

where  $\boldsymbol{\Phi}_{\Gamma}$  is the shape function matrix to discretize the loading at the surface area  $\partial\Omega_4$ ;  $\mathbf{B} = \nabla\boldsymbol{\Phi}$  is the displacement-strain matrix;  $\mathbf{C} = \int_{\Omega} \boldsymbol{\phi}^T c \boldsymbol{\phi} d\Omega$  is the damping matrix;  $\mathbf{M} = \int_{\Omega} \boldsymbol{\phi}^T \rho \boldsymbol{\phi} d\Omega$  is the mass matrix; and  $R(t - \tau)$  is a relaxation modulus matrix such that:

$$R(t - \tau) := \mathbf{B}^T \mathbf{R}(t - \tau) \mathbf{B} \quad (4-29)$$

The Rayleigh damping model is adopted in this research for determining the damping matrix as follows (Chopra 2001, Cook 2002):

$$\mathbf{C} = \alpha \mathbf{M} + \beta \mathbf{K} \quad (4-30)\text{-a}$$

$$\alpha = \frac{2\xi \omega_1 \omega_2}{\omega_1 + \omega_2} \quad (4-30)\text{-b}$$

$$\beta = \frac{2\xi}{\omega_1 + \omega_2} \quad (4-30)\text{-c}$$

where  $\alpha, \beta$  are Rayleigh coefficients;  $\mathbf{M}$  is mass matrix, and  $\mathbf{K}$  is elastic stiffness matrix.

## 4.4.2 Computation of Gradient Vector

Computation of gradient includes three steps of consequence (see Equation (4-15)-(4-17)), and the numerical solutions for the specific dynamic viscoelastic multilayer system are developed as follows.

### 4.4.2.1 State equation to determine deflection $u$

Applying the first order variation of the Lagrangian with respect to test function variable  $p$ , the governing state equation weak form can be formed as follows:

$$\begin{aligned} \frac{\partial \mathcal{L}}{\partial p} = & \int_0^{t_d} \int_{\Omega} \int_0^t R(t - \tau) \frac{\partial(u(\tau))}{\partial\tau} d\tau \hat{p}(t) d\Omega dt + \int_0^{t_d} \mathbf{C} \frac{\partial u(t)}{\partial t} \hat{p}(t) dt + \int_0^{t_d} \mathbf{M} \frac{\partial^2 u}{\partial t^2} \hat{p}(t) dt + \\ & \int_0^{t_d} b \hat{p}(t) dt - \int_0^{t_d} \int_{\partial\Omega_4} \boldsymbol{\Phi}_{\Gamma}^T f \hat{p}(t) ds dt = 0 \end{aligned} \quad (4-31)$$

The numerical solution of  $u$  is presented with accompanying details in Chapter 3. The computation begins at the first time step ( $t_{n=1}$ ) and evolves until the end of time period  $t_d$ .

#### 4.4.2.2 Adjoint equation to determine test function $p$

The numerical solution of the test function  $p$  step-by-step for the dynamic viscoelastic multilayer system was developed in the following manner:

##### *Galerkin Method for the Weak Form*

Using the Galerkin method, applying the first order variation of the Larangian (4-28) with respect to displacement variable  $u$ , the weak form of the adjoint equation can be achieved as follows:

$$\begin{aligned} \frac{\partial \mathcal{L}}{\partial u} = & \int_0^{t_d} \int_{\Omega_5} \boldsymbol{\Phi}^T (u - u_{obs}) \boldsymbol{\Phi} \hat{u} ds dt + \int_0^{t_d} \int_{\Omega} \frac{\partial}{\partial u} \left[ \int_0^t R(t - \tau) \frac{\partial(u(\tau))}{\partial \tau} d\tau \right] d\Omega p(t) dt + \\ & \frac{\partial}{\partial u} \left[ \int_0^{t_d} \mathbf{C} \frac{\partial u}{\partial t} p(t) dt \right] + \frac{\partial}{\partial u} \left[ \int_0^{t_d} \mathbf{M} \frac{\partial^2 u}{\partial t^2} p(t) dt \right] = 0 \end{aligned} \quad (4-32)$$

$$\text{Define } \mathcal{L}_d := \mathbf{M} \int_0^{t_d} \frac{\partial^2 u(t)}{\partial t^2} p(t) dt$$

$\mathcal{L}_d$  can be re-derived as follows according to the integration by parts:

$$\begin{aligned} \mathcal{L}_d = & \int_0^{t_d} \mathbf{M} p(t) d \left( \frac{\partial u}{\partial t} \right) = \int_{\Omega} \mathbf{M} \left( p(t_d) \frac{\partial u(t_d)}{\partial t} - p(0) \frac{\partial u(0)}{\partial t} \right) d\Omega - \int_0^{t_d} \mathbf{M} \frac{\partial p(t)}{\partial t} du(t) = \\ & - \int_{\Omega} \mathbf{M} p(0) \frac{\partial u(0)}{\partial t} d\Omega + \int_0^{t_d} \mathbf{M} \frac{\partial^2 p(t)}{\partial t^2} u(t) dt \quad (\text{given } p(t_d) = 0 \text{ \& } u(0) = 0) \end{aligned} \quad (4-33)$$

Define:

$$\mathcal{L}_c := \int_0^{t_d} \mathbf{C} \frac{\partial u}{\partial t} p(t) dt \quad (4-34)$$

According to the integration by parts,  $\mathcal{L}_c$  can be re-derived as follows:

$$\mathcal{L}_c = \int_0^{t_d} \mathbf{C} p(t) du(t) = - \int_0^{t_d} \mathbf{C} \frac{\partial p(t)}{\partial t} u(t) dt \quad (4-35)$$

Define:

$$\mathcal{L}_R := \int_0^{t_d} \int_0^t \hat{u}(\tau) \frac{\partial R(t-\tau)}{\partial \tau} p(t) d\tau dt \quad (4-36)$$

This is a double integral of function, first for the time domain  $\tau \in [0, t]$  and then for the second integration with a time domain of  $t \in [0, t_d]$  for  $0 < \tau < t < t_d$ , as shown in Figure 68a. For the numerical computation purpose (to take  $\hat{u}(\tau)$  out of the  $\tau \in [0, t]$  integration and then be dismissed for solving  $p(t)$ ), this integration is converted to an integration with a reversed order: with respect to  $t$  first and then  $\tau$ , as shown in Figure 68b as follows:

$$\mathcal{L}_R = \int_0^{t_d} \hat{u}(\tau) \left[ \int_\tau^{t_d} \frac{\partial R(t-\tau)}{\partial \tau} p(t) dt \right] d\tau \quad (4-37)$$

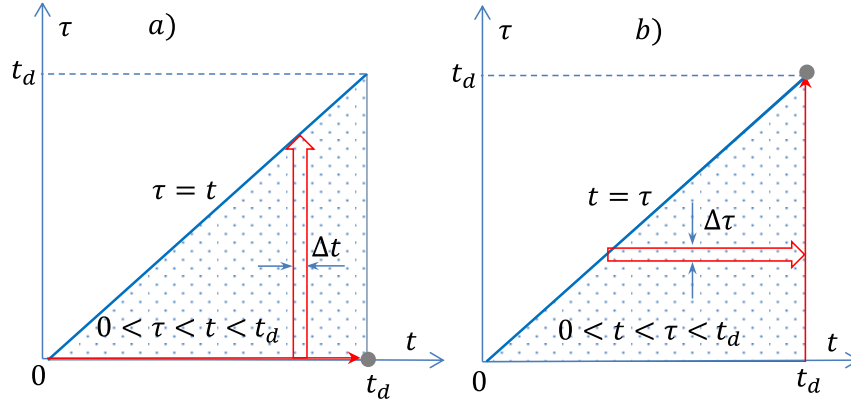


**Figure 68. Integration of 2-D time field of  $0 < \tau < t < t_d$ .**

$t$  and  $\tau$  notations are shifted to each other to arrive at the new form of  $\mathcal{L}_R$ :

$$\mathcal{L}_R = \int_0^{t_d} \hat{u}(t) \int_t^{t_d} \frac{\partial R(\tau-t)}{\partial t} p(\tau) d\tau dt \quad (4-38)$$

Substitute Equation (4-33), (4-35) and (4-38) into (4-32) to re-derive the weak form of the adjoint equation as follows:

$$\begin{aligned} & \int_0^{t_d} \int_{\partial\Omega_s} \Phi^T (u - u_{obs}) \Phi \hat{u}(t) d\Omega dt + \int_0^{t_d} \hat{u}(t) \int_{\Omega} R(0) p(t) d\Omega dt - \\ & \int_0^{t_d} \hat{u}(t) \int_{\Omega} \left[ \int_t^{t_d} \frac{\partial R(\tau-t)}{\partial t} p(\tau) d\tau \right] d\Omega dt + \int_0^{t_d} \hat{u}(t) \mathbf{C} \frac{\partial p(t)}{\partial t} dt + \int_0^{t_d} \hat{u}(t) \mathbf{M} \frac{\partial^2 p(t)}{\partial t^2} dt = 0 \end{aligned} \quad (4-39)$$

$\forall \hat{u} \in \Omega, \forall t \in [0, t_d]$  and thus  $\hat{u}(t)$  can be dismissed on both sides, such that the following equilibrium satisfies  $\forall t \in [0, t_d]$ :

$$\int_{\partial\Omega_5} \Phi^T (u - u_{obs}) \Phi d\Omega + \int_{\Omega} R(0) p(t) d\Omega - \int_{\Omega} \int_t^{t_d} \frac{\partial R(\tau-t)}{\partial t} p(\tau) d\tau d\Omega - \mathbf{C} \frac{\partial p(t)}{\partial t} + \mathbf{M} \frac{\partial^2 p(t)}{\partial t^2} = 0 \quad (4-40)$$

According to the chain rule and integration by parts, the third term can be derived as follows:

$$\begin{aligned} \int_0^{t_d} \hat{u}(t) \int_t^{t_d} \frac{\partial R(\tau-t)}{\partial t} p(\tau) d\tau dt &= \int_0^{t_d} \hat{u}(t) \int_t^{t_d} \frac{\partial R(\tau-t)}{\partial(\tau-t)} \frac{\partial(\tau-t)}{\partial t} p(\tau) d\tau dt = \\ &= - \int_0^{t_d} \int_{\tau=t}^{\tau=t_d} \hat{u}(t) p(\tau) dR(\tau-t) dt = \int_0^{t_d} \hat{u}(t) R(0) p(t) dt - \int_0^{t_d} \hat{u}(t) \int_{t_d}^t R(\tau-t) \frac{\partial p(\tau)}{\partial \tau} d\tau dt \end{aligned} \quad (4-41)$$

Substitute Equation (4-41) into Equation (4-40) to arrive at an equilibrium for the solution of test function  $p$ :

$$\int_{\Omega} \int_{t_d}^t R(\tau-t) \frac{\partial p(\tau)}{\partial \tau} d\tau d\Omega - \mathbf{C} \frac{\partial p(t)}{\partial t} + \mathbf{M} \frac{\partial^2 p(t)}{\partial t^2} = - \int_{\partial\Omega_5} \Phi^T (u - u_{obs}) \Phi d\Omega \quad (4-42)$$

The term  $\int_{t_d}^t R(\tau-t) \frac{\partial p(\tau)}{\partial \tau} d\tau$  is an integration of time  $\tau \in [t_d, t]$  as shown in Figure 69. The total time is broken into  $n$  time steps, and the calculation at time  $t$  is an integration with respect to  $\tau \in [t_d, t]$ . Therefore, at each time step, the calculation starts from the loading period end of  $t_d$  which is assigned as the 0<sup>th</sup> time step, and then the time step of 1, 2, ...  $n$  is solved in a backward order, until the last time step at the time of zero ( $t_n = 0$ ) is reached as shown in Figure 69. The time order for  $p$  solution is opposite to that for the solution of displacement  $u$  as discussed in Chapter 3.

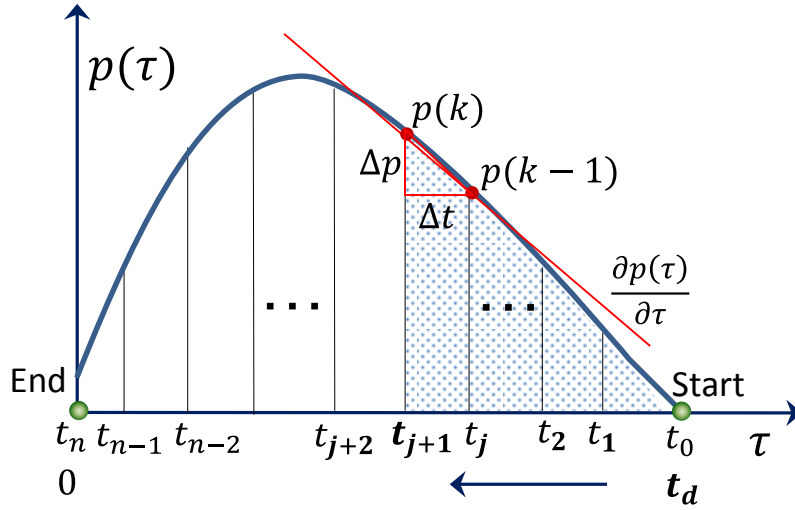


**Figure 69. Time discretization for solution of test function.**

The  $\frac{\partial p(\tau)}{\partial \tau}$  is a tangent, which can be linearly approximated using the Euler method or forward finite difference method (FDM) as follows:

$$\frac{\partial p(\tau)}{\partial \tau} = \lim_{\Delta \tau} \frac{p(\tau + \Delta \tau) - p(\tau)}{\Delta \tau} \approx \frac{p(j) - p(j-1)}{t_{j+1} - t_j} \quad \forall \tau \in [t_{j-1}, t_j] \quad (4-43)$$

Given a very small time step length, the solution would be accurate enough. Substitute equation (4-43) into (4-42):

$$\sum_{j=1}^k J_p(j) \frac{p(j) - p(j-1)}{\Delta t} - \mathbf{C} \frac{\partial p(t)}{\partial t} + \mathbf{M} \frac{\partial^2 p(t)}{\partial t^2} = - \int_{\partial \Omega_s} \Phi^T (u - u_{obs}) \Phi d\Omega \quad (4-44)$$

where  $j$  is a sub-time step of the viscoelastic solution;  $j = 1, 2, 3 \dots k$  for each of  $k = 1, 2, 3 \dots n$ ;  $k$  is the current time step with a time  $t = t_k$ ;  $t_0 = t_d$  ( $t_d$  is the total loading time at the end),  $t_1 = t_d - \Delta t$ ,  $t_2 = t_d - 2\Delta t$ , ...  $t_n = 0$ ;  $\Delta t$  is a negative backward time step length that equals to  $(t_j - t_{j-1})$ ; and  $J_p(j)$  is defined as a viscoelastic stiffness matrix at time step  $j$  as follows:

$$J_p(j) := \int_{\Omega} \int_{t_{j-1}}^{t_j} R(\tau - t) d\tau d\Omega \quad (4-45)$$

The adjoint weak form of Equation (4-44) can be briefed and rearranged as follows:

$$\sum_{j=1}^k \mathbf{J}_p(j) \frac{p(t_j) - p(t_{j-1})}{\Delta t} - \mathbf{C} \frac{\partial p(t)}{\partial t} dt + \mathbf{M} \frac{\partial^2 p(t)}{\partial t^2} dt = \mathfrak{R}_u \quad (4-46)$$

where  $\mathbf{M}$  is mass matrix;  $\mathbf{C}$  is damping matrix;  $\mathfrak{R}_u$  is a “displacement misfit vector,”  $R_u = \int_{\Omega \partial \mathfrak{s}} \boldsymbol{\Phi}^T (u_{obs} - u) \boldsymbol{\Phi} d\Omega dt$ .

### Viscoelastic Stiffness Matrix Solution

The numerical solution of the viscoelastic stiffness matrix  $\mathbf{J}_p(j)$  is described as follows. When the Poisson’s ratio  $\nu$  is considered constant, the shear and bulk relaxation moduli could be determined from the relaxation modulus as follows:

$$G(t) = \frac{E(t)}{2(1+\nu)} \quad (4-47)\text{-a}$$

$$K(t) = \frac{E(t)}{3(1-2\nu)} \quad (4-47)\text{-b}$$

where  $\nu$  is Poisson’s ratio and  $E(t)$  is the relaxation modulus.

Substitute Equation (4-47) into Equation (4-29) to arrive at the new form of the relaxation modulus matrix as follows:

$$R(\tau - t) = \mathbf{J}_B E(\tau - t) \quad (4-48)$$

where  $\mathbf{J}_B$  is a VE shape function matrix defined as follows:

$$\mathbf{J}_B := \int_{\Omega} \mathbf{B}^T \left[ \frac{1}{1+\nu} \left( \frac{1}{2} [\boldsymbol{\nabla} + \boldsymbol{\nabla}^T] - \frac{1}{3} \boldsymbol{\nabla} \cdot \right) d\tau + \frac{1}{1-2\nu} \mathbf{I} \int_0^t \left( \frac{1}{3} \boldsymbol{\nabla} \cdot \right) \right] \mathbf{B} d\Omega \quad (4-49)$$

Substitute Equation (4-48) into Equation (4-45), the VE stiffness matrix for  $p$  solution  $\mathbf{J}_p(j)$  can be derived as follows:

$$\begin{aligned} \mathbf{J}_p(j) &= \mathbf{J}_B \int_{t_{j-1}}^{t_j} E(\tau - t) d\tau = \mathbf{J}_B \int_{t_{j-1}}^{t_j} \left( E_{\infty} + \sum_{i=1}^N E_i e^{-\frac{E_i}{\eta_i}(\tau-t)} \right) d\tau = \mathbf{J}_B \left( E_{\infty} \Delta t - \right. \\ &\left. \sum_i^N \eta_i \left[ e^{-\frac{E_i}{\eta_i}(t_j-t)} - e^{-\frac{E_i}{\eta_i}(t_{j-1}-t)} \right] \right) \end{aligned} \quad (4-50)$$

Thus, given  $\mathbf{J}_B$  and relaxation modulus  $E(t)$ ,  $\mathbf{J}_p(j)$  can be numerically solved.

### Time Discretization and Linear System

The Houbolt finite-difference for time discretization of velocity and acceleration is adopted due to its ability to use a relatively longer time step length than many other methods (Bathe 1996):

$$\frac{\partial p^2(k)}{\partial t^2} = \frac{2p(k)-5p(k-1)+4p(k-2)-p(k-3)}{\Delta t^2} \quad (4-51)\text{-a}$$

$$\frac{\partial p(k)}{\partial t} = \frac{11p(k)-18p(k-1)+9p(k-2)-2p(k-3)}{6\Delta t} \quad (4-51)\text{-b}$$

Substitute Equation (4-51) into Equation (4-46) and rearrange it as follows:

$$\sum_{j=1}^k J_p(j) \frac{p(j)-p(j-1)}{\Delta t} - \mathbf{C} \frac{11p(k)-18p(k-1)+9p(k-2)-2p(k-3)}{6\Delta t} + \mathbf{M} \frac{2p(k)-5p(k-1)+4p(k-2)-p(k-3)}{\Delta t^2} dt = \mathfrak{R}_u \quad (4-52)$$

where  $p(j)$  is  $p$  solution at time step of  $j$  as  $t = t_j$ ;  $p(j - 1)$  is  $p$  at time step of  $j - 1$ .

Equation (4-52) can be re-arranged as follows:

$$\left[ \frac{J_p(k)}{\Delta t} + \frac{2\mathbf{M}}{\Delta t^2} - \frac{11\mathbf{C}}{6\Delta t} \right] p(k) = \mathfrak{R}_u(t) + J_p(k) \frac{p(k-1)}{\Delta t} - \sum_{j=1}^{k-1} J_p(j) \frac{p(j)-p(j-1)}{\Delta t} - \mathbf{C} \frac{18p(k-1)-9p(k-2)+2p(k-3)}{6\Delta t} + \mathbf{M} \frac{5p(k-1)-4p(k-2)+p(k-3)}{\Delta t^2} \quad (4-53)$$

This equilibrium form can be briefed as a final linear system:

$$\mathbf{K}_{\text{dve}} p(k) = \mathfrak{R}_p^* \quad (4-54)$$

where  $\mathbf{K}_{\text{dve}}$  is the dynamic viscoelastic stiffness matrix and  $\mathfrak{R}_p^*$  is the vector.

$$\mathbf{K}_p = \left[ \frac{J_p(k)}{\Delta t} + \frac{2\mathbf{M}}{\Delta t^2} - \frac{11\mathbf{C}}{6\Delta t} \right] \quad (4-55)$$

$$\mathfrak{R}_p^* = \mathfrak{R}_u(t) - \sum_{j=1}^{k-1} J_p(j) \frac{p(j)-p(j-1)}{\Delta t} + \left( \frac{J_p(k)}{\Delta t} + \frac{5\mathbf{M}}{\Delta t^2} - \frac{3\mathbf{C}}{\Delta t} \right) p(k-1) - \left( \frac{4\mathbf{M}}{\Delta t^2} - \frac{3\mathbf{C}}{2\Delta t} \right) p(k-2) + \left( \frac{\mathbf{M}}{\Delta t^2} - \frac{\mathbf{C}}{3\Delta t} \right) p(k-3) \quad (4-56)$$

By assembling all elements of each layer including both the viscoelastic and elastic materials, the global linear system can be formed as follows:

$$\mathbf{K}_p u(t) = \mathfrak{R}_p^* \quad (4-57)$$

where,  $\mathbf{K}_p$  is global stiffness matrix of the multilayer system, a  $2n_N \times 2n_N$  matrix with  $n_N$  as the total FE node number, expressed as follows:

$$\mathbf{K}_p = \mathbf{K}_E + \left[ \frac{J(k)}{\Delta t} - \frac{11C}{6\Delta t} + \frac{2M}{\Delta t^2} \right] \quad (4-58)$$

where  $\mathbf{K}_E$  is global stiffness matrix of the elastic layers, a  $2n_N \times 2n_N$  matrix, and the element values at the viscoelastic layers are all zeroed.

To solve the global linear system, the factorization method is employed to decompose the stiffness matrix  $\mathbf{K}_p$  to an upper and a lower triangular matrix ( $\mathbf{L}$  and  $\mathbf{U}$ , respectively) following the LU factorization rule as discussed in Chapter 3. The global linear systems can be solved by the following:

$$\mathbf{L}y = \mathfrak{R}_p^* \quad (4-59)\text{-a}$$

$$\mathbf{U}p = y \quad (4-59)\text{-b}$$

By solving these two linear equations, the test function  $p(t)$  is computed for  $t = t_d, t_{n-1}, t_{n-1} \dots t_2, t_1, t_0 = 0$  (reversed order of times).

#### 4.4.2.3 Decision equation to determine gradient $\mathbf{g}$

*Weak Form*

The first order decision or control equation is formed by applying the first order variation of the Lagrangian with respect to material model parameter  $m$  as follows:

$$\begin{aligned} \frac{\partial \mathcal{L}}{\partial m} = \int_{\Omega} \mathbf{g} \cdot \hat{\mathbf{m}} = r \int_{\Omega} (m - m^*) \cdot \hat{\mathbf{m}} d\Omega + \int_0^{t_d} \int_{\Omega} \int_0^t \frac{\partial R(t-\tau)}{\partial m} \frac{\partial(u(\tau))}{\partial \tau} d\tau p(t) \cdot \hat{\mathbf{m}} d\Omega dt + \\ \int_0^{t_d} \frac{\partial \mathbf{C}}{\partial m} \frac{\partial u(t)}{\partial t} p(t) \cdot \hat{\mathbf{m}} dt \end{aligned} \quad (4-60)$$

where  $\mathbf{C} = \alpha \mathbf{M} + \beta \mathbf{K}$  ( $\alpha, \beta$  is the Rayleigh damping coefficients,  $\mathbf{M}$  is mass matrix and  $\mathbf{K}$  is elastic stiffness matrix);  $\frac{\partial \mathbf{C}}{\partial m} = \beta \frac{\partial \mathbf{K}}{\partial m}$ .

Substitute  $\mathbf{g} = \Phi \mathbf{g}$  and  $\hat{\mathbf{m}} = \Phi \hat{\mathbf{m}}$  ( $\mathbf{g}$  and  $\hat{\mathbf{m}}$  are those discretized at FE nodes), where  $\Phi$  is the shape function.  $\Phi$  is taken as 1 since the material model parameters are space independent for the same layer of the multilayer system.  $\hat{\mathbf{m}}$  is arbitrary and thus it can be

dismissed on both sides of Equation (4-60). Therefore, the gradient  $g$  is determined as follows:

$$g = \gamma(m - m^*) + \int_0^{t_d} \int_{\Omega} \int_0^t \frac{\partial R(t-\tau)}{\partial m} \frac{\partial(u(\tau))}{\partial \tau} d\tau p(t) d\Omega dt + \beta \frac{\partial \mathbf{K}}{\partial m} \int_0^{t_d} \frac{\partial u(t)}{\partial t} p(t) dt \quad (4-61)$$

$$\text{Define the relaxation modulus derivative: } R_m := \frac{\partial R(t-\tau)}{\partial m}$$

$R_m$  is a second rank matrix with a size of  $2n_N \times n_m$  ( $n_N$  is the total FE node number,  $n_m$  is the material model parameter number). For each  $R_m(i)$  with regard to the  $i^{\text{th}}$  material model parameter:

$$R_m(i) = \frac{\partial R(t-\tau)}{\partial m_i} \text{ for } i = 1, 2, 3 \dots n_m \quad (4-62)$$

where  $R_m(i)$  is the differential of  $R$  with respect to the  $i^{\text{th}}$  material model parameter;  $m_i$  is the  $i^{\text{th}}$  material model parameter,  $i = 1, 2, 3 \dots n_m$ .

Define the viscoelastic stiffness matrix derivative at the  $j^{\text{th}}$  time step as follows:

$$J_{\partial m}(j) := \int_{\Omega} \int_{t_{j-1}}^{t_j} \frac{\partial R(t-\tau)}{\partial m} d\tau d\Omega \quad (4-63)$$

Discretize the displacement tangent following the Euler method:

$$\frac{\partial(u(\tau))}{\partial \tau} = \frac{u(t_j) - u(t_{j-1})}{\Delta t} \quad (4-64)$$

Substitute Equation (4-63) and (4-64) into Equation (4-61) to arrive at a new form for the solution of gradient:

$$g = \gamma(m - m^*) + \int_0^{t_d} \left[ \sum_{j=1}^k J_{\partial m}(j) \frac{u(t_j) - u(t_{j-1})}{\Delta t} \right] \cdot p(t) dt + \beta \frac{\partial \mathbf{K}}{\partial m} \int_0^{t_d} \frac{\partial u(t)}{\partial t} p(t) dt \quad (4-65)$$

where  $u(t)$ ,  $p(t)$  are the displacement and test function solved in the earlier sections. For each material model parameter, gradient  $g_i$  can be expressed as follows:

$$g_i = \gamma(m - m^*) + \int_0^{t_d} \left[ \sum_{j=1}^k J_{\partial m}(j) \frac{u(t_j) - u(t_{j-1})}{\Delta t} \right] \cdot p(t) dt + \beta \frac{\partial \mathbf{K}}{\partial m_i} \int_0^{t_d} \frac{\partial u(t)}{\partial t} p(t) dt \quad (4-66)$$

*Time Discretization and Solution of Viscoelastic Layers*

Break the time  $t \in [0, t_d]$  into  $n$  steps, as shown in Figure 70. Applying Euler's method, the integration of  $p$  with time can be discretized as follows:

$$\int_0^{t_d} p(t) dt = \sum_{k=1}^n (p(t_{k-1}) + p(t_k)) \frac{\Delta t}{2} \quad (4-67)$$

Substituting Equation (4-67) into (4-66) and following the Trapezoidal rule, the gradient for each material model parameter at the time-discretized form can be derived as follows:

$$g_i = \gamma(m_i - m_i^*) + \sum_{k=1}^n \sum_{j=1}^k J_{\partial m}(j) [u(t_j) - u(t_{j-1})] \cdot [p(t_{k-1}) + p(t_k)] \frac{\Delta t}{2} + \frac{1}{2} \beta \frac{\partial K}{\partial m_i} \sum_{k=1}^n [u(t_k) - u(t_{k-1})] \cdot [p(t_{k-1}) + p(t_k)] \quad (4-68)$$

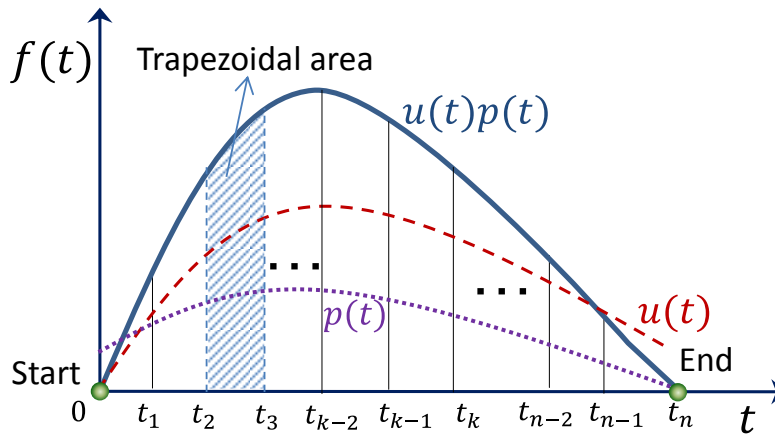


**Figure 70. Integration of the combined function of displacement and test function.**

For the viscoelastic material, the numerical solution of  $J_{\partial m}(j)$  is described as follows:

$$J_{\partial m}(j) = \int_{t_{j-1}}^{t_j} \frac{\partial E(t-\tau)}{\partial m_i} J_B d\tau \quad (4-69)$$

For the elastic material layers of the multilayer system:

$$J_{\partial m}(j) = \int_{t_{j-1}}^{t_j} \frac{\partial E_i}{\partial E_i} J_B d\tau = J_B \Delta t \quad (4-70)$$

where  $\Delta t$  is the time step length.

For example, for a multilayer structure with one layer considered VE, and the other layers are considered elastic, the material parameter vector can be expressed as:

$$\mathbf{m} = [E_0, E_1, E_2, E_3 \dots E_N, \eta_1, \eta_2, \eta_3 \dots \eta_N, E_{2N+2} \dots E_{n-1}, E_n]^T \quad (4-71)$$

where  $E_0$  is the first spring elastic modulus;  $E_i$  and  $\eta_i$  for  $i=1,2,\dots,N$  are the spring elastic modulus and dashpot viscosity of the parallel series, of the generalized Maxwell model;  $E_i$  for  $i=2N+2,\dots,n$  is the elastic modulus of the elastic layers. The gradient for the first material model parameter  $E_\infty$  can be derived as follows:

$$g_1 = \gamma(E_\infty - E_\infty^*) + \sum_{k=1}^n \left( \sum_{j=1}^k \frac{\partial E(t-\tau)}{\partial E_\infty} \mathbf{J}_B [u(t_j) - u(t_{j-1})] \right) \cdot [p(t_{k-1}) + p(t_k)] \frac{\Delta t}{2} + \frac{1}{2} \beta \mathbf{J}_B \sum_{k=1}^n [u(t_k) - u(t_{k-1})] \cdot [p(t_{k-1}) + p(t_k)] \quad (4-72)$$

where  $\mathbf{J}_B$  is the VE shape function matrix (see Equation (4-49));  $E_\infty$  is the elastic modulus at infinite time (see Figure 65).

The derivative of relaxation modulus to  $E_\infty$  is:

$$\frac{\partial E(t-\tau)}{\partial E_\infty} = \partial(E_\infty + \sum_{i=1}^N G_i e^{-\frac{E_i}{\eta_i} t}) / \partial E_\infty = 1 \quad (4-73)$$

Therefore, the gradient can be determined as follows:

$$g_1 = \gamma(E_\infty - E_\infty^*) + \frac{1}{2} \sum_{k=1}^n \mathbf{J}_B u(t_k) \cdot [p(t_{k-1}) + p(t_k)] \Delta t + \frac{1}{2} \beta \mathbf{J}_B \sum_{k=1}^n [u(t_k) - u(t_{k-1})] \cdot [p(t_{k-1}) + p(t_k)] \quad (4-74)$$

For the  $i^{th}$  spring modulus of the generalized Maxwell of  $i = 1,2,3 \dots N$  (total  $N$  springs in parallel)

$$g_{i+1} = \gamma(E_i - E_i^*) + \sum_{k=1}^n \sum_{j=1}^k \int_{t_{j-1}}^{t_j} \frac{\partial E(t-\tau)}{\partial E_i} \mathbf{J}_B d\tau [u(t_j) - u(t_{j-1})] \cdot \frac{(p(t_{k-1}) + p(t_k))}{2} + \beta \mathbf{J}_B \sum_{k=1}^n [u(t_k) - u(t_{k-1})] \cdot p(t_k) \quad (4-75)$$

where the differential of relaxation modulus is derived as:

$$\frac{\partial E(t-\tau)}{\partial E_i} = \partial \left( E_\infty + \sum_{i=1}^N E_i e^{-\frac{E_i}{\eta_i} t} \right) / \partial E_i = e^{-\frac{E_i}{\eta_i} (t-\tau)} - \frac{E_i}{\eta_i} (t-\tau) e^{-\frac{E_i}{\eta_i} (t-\tau)} \quad (4-76)$$

$$\int_{t_{j-1}}^{t_j} \frac{\partial E(t-\tau)}{\partial E_i} d\tau = \int_{t_{j-1}}^{t_j} \left[ e^{-\frac{E_i}{\eta_i}(t-\tau)} - \frac{E_i}{\eta_i} (t-\tau) e^{-\frac{E_i}{\eta_i}(t-\tau)} \right] d\tau \quad (4-77)$$

where  $E_i$  is the elastic modulus of the  $i^{\text{th}}$  spring element for  $i = 1, 2, 3 \dots N$ . The integration terms in Equation (4-77) can be derived as follows:

$$\int_{t_{j-1}}^{t_j} e^{-\frac{E_i}{\eta_i}(t-\tau)} d\tau = \frac{\eta_i}{E_i} \left[ e^{-\frac{E_i}{\eta_i}(t-t_j)} - e^{-\frac{E_i}{\eta_i}(t-t_{j-1})} \right] \quad (4-78)$$

$$\int_{t_{j-1}}^{t_j} \frac{E_i}{\eta_i} (t-\tau) e^{-\frac{E_i}{\eta_i}(t-\tau)} d\tau = \int_{t_{j-1}}^{t_j} (t-\tau) de^{-\frac{E_i}{\eta_i}(t-\tau)} = \left[ (t-t_j) e^{-\frac{E_i}{\eta_i}(t-t_j)} - (t-t_{j-1}) e^{-\frac{E_i}{\eta_i}(t-t_{j-1})} \right] + \frac{\eta_i}{E_i} \left[ e^{-\frac{E_i}{\eta_i}(t-t_j)} - e^{-\frac{E_i}{\eta_i}(t-t_{j-1})} \right] \quad (4-79)$$

Substitute Equation (4-76) to (4-79) into Equation (4-75):

$$g_{i+1} = \gamma(E_i - E_i^*) + \sum_{k=1}^n \sum_{j=1}^k \left( (t-t_{j-1}) e^{-\frac{E_i}{\eta_i}(t-t_{j-1})} - (t-t_j) e^{-\frac{E_i}{\eta_i}(t-t_j)} \right) J_B(u(t_j) - u(t_{j-1})) \cdot \frac{(p(t_{k-1}) + p(t_k))}{2} \quad (4-80)$$

For the viscosity of generalized Maxwell model's  $i^{\text{th}}$  dashpot,  $i = 1, 2, 3 \dots N$ :

$$g_{i+N+1} = \gamma(\eta_i - \eta_i^*) + \sum_{k=1}^n \sum_{j=1}^k \int_{t_{j-1}}^{t_j} \frac{\partial E(t-\tau)}{\partial \eta_i} d\tau J_B[u(t_j) - u(t_{j-1})] \cdot [p(t_{k-1}) + p(t_k)] \frac{\Delta t}{2} \quad (4-81)$$

$$\frac{\partial E(t-\tau)}{\partial \eta_i} = \partial \left( E_\infty + \sum_{i=1}^N E_i e^{-\frac{E_i}{\eta_i} t} \right) / \partial \eta_i = \frac{E_i^2}{\eta_i^2} (t-\tau) e^{-\frac{E_i}{\eta_i}(t-\tau)} \quad (4-82)$$

Substitute Equation (4-82) into Equation (4-81):

$$g_{i+N+1} = \gamma(\eta_i - \eta_i^*) + \sum_{k=1}^n \sum_{j=1}^k \int_{t_{j-1}}^{t_j} \frac{E_i^2}{\eta_i^2} (t-\tau) e^{-\frac{E_i}{\eta_i}(t-\tau)} d\tau J_B \left[ \frac{u(t_j) - u(t_{j-1})}{\Delta t} \right] \cdot [p(t_{k-1}) + p(t_k)] \frac{\Delta t}{2} \quad (4-83)$$

According to the integration by parts, the integration term in Equation (4-83) can be rederived as:

$$\int_{t_{j-1}}^{t_j} \frac{E_i^2}{\eta_i^2} (t - \tau) e^{-\frac{E_i}{\eta_i}(t-\tau)} d\tau = \int_{t_{j-1}}^{t_j} \frac{E_i}{\eta_i} (t - \tau) d e^{-\frac{E_i}{\eta_i}(t-\tau)} = \left[ \frac{E_i}{\eta_i} (t - t_j) e^{-\frac{E_i}{\eta_i}(t-t_j)} - \frac{E_i}{\eta_i} (t - t_{j-1}) e^{-\frac{E_i}{\eta_i}(t-t_{j-1})} \right] + \left[ e^{-\frac{E_i}{\eta_i}(t-t_j)} - e^{-\frac{E_i}{\eta_i}(t-t_{j-1})} \right] \quad (4-84)$$

Substitute Equation (4-84) into Equation (4-83):

$$g_{i+N+1} = \gamma(\eta_i - \eta_i^*) + \frac{1}{V_{ve}} \sum_{k=1}^n \sum_{j=1}^k \left( \left[ \frac{E_i}{\eta_i} (t - t_j) e^{-\frac{E_i}{\eta_i}(t-t_j)} - \frac{E_i}{\eta_i} (t - t_{j-1}) e^{-\frac{E_i}{\eta_i}(t-t_{j-1})} \right] + \left[ e^{-\frac{E_i}{\eta_i}(t-t_j)} - e^{-\frac{E_i}{\eta_i}(t-t_{j-1})} \right] \right) \mathbf{J}_{\mathbf{B}} (u(t_j) - u(t_{j-1})) \cdot \frac{(p(t_{k-1})+p(t_k))}{2} \quad (4-85)$$

It could be rearranged as follows to arrive at the final discretized form:

$$g_{i+N+1} = \gamma(\eta_i - \eta_i^*) + \frac{1}{V_{ve}} \sum_{k=1}^n \sum_{j=1}^k \left[ \frac{E_i(t_k-t_j)+\eta_i}{\eta_i} e^{-\frac{E_i}{\eta_i}(t_k-t_j)} - \frac{E_i(t_k-t_{j-1})+\eta_i}{\eta_i} e^{-\frac{E_i}{\eta_i}(t_k-t_{j-1})} \right] \mathbf{J}_{\mathbf{B}} (u(t_j) - u(t_{j-1})) \cdot \frac{(p(t_{k-1})+p(t_k))}{2} \quad (4-86)$$

#### *Gradient Solution of Moduli of Elastic Layers*

For the gradient of the elastic modulus  $E_i$  of the elastic composite layer(s) for  $i = 2N + 2 \dots n - 1, n$  ( $n$  is the total material model parameter number). The gradient is calculated as follows:

$$g_i = \gamma(E_i - E_i^*) + \int_0^{t_d} \frac{\partial \mathbf{K}_{\mathbf{e}}}{\partial E_i} u(t) \cdot p(t) dt + \int_0^{t_d} \frac{\partial \mathbf{K}_{\mathbf{e}}}{\partial E_i} \frac{\partial u(t)}{\partial t} \cdot p(t) dt = \gamma(E_i - E_i^*) + \int_0^{t_d} \mathbf{K}_{\partial \mathbf{E}} u(t) \cdot p(t) dt + \beta \int_0^{t_d} \mathbf{K}_{\partial \mathbf{E}} \frac{\partial u(t)}{\partial t} \cdot p(t) dt \quad (4-87)$$

where  $E_i$  is the elastic modulus of the  $i^{th}$  elastic layer of the multilayer system;  $E_i^*$  is the elastic moduli range for penalization;  $\mathbf{K}_{\mathbf{e}}$  is the elastic stiffness matrix;  $\mathbf{K}_{\partial \mathbf{E}}$  is the elastic stiffness matrix derivative such that  $\mathbf{K}_{\partial \mathbf{E}} = \frac{\partial \mathbf{K}_{\mathbf{e}}}{\partial \mathbf{E}}$ . After assembling all the element values by summing up all values at the same nodes, the gradient can be determined.

$$g_i = \gamma(E_i - E_i^*) + \sum_{k=1}^n \mathbf{K}_{\partial \mathbf{E}} [u(t_k) \cdot p(t_k) + u(t_{k-1}) \cdot p(t_{k-1})] \frac{\Delta t}{2} + \beta \sum_{k=1}^n \mathbf{K}_{\partial \mathbf{E}} [u(t_k) - u(t_{k-1})] \cdot \frac{[p(t_k) + p(t_{k-1})]}{2} \quad (4-88)$$

#### 4.4.3 Second Order Variational Method Computing Hessian Matrix

The mathematical derivations of Hessian matrix of the dynamic viscoelastic multilayer systems are developed and detailed in the following. Computation of Hessian matrix involves three steps in sequence (see Equations (4-19)-(4-21)). The numerical solutions are developed and detailed in the followings.

##### 4.4.3.1 Incremental state equation to determine incremental deflection $\tilde{u}$

The numerical solution of Equation (4-19) consists of three terms which are computed as follows in sequence:

The second order variation with respect to  $p$ :

$$\frac{\partial \mathcal{L}(\hat{p})(\hat{p})}{\partial^2 p} = \frac{\partial}{\partial p} \left( \frac{\partial \mathcal{L}}{\partial p} \right) = 0 \quad (4-89)$$

The second order variation with respect to  $u$ , which is equal to the first order variation of  $\partial \mathcal{L} / \partial p$  (see Equation (4-31) with respect to  $u$ :

$$\begin{aligned} \frac{\partial \mathcal{L}(\hat{p})(\tilde{u})}{\partial p \partial u} &= \int_0^{t_d} \int_{\Omega} \left( \int_0^t R(t-\tau) \frac{\partial(\tilde{u}(\tau))}{\partial \tau} d\tau \right) \hat{p}(t) d\Omega dt + \int_0^{t_d} \mathbf{C} \frac{\partial \tilde{u}(t)}{\partial t} \cdot \hat{\mathbf{p}} dt + \\ &\int_0^{t_d} \mathbf{M} \frac{\partial^2 \tilde{u}}{\partial t^2} \hat{p}(t) dt \quad (4-90) \end{aligned}$$

The second order variation with respect to  $m$ :

$$\begin{aligned} \frac{\partial \mathcal{L}(\hat{p})(\tilde{m})}{\partial p \partial m} &= \int_0^{t_d} \frac{\partial}{\partial m} \left( \int_{\Omega} \int_0^t R(t-\tau) \frac{\partial(u(\tau))}{\partial \tau} d\tau \hat{p}(t) d\Omega \right) dt + \frac{\partial}{\partial m} \int_0^{t_d} \mathbf{C} \frac{\partial u(t)}{\partial t} \hat{p}(t) dt = \\ &\int_0^{t_d} \left( \int_{\Omega} \int_0^t \frac{\partial R(t-\tau)}{\partial m} \frac{\partial(u(\tau))}{\partial \tau} d\tau \hat{p}(t) d\Omega \right) dt + \beta \frac{\partial \mathbf{K}}{\partial m} \int_0^{t_d} \frac{\partial u(t)}{\partial t} \hat{p}(t) dt \quad (4-91) \end{aligned}$$

where the viscoelastic stress term can be reformulated as follows:

$$\begin{aligned}\sigma(t)_R &= \int_0^t R(t-\tau) \frac{\partial(u(\tau))}{\partial\tau} d\tau = \int_0^t R(t-\tau) du(\tau) = R(0)u(t) - \\ &\int_0^t u(\tau) \frac{\partial R(t-\tau)}{\partial\tau} d\tau \quad (\text{given } u(0) = 0)\end{aligned}\quad (4-92)$$

Substitute Equation (4-92) into Equation (4-91):

$$\begin{aligned}\frac{\partial\mathcal{L}(\hat{p})(\bar{m})}{\partial p\partial m} &= \int_0^{t_d} \frac{\partial}{\partial m} \left( \int_{\Omega} \left[ R(0)u(t) - \int_0^t u(\tau) \frac{\partial R(t-\tau)}{\partial\tau} d\tau \right] \hat{p}(t) d\Omega \right) dt + \frac{\partial}{\partial m} \int_0^{t_d} \mathbf{C} \frac{\partial u(t)}{\partial t} \hat{p}(t) dt = \\ &\int_0^{t_d} \left( \int_{\Omega} \frac{\partial R(0)}{\partial m} u(t) \hat{p}(t) - \int_{\Omega} \int_0^t u(\tau) \frac{\partial^2 R(t-\tau)}{\partial\tau\partial m} d\tau \hat{p}(t) d\Omega \right) dt + \beta \frac{\partial\mathbf{K}}{\partial m} \int_0^{t_d} \frac{\partial u(t)}{\partial t} \hat{p}(t) dt\end{aligned}\quad (4-93)$$

Sum Equations (4-89), (4-90) and (4-93) and zero it:

$$\begin{aligned}&\int_0^{t_d} \int_{\Omega} \left( \int_0^t R(t-\tau) \frac{\partial(\tilde{u}(\tau))}{\partial\tau} d\tau \right) \hat{p}(t) d\Omega dt + \int_0^{t_d} \mathbf{C} \frac{\partial\tilde{u}(t)}{\partial t} \hat{p}(t) dt + \int_0^{t_d} \mathbf{M} \frac{\partial^2\tilde{u}}{\partial t^2} \hat{p}(t) dt + \\ &\int_0^{t_d} \left( \int_{\Omega} \frac{\partial R(0)}{\partial m} u(t) \hat{p}(t) - \int_{\Omega} \int_0^t u(\tau) \frac{\partial^2 R(t-\tau)}{\partial\tau\partial m} d\tau \hat{p}(t) d\Omega \right) dt + \beta \frac{\partial\mathbf{K}}{\partial m} \int_0^{t_d} \frac{\partial u(t)}{\partial t} \hat{p}(t) dt = 0\end{aligned}\quad (4-94)$$

Equation (4-94) is subjected to  $\hat{p}(t) \in \Omega \times [0, t_d]$ , and thus  $\hat{p}(t)$  can be dismissed on both sides, and  $\forall t \in [0, t_d]$ ; hence, the following equation satisfies:

$$\begin{aligned}&\int_{\Omega} \int_0^t R(t-\tau) \frac{\partial(\tilde{u}(\tau))}{\partial\tau} d\tau d\Omega + \mathbf{C} \frac{\partial\tilde{u}(t)}{\partial t} + \mathbf{M} \frac{\partial^2\tilde{u}(t)}{\partial t^2} + \int_0^{t_d} \left( \int_{\Omega} \frac{\partial R(0)}{\partial m} u(t) - \right. \\ &\left. \int_{\Omega} \int_0^t u(\tau) \frac{\partial^2 R(t-\tau)}{\partial\tau\partial m} \right) d\tau d\Omega dt + \beta \frac{\partial\mathbf{K}}{\partial m} \frac{\partial u(t)}{\partial t} = 0\end{aligned}\quad (4-95)$$

where  $\frac{\partial R(0)}{\partial m}$  is a matrix with size of  $2n_N \times N_m$ , the  $i^{\text{th}}$  column of the matrix is  $\frac{\partial R(0)}{\partial m_i}$  for  $i = 1, 2, 3 \dots N_m$ ;  $\frac{\partial R(t-\tau)}{\partial m}$  is differential of  $R(t-\tau)$  with respect to  $m$ , a matrix with size of  $2n_N \times N_m$ , the  $i^{\text{th}}$  column of the matrix is  $\frac{\partial R(t-\tau)}{\partial m_i}$  for  $i = 1, 2, 3 \dots N_m$ ;  $n_N$  is the total FE node number, and  $N_m$  is the material model parameter number.

$$\int_0^t \frac{\partial^2 R(t-\tau)}{\partial\tau\partial m} u(\tau) d\tau = \int_0^t u(\tau) d \left( \frac{\partial R(t-\tau)}{\partial m} \right) = u(t) \frac{\partial R(0)}{\partial m} - \int_0^t \frac{\partial R(t-\tau)}{\partial m} \frac{\partial u(\tau)}{\partial\tau} d\tau\quad (4-96)$$

Substitute Equation (4-96) into (4-95):

$$\begin{aligned}&\int_{\Omega} \int_0^t R(t-\tau) \frac{\partial(\tilde{u}(\tau))}{\partial\tau} d\tau d\Omega + \mathbf{C} \frac{\partial\tilde{u}(t)}{\partial t} + \mathbf{M} \frac{\partial^2\tilde{u}(t)}{\partial t^2} + \int_{\Omega} \int_0^t \frac{\partial R(t-\tau)}{\partial m} \frac{\partial u(\tau)}{\partial\tau} d\tau d\Omega + \\ &\beta \frac{\partial\mathbf{K}}{\partial m} \frac{\partial u(t)}{\partial t} = 0\end{aligned}\quad (4-97)$$

Discretize the velocity and acceleration following the Houbolt method (Houbolt 1950, Bathe 1996):

$$\frac{\partial \tilde{u}(\tau)}{\partial t} = \frac{11\tilde{u}(k) - 18\tilde{u}(k-1) + 9\tilde{u}(k-2) - 2\tilde{u}(k-3)}{6\Delta t} \quad (4-98)\text{-a}$$

$$\frac{\partial \tilde{u}^2(k)}{\partial t^2} = \frac{2\tilde{u}(k) - 5\tilde{u}(k-1) + 4\tilde{u}(k-2) - \tilde{u}(k-3)}{\Delta t^2} \quad (4-98)\text{-b}$$

Then Equation (4-97) can be re-expressed as follows:

$$\begin{aligned} & \sum_{j=1}^k \mathbf{J}(j) \frac{\tilde{u}(t_j) - \tilde{u}(t_{j-1})}{\Delta t} + \mathbf{C} \frac{11\tilde{u}(k) - 18\tilde{u}(k-1) + 9\tilde{u}(k-2) - 2\tilde{u}(k-3)}{6\Delta t} + \\ & \mathbf{M} \frac{2\tilde{u}(k) - 5\tilde{u}(k-1) + 4\tilde{u}(k-2) - \tilde{u}(k-3)}{\Delta t^2} + \sum_{j=1}^k \mathbf{J}_{\partial m}(j) \frac{u(t_j) - u(t_{j-1})}{\Delta t} + \beta \frac{\partial \mathbf{K}}{\partial m} \frac{\partial u(t)}{\partial t} = 0 \end{aligned} \quad (4-99)$$

where  $\mathbf{J}(j) = \int_{\Omega} \int_{t_{j-1}}^{t_j} R(t - \tau) d\tau d\Omega$  is the viscoelastic stiffness matrix;  $\mathbf{J}_{\partial m}(j) = \int_{\Omega} \int_{t_{j-1}}^{t_j} \frac{\partial R(t - \tau)}{\partial m} d\tau d\Omega$  is the viscoelastic stiffness matrix derivative.

Equation (4-99) can be rearranged as follows:

$$\begin{aligned} & \left[ \frac{\mathbf{J}(k)}{\Delta t} + \frac{2\mathbf{M}}{\Delta t^2} + \frac{11\mathbf{C}}{6\Delta t} \right] \tilde{u}(k) = \frac{\mathbf{J}(k)}{\Delta t} \tilde{u}(k-1) - \sum_{j=1}^{k-1} \mathbf{J}(j) \frac{\tilde{u}(t_j) - \tilde{u}(t_{j-1})}{\Delta t} - \\ & \mathbf{C} \frac{-18\tilde{u}(k-1) + 9\tilde{u}(k-2) - 2\tilde{u}(k-3)}{6\Delta t} - \mathbf{M} \frac{-5\tilde{u}(k-1) + 4\tilde{u}(k-2) - \tilde{u}(k-3)}{\Delta t^2} - \sum_{j=1}^k \mathbf{J}_{\partial m}(j) \frac{u(t_j) - u(t_{j-1})}{\Delta t} - \\ & \beta \frac{\partial \mathbf{K}}{\partial m} \frac{11u(k) - 18u(k-1) + 9u(k-2) - 2u(k-3)}{6\Delta t} \end{aligned} \quad (4-100)$$

where  $\mathbf{M}$  is the mass matrix;  $\mathbf{J}_{\partial m}(k)$  is the viscoelastic stiffness matrix derivative;  $\tilde{u}(k-1)$ ,  $\tilde{u}(k-2)$ ,  $\tilde{u}(k-3)$  are computed results at previous time steps; and  $u(j)$  for  $j = k$  to  $k-3$  are computed  $u$  values earlier.

Equation (4-100) can be re-reduced to:

$$\tilde{\mathbf{K}}_u \tilde{u}(k) = \tilde{\mathfrak{R}}_u \quad (4-101)$$

where  $\tilde{\mathbf{K}}_u$  is a stiffness matrix ( $\tilde{\mathbf{K}}_u = \frac{\mathbf{J}(k)}{\Delta t} + \frac{2\mathbf{M}}{\Delta t^2} + \frac{11\mathbf{C}}{6\Delta t}$ );  $\tilde{\mathfrak{R}}_u$  is a reaction force.

$$\begin{aligned} \tilde{\mathbf{R}}_u = & \left( \frac{J(k)}{\Delta t} + \frac{3\mathbf{C}}{\Delta t} + \frac{5\mathbf{M}}{\Delta t^2} \right) \tilde{u}(k-1) - \left( \frac{3\mathbf{C}}{2\Delta t} + \frac{4\mathbf{M}}{\Delta t^2} \right) \tilde{u}(k-2) + \left( \frac{\mathbf{C}}{3\Delta t} + \frac{\mathbf{M}}{\Delta t^2} \right) \tilde{u}(k-3) - \\ & \sum_{j=1}^{k-1} \mathbf{J}(j) \frac{\tilde{u}(t_j) - \tilde{u}(t_{j-1})}{\Delta t} - \sum_{j=1}^k \mathbf{J} \partial m(j) \frac{u(t_j) - u(t_{j-1})}{\Delta t} - \beta \frac{\partial \mathbf{K}}{\partial m} \frac{11u(k) - 18u(k-1) + 9u(k-2) - 2u(k-3)}{6\Delta t} \end{aligned} \quad (4-102)$$

After assembling values of all elements, the global linear system can be formed and solved to determine the incremental displacement  $\tilde{u}(t)$ .

#### 4.4.3.2 Incremental adjoint equation to determine incremental test function $\tilde{p}$

To find the incremental test function, the second order variations of the Lagrangian is computed following Equation (4-20). Each term in Equation (4-20) is computed as follows in sequence:

The second order variation with respect to  $p$ , which is equal to the first order variation of  $\partial \mathcal{L} / \partial u$  (see Equation (4-39) with respect to  $p$ :

$$\begin{aligned} \frac{\partial \mathcal{L}(\hat{u}) \mathcal{L}(\tilde{p})}{\partial u \partial p} = & \int_0^{t_d} \int_{\Omega} \hat{u}(t) \int_t^{t_d} R(\tau - t) \frac{\partial \tilde{p}(\tau)}{\partial \tau} d\tau d\Omega dt - \int_0^{t_d} \hat{u}(t) \mathbf{C} \frac{\partial \tilde{p}(t)}{\partial t} dt + \\ & \int_0^{t_d} \hat{u}(t) \mathbf{M} \frac{\partial^2 \tilde{p}(t)}{\partial t^2} dt \quad (4-103) \end{aligned}$$

The second order variation with respect to  $u$ , which is equal to the first order variation of  $\partial \mathcal{L} / \partial u$  Equation (4-39) with respect to  $u$ :

$$\frac{\partial \mathcal{L}(\hat{u}) \mathcal{L}(\tilde{u})}{\partial^2 u} = \int_0^{t_d} \int_{\Omega} \mathbf{\Phi}^T \tilde{u} \hat{u} \boldsymbol{\phi} d\Omega dt = \int_0^{t_d} \mathbf{M}_0 \tilde{u} \hat{u} dt \quad (4-104)$$

where  $\mathbf{M}_0$  is a mass matrix unit expressed as follows:

$$\mathbf{M}_0 = \int_{\Omega} \mathbf{\Phi}^T \boldsymbol{\phi} d\Omega = \frac{\mathbf{M}}{\rho} \quad (4-105)$$

The second order variation of Lagrangian with respect to  $m$ , which equals to the first order variation of  $\partial \mathcal{L} / \partial u$  with respect to  $m$  can be derived as:

$$\frac{\partial \ell \mathcal{L}(\hat{u}) \mathcal{L}(\tilde{m})}{\partial u \partial m} = \int_0^{t_d} \frac{\partial}{\partial m} \int_{\Omega} \hat{u}(t) \int_t^{t_d} R(\tau - t) \frac{\partial p(\tau)}{\partial \tau} d\tau d\Omega dt - \frac{\partial}{\partial m} \int_0^{t_d} \hat{u}(t) \mathbf{C} \frac{\partial p(t)}{\partial t} dt \quad (4-106)$$

Sum these three terms and zero it as follows:

$$\begin{aligned}
& \int_0^{t_d} \int_{\Omega} \hat{u}(t) \int_t^{t_d} R(\tau - t) \frac{\partial \tilde{p}(\tau)}{\partial \tau} d\tau d\Omega dt - \int_0^{t_d} \hat{u}(t) \mathbf{C} \frac{\partial \tilde{p}(t)}{\partial t} dt + \int_0^{t_d} \hat{u}(t) \mathbf{M} \frac{\partial^2 \tilde{p}(t)}{\partial t^2} dt + \\
& \int_0^{t_d} \mathbf{M}_0 \tilde{u} \hat{u} dt + \int_0^{t_d} \frac{\partial}{\partial m} \int_{\Omega} \hat{u}(t) \int_t^{t_d} R(\tau - t) \frac{\partial p(\tau)}{\partial \tau} d\tau d\Omega dt - \beta \frac{\partial \mathbf{K}}{\partial m} \int_0^{t_d} \hat{u}(t) \frac{\partial p(t)}{\partial t} dt = 0
\end{aligned} \tag{4-107}$$

It is subjected to  $\forall \hat{u}(t) \in \Omega \times [0, t_d]$ , and thus  $\hat{u}(t)$  can be dismissed on both sides and  $\forall t \in [0, t_d]$  the following equation satisfies:

$$\begin{aligned}
& \int_{\Omega} \int_t^{t_d} R(\tau - t) \frac{\partial \tilde{p}(\tau)}{\partial \tau} d\tau d\Omega - \mathbf{C} \frac{\partial \tilde{p}(t)}{\partial t} + \mathbf{M} \frac{\partial^2 \tilde{p}(t)}{\partial t^2} + \mathbf{M}_0 \tilde{u} + \int_{\Omega} \int_t^{t_d} \frac{\partial R(\tau - t)}{\partial m} \frac{\partial p(\tau)}{\partial \tau} d\tau d\Omega - \\
& \beta \frac{\partial \mathbf{K}}{\partial m} \frac{\partial p(t)}{\partial t} = 0
\end{aligned} \tag{4-108}$$

Discretize the first and second order differentials of  $\tilde{p}(t)$  with the Houbolt method (Houbolt 1950, Bathe 1996):

$$\frac{\partial \tilde{p}(t)}{\partial t} = \frac{11\tilde{p}(k) - 18\tilde{p}(k-1) + 9\tilde{p}(k-2) - 2\tilde{p}(k-3)}{6\Delta t} \tag{4-109-a}$$

$$\frac{\partial^2 \tilde{p}(t)}{\partial t^2} = \frac{2\tilde{p}(k) - 5\tilde{p}(k-1) + 4\tilde{p}(k-2) - \tilde{p}(k-3)}{\Delta t^2} \tag{4-109-b}$$

The tangent is discretized following the explicit Euler rule:

$$\frac{\partial \tilde{p}(\tau)}{\partial \tau} = \frac{\tilde{p}(t_j) - \tilde{p}(t_{j-1})}{\Delta t} \tag{4-110}$$

Then Equation (4-108) can be re-derived as follows:

$$\begin{aligned}
& \int_{\Omega} \sum_{j=1}^k \int_{t_{j-1}}^{t_j} R(t - \tau) d\tau d\Omega \frac{\tilde{p}(t_k) - \tilde{p}(t_{k-1})}{\Delta t} - \mathbf{C} \frac{11\tilde{p}(k) - 18\tilde{p}(k-1) + 9\tilde{p}(k-2) - 2\tilde{p}(k-3)}{6\Delta t} + \\
& \mathbf{M} \frac{2\tilde{p}(k) - 5\tilde{p}(k-1) + 4\tilde{p}(k-2) - \tilde{p}(k-3)}{\Delta t^2} = -\mathbf{M}_0 \tilde{u}(t) - \int_{\Omega} \sum_{j=1}^k \int_{t_{j-1}}^{t_j} \frac{\partial R(t - \tau)}{\partial m} d\tau d\Omega \frac{p(t_k) - p(t_{k-1})}{\Delta t} + \\
& \beta \frac{\partial \mathbf{K}}{\partial m} \frac{11p(k) - 18p(k-1) + 9p(k-2) - 2p(k-3)}{6\Delta t}
\end{aligned} \tag{4-111}$$

It can be briefed and rearranged as follows:

$$\begin{aligned}
& \sum_{j=1}^k \mathbf{J}(k) \frac{\tilde{p}(t_k) - \tilde{p}(t_{k-1})}{\Delta t} - \mathbf{C} \frac{11\tilde{p}(k) - 18\tilde{p}(k-1) + 9\tilde{p}(k-2) - 2\tilde{p}(k-3)}{6\Delta t} + \\
& \mathbf{M} \frac{2\tilde{p}(k) - 5\tilde{p}(k-1) + 4\tilde{p}(k-2) - \tilde{p}(k-3)}{\Delta t^2} = -\mathbf{M}_0 \tilde{u}(t) - \sum_{j=1}^k \mathbf{J}_{\partial m}(j) \frac{p(t_k) - p(t_{k-1})}{\Delta t} - \\
& \beta \frac{\partial \mathbf{K}}{\partial m} \frac{11p(k) - 18p(k-1) + 9p(k-2) - 2p(k-3)}{6\Delta t}
\end{aligned} \tag{4-112}$$

where  $\mathbf{J}(\mathbf{k}) = \int_{t_{j-1}}^{t_j} R(t - \tau) d\tau$  is the viscoelastic stiffness matrix;  $\mathbf{J}_{\partial m}(j) = \int_{\Omega} \int_{t_{j-1}}^{t_j} \frac{\partial R(t - \tau)}{\partial m} d\tau d\Omega$  is the viscoelastic stiffness matrix derivative; and  $\tilde{u}(t) = \tilde{u}(k)$  is calculated value at the current or  $k^{th}$  time step as discussed above.

Equation (4-112) can be rearranged as follows for building the linear system:

$$\begin{aligned} \left[ \frac{\mathbf{J}(k)}{\Delta t} + \frac{2\mathbf{M}}{t^2} - \frac{11\mathbf{C}}{6\Delta t} \right] \tilde{p}(t_k) &= \mathbf{J}(k) \frac{\tilde{p}(t_{k-1})}{\Delta t} - \sum_{j=1}^{k-1} \mathbf{J}(k) \frac{\tilde{p}(t_k) - \tilde{p}(t_{k-1})}{\Delta t} + \\ \mathbf{C} \frac{-18\tilde{p}(k-1) + 9\tilde{p}(k-2) - 2p(k-3)}{6\Delta t} - \mathbf{M} \frac{-5\tilde{p}(k-1) + 4\tilde{p}(k-2) - \tilde{p}(k-3)}{\Delta t^2} - \mathbf{M}_0 \tilde{u}(k) - \\ \sum_{j=1}^k \mathbf{J}_{\partial m}(j) \frac{p(t_j) - p(t_{j-1})}{\Delta t} - \beta \frac{\partial \mathbf{K}}{\partial m} \frac{11p(k) - 18p(k-1) + 9p(k-2) - 2p(k-3)}{6\Delta t} \end{aligned} \quad (4-113)$$

Combining the dynamic viscoelastic feature of the viscoelastic layers and the dynamic elastic feature of other elastic materials, the linear system can be derived as:

$$\begin{aligned} \left[ \mathbf{K}_e + \frac{\mathbf{J}(k)}{\Delta t} + \frac{2\mathbf{M}}{t^2} - \frac{11\mathbf{C}}{6\Delta t} \right] \tilde{p}(t_k) &= \mathbf{J}(k) \frac{\tilde{p}(t_{k-1})}{\Delta t} - \sum_{j=1}^{k-1} \mathbf{J}(k) \frac{\tilde{p}(t_k) - \tilde{p}(t_{k-1})}{\Delta t} + \\ \mathbf{C} \frac{-18\tilde{p}(k-1) + 9\tilde{p}(k-2) - 2p(k-3)}{6\Delta t} - \mathbf{M} \frac{-5\tilde{p}(k-1) + 4\tilde{p}(k-2) - \tilde{p}(k-3)}{\Delta t^2} - \mathbf{M}_0 \tilde{u}(k) - \\ \sum_{j=1}^k \mathbf{J}_{\partial m}(j) \frac{p(t_j) - p(t_{j-1})}{\Delta t} - \beta \frac{\partial \mathbf{K}}{\partial m} \frac{11p(k) - 18p(k-1) + 9p(k-2) - 2p(k-3)}{6\Delta t} \end{aligned} \quad (4-114)$$

where  $\mathbf{K}_e$  is the elastic stiffness matrix of the elastic layer(s) of the multilayer system,  $2n_N \times 2n_N$  matrix ( $n_N$  is the total FE node number); for the viscoelastic layers the element values are all zeroed.

For the global system after assembling all element and node values, Equation (4-114) can be re-reduced to:

$$\tilde{\mathbf{K}}_p \tilde{P}(k) = \tilde{\mathfrak{R}}_p \quad (4-115)$$

where  $\tilde{\mathbf{K}}_p$  is stiffness matrix for test function linear system and  $\tilde{\mathfrak{R}}_p$  is a reaction force for test function linear system:

$$\tilde{\mathbf{K}}_p = \mathbf{K}_e + \frac{\mathbf{J}(k)}{\Delta t} + \frac{2\mathbf{M}}{t^2} - \frac{11\mathbf{C}}{6\Delta t} \quad (4-116)$$

$$\tilde{\mathfrak{R}}_p =$$

$$\begin{aligned}
& \left( \frac{J(k)}{\Delta t} - \frac{3C}{\Delta t} + \frac{5M}{\Delta t^2} \right) \tilde{p}(t_{k-1}) + \left( \frac{3C}{2\Delta t} - \frac{4M}{\Delta t^2} \right) \tilde{p}(t_{k-2}) - \left( \frac{C}{3\Delta t} - \frac{M}{\Delta t^2} \right) \tilde{p}(t_{k-3}) - \\
& \sum_{j=1}^{k-1} J(k) \frac{\tilde{p}(t_k) - \tilde{p}(t_{k-1})}{\Delta t} - \mathbf{M}_0 \tilde{u}(k) - \sum_{j=1}^k J_{\partial m}(j) \frac{p(t_j) - p(t_{j-1})}{\Delta t} - \\
& \beta \frac{\partial \mathbf{K}}{\partial m} \frac{11p(k) - 18p(k-1) + 9p(k-2) - 2p(k-3)}{6\Delta t}
\end{aligned} \tag{4-117}$$

Thus, the global linear system is formed and solved to determine the incremental test function  $\tilde{p}(t)$ .

#### 4.4.3.3 Incremental decision equation to determine Hessian

Given the incremental response and test function calculated above, the Hessian matrix can be determined following Equation (4-21), in which each term is numerically computed as follows in sequence:

Second order variation of Lagrangian with respect to  $p$ , which is equal to the first order variation of  $\partial \mathcal{L} / \partial m$  (see Equation (4-60)) with respect to  $p$  as follows:

$$\frac{\partial \mathcal{L}(\hat{m}) \mathcal{L}(\tilde{p})}{\partial m \partial p} = \int_0^{t_d} \int_{\Omega} \int_0^t \frac{\partial R(t-\tau)}{\partial m} \frac{\partial(u(\tau))}{\partial \tau} \hat{m} d\tau \tilde{p}(t) d\Omega dt \tag{4-118}$$

Second order variation of Lagrangian with respect to  $u$ , which is equal to the first order variation of  $\partial \mathcal{L} / \partial m$  (see Equation (4-60)) with respect to  $u$  as follows:

$$\frac{\partial \mathcal{L}(\hat{m}) \ell(\tilde{u})}{\partial m \partial u} = \int_0^{t_d} \int_{\Omega} \int_0^t \frac{\partial R(t-\tau)}{\partial m} \frac{\partial(\tilde{u}(\tau))}{\partial \tau} \hat{m} d\tau p(t) d\Omega dt \tag{4-119}$$

Second order variation of Lagrangian with respect to  $m$ , which is equal to the first order variation of  $\partial \mathcal{L} / \partial m$  (see Equation (4-60)) with respect to  $m$  as follows:

$$\frac{\partial \mathcal{L}(\hat{m}) \mathcal{L}(\tilde{m})}{\partial^2 m} = \alpha \int_{\Omega} \hat{m} \tilde{m} d\Omega + \left[ \int_0^{t_d} \int_{\Omega} \left( \int_0^t \frac{\partial^2 R(t-\tau)}{\partial m^2} \frac{\partial(u(\tau))}{\partial \tau} \hat{m} d\tau \right) d\Omega p(t) dt \right] \tag{4-120}$$

Sum these three terms to determine hessian matrix:

$$\begin{aligned}
\int \mathbf{H} \cdot \hat{\mathbf{m}} d\Omega &= \int_0^{t_d} \int_{\Omega} \int_0^t \frac{\partial R(t-\tau)}{\partial m} \frac{\partial(u(\tau))}{\partial \tau} d\tau \tilde{p}(t) \cdot \hat{\mathbf{m}} d\Omega dt + \int_0^{t_d} \int_{\Omega} \int_0^t \frac{\partial R(t-\tau)}{\partial m} \frac{\partial(\tilde{u}(\tau))}{\partial \tau} d\tau p(t) \cdot \\
&\hat{\mathbf{m}} d\Omega dt + \alpha \int_{\Omega} \tilde{m} \cdot \hat{\mathbf{m}} d\Omega + \left[ \int_0^{t_d} \int_{\Omega} \left( \int_0^t \frac{\partial^2 R(t-\tau)}{\partial m^2} \frac{\partial(u(\tau))}{\partial \tau} d\tau \right) d\Omega p(t) \cdot \hat{\mathbf{m}} dt \right]
\end{aligned} \tag{4-121}$$

Substitute  $\mathbf{H} = \Phi \mathbf{H}$  and  $\hat{\mathbf{m}} = \Phi \hat{\mathbf{m}}$  ( $\mathbf{H}$  and  $\hat{\mathbf{m}}$  are those at FE nodes), where  $\Phi$  is the shape function.  $\Phi$  is taken as 1 since the material model parameters are constants for the same layer of the multilayer system.  $\hat{\mathbf{m}}$  is arbitrary and thus vanishes on both sides. Therefore, the Hessian matrix can be determined as follows:

$$\begin{aligned} H = & \int_0^{t_d} \int_{\Omega} \int_0^t \mathbf{J}_{\partial \mathbf{m}} \frac{u(t_j) - u(t_{j-1})}{\Delta t} d\tau \tilde{p}(t) d\Omega dt + \\ & \int_0^{t_d} \int_{\Omega} \sum_{j=1}^k \int_{t_{j-1}}^{t_j} \mathbf{J}_{\partial \mathbf{m}} d\tau \frac{\tilde{u}(t_j) - \tilde{u}(t_{j-1})}{\Delta t} p(t) dt + \gamma \tilde{\mathbf{m}} + \\ & \int_0^{t_d} \int_{\Omega} \sum_{j=1}^k \mathbf{J}_{\partial^2 \mathbf{m}} \frac{u(t_j) - u(t_{j-1})}{\Delta t} p(t) d\Omega dt \end{aligned} \quad (4-122)$$

where  $\mathbf{J}_{\partial \mathbf{m}} = \frac{\partial R(t-\tau)}{\partial \mathbf{m}}$ ;  $\tilde{\mathbf{m}}$  is the search direction which can be approximated from the one in the last iteration step;  $\mathbf{J}_{\partial^2 \mathbf{m}}$  is the second order differential of viscoelastic stiffness matrix.  $\mathbf{J}_{\partial^2 \mathbf{m}}$  is defined as follows:

$$\mathbf{J}_{\partial^2 \mathbf{m}} := \int_{\Omega} \int_{t_{j-1}}^{t_j} \frac{\partial^2 R(t-\tau)}{\partial \mathbf{m}^2} d\tau \quad (4-123)$$

Discretize  $\tilde{p}(t) = \frac{[\tilde{p}(t_{k-1}) + \tilde{p}(t_k)]}{2}$  and  $p(t) = \frac{[p(t_{k-1}) + p(t_k)]}{2}$  following the Euler's method and the Hessian matrix can be discretized as follows:

$$\begin{aligned} H = & \sum_{k=1}^n \sum_{j=1}^k [u(t_j) - u(t_{j-1})] \mathbf{J}_{\partial \mathbf{m}}(j) \frac{[\tilde{p}(t_{k-1}) + \tilde{p}(t_k)]}{2} + \sum_{k=1}^n \sum_{j=1}^k \mathbf{J}_{\partial \mathbf{m}}(j) [\tilde{u}(t_j) - \\ & \tilde{u}(t_{j-1})] \frac{[p(t_{k-1}) + p(t_k)]}{2} + \gamma \tilde{\mathbf{m}} + \sum_{k=1}^n \sum_{j=1}^k \mathbf{J}_{\partial^2 \mathbf{m}}(k) (u(t_j) - u(t_{j-1})) \frac{[p(t_{k-1}) + p(t_k)]}{2} \end{aligned} \quad (4-124)$$

$\mathbf{J}_{\partial^2 \mathbf{m}}$  is a matrix with a size of  $2n_N \times n_m$  ( $n_N$  is the total node number and  $n_m$  is the material model parameter number). The key is to calculate  $\mathbf{J}_{\partial^2 \mathbf{m}}$  in which the differential term can be derived as follows:

For the viscoelastic layers:

$$\frac{\partial^2 R(t-\tau)}{\partial m_1^2} = \frac{\partial^2 R(t-\tau)}{\partial E_0^2} = 0 \quad (4-125)$$

where  $E_0$  is the first elastic modulus of the spring; and for  $i = 1, 2, \dots, N$ :

$$\frac{\partial E(t-\tau)}{\partial^2 E_i} = \frac{\partial}{\partial E_i} \left[ e^{-\frac{E_i}{\eta_i}(t-\tau)} - \frac{E_i}{\eta_i}(t-\tau)e^{-\frac{E_i}{\eta_i}(t-\tau)} \right] = \left[ \frac{2}{\eta_i}(t-\tau)e^{-\frac{E_i}{\eta_i}(t-\tau)} + \frac{E_i}{\eta_i^2}(t-\tau)^2 e^{-\frac{E_i}{\eta_i}(t-\tau)} \right] \quad (4-126)$$

$$\frac{\partial E(t-\tau)}{\partial^2 \eta_i} = \frac{\partial}{\partial \eta_i} \left[ \frac{E_i^2}{\eta_i^2}(t-\tau)e^{-\frac{E_i}{\eta_i}(t-\tau)} \right] = -\frac{2E_i^2}{\eta_i^3}(t-\tau)e^{-\frac{E_i}{\eta_i}(t-\tau)} + \frac{E_i^3}{\eta_i^4}(t-\tau)^2 e^{-\frac{E_i}{\eta_i}(t-\tau)} \quad (4-127)$$

For the elastic layers:

$$\frac{\partial E(t-\tau)}{\partial^2 E_i} = 0 \quad (4-128)$$

With these terms derived,  $J_{\partial^2 m}$  is computed following Equation (4-123).

#### 4.4.4 BFGS Algorithm for Hessian Matrix Computation

The computation of the Hessian matrix of the 2<sup>nd</sup> order differentials involves numerical complexity and could be very costly with additional solutions of two linear systems. An alternative option is to use the Broyden-Fletcher-Goldfarb-Shanno (BFGS) algorithm to approximate the Hessian matrix (developed by Broyden), where no linear system solutions are needed. With the BFGS algorithm, the Hessian matrix is calculated as a function of the search direction and step length at the previous iteration, and the gradient at both the current and previous iteration steps:

$$H_{k+1} = H_k + \frac{\Delta g \Delta g^T}{\Delta g^T \Delta m} - \frac{H_k \Delta m \Delta m^T H_k}{\Delta m^T H_k \Delta m} \quad (4-129)$$

where  $H_k$  is Hessian matrix at iteration step  $k$ ;  $\Delta g = g_{k+1} - g_k$  is the gradient variation at the current and previous iteration step;  $\Delta m = \alpha_k m_k$  is the material model parameter variation,  $\alpha_k$  is step length, and  $m_k$  is search direction.  $H_0$  is set as an identify matrix  $\mathbf{I}$ .

#### 4.4.5 Inverse Computation of Material Properties

Following the procedure described in Section 4.3, the material model parameters including the generalized Maxwell model (Prony series) parameters and elastic moduli are inverted. For the VE material, the master curve of dynamic modulus  $E^*$  can be

determined from the inverted relaxation modulus  $E(t)$  through the Laplace transformation as follows (Park and Schapery 1999):

$$E^*(\omega) = i\omega \ell[E(x)']_{s=i\omega} = i\omega \int_0^{\infty} E(\tau)e^{-i\omega\tau} d\tau \quad (4-130)$$

where  $E(x)$  is relaxation modulus;  $\omega$  is angular frequency;  $i$  is imaginary unit of complex number;  $\ell$  is Laplace transformation;  $s$  is the transform variable, and  $\tau = t - x$ .

Accordingly, the storage and loss modulus (real and imaginary part) and phase angle  $\delta$  could be expanded as follows:

$$E'(f) = E_{\infty} + \sum_{i=1}^n \frac{4E_i\tau_i^2\pi^2 f^2}{1+4\tau_i^2\pi^2 f^2} = E_{\infty} + \sum_{i=1}^n \frac{4E_i\pi^2 f^2}{1/\tau_i^2+4\pi^2 f^2} \quad (4-131)\text{-a}$$

$$E''(f) = \sum_{i=1}^n \frac{2E_i\tau_i\pi f}{1+4\tau_i^2\pi^2 f^2} = \sum_{i=1}^n \frac{2E_i\pi f}{1/\tau_i+4\tau_i\pi^2 f^2} \quad (4-131)\text{-b}$$

$$\delta = \tan^{-1} \frac{E'}{E''} \quad (4-131)\text{-c}$$

where  $f = \omega/2\pi$  is the frequency (Hz).

## 4.5. Computer Program Development and Validation

### 4.5.1 Computer Program Development

A computer program written in Intel Visual Fortran® (IVF) language was developed for the entire numerical computation. Figure 71 shows the flow chart of the inverse computation of the developed computer coding. The inputs include the dynamic loading time histories and the model geometry information. Two core modules were designed: I) R-G-H Module for the computations of displacement response, gradient, and Hessian matrix which is calculated based on the BFGS algorithm; and II) Inverse Computation Module, which performs inverse computation for the search direction, step length, and updated material model parameter values of each iteration. Module II calls Module I during each iteration procedure. It outputs the inversed material model parameter values.

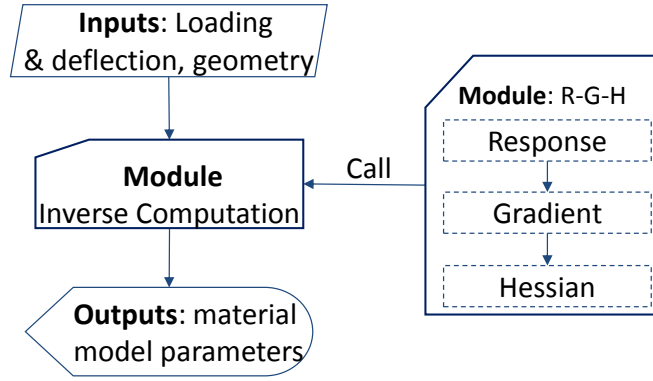


**Figure 71. Flow chart of the developed computer program for inverse computation.**

## 4.5.2 Validation Method

### 4.5.2.1 Validation of gradient

According to the Lagrangian theory, the gradient could also be calculated from the cost function as follows:

$$g = \lim_{\Delta m \rightarrow 0} \frac{\Delta J}{\Delta m} \quad (4-132)$$

where  $J$  is the cost function,  $\Delta m$  is a variation of material property.

According to the finite difference method, given a sufficiently small  $\Delta m$ , the gradient of the  $i^{th}$  material model parameter for  $i = 1, 2, 3 \dots n$ , can be approximated as follows (the regularization term is zeroed here when  $m$  is within range):

$$g_i = \frac{\Delta J}{\Delta m} = \frac{J(m+\Delta m_i) - J(m_i)}{\Delta m_i} = \frac{1}{2\Delta m} \int_0^{t_d} \int_{\partial\Omega_5} (u(m_i + \Delta m_i) - u_{obs})^2 dsdt - \frac{1}{2\Delta m} \int_0^{t_d} \int_{\partial\Omega_5} (u(m_i) - u_{obs})^2 dsdt = \frac{1}{2\Delta m} \int_0^{t_d} \int_{\partial\Omega_5} [u(m_i + \Delta m_i) + u(m_i) - 2u_{obs}] \cdot [u(m_i + \Delta m_i) - u(m_i)] dsdt \quad (4-133)$$

### 4.5.2.2 Validation of material property inversion

A theoretical validation method is proposed as follows:

Step 1: The first step is to accept following information: (a) material model parameters as true values, including the VE model parameters (e.g.,  $E_i$  and  $\eta_i$  of the

generalized Maxwell model from experimental data), and elastic moduli of elastic layers; (b) model geometry; (c) Poisson's ratio, which is not inverted in this research, and (d) the measured loading pulse.

Step 2: Given data from (a) to (d) in Step 1, the deflection responses at those geophone places are simulated using FE method. The simulated response (e.g., deflection) time history is treated as observations  $u_{obs}$  and true values.

Step 3: Now, given the  $u_{obs}$  and loading history, the material model parameters are inverted and named as  $m$ ;

Step 4: For validation, the inverted material model parameter values are compared with the true values given in Step 1.

An alternative experimental validation approach has also been employed, where the material dynamic moduli of asphalt concrete, are measured in the laboratory and compared with the inverse results. However, one should note that the experimental test conditions are carried out on a small scale (e.g., 6" × 4" cylinder) are very different than the in-situ condition where solids are confined in a large body. Therefore, there may be noticeable differences between the inverse results and experimental measurements.

## **4.6. Implementation**

The developed model and numerical method was implemented into a multilayer flexible pavement structure with AC as the surface layer, under the falling weight deflectometer (FWD) nondestructive test.

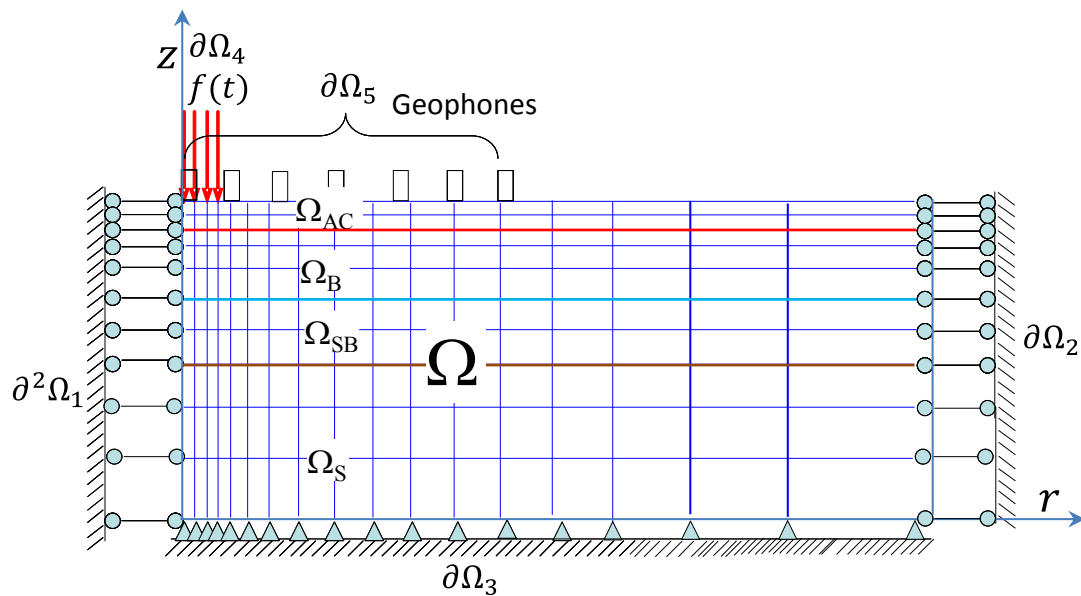
### **4.6.1 Experimental Design**

As shown in Figure 72 during the FWD test, a mass is dropped on the plate to induce a dynamic loading pulse to emulate the vehicle loading (e.g, stress amplitude of 500 kPa). The loading pulse with time (e.g., every 0.06 second) was recorded by a loading sensor. Several geophones (displacement sensors) were set at a variable distances

(e.g., 0 to 1.5m) to measure the vertical deflection response pulses in a short time period such as 0.1 second.



a)



b)

**Figure 72. a) Highway pavement under FWD tests; b) axisymmetric structure model.**

#### 4.6.2 Pavement Model Domain and Numerical Solution

Because of the much larger size of the model domain (e.g., a 400 m<sup>2</sup> parking lot) as compared to the small loading area (e.g., 0.15 m radius of loading plate), an axisymmetric layered model has been used commonly to describe this problem (Xu and

Prozzi 2014) as shown in Figure 72b. The 8-node two-dimensional ring element was used to model the space domain and the three-node, one-dimensional element was used to model the loading area of the axisymmetric model (see Figure 72). The displacements at boundaries and the geophone area are as follows:

$$u_r = 0 \in \partial^2\Omega_1 \times [0, t] \quad (4-134)\text{-a}$$

$$u_r = 0 \in \partial\Omega_2 \times \partial, t] \quad (4-134)\text{-b}$$

$$u_r = 0 \in \partial\Omega_2 \times [0, t] \quad (4-134)\text{-c}$$

$$u_z = 0 \in \partial\Omega_3 \times [0, t] \quad (4-134)\text{-d}$$

$$u_5(t) = u(t) \in \partial\Omega_5 \times [0, t] \quad (4-134)\text{-e}$$

where  $\partial^2\Omega_1$  is the axisymmetric line of the model;  $\partial\Omega_2$  is the boundary area of the far field;  $\partial\Omega_3$  is the boundary area at the model bottom; and  $\partial\Omega_5$  is the loading area. AC is a typical VE material under short loading pulses and is temperature dependent (Xu and Solaimanian 2009). Furthermore, it is modeled by the generalized Maxwell model. Other materials could be considered damped elastic. The material vector could be expressed as follows:

$$\bar{\mathbf{m}} = [E_0, E_{i=1,2,3 \dots N}, E_b, \eta_{i=1,2,3 \dots N}, E_b, E_{sb}, E_s]^T \quad (4-135)$$

where,  $E_b$  is elastic modulus of base layer,  $E_{sb}$  is elastic modulus of subbase layer,  $E_s$  is elastic modulus of soil,  $E_i$  is elastic modulus of  $i^{th}$  spring of the generalized Maxwell model of AC layer for  $i = 1,2,3 \dots N$ ,  $\eta_i$  is viscosity of the  $i^{th}$  dashpot of the generalized Maxwell model of AC layer for  $i = 1,2,3 \dots N$ ,  $N$  is the term number of the spring and dashpot series of the VE model of AC layer.

The finite element (FE) method is developed for the numerical solution. As shown in **Figure 73**, the isoparametric 8-node ring element is used for the model body of the space domain, and the 2-node surface element is used for the surface tracking area under FWD loading. The ring element uses 4 Gauss points at the local coordinates of  $(\xi, \psi) = (-\frac{1}{\sqrt{3}}, \frac{1}{\sqrt{3}}), (\frac{1}{\sqrt{3}}, \frac{1}{\sqrt{3}}), (-\frac{1}{\sqrt{3}}, -\frac{1}{\sqrt{3}}),$  and  $(\frac{1}{\sqrt{3}}, -\frac{1}{\sqrt{3}})$ .

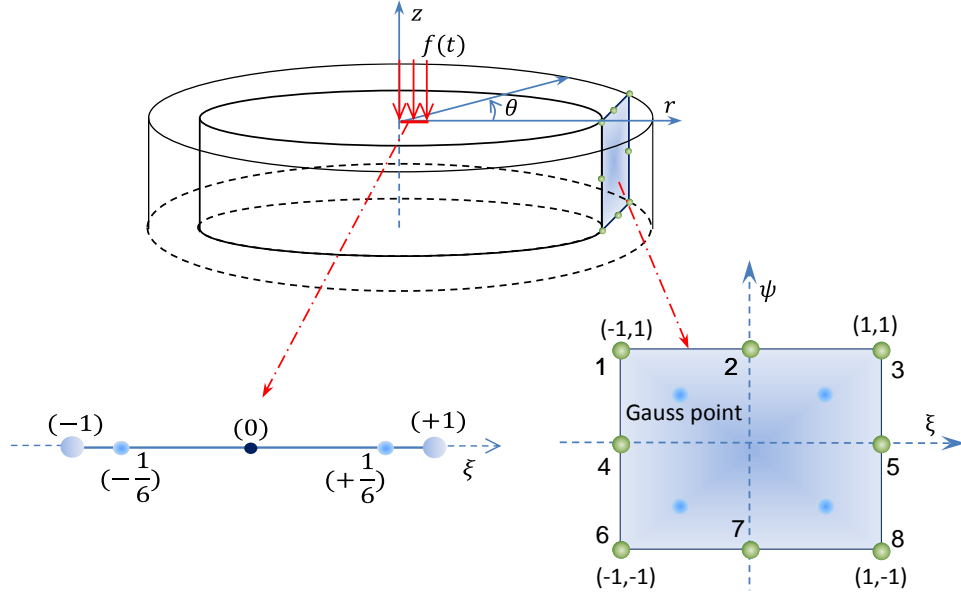


**Figure 73. Isoparametric finite elements and Gauss points for the domain body and loading area.**

The inverse computation is performed following the numerical solution method discussed earlier. The reaction vector of each element  $\mathfrak{R}_u^e$  can be discretized to Gauss points in space for the numerical solution as follows:

$$\mathfrak{R}_u^e = \sum_{k=1}^{n_G} \sum_{l=1}^{n_G} w_k w_l 2\pi r(\xi_k, \psi_l) J_\Omega(\xi_k, \psi_l) \Phi^T(\xi_k, \psi_l) [u(\xi_k, \psi_l) - u_{obs}(\xi_k, \psi_l)] \quad (4-136)$$

where  $u(\xi_k, \psi_l)$  is the deflection at the local coordinate of  $(\xi_k, \psi_l)$ ;  $u_{obs}(\xi_k, \psi_l)$  is the observed deflection;  $n_G$  is the number of Gauss point at one direction,  $n_G = 2$ ;  $w_l$  and  $w_k$  are weight functions,  $w_k = w_l = 1$ ; and  $J_\Omega$  is the determinant of Jacob function, which is equal to the area of the element ( $drdz$ ).

The viscoelastic stiffness matrix for each element  $J_p^e$  is discretized as follows:

$$J_p^e(k) = \sum_{m=1}^{n_G} \sum_{l=1}^{n_G} w_m w_l 2\pi r(\xi_m, \psi_l) J_\Omega(\xi_m, \psi_l) J_B \left( E_0 \Delta t - \sum_i^N \left[ \eta_i e^{-\frac{E_i}{\eta_i}(t_j-t)} - \eta_i e^{-\frac{E_i}{\eta_i}(t_{j-1}-t)} \right] \right) \quad (4-137)$$

The mass matrix of a single element is discretized in space as follows:

$$\mathbf{M}^e = \sum_{m=1}^{n_G} \sum_{l=1}^{n_G} w_m w_l \Phi^T(\xi_m, \psi_l) \rho \Phi(\xi_m, \psi_l) 2\pi r(\xi_m, \psi_l) J_\Omega(\xi_m, \psi_l) \quad (4-138)$$

The first order variation of the viscoelastic stiffness with respect to material model parameter  $m$  is discretized in space as follows for a single element:

$$J_{\partial m}^e = \sum_{k=1}^{n_G} \sum_{l=1}^{n_G} w_k w_l \Phi^T(\xi_k, \psi_l) \Phi(\xi_k, \psi_l) 2\pi r(\xi_k, \psi_l) J_{\Omega}(\xi_k, \psi_l) \int_{t_{j-1}}^{t_j} \frac{\partial R(t-\tau)}{\partial m} d\tau \quad (4-139)$$

where  $\int_{t_{j-1}}^{t_j} \frac{\partial R(t-\tau)}{\partial m} d\tau$  is solved in Section 4.4 with details.

The second order variation of the viscoelastic stiffness matrix with respect to material model parameter  $m$  is discretized in space as follows for a single element:

$$J_{\partial^2 m}^e = \sum_{k=1}^{n_G} \sum_{l=1}^{n_G} w_k w_l \Phi^T(\xi_k, \psi_l) \Phi(\xi_k, \psi_l) 2\pi r(\xi_k, \psi_l) J_{\Omega}(\xi_k, \psi_l) \int_{t_{j-1}}^{t_j} \frac{\partial^2 R(t-\tau)}{\partial m^2} d\tau \quad (4-140)$$

The global matrixes of the above items can be formed by assembling values at each node of elements and then substitute into the linear systems discussed earlier for numerical solutions of the inverse model.

### 4.6.3 Examples and Results Analysis

#### 4.6.3.1 Example 1-A theoretical validation

The FWD loading pulse was collected on I-95 in Florida as shown in Figure 74. The loading plate size was 5.9 inch in radius. A master curve of the dynamic moduli of AC mixture was given as true values. Given the loading pulse and true material properties, deflection responses at the distances of 0, 8, 12, 18, 24, 36, and 60 inches were simulated. Figure 74 shows the loading pulses and deflection observations. The damping properties are given as known values. Consequently, inverse computation was conducted and generalized Maxwell model parameters were inverted.

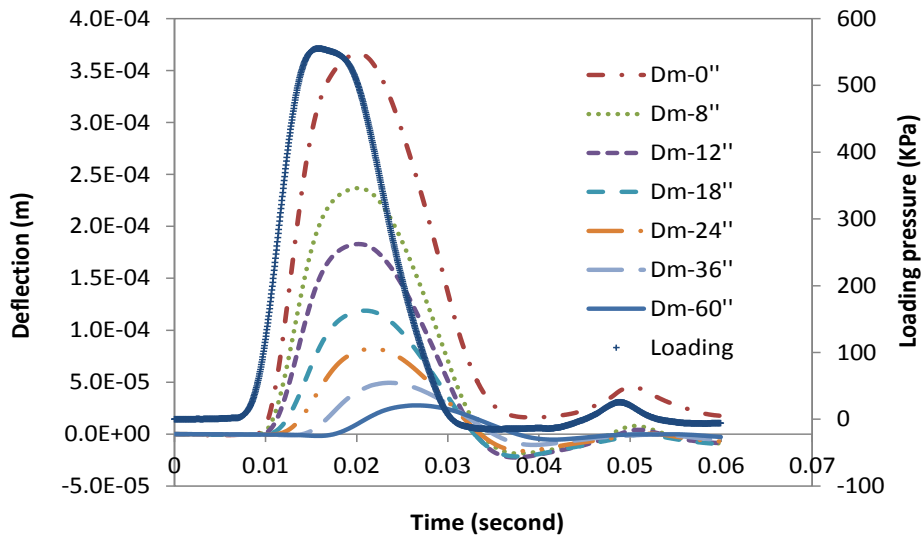


**Figure 74. Loading pulse and deflection observations.**

**Figure 75** presents the inverted deflections versus the observations with a relatively close match. **Figure 76** presents the deformation-force loop, in which the max deformation appears after the peak loading with a phase lag of about 25°C due to the material viscosity. **Figure 77** presents the simulated test function pulses, which is extremely small, indicating a small deflection misfit.

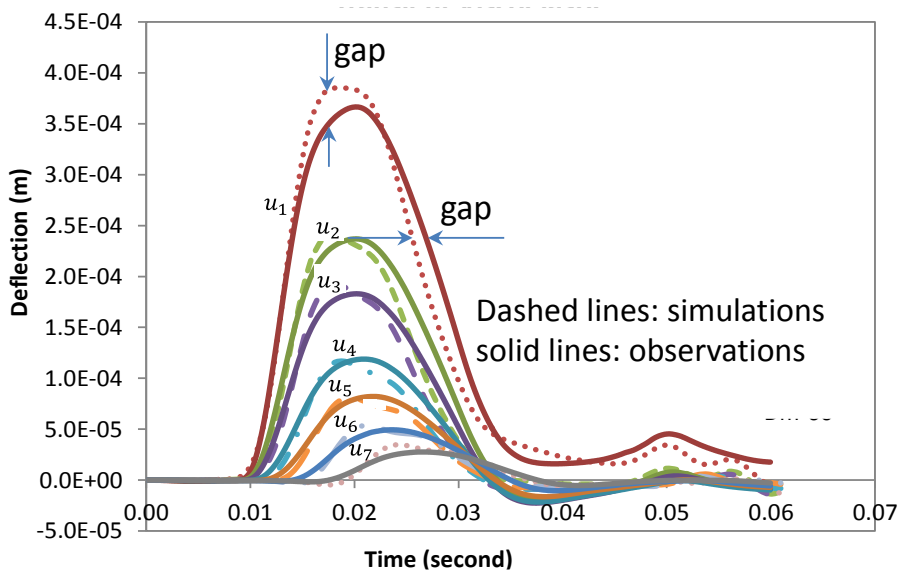


**Figure 75. Inverted deflections vs. observations ( $u_i$  is deflection at  $i^{th}$  distance).**

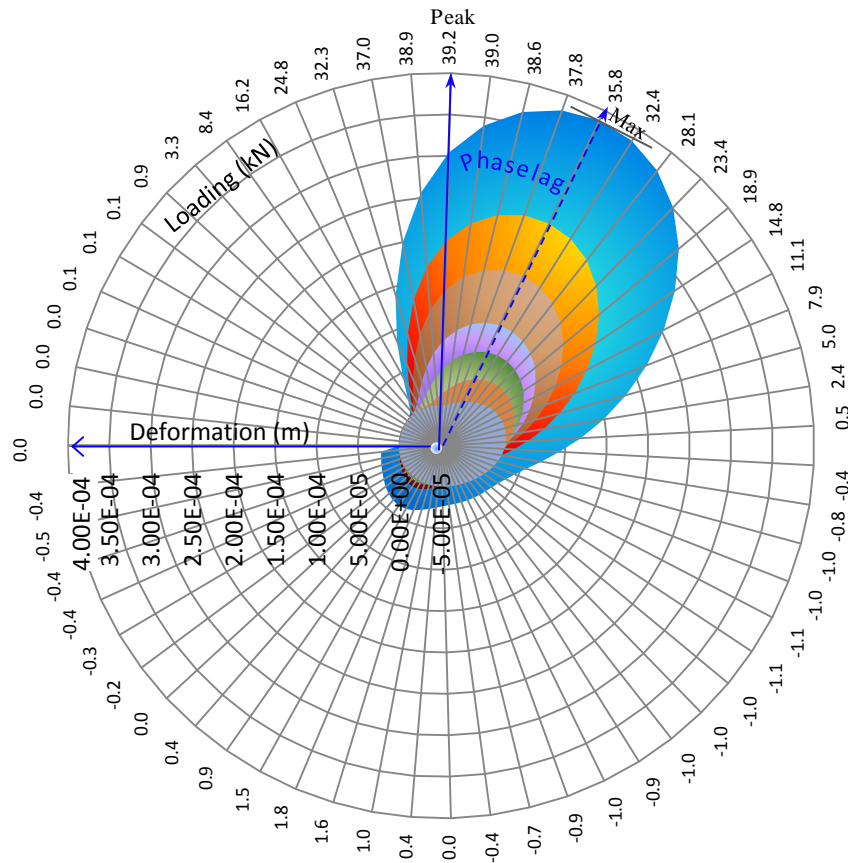


**Figure 76. Inverted deflections - loading loop.**

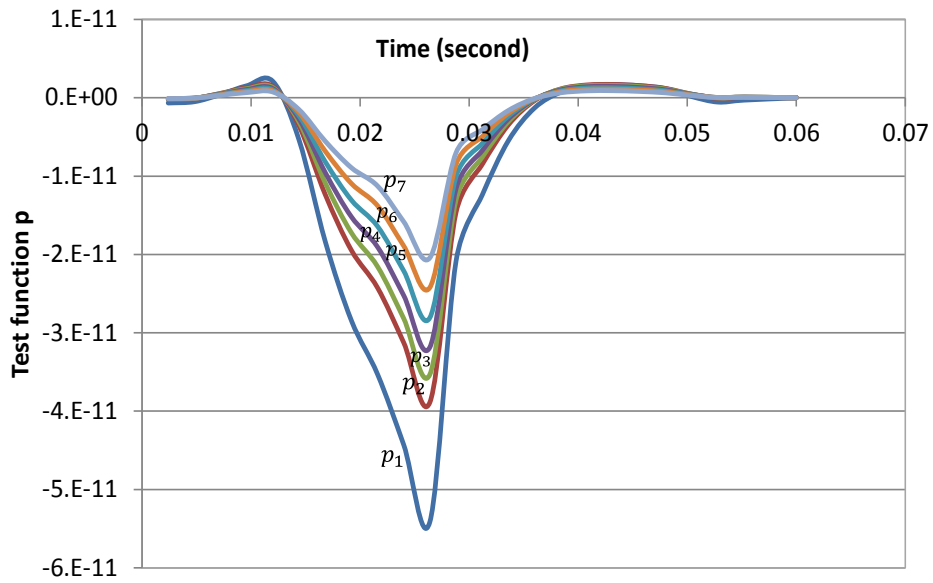


**Figure 77. Simulated test function pulses ( $p_i$  is test function at  $i^{th}$  distance).**

Figure 78 presents the inverted dynamic moduli in Prony series versus true values fitted by the smooth sigmoidal function. Results indicate that the inverse results of  $E'$  are close to the given true values. Inversed  $E''$  values oscillate, which could be explained by the limitation of the generalized Maxwell model in Prony series as it produces non-smooth master curves for the AC material, as already proven (Xu 2007; Xu and Solaimanian 2010). Figure 79 presents the inverted deflections with time (for part of the model).

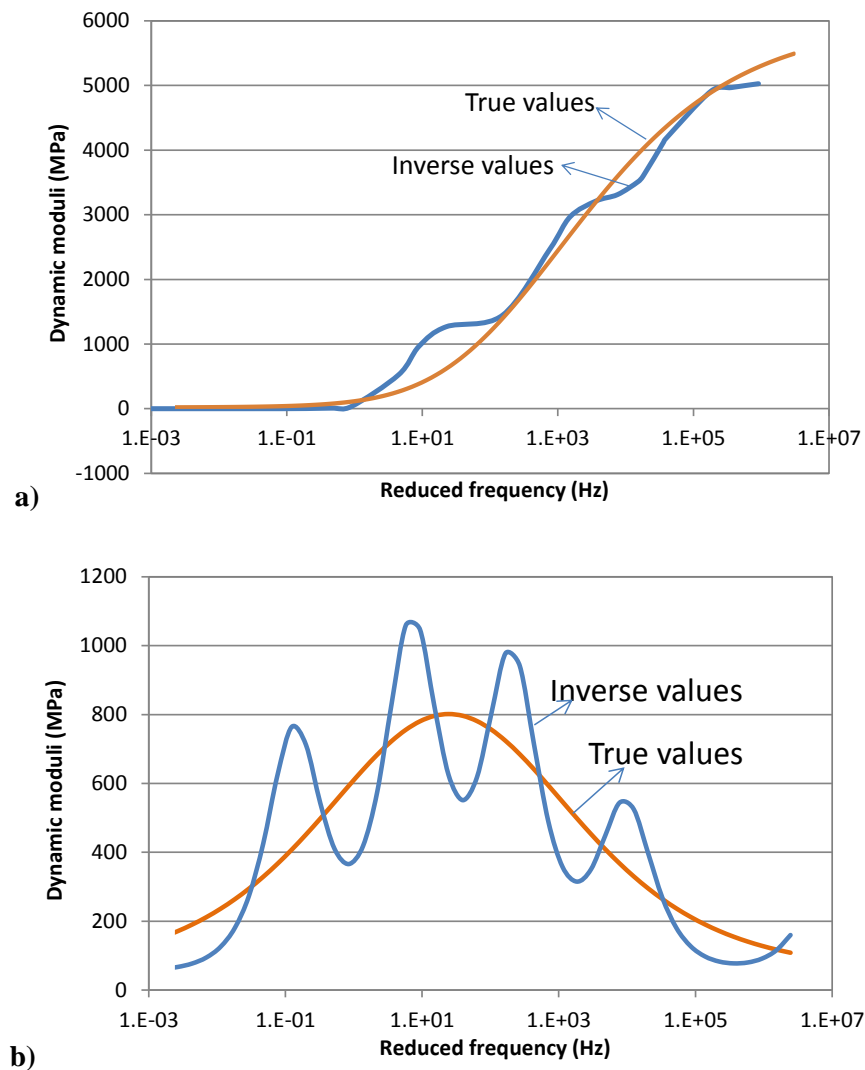


**Figure 78. Inverse computation results of master curve in Prony series vs. true values fitted in sigmoidal function: a) storage modulus and b) loss modulus.**

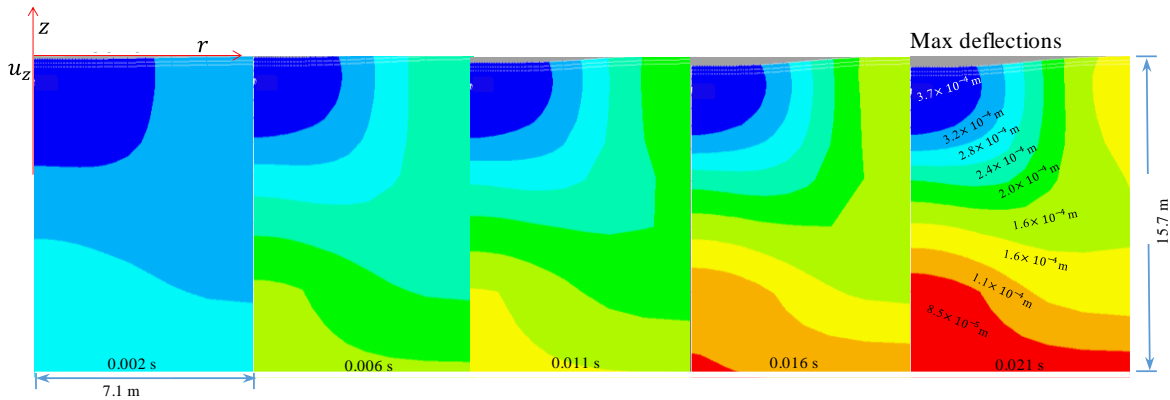


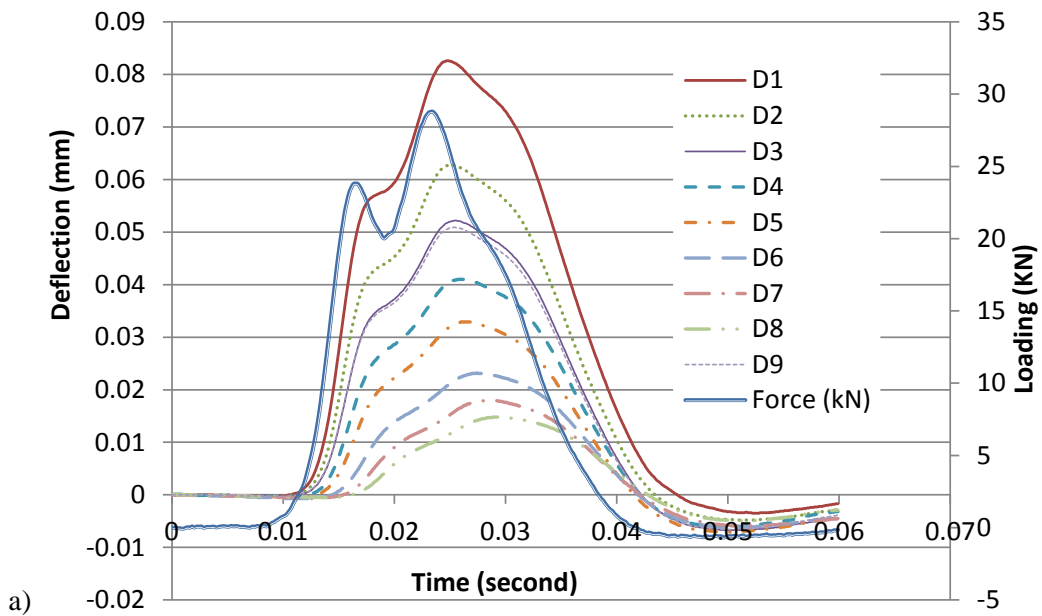
**Figure 79. Inverted deflections with time.**

#### 4.6.3.2 Example 2- LTPP test data in Florida

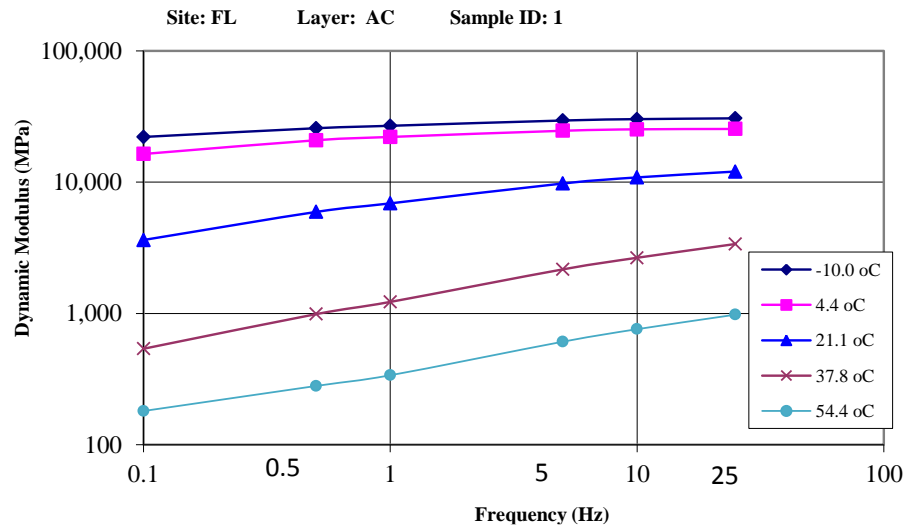
Table 11 presents the site information of one FWD test conducted in Florida. Figure 80 presents the FWD measured loading and deflection pulses, and laboratory measured dynamic moduli of the Superpave mixture at six frequencies and five temperatures (data from LTPP). The deflections (D1 to D9) were measured at the distances of 0, 8, 12, -12, 18, 24, 36, 48, and 60 inch. A sudden “drop” of the loading pulse at around 0.02 seconds was observed, which was induced by the buffer of the drop plate of the Dynatest equipment.

**Table 11. FWD test site information**

| State Code | SHRP_ID | AC Thick (inch) | Construction Date | Sample Date | State | Layer No. |
|------------|---------|-----------------|-------------------|-------------|-------|-----------|
| 12         | 4106    | 8.2             | 11/15/2003        | 2004        | FL    | 5         |



a)



b)

**Figure 80. LTPP data: a) FWD measured loading and deflection pulses and b) laboratory measured dynamic moduli.**

The master curve of dynamic moduli ( $|E^*|$ ) at the reduced frequency was constructed following the time-temperature superposition rule and fitted with the sigmoidal function. Figure 81 presents the inverted material model parameters and the dynamic moduli master curve of generalized Maxwell model vs. laboratory constructed sigmoidal function.

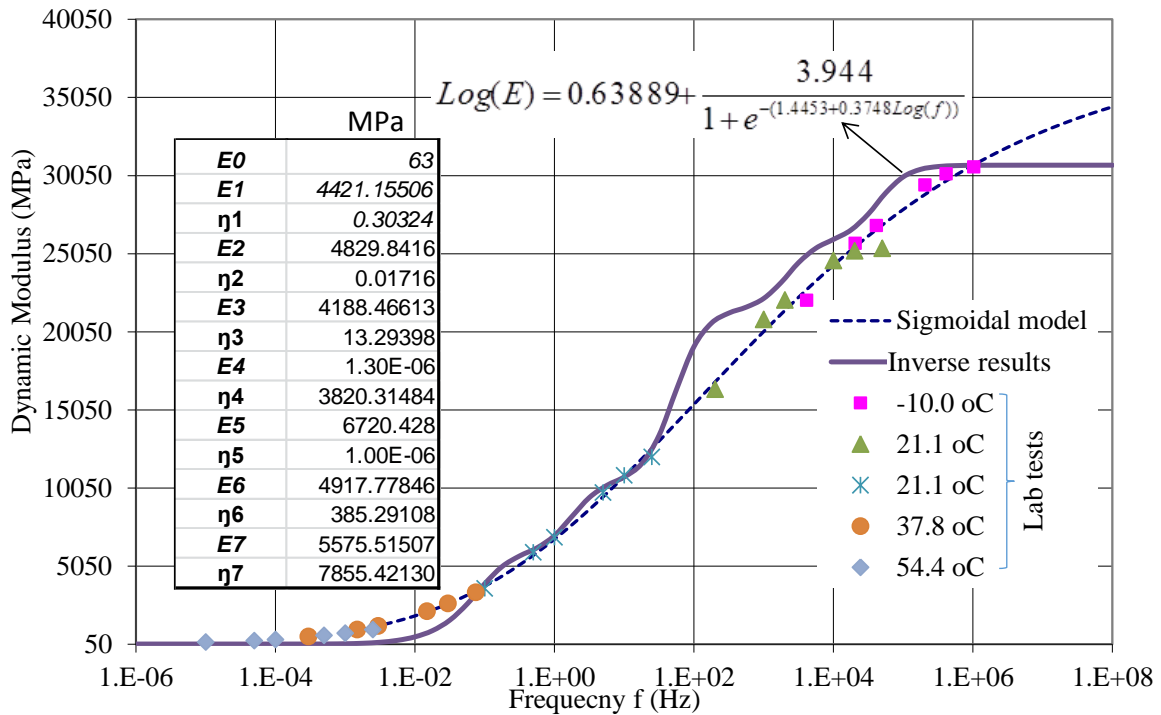


**Figure 81. Inverse results vs. measurements.**

Table 12 presents the back-calculated moduli for the unbound materials (base, subbase, and subgrade) versus laboratory measurements (from the LTPP database). Laboratory tests were conducted from 1992 to 1993 on 30 samples. Results indicate that the back-calculation results are closer to that of the maximum values of the laboratory measurements and generally larger than the median values. The difference may be explained by the following reasons: 1) the laboratory test conditions of axial loadings applied on a small specimen is different than the in-situ conditions of an actual pavement structure under vehicle loading; 2) during the laboratory testing, variable axial loading levels were applied, resulting in variable moduli values (see Table 12); and 3) FWD tests, used for backcalculation, were performed in a different date than laboratory testing, during which the moduli of the unbound materials could change due to repeated loading effects and the changing of environmental conditions (e.g. moisture).

**Table 12. Back-calculated unbound material modulus vs. measurements in MPa**

|          | Laboratory tested |     |      |        | Inverted |
|----------|-------------------|-----|------|--------|----------|
|          | Min               | Max | Mean | Median | Single   |
| Base     | 94                | 413 | 233  | 238    | 428      |
| Subbase  | 63                | 409 | 192  | 192    | 359      |
| Subgrade | 48                | 114 | 82   | 82     | 201      |

**Table 13** presents the backcalculated elastic moduli of each layer using the ModTag software (data were provided by Dr. Nima Kargah-Ostadi from Fugro in May 2014). Note that the FWD tests used for backcalculation were performed in 1989 and 1994, and the peak loadings and deflections were used for backcalculation. Results indicate that the backcalculated moduli using ModTag vary within a relatively large range, and the median modulus values of subbase and subgrade were much larger than that of laboratory measurements (**Table 13** vs. **Table 12**).

**Table 13. Backcalculated elastic moduli using ModTag (MPa)**

|          | Min  | Max    | Median |
|----------|------|--------|--------|
| AC       | 7520 | 15000  | 9855   |
| Base     | 49   | 584    | 187    |
| Subbase  | 286  | 243000 | 1260   |
| Subgrade | 63   | 5980   | 706    |

#### 4.6.3.3 Example 3-seasonal monitoring test

Figure 82 presents the seasonal FWD testing data on a three-layer flexible pavement in Indiana in 2007. The AC and treated base layer had a thickness of 6 and 9 inches, respectively. The geophone positions were set at 0, 8, 12, -12, 24, 36, and 60 inches to collect deflection pulses (d1 to d7, respectively).

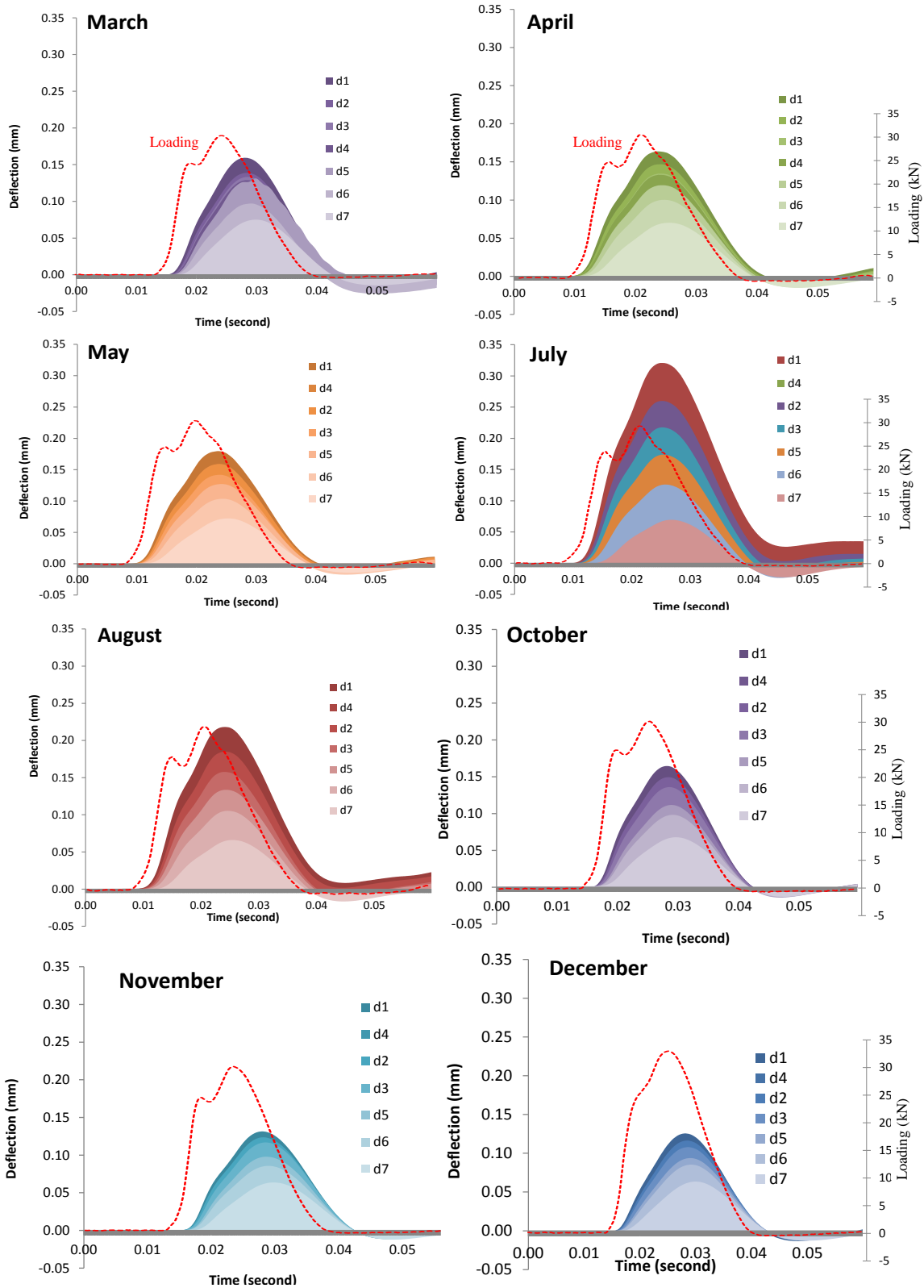


Figure 82. Seasonal FWD tests on the West Lafayette Test Track 2007.

The fast Fourier transforms (FFT) of the FWD loading and deflections from April, August, and December were performed, with results shown in Figure 83. Results indicate that the vast majority of energy occurs before the frequency of 200 Hz (i.e., 5 to 200 Hz with only around 5% of the area left out on the left and right sides).

For the inverse computation, it is reasonable to assume that the moduli of soil and base are constant at different seasons within one year. The inverted moduli of treated base and soil were 3,447 MPa and 55 MPa, respectively. Figure 84 presents the inverted master curve of AC dynamic moduli in April, August, and December. The inverted moduli transit from the rubbery stage (with the minimum modulus) to the glassy stage (purely elastic with highest modulus) with frequency increase. The 6" AC layer plays a major role towards explaining the deflection changes due to seasonal temperature variation. The results clearly showed that in the winter condition (i.e., December) AC material had a much higher modulus value than that in the summer condition (e.g. August). This confirms the temperature dependency of material viscoelasticity. This frequency range (5-200 Hz) was highlighted in the master curve of the AC dynamic moduli, covering the majority of the FWD test frequencies.

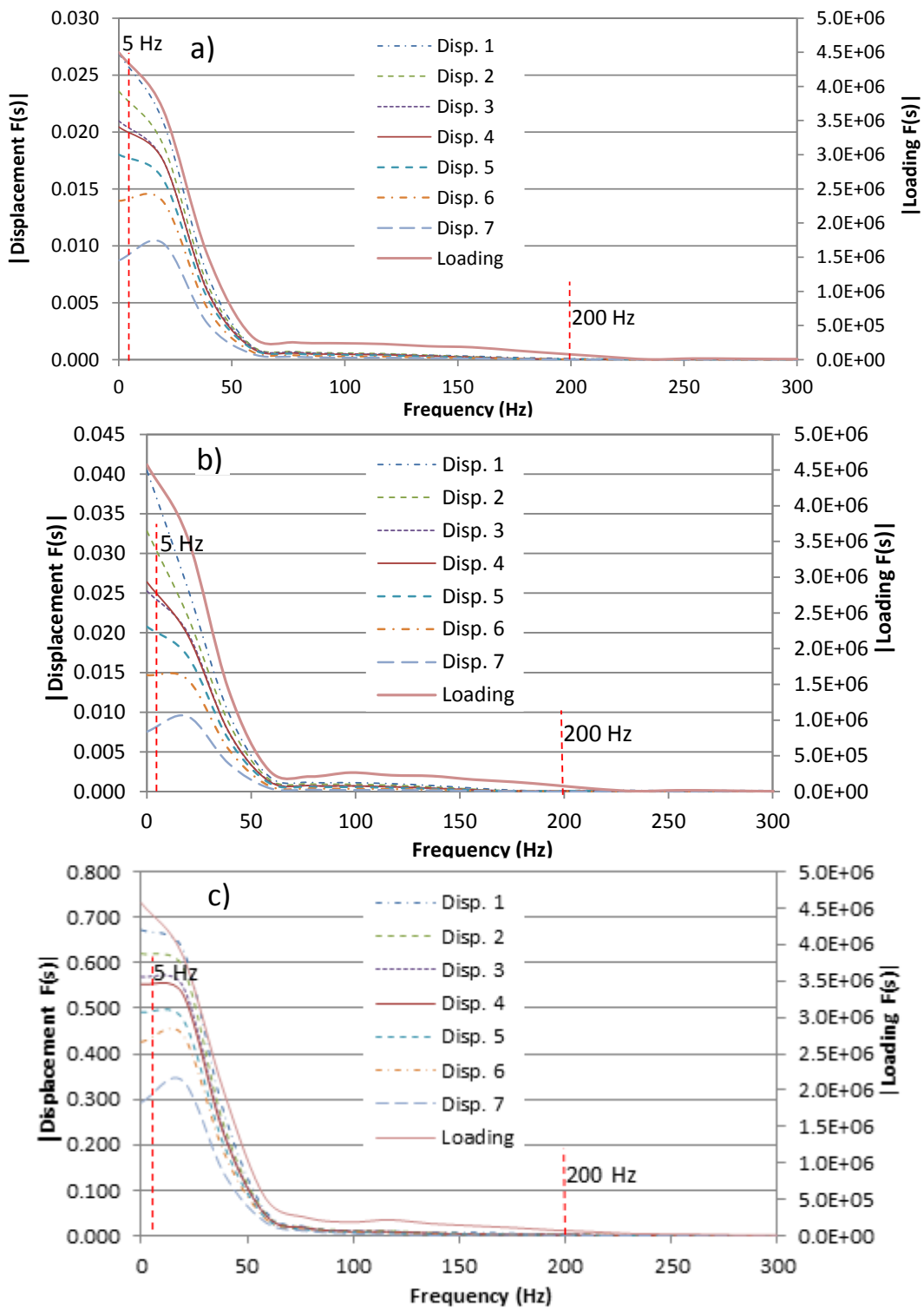


Figure 83. Frequency domain of FWD test after fast Fourier transform: a) April, b) August, and c) December.

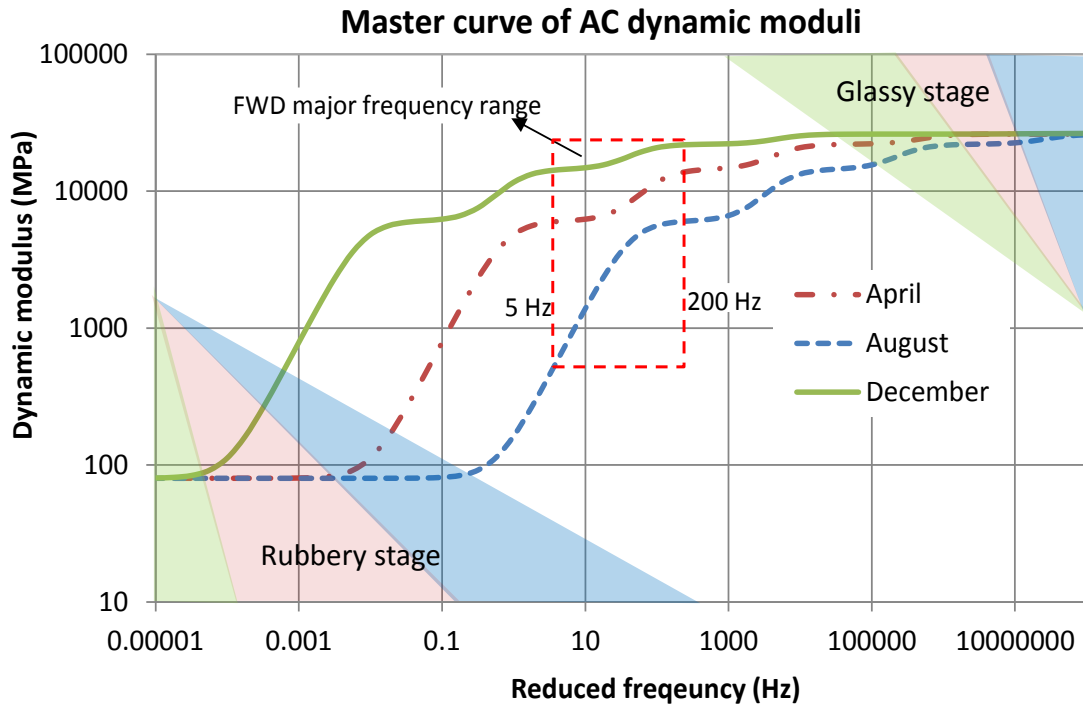


Figure 84. Inverted master curves of dynamic moduli of asphalt concrete.

#### 4.7. Summary

This Chapter developed a Lagrangian optimization method for inverting dynamic moduli and VE (viscoelastic) properties of multilayer systems. Mathematical derivations, a finite element numerical solution method, and an independent computer coding for a dynamic viscoelastic inverse problem of multilayer systems were developed and applied to the flexible pavements using the FWD time records of loading and deflection pulses. The main research findings are summarized next.

This method is based on the Lagrangian function as constrained by the PDE governing state equation with modified Armijo rule to determine the step length. Compared to the two-stage approach, the developed method improves computation speed significantly when dealing with a relatively larger scale model parameter number. The developed model was implemented into three FWD test sites.

## Chapter 5: Conclusion

### 5.1 Main Findings

- 1) This research developed a finite element and Newton-Raphson model for inverse computing the elastic moduli of multilayer flexible pavements. It was a two-stage approach. An elastic FE model with infinite elements at boundaries was developed to simulate responses, and then a Newton-Raphson method was proposed for the inversion of elastic moduli in which the gradient was estimated from response outputs using the finite difference method. Compared to most existing two-stage elastic backcalculation methods, the new features of the method included: a) incorporation of the FHWA's area method for seed moduli estimation, which has improved the engineering accuracy to address the common issue of a no-unique backcalculation solution, and b) the ability to account for the nonlinear temperature profile and associated moduli variations of the asphalt layer based on the simple AASHTO 1993 temperature model. An independent FORTRAN code was developed to implement the computation. Monte Carlo simulations for each layer of a four-layer pavement structure showed that the two-stage method is accurate and sufficient for the inverse problem of static, elastic multilayer systems with a small scale of model parameters (e.g., a few elastic moduli). Sensitivity analysis results demonstrated that the seed moduli only have a small effect on numerical accuracy; however, this can affect the inverted moduli values significantly, especially for the top asphalt layer. The inverted moduli of unbound materials (base/sub-base/soil), especially soil, are much less sensitive to the seed moduli values as compared to that of the asphalt layer.
- 2) As an extension to the static-elastic FE model developed above, this research developed a time-domain dynamic-viscoelastic-system damping-coupled finite element (FE) model and a Galerkin-based numerical solution method for simulating dynamic viscoelastic responses of a layered half space structure under loading pulses. An independent FORTRAN computer code was developed for the

numerical computation, and validated by means on an analytical solutions (static and elastic) and numerical modeling (dynamic and viscoelastic). A combined Houbolt, central and forward finite differences method was proposed for time discretization of velocity and acceleration, which reduces the time-step length and computer speed. Compared to most existing computer methods for a layered half space, the approach developed here represents a more comprehensive model because it accounts for the coupled dynamic loading, damping effects, and material's viscoelastic behavior over time. The model has been implemented to study flexible pavements under FWD testing and vehicle loading. Simulation results of FWD testing demonstrated that a dynamic viscoelastic model considering damping can better emulate the in-service conditions than does the dynamic elastic or dynamic viscoelastic model without considering damping. Specifically, dynamic inertia contributes primarily to the time offset, and the damping further adds to this effect and reduces deflection value. The material viscoelastic behavior could contribute significantly to the deflection magnitudes and shape of the deflection basin. The model developed and computer method are also able to simulate two critical environment-associated conditions: a) the temperature profile or variation at depth; and b) the space dependent moduli profile at depth such as that of soil caused by moisture variations. The model and computer method could serve as a potential means to advance the structural analysis methods, such as the one used in the national MEPDG. They could also be used for other multilayer systems such as laminate and disk structures with different length and time scales.

- 3) With the dynamic viscoelastic forward model developed above, this research led to develop a Lagrangian optimization method with PDE constraints to invert the dynamic moduli and viscoelastic (VE) properties of multilayer systems. Mathematical derivations for solving the dynamic VE inverse problem of the multilayer systems were also developed. The Armijo rule was modified to determine a stable step length. An independent FORTRAN code was developed

for the numerical implementation. The method was implemented to analyze flexible pavements under FWD tests. FWD test data were collected from both in-situ tests and the LTPP database during different seasons. With the inputs of loading pulse and deflection time history data, the method inverts the dynamic moduli master curve and material viscoelastic properties. Both experimental and numerical analyses demonstrated the material viscoelastic behaviors. Compared to the two-stage approach developed in the first task's development of a finite element and Newton-Raphson model, the method developed here involves more complex mathematical derivations. However, it has certain advantages when dealing with larger scale model parameters, in that it improves numerical accuracy and computation speed significantly. Therefore, this method is recommended for inverse problems that consider more complex conditions with a relatively large model parameter number when time- or space-dependent properties are considered such as frequency-temperature-dependent material viscoelasticity.

## **5.2 Future Study**

- 1) The generalized Maxwell viscoelastic material model in the Prony series does not capture the true response of the material as it fails to represent a smooth master curve of relaxation and dynamic moduli. Other material models may be developed to improve the physical fitting;
- 2) Other damping models besides the Rayleigh damping model may be explored to consider nonlinear properties of materials;
- 3) Some special conditions of the soil and pavement structures were not considered, including at least the following: a) the bedrock of the soil foundation and b) the temperature profile and variation; and c) the space dependency of asphalt concrete's properties.
- 4) The study of Lagrangian optimization method and its implementations are limited. For example, sensitivity analysis should be conducted to study the

- influence factors of material seed values and more implementation samples should be tested;
- 5) The developed Lagrangian optimization inverse method could be extended to consider more complex situations including the material and structure nonlinearity and space dependency for large-scale model parameter inversion problems;
  - 6) Independent computer coding for these numerical methods were developed, which have potential for industry applications;
  - 7) The developed methods may be applied and extended to other multilayer systems such as polymers, tissues, and infrastructures (e.g. bridge decks, sandwich structures, composite plates, and earthwork) with various boundary conditions, time and length scales for forward and inverse problems.

## **Bibliography**

1. Adhikari, S., and Woodhouse, J., 2001. Identification of damping: part I, viscous damping. *Journal of Sound and Vibration* 243, 43–61.
2. Al-Khoury, R., Kasbergen, C., Scarpas, A., Blaauwendraad, J., 2001. Spectral element technique for efficient parameter identification of layered media: Part II: Inverse calculation. *International Journal of Solids and Structures* 38, 8753-8772.
3. Alavi, S., LeCates, J., and Tavaers, M.P., 2008. Falling weight deflectometer usage – a synthesis of highway practice. *NCHRP Synthesis 381*, Transportation Research Board. Washington, D.C.
4. American Association of State Highway and Transportation Officials (AASHTO), 1993. *AASHTO Guide for Design of Pavement Structures*, Washington, D.C.
5. Applied Research Associate (ARA), Inc., 2004. *Guide for mechanistic-empirical design of new and rehabilitated pavement structures*. NCHRP 1-37A Final Report, Washington, D.C.
6. Al-Qadi, I., Yoo, P., Elseifi, M., and Nelson, S., 2009. Creep behavior of hot-mix asphalt due to heavy vehicular tire loading. *Journal of Engineering Mechanics* 135, 1265–1273.
7. American Association of State Highway and Transportation Officials (AASHTO), 1993. *AASHTO Guide for Design of Pavement Structures*, Washington, D.C.
8. ANSYS Inc., 2013. *ANSYS 14.5 Release Highlights*. <http://www.ansys.com/Products/ANSYS+14.5+Release+Highlights>
9. Applied Research Associate, Inc., 2004. *Guide for mechanistic-empirical design of new and rehabilitated pavement structures*. NCHRP 1-37A Final Report, Washington, D.C.
10. Aouad, M.F., 1993. *Evaluation of Flexible Pavements and subgrades using the spectral-analysis-of-surface-waves (SASW) method*. Ph.D. Dissertation, the University of Texas at Austin.

11. Araújo, A.L., Cristovao, Soares, M.M.S., Soares, C.A.M., Herskovits, J., 2010. Characterisation by inverse techniques of elastic, VE and piezoelectric properties of anisotropic sandwich adaptive structures. *Applied Composite Materials* 17, 543–556.
12. Araújo, A.L., Soares, C.M.M., Herskovits, J., Pedersen, P., 2009. Estimation of piezoelastic and VE properties in laminated structures. *Composite Structures* 87, 168–174.
13. ASTM, 2011. Standard Test Method for Determining the Resilient Modulus of Bituminous Mixtures by Indirect Tension Test, ASTM D 7369 – 11.
14. Ayadi, A.E, Picoux, B., Lefeuvre-Mesgouez, G., Mesgouez, A., and Petit, C., 2012. An improved dynamic model for the study of a flexible pavement. *Advances in Engineering Software* 44, 44-53.
15. Ayre, R.S., 1976. Transient response to step and pulse functions, in “C.E., Shock and Vibration Handbook” edited by Harris, C.M. and Crede. McGraw-Hill Book Company, 2<sup>nd</sup> edition.
16. Bathe, K.J., 1996. *Finite Element Procedures*, Prentice Hall, Upper Saddle River, New Jersey, 1st editon.
17. Bettess, P., 1980. More on *infinite elements*, *International Journal for Numerical Methods in Engineering*, 15, 1613–1626.
18. Blab, R. and Harvey, J.T., 2002. Modeling measured 3D tire contact stresses in a viscoelastic FE pavement. *International Journal of Geomechanics* 2, 271–290.
19. Birgisson, B., Crouch, S.L., Newcomb, D.E., 1997. Static and dynamic boundary element methods for layered pavement systems, Report no. CTS 97-06, University of Minnesota.
20. Boumediene, F., Cadou, J-M, Duigou, L., Daya , EI. M., 2014. A reduction model for eigen solutions of damped viscoelastic sandwich structures. *Mechanics Research Communications* 57, 74–81.
21. Boussinesq, J., 1885. *Applications des Potentials a l’Etude de l’Equilibre et Mouvement des Solides Elastiques*, Gauthier-Villard, Paris.

22. Brigham, J. C., Aquino, W., Mitri, F.G., Greenleaf, J.F., and Fatemi, M., 2007. Inverse estimation of VE material properties for solids immersed in fluids using vibroacoustic techniques. *Journal of Applied Physics* 101, 023509.
23. Broutin, M., Theillout, J.N., 2010. Towards a Dynamic Backcalculation Procedure for HWD; A full-scale validation experiment, 2010 FAA worldwide airport technology transfer conference, Atlantic City, New Jersey, USA.
24. Cao, P., Zhou, C., Feng, D., Zhao, Y., and Huang, B., 2013. A 3D direct vehicle-pavement coupling dynamic model and its application on analysis of asphalt pavement dynamic response. *Mathematical Problems in Engineering*, 1-8.
25. Catheline, S., Gennisson, J.L., Delon, G., Fink, M., Sinkus, R., Abouelkaram, S., and Culiolic, J., 2004. Measurement of VE properties of homogeneous soft solid using transient elastography: An inverse problem approach. *J. Acoust. Soc. Am.* 116, 3734–3741.
26. Chaillat, S. and Bonnet, M., 2014. A new Fast Multipole formulation for the elastodynamic half-space Green's tensor, *Journal of Computational Physics* 258, 787-808.
27. Chatti, K., Yun, K.K., 1996. SAPSI-M: computer program for analyzing asphalt concrete pavements under moving arbitrary loads. *Transportation Research Record: Journal of the Transportation Research Board* 1539, 88-95.
28. Chopra, A.K., 2001. *Dynamics of Structures*, Prentice Hall, Upper Saddle River, New Jersey, 2nd edition.
29. Choi, J., Wu, R., Pestana, J., and Harvey, J., 2010. New Layer-Moduli Back-Calculation Method Based on the Constrained Extended Kalman Filter. *J. Transp. Eng.*, 136, 20–30.
30. Christensen, R.M., 1982. *Theory of Viscoelasticity*, 2nd edition, Academic Press, Inc.
31. Cobb III, C.H., 2004. Summer Skin Care: Get your vitamin D in moderation. [http://www.hughston.com/hha/a\\_17\\_3\\_4.htm](http://www.hughston.com/hha/a_17_3_4.htm)

32. Cook, R.D., Malkus, D.S., Plesha, M.E., Witt, R.J., 2002. Concepts and Applications of Finite Element Analysis, John Wiley & Sons. Inc., 4th edition.
33. Dave, E., Paulino, G., and Buttlar, W., 2011. Viscoelastic functionally graded finite-element method using correspondence principle. *Journal of Materials in Civil Engineering* 23, Special Issue: Multiscale and Micromechanical Modeling of Asphalt Mixes, 39–48.
34. Dong, Q.X. , Hachiya, Y., Takahashi, O. , Tsubokawa, Y., and Matsui, K., 2002. An efficient backcalculation algorithm of time domain for large-scale pavement structures using Ritz vectors, *Finite Elements in Analysis and Design*. 38, 1131-1150.
35. Dynatest, 2010. Elmod<sup>®</sup> (evaluation of layer moduli and overlay design), <http://www.dynatest.com/software/elmod.aspx>
36. Dvornik, M., Vansteenkiste, A., and Waeyenberge, B.V., 2013. Micromagnetic modeling of anisotropic damping in magnetic nanoelements. *Physical Review B* 88, 054427: 1-6.
37. Dynatest, ELMOD, <http://www.dynatest.com/software/elmod.aspx>
38. Engl, H., Hanke, M., and Neubauer, A., 1996. Regularization of Inverse Problems, Dordrecht, second edition.
39. Ern, A., J.L. Guermond, J.L., 2004. Theory and Practice of Finite Elements, Springer, New York.
40. Federal Highway Administration (FHWA), 2012. Long-Term Pavement Performance (LTPP) Products Online. <http://www.ltp-pp-products.com/>
41. Felippa, C., 2011. Advanced Finite Element Methods for Solids, Plates and Shells, University of Colorado at Boulder.
42. Fernando, E. and Liu, W., 2002. Dynamic Analysis of FWD Data for Pavement Evaluation, Bearing Capacity of Roads, Railway and Airfields, Correia & Branco, Swets & Zeitlinger, Lisse.
43. Ern, A., Guermond, J.L., 2004. Theory and practice of finite elements, Springer.

44. Felippa, C., 2011. Advanced Finite Element Methods for Solids, Plates and Shells, University of Colorado at Boulder online document.
45. Foinquinos, R., Roesset, J.M., and Stokoe, K.H., 1993. FWD-DYN: A Computer Program for Forward Analysis and Inversion of Falling Weight Deflection Data. Research report 1970-1F, Center for Transportation Research, The University of Texas at Austin, Austin, Texas.
46. Foinquinos, R., 1995. Dynamic nondestructive testing of pavements, Ph.D. dissertation, University of Texas at Austin, Austin.
47. Foinquinos, R., Roesset, J.M., 2000. Elastic Layered Half-spaces subjected to dynamic surface loads, in E. Kausel, G. Manolis, editors, Wave motion in ear engineering, WIT Press, Southampton, 141-191.
48. Giavazzi, S., Ganatea, M.F., Trkov, M., Šuštarčič, P., Rodič, T., 2010. Inverse determination of VE properties of human fingertip skin. *Materials and Geoenvironment* 57, 1–16.
49. Gopalakrishnan, K., and Manik, A., 2010. Co-variance matrix adaptation evolution strategy for pavement backcalculation next term, *Construction & Building Materials*. 24, 2177-2187.
50. Gottlieb, O, and Habib, G., 2011. Non-linear model-based estimation of quadratic and cubic damping mechanisms governing the dynamics of a chaotic spherical pendulum. *Journal of Vibration and Control* 18, 536–547.
51. Gu, C.X. Yu, Y., and C. Wang, Surgical treatment for diffuse coronary artery diseases, Chapter 16. In *Book of Artery Bypass* edited by W.S. Aronow, first edition, InTech, 2013.
52. Guénette, R., Fortin, M., 1995. A new mixed finite element method for computing viscoelastic flows. *Non-Newtonian Fluid Mech.* 60, 27-52.
53. Hadidi, R. and Gucunski, N., 2010. “Comparative Study of the Static and Dynamic Falling. Weight Deflectometer *Backcalculation* Using the Probabilistic Approach”, ASCE. *Journal of Transportation Engineering*, 136, 196-204.

54. Hardy, G.H., Wright, E.M., Wiles, A., Heath-Brown, R., Silverman, J., 1980. An Introduction to the Theory of Numbers, 5th edition, Oxford Science Publications.
55. Harichandran, R.S., Mahmood, T., Raab, A.R., and Baladi, G.Y., 1993. Modified newton algorithm for backcalculation of pavement layer properties. *Transportation Research Record* 1384, 14-22.
56. Harichandran, R.S., and Baladi, G.Y., 2000. MICHPAVE User's Manual, Version 1.2 for DOS. Michigan State University, East Lansing.
57. Herskovits, J., Dubeux, V., Soares, C.M.M., Araujo, A.L., 2004. Interior point algorithms for nonlinear least squares problems. *Inverse Problem Science and Engineering* 12, 211–223.
58. Howard, I., and Warren, K., 2009. Finite-element modeling of instrumented flexible pavements under stationary transient loading. *J. Transp. Eng.* 135, 53–61.
59. Hopman, P.C., 1996. The visco-elastic multilayer program VEROAD. *Heron* 41, 71-91.
60. Hossain, S.S., Hossainy, S.F.A., Bazilevs, Y., Calo, V.M., and Hughes, T.J.R., 2012. Mathematical modeling of coupled drug and drug-encapsulated nanoparticle transport in patient-specific coronary artery walls. *Comput Mech* 49, 213–242.
61. Houbolt, J.C., 1950. A recurrence matrix solution for the dynamic response of elastic aircraft. *Journal of the Aeronautical Sciences* 17, 540-550.
62. Huang, Y.H., 2003. *Pavement Analysis and Design*, Prentice Hall, 2nd edition.
63. Hussein, M.I., and Frazier, M.J., 2010. Band structure of phononic crystals with general damping. *Journal of Applied Physics* 108, 093506.
64. Huhtala, M., 1986. The effect of different trucks on road pavements. *International Symposium on Heavy Vehicle Weights and Dimensions*, Kelowna, British Columbia, Proceedings, 151-159.
65. Johnson, A.M., Baus, R.L. Alternative method for temperature correction of backcalculated equivalent pavement Moduli, *Transportation Research Record*, 1355 (1992) 75-81.

66. Ju, S.H. and Ni, S.H., 2007. Determining Rayleigh damping parameters of soils for finite element analysis. *Int. J. Numerical and analytical methods in geomechanics* 31, 1239–1255.
67. Kang, Y.V., 1998 Multifrequency Backcalculation of Pavement-Layer Moduli, *Journal of Transportation Engineering* 124, 73-81.
68. Kassem, E., Grasley, Z.C., and Masad, E., 2013. Viscoelastic Poisson's ratio of asphalt mixtures. *Journal of Materials in Civil Engineering* 13, 162-169.
69. Kausel, E., Park, J. 2006. Response of Layered Half-Space Obtained Directly in the Time Domain, Part II: SV-P and Three-Dimensional Sources. *Bulletin of the Seismological Society of America* 96, 1810–1826.
70. Kausel, E. 2012. Lamb's problem at its simplest. *Proceedings of the Royal Society A: Mathematical, Physical and Engineering Sciences* 469, 2012.0462.
71. Kim, J., 2011. General viscoelastic solutions for multilayered systems subjected to static and moving loads. *J. Mater. Civ. Eng.*, 23, 1007–1016.
72. Kim, J.H., and Paulino, G.H., 2002. Isoparametric graded finite elements for nonhomogeneous isotropic and orthotropic materials 69, 502-514.
73. Kim, J., Kim, K., and Sohn, H., 2013. In situ measurement of structural mass, stiffness, and damping using a reaction force actuator and a laser Doppler, vibrometer. *Smart Materials and Structures* 22, 1-11.
74. Kim, M., 2007. Three – dimensional finite element analysis of flexible pavement considering nonlinear pavement foundation behavior, Dissertation, University of Illinois at Urbana Champion.
75. Kausel, E. 2012. Lamb's problem at its simplest. *Proceedings of the Royal Society A: Mathematical, Physical and Engineering Sciences* 469, 20120462.
76. Kim, J., 2011. General viscoelastic solutions for multilayered systems subjected to static and moving loads. *Journal of Materials in Civil Engineering*, 23, 1007–1016.

77. Komvopoulos, K., Yang, J., 2006. Dynamic analysis of single and cyclic indentation of an elastic–plastic multi-layered medium by a rigid fractal surface. *Journal of the Mechanics and Physics of Solids* 54, 927–950.
78. Kopperman, S., Tiller, G., and Tseng, M., 1986. ELSYM5: Interactive microcomputer version: User’s manual, FHWA-TS-87-206. Federal Highway Administration, Washington, D.C.
79. Kutay, M.E., Chatti, K. and Lei, L. 2011. Backcalculation of Dynamic Modulus from FWD Deflection Data”, *Transportation Research Record: Journal of the Transportation Research Board*, TRR 2227, 87-96.
80. Labonnote, N., Rønnquist, A., Malo, K.A., 2013. Modified hysteretic damping model applied to Timoshenko timber beams. *Computers and Structures* 121, 22–31.
81. Lamb, H., 1904. On the propagation of tremors over the surface of an elastic solid, *Phil. Trans. Roy. Soc. (London)*, Ser. A 203, 1- 42.
82. Lee, M.A., 1976. Resilient modulus and dynamic poisson’s ratio of asphalt concrete mixes, MS thesis, McMaster University, Ontario, Canada.
83. Lee, H.S., 2013. ViscoWave – a new solution for viscoelastic wave propagation of layered structures subjected to an impact load, *International Journal of Pavement Engineering* (in press).
84. Lei, F., Szeri, A.Z., 2007. Inverse analysis of constitutive models: biological soft tissues. *Journal of Biomechanics* 40, 936–940.
85. Lesieutre, G. A., and Mingori, D. L., 1990. Finite element modeling of frequency-dependent material proper-ties using augmented thermodynamic fields. *Control and Dynamics* 13, 1040–1050.
86. Levenberg, E., 2012. Inverse analysis of VE pavement properties using data from embedded instrumentation. *International Journal for Numerical and Analytical Methods in Geomechanics* 37, 1016–1033.
87. Levenberg , E., 2013. Analysis of pavement response to subsurface deformations. *Computers and Geotechnics* 50, 79–88.

88. Li, Y., Tang, S., Abberton, B.C., Kröger, M., Burkhart, C., Jiang, B., Papakonstantopoulos, G.J., Poldneff, M., Liu, W.K., 2012. A predictive multiscale computational framework for viscoelastic properties of linear polymers. *Polymer* 53, 5935-5952.
89. Liang, R.Y. and Zhu, J.X., 1998. Efficient computation algorithms for forward and backward analysis of a dynamic pavement system. *Computers & Structures*, 69, 255-263.
90. Loizos, A., Scarpas, A., 2005. Verification of falling weight deflectometer back analysis using dynamic finite elements simulation. *International Journal of Pavement Engineering* 6, 115–123.
91. Makris, N., 1995. Time domain analysis of generalized viscoelastic models. *Soil Dynamics and Earthquake Engineering* 14, 375-386.
92. Magnuson, A. H., R. L. Lytton, and Briggs R., 1991. Comparison of Computer Predictions and Field Data for Dynamic Analysis of Falling-Weight Deflectometer Data, *Transportation Research Record*, No.1293, TRB, National Research Council, Washington D C, 61-71.
93. McTavish, D. J., and Hughes, P. C., 1993. Modeling of linear viscoelastic space structures. *Transactions of ASME, Journal of Vibration and Acoustics* 115, 103–110.
94. Meier, R.W., Alexander, D.R., Freeman, R.B., 1997. Using artificial neural networks as a forward approach to backcalculation. *Transportation Research Record* 1570, 126-133.
95. Michalak, C.H. and Scullion, T., 1995. MODULUS 5.0: user's manual, *Research Report 1987-1 of Texas Transportation Institute*. College Station, Texas.
96. Miller, G.F and Pursey, H., 1954. The field and radiation impedance of mechanical radiators on the free surface of a semi-infinite isotropic solid. *Proceedings of the Royal Society A* 223, 521-541.

97. Mo, L.T., Huurman, M., Wu, S.P., Molenaar, A.A.A., 2008. 2D and 3D meso-scale finite element models for raveling analysis of porous asphalt concrete. *Finite Elements in Analysis and Design* 44, 186–196.
98. Motamed, A., Bhasin, A., and Liechti, K. M., 2013. Constitutive modeling of the nonlinearly viscoelastic response of asphalt binders; incorporating three-dimensional effects. *Mechanics of Time-Dependent Materials*, 17, 83–109.
99. Nazarian, S., Stokoe, K.H., Briggs, R.C., 1987. Nondestructively delineating changes in modulus profiles of secondary roads, *Transportation Research Record: Journal of the Transportation Research Board* 1136, 96-107.
100. Nocedal, J. and Wright, S.J., 2006. *Numerical Optimization*, second edition, Springer-Verlag.
101. Omez-Ramirez, F., and Thompson, M. R., 2001. *Characterizing Aircraft Multiple Wheel Load Interaction for Airport Flexible Pavement Design*. University of Illinois at Urbana-Champaign, IL.
102. Oppenheim, A.V. and Schaffer, R.W., 1975. *Digital Signal Processing*. Prentice-Hall, Inc., Englewood Cliffs, New Jersey.
103. Pan, E., Han, F., 2005. Green's functions for transversely isotropic piezoelectric functionally graded multilayered half spaces. *International Journal of Solids and Structures* 42, 3207-3233.
104. Park, D., and Hashash, Y. M. A., 2004. Soil damping formulation in nonlinear time domain site response analysis. *Journal of Earthquake Engineering* 8, 249-274.
105. Park, S.W., Schapery, R.A., 1999, Methods of interconversion between linear viscoelastic material functions. Part I—a numerical method based on Prony series, *International Journal of Solids and Structures* 36, 1653-1675.
106. Pellinen, T.K., 2001. *Investigation of the Use of Dynamic Modulus as Indicator of Hot-Mix Asphalt Performance*. Ph.D. Dissertation, Arizona State University.
107. PhysicsWorld, Physicists propose 'wireless' solar cells, News Feb 18, 2013. <http://physicsworld.com/cws/article/news/2013/feb/18/physicists-propose-wireless-solar-cells>

108. Pisanò, F., Jeremić, B., 2014. Simulating stiffness degradation and damping in soils via a simple visco-elastic-plastic model. *Soil Dynamics and Earthquake Engineering* 63, 98–109.
109. Pronk, A.C., 2003, Revival of the Huet-Saegh response model – notes on the Hue-Sayegh rheological model, DWW-2003-029, Rhed, Deft.
110. Puthanpurayil, A.M., Dhakal, R.P., and Carr, A.J., 2011. Modeling of in-structure damping: a review of the state-of-the-art. *Proceedings of the Ninth Pacific Conference on Earthquake Engineering, Building an Earthquake-Resilient Society*, 2011, Auckland, New Zealand.
111. Qin, J., 2010. Predicting Flexible Pavement Structural Response Using Falling Weight Deflectometer Deflections, Thesis, Ohio University.
112. Sadd, H.M., 2009. *Elasticity — theory, applications, and numerics*, Linacre House, Jordan Hill.
113. Saltan, M., and Sezgin, H., 2007. Hybrid neural network and finite element modeling of sub-base layer next term material properties in flexible pavements, *Materials & Design*. 28. 1725-1730.
114. Saltan, M., Terzi, S., and Küçükşille, E.U., 2011. Backcalculation of pavement layer moduli and Poisson's ratio using data mining, *Expert Systems with Applications*. 38, 2600-2608.
115. Saouma, V., Miura F., Lebon, G., Yagome, Y., 2011. A simplified 3D model for soil-structure interaction with radiation damping and free field input. *Bulletin Earthquake Engineering* 9, 1387–1402.
116. Scarpas, A, Al-Khoury, R, Van Gurp, C., Erkens, S., 1997. Finite element simulation of damage development in asphalt concrete pavements. *Eighth International Conference on Asphalt Pavements*, Washington D.C., 673-692.
117. Scarpas, A., Blaauwendraad, J., 2002. Spectral Element Technique for Efficient Parameter Identification of Layered Media. Part III: Viscoelastic Aspects. *International Journal of Solids and Structures*, 39, 2189-2201.

118. Seed, H.B., Wong, R.T., Idriss, I.M., and Tokimatsu, K., 1984. Moduli and damping factors for dynamic analysis of cohesionless soils. Earthquake Engineering Research Center Report UCB/EERC-84/14. Berkeley, California.
119. Sharma, S., and Das, A., 2008, Backcalculation of pavement layer moduli from falling weight deflectometer data using an artificial neural network. Canadian Journal of Civil Engineering, 35, 57-66
- Shaw, S., Warby, M.K., Whiteman, J.R., Dawson, C., and Wheeler, M.F., 1994. Numerical techniques for the treatment of quasistatic viscoelastic stress problems in linear isotropic solids. Computer Methods in Applied Mechanics and Engineering 118, 211-237.
120. Shaw, S. and Whiteman, J.R., 2000. Adaptive space-time finite element solution for volterra equations arising in viscoelasticity problems. Journal of Computational and Applied Mathematics 125, 337-345.
121. Shaw, S. and Whiteman, J. R., 2000. Numerical Solution of Linear Quasistatic Hereditary Viscoelasticity Problems. SIAM J. Numer. Anal. 38, 80-97.
122. Shell Global Inc., 1998. BANDS 2.0, BISAR 3.0 SPDM 3.0 – Software and User Manuals, Research and Technology Center.
- Sims, A. M., Stait-Gardner, T., Fong, L., Morley, J.W., Price, W.S., Hoffman, M., Simmons, A., Chindhelm, K., 2010. Elastic and viscoelastic properties of porcine subdermal fat using MRI and inverse FEA. Biomech Model Mechanobiol 9,703-711.
123. Sivanesarwan, N., Kramer, S.L., and Mahoney, J.P., 1991. Advanced backcalculation using a nonlinear least squares optimization technique. Transportation Research Record 1293, 93-102.
124. Sivanesarwan, N., Pierce, L.M., and Mahoney, J.P., 2001. Everseries pavement analysis programs, Washington Department of Transportation Report. Olympia, WA.
125. Slaughter, W. S., 2002. The linearized theory of elasticity, Birkhäuser Basel, Edition: 2002.

126. Siddharthan, R.V., Yao, J., and Sebaaly, P.E., 1998. Pavement strain from moving dynamic 3-D load distribution. *Journal of Transportation Engineering* 124, 557-566.
127. Siddharthan, R.V., Krishnamenon, N., and Sebaaly, P.E., 2000. Pavement response evaluation using finite-layer approach. *Transportation Research Record* 1709, 43-49.
128. Siddharthan, R.V., Krishnamenon, N., El-Mously, M., and Sebaaly, P.E., 2002. Investigation of tire contact stress distributions on pavement response. *Journal of Transportation Engineering* 128, 136-144.
129. Stubstad, R.N., Jiang, Y.J., and Lukanen, E.O., 2006. Guidelines for review and evaluation of backcalculation results, *FHWA-HRT-05-152 report*.
130. Sudhir Varma, M. Emin Kutay and Eyal Levenberg, 2013. A Viscoelastic Genetic Algorithm for Inverse Analysis of Asphalt. Layer Properties from Falling Weight Deflections". *Transportation Research Record*, 13-4091, 38-46.
131. Sun, L., Pan, Y., Gu, W., 2013. High-order thin layer method for viscoelastic wave propagation in stratified media. *Computer Methods in Applied Mechanics and Engineering* 257, 65-76.
132. Sun, Y., Yang, J., and Jiang, Y., 2014. A Theoretical analysis of thermoelastic damping model in laminated trilayered circular plate resonators. *World Journal of Mechanics* 4, 102-111.
133. Texas Transportation Institute (TTI), 2009. User's Manual for Finite Element Pavement Response Analysis Software TTI-PAVE, ICAR-508 final report.
134. Tileylioglu, S., Stewart, J.P., and Nigbor, R.L., 2011. Dynamic stiffness and damping of a shallow foundation from forced vibration of a field test structure. *Journal of Geotechnical and Geoenvironmental Engineering* 137, 344-353.
135. Timonin, A.M., 2013. Finite-Layer Method: a unified approach to a numerical analysis of interlaminar stresses, large deflections, and delamination stability of

- composites part 1. Linear behavior. *Mechanics of Composite Materials* 49, 231-244.
136. Tronto, J., Bordonal, A.C., Naal, Z., and Valim, J.B., 2013. Conducting polymers/layered double hydroxides intercalated nanocomposites. *Materials Science -Advanced Topics*, Chapter 1, first edition.
137. Uddin, W. and Garza, S., 2004. 3D-FE modeling and simulation of airfield pavements subjected to FWD impact load pulse and wheel loads. *Airfield Pavements*, 304-315.
138. Uddin, W. and Ricalde, L., 2007. Simulation of falling weight deflectometer for in-situ material characterization of highway and airport pavements. 6th European LS-DYNA Conference: Gothenburg.
139. Uzan, J., 1994. Dynamic linear back calculation of pavement material parameters, *Journal of Transportation Engineering* 120, 109-126.
140. University of Nevada at Reno (UNR), 2013. 3D-Move Analysis Software, Version 2.1, released on June 2013.  
<http://www.arc.unr.edu/Software.html#3DMove>
141. Varma, S., Kutay, E., and Levenberg, E., 2013. A VE genetic algorithm for inverse analysis of asphalt layer properties from falling weight deflections. *Transportation Research Record*.
142. Williams, M.L., Landel, R.F., Ferry, J.D., 1955. Temperature dependency of relaxation mechanisms in amorphous polymers and other glass forming liquids. *J. Amer. Chem. Soc.* 77, 3701-3707.
143. Wang, F., Lytton, R., 1993. System identification method for backcalculating pavement layer properties. *Transportation Research Record* 1384, 1-7.
144. Wang, H. and I.L. Al-Qadi, 2009. Combined effect of moving wheel loading and three-dimensional contact stresses on perpetual pavement responses. *Journal of Transportation Research Board* 2095, 53-61.
145. Weaver, S., 2012. Aging Effects on Subcutaneous Fat – Decreased on the Face and Increased on the Belly. <<http://blog.drseymourweaver.com/>>.

146. Xu, F., Lu, T.J., Seffen, K.A., 2008. Biothermomechanics of skin tissues. *Journal of the Mechanics and Physics of Solids* 56, 1852–1884.
147. Xu, Q., 2007. Modeling Mechanical and Thermal Behaviors of Asphalt Concrete for Laboratory Testing Applications. Thesis, Penn State.
148. Xu, Q., Solaimanian, M., 2009. Modeling linear viscoelastic properties of asphalt concrete by the Huet–Sayegh model. *International Journal of Pavement Engineering* 10, 401-422.
149. Xu, Q., Prozzi, J.A., 2014. A finite-element and Newton-Raphson method for inverse computing multilayer moduli. *Finite Elements in Analysis and Design* 81, 57-68.
150. Xu, Q., Solaimanian, M., 2009. Modelling linear viscoelastic properties of asphalt concrete by the Huet–Sayegh model. *International Journal of Pavement Engineering* 10, 401-422.
151. Xu, Q., Solaimanian, M., 2010. Modeling temperature distribution and thermal property of asphalt concrete for laboratory testing applications. *Construction and Building Materials* 24, 487–497.
152. Yoo, P.J., 2007. Flexible Pavement Dynamic Response Analysis and Validation for Various Tire Configurations. Ph.D. Dissertation, University of Illinois at Urbana Champaign, Urbana.
153. Zhao, R., Wyss, K., and Simmons, C.A., 2009. Comparison of analytical and inverse finite element approaches to estimate cell VE properties by micropipette aspiration. *Journal of Biomechanics* 42, 2768-2773.
154. Zhong, X.Z., Zeng, X., and Rose, J.G., 2002. Shear Modulus and Damping Ratio of Rubber-modified Asphalt Mixes and Unsaturated Subgrade Soils. *Journal of Materials in Civil Engineering* 14, 496-502.

## Vita

Qinwu Xu was born in Hunan, China. He received a Bachelor of Engineering degree in Civil Engineering with a minor in Computer Science in 2001, and a Master of Science in Road and Railway Engineering in 2004, both from Chang'an University. After relocating to the US, he earned a Master of Science degree in Civil Engineering from Penn State in 2007. He attended the University of Texas at Austin from 09/2008 to 05/2014 and received his PhD in Civil Engineering in summer 2014.

As a graduate researcher, he worked in finite element modeling polymer modified overlay and waterproof membranes for concrete bridges; developed methods to measure and invert heat transfer properties of asphalt concretes at Chang'an University and Penn State, respectively. He also studied the mechanism and design methods of fiber & polymer reinforced composites during his Ph.D. study. Xu's industrial experience includes more than 6.5 years as a project manager for the Transtec Group, Inc. in Austin, TX from 06/2007 to 01/2014. He was a leading researcher for the model developments of the Federal Highway Administration (FHWA)'s High Performance Paving III (HIPERPAV III<sup>®</sup>) software and the Intelligent Compaction Systems. Xu is the first author of the "Computer-Based Guidelines for Concrete Pavement — HIPERPAV III User Manual" (FHWA-HRT-09-048), and the 2<sup>nd</sup> author for "Accelerated Implementation of Intelligent Compaction Technology for Embankment Subgrade Soils, Aggregate Base, and Asphalt Pavement Materials" (FHWA-IF-12-002).

He was one of the "University's Top 10 Outstanding Graduate Students" in 2003 and "Excellent Graduate Student of Shaanxi Province" in 2004. Xu is currently a young member of the Transportation Research Board (TRB) committee AFD80.

Xu has over 30 publications in peer reviewed journals. One publication was nominated for TRB's 2009 K.B. Woods Best Paper Award. Two of them topped the most downloaded lists for 2009–2010 in *Materials Science and Engineering: A* and *Materials & Design* by ScienceDirect.

Email: [qinwu.xu@yahoo.com](mailto:qinwu.xu@yahoo.com)

This dissertation was typed by Qinwu Xu